Construction of Metal-Organic Cages with Bimetallic Motifs and Self-Assembly of a Molecular Knot

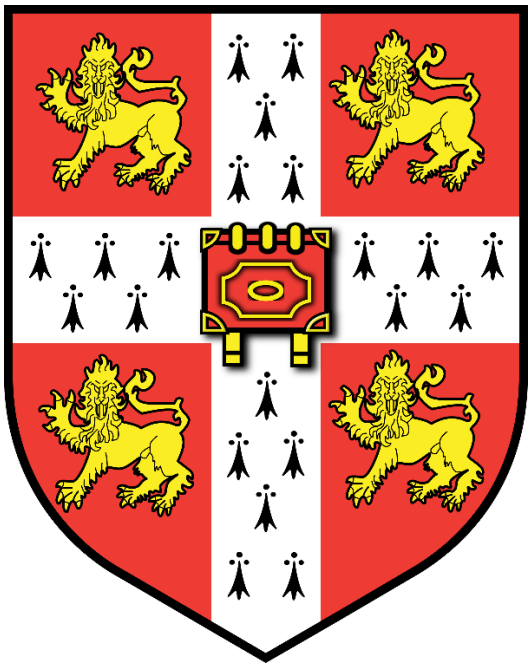

John Patrick Carpenter

Jesus College

July 2019

A dissertation submitted to the University of Cambridge as part of the

Doctor of Philosophy

Declaration

I hereby declare that this dissertation, entitled *Construction of Metal-Organic Cages with Bimetallic Motifs and Self-Assembly of a Molecular Knot*, is the result of work that I have undertaken in the University Chemical Laboratory at the University of Cambridge between October 2015 and July 2019. Except where stated to the contrary, this dissertation is my own work; credit for results obtained from collaboration with other parties is referenced to directly in the text. Figures that have been reproduced or adapted from other sources are indicated as such in their corresponding caption references. Aspects of the results presented herein have been published in peer-reviewed journals; original publications are referenced in the main text and a list of publications is included. This dissertation has not been, nor is currently being, submitted for any other degree, diploma or other academic qualification at this or any other university. It does not exceed 60,000 words in length.

John Patrick Carpenter

Abstract

Construction of Metal-Organic Cages with Bimetallic Motifs and Self-Assembly of a Molecular Knot

This thesis can be divided into two parts. These two sections differ not only in terms of the molecular structures they are concerned with, but also in their general approach to designing new, complex metal-organic structures.

The first portion of the thesis focuses on the self-assembly of metal-organic polyhedra built around bimetallic complexes. The components were specifically chosen to increase the chances of serendipitous and unexpected results coming about. A series of such structures are presented; a dicopper(I)- and disilver(I)-based octahedra, hetero-bimetallic cadmium(II)-copper(I) tetrahedral and a family of disilver(I)-based trigonal prism. Each of these structures are constructed around previously unreported coordination motifs. Nearly all of the results in this part of the thesis were arrived at through serendipity.

The second part takes an entirely different approach to the design of complex architectures. While it builds upon serendipitous results generate in the Nitschke group several years prior, it is a hypothesis-driven endeavour. A topologically complex molecular knot with eight crossings is reported. The ability of enantiopure subcomponents to affect the handedness of the knot is also investigated, with this work ultimately aiming toward the enantioselective synthesis of a purely topologically chiral molecules.

The thesis concludes with a chapter detailing conclusions drawn from this body of results and future work which follows from it on the synthesis of even more topologically complex structures.

John Patrick Carpenter

Acknowledgements

I would like to thank my supervisor, Prof Jonathan Nitschke, for your support, mentorship and insight throughout my PhD. You have allowed me a level of autonomy to pursue my ideas, goals and ambitions that I will always appreciate and value.

I would also like to thank the staff in the Cambridge Chemistry Department who have diligently aided me in my experiments. In particular, Dr Andrew Bond, Paul Skelton, Asha Boodhum, Duncan Howe, Andrew Mason and Dr Peter Grice deserve thanks, much of my work couldn't have happened without your technical support and intellectual input.

To all of the unfortunate souls who have had to work with me at Diamond and put up with my "that's obviously never going to diffract" samples – sorry about that. Tanya, Marion, Felix, Roy and Hugh – you have somehow managed to make what should have been a harrowing event quite an enjoyable memory.

To everybody in lab 354/353, thank you all for everything over the past four years, I really have thoroughly enjoy the experience. I'd particularly like to thank all of the members, past and present, of the office of dysfunctional materials, but particularly to Jake and Julia for seeing me through the good old iminoboronate days. Felix, Alex and Patrick for many great falafels and conversations. Tanya, Roy and Charlie for listening to an inordinate amount of rambling on my part about research. And everybody else for making my PhD such an enlivening and engaging experience.

The ResMoSys ITN is acknowledged for funding this work.

I wouldn't have had the opportunity to do this PhD if it weren't for Mammy, Daddy, Peter, Colm, Mary, Tom and Kevin supporting me all the way along. The same to all the rest of my family and my good friends. Finally, thank you Jess for enduring me, particularly through the write-up period. You've done an amazing job advising and encouraging me at the most testing points. I love you all.

Publications

(1) J. P. Carpenter, C. T. McTernan, T. K. Ronson, J. R. Nitschke, *J. Am. Chem. Soc.* **2019**, *J. Am. Chem. Soc.* **2019**, *141*, 11409-11413.

(2) F. J. Rizzuto, J. P. Carpenter, J. R. Nitschke, *J. Am. Chem. Soc.* **2019**, *141*, 9087-9095.

Abbreviations and Symbols

CD	Circular Dichroism
COSY	Correlation Spectroscopy
DOSY	Diffusion Ordered Spectroscopy
equiv/eq	Equivalents
ESI	Electrospray Ionisation
fac	Facial
HMBC	Heteronuclear Multiple Bond Coherence
HOMO	Highest Occupied Molecular Orbital
HSQC	Heteronuclear Multiple Quantum Coherence
mer	Meridional
MS	Mass Spectrometry
MxLy	A metal complex with x number of metals (M) and y number of ligands (L)
NIR	Near-Infrared
NMR	Nuclear Magnetic Resonance
NOE	Nuclear Overhauser Effect
NOESY	Nuclear Overhauser Effect Correlation Spectroscopy
$NTf2^-$	triflimide; bis(trifluoromethanesulfonyl)imide
OTf^-	triflate; trifluoromethanesulfonate
PCBM	[6,6]-phenyl C61 butyric acid methyl ester
ROESY	Rotating-Frame Nuclear Overhauser Effect Correlation Spectroscopy
RT	Room Temperature
SCXRD	Single Crystal X-ray Diffraction
UV-Vis	Ultraviolet-visible
δ	Chemical Shift

Table of Contents

1

Introduction

This Chapter will provide an introduction to, and general overview of, synthetic molecular self-assembly. Processes enabled by dynamic covalent chemistry and metal-coordination driven assembly will receive particular attention, as they are the cornerstone on which the work described in this thesis is built.

Subcomponent self-assembly, which can be described as an amalgamation of dynamic covalent chemistry and metal-coordination driven assembly, is also described. The features of this approach which give rise to its propensity for producing such structural diversity are also detailed.

The role of the flexibility and rigidity of certain building blocks is discussed. Cases where incorporation of flexible linkages into the organic building blocks has led to new and unprecedented structures are highlighted. Finally, the use of bimetallic complexes in molecular self-assembly is discussed. Particular attention is paid to the paddle-wheel motif which is the most commonly occurring bimetallic motif in synthetic self-assembled systems.

Each subsequent Chapter in this thesis will begin with a section introducing the concepts and chemistry relating specifically to that Chapter. In particular, Chapters 3 and 4 will begin with introduction to the bimetallic motifs most relevant to the work described therein. Chapters 5 and 6 will introduce material relevant to molecular topology and topological chirality.

1.1 Molecular Self-Assembly

Molecular self-assembly is the process whereby individual molecules form a defined larger species, by means of thermodynamically-driven reactions and interactions.[1] The concept of spontaneous ordering of matter spans across most, if not all, of the sciences. The process's ubiquity is evidenced by the range of different processes and contexts in which it occurs, from crystal nucleation and growth[2] to galactic superstructures.[3]

Regardless of the arena, one common feature of the process occurring in these systems is that it requires the dissipation of energy.[4] In other words, the formation of an ordered state, be it a larger structure or a pattern, will only occur if the interactions that drive the formation result in a net dissipation of energy. Harnessing this process in synthetic systems is one of the core challenges which supramolecular chemistry aims to address.[5]

One of the key features of self-assembled structures is that the interactions which hold them together are reversible under the conditions of formation.[6,7] This allows for the forming and breaking of bonds and interactions holding the building blocks together. This process of continual reformation of the reaction mixture's components allows the system to sample a range of different chemical configurations. Each of these different states will have a discrete energy associated with it. If the system is under thermodynamic control then, with time, the components will equilibrate toward the configuration which minimises the Gibbs free energy of the overall system. This process is commonly referred to as error-checking.

Many different reversible interactions have been described which enable this process to occur. With bond dissociation energies less than those of typical covalent bonds (which range from $150 - 450\ \text{kJ mol}^{-1}$), non-covalent bonding such as van der Waals interactions, π–π interactions, electrostatic effects, hydrogen and halogen bonding and the hydrophobic effect have been studied extensively in the context of self-assembly.[8,9] Whilst the individual interactions between the building blocks are weak, when enough act in concert they are capable of forming stable structures.

1.2 Imine Condensation

Dynamic combinatorial chemistry[10,11] is an area of supramolecular chemistry in which the reversible bonding of simple molecular blocks produces more complex structures under thermodynamic control.[12] Imine bond formation is one of several covalent bond forming reactions that can form and dissociate in a reversible manner. This property has led to its extensive employment in the area of molecular self-assembly.[13]

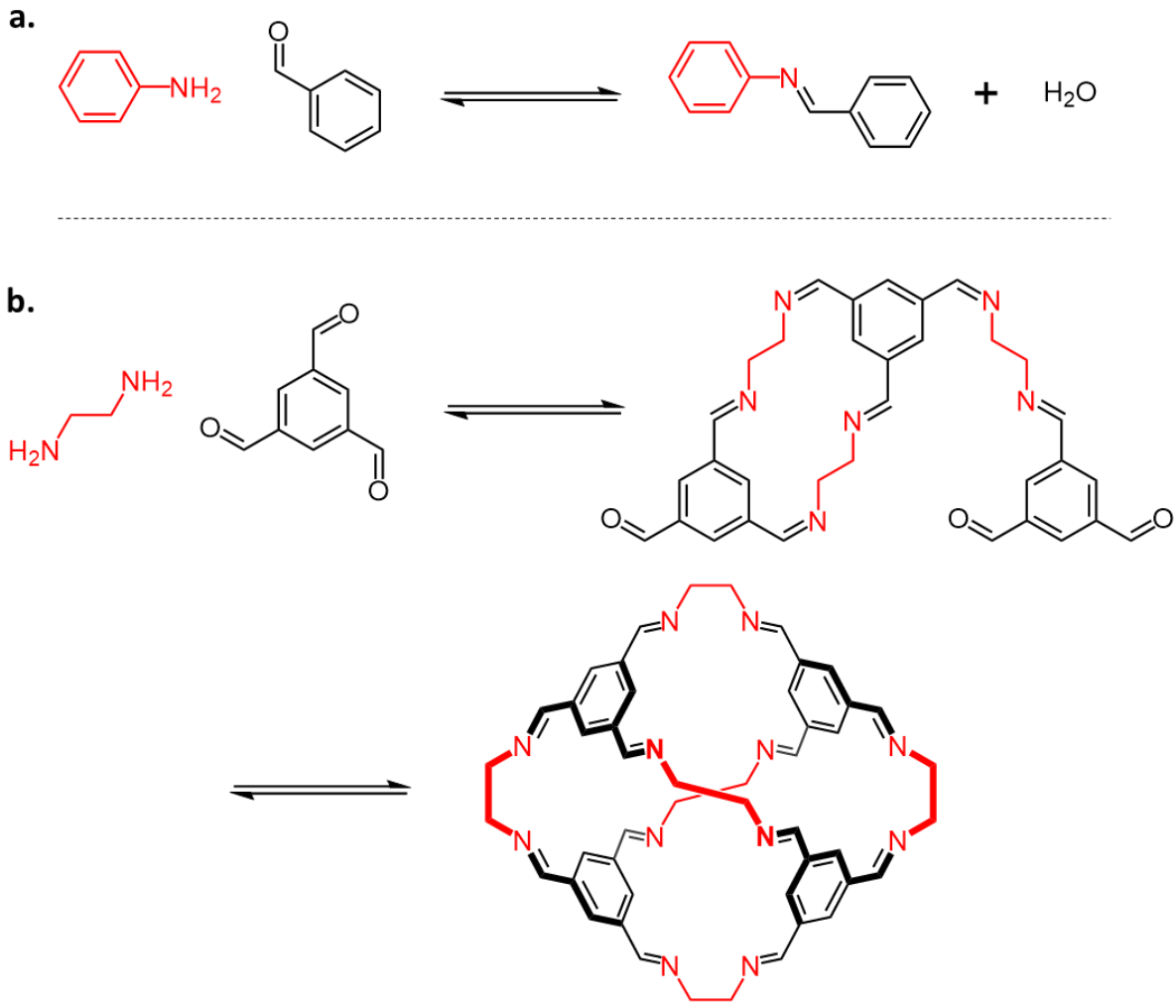

Figure 1.1 | **a.** An example of an imine condensation between aniline and benzaldehyde. **b.** This reversible reaction has been employed extensively in the synthesis of various molecular cages, such as this octahedron by Cooper *et al.*[14]

Reversible condensation of a nucleophilic amine with an electrophilic carbonyl group, as shown in Figure 1.1, generates a dynamic imine bond and one equivalent of water. This new functionality may now react in a variety of different ways, as the imine can behave as both a nucleophile and an electrophile. It is prone to hydrolysis back to the original amine and carbonyl compound. Exchange reactions are also possible, whereby an amine can displace the amine already incorporated into the imine, particularly if it is more nucleophilic.[15]

Such moieties have been employed extensively in the synthesis of a range of self-assembled molecules. The Cooper group have shown how the reaction of a variety of multitopic amine-based components with trialdehyde-based building blocks can lead to the formation of a range of three-dimensional cage molecules (Figure 1.1).[14]

When considering the assembly of these large covalent self-assembled structures, a number of factors must be taken into consideration. First, the system will tend toward the structures which maximise the number of energetically-favourable bond formations and interactions (π–π interactions, hydrogen bonding, etc.). Simultaneously, the system will aim to maximise the number of particles in the system, as a direct consequence of the second law of thermodynamics. The interplay of these enthalpic and entropic effects has led to many unexpected outcomes in synthetic self-assembled structures.[16–18]

The labile nature of the imine bond is therefore of central importance, enabling error-checking, which in turn facilitates the formation of complex and intricate structures. However, the presence of this functional group in the resulting structures often means that they are relatively fragile and unstable under most conditions other than those in which they were formed. Destruction of the self-assembled structure can be induced by changes in solvent composition, concentration, temperature, addition of nucleophiles or electrophiles and pH changes.[19]

Kinetic trapping of these reversible imine functionalities is possible. Imines, particularly in their charged iminium state, are prone to reduction. Treating the isolated imine with a simple reducing agent, such as sodium borohydride, leads the formation of the corresponding secondary amine and is referred to as indirect reductive amination (as the imine must be formed before the reducing agent is introduced).[20,21]

Direct reductive amination employs weaker reducing agents (such as sodium cyanoborohydride or triacetoxyborohydride) which are reactive toward the imine functionality, but not towards the relatively inert precursory carbonyl group. This allows the amine and

carbonyl groups to react together before the imine is reduced, yielding the secondary amine in a one-pot procedure.[22]

Such methods have been employed to produce purely organic molecular Borromean links[23] and molecular capsules,[24] which would otherwise have been unstable upon demetallation. It should be noted that these works reported relatively modest yields.

1.3 Metal-Organic Polyhedra

The field of coordination-driven self-assembly has led to the generation of many intricate and complex architectures over the years. Structures as diverse as cages,[25] helicates,[26] polymers,[27] and molecular knots have been synthesised by such means.[28]

The ubiquity of metal-ligand interactions in synthetic self-assembling systems arises from a number of key features of this type of interaction. Firstly, the dative bond which forms between the metal cation and the ligand is reversible, a prerequisite feature in any self-assembly process.[29] Exquisite control over the strength of these interactions is also possible. The strength of bonding is dependent on both the nature of the metal cation and of the ligand. Indeed the water exchange rate constant k_{H2O}, a measure of the metal-ligand bond strength, is known to vary over twenty orders of magnitude for different metal-ligand combinations.[30]

Secondly, metal-ligand interactions can impart directionality, restricting ligands so that that they will protrude from each of the metal centres at certain predictable angles. This structural rigidity arises from the preferred coordination geometries of the metal cations.[31–33]

The directional bonding approach, perhaps best exemplified in the work of Fujita[31] and Stang[32] relies on the use of either bent or linear organic building blocks, which act as ligands, and a metal cation, typically Pd^{II} (Figure 1.2). The direction at which the ligands radiate out from the metal centres dictates the nature of the larger assembly, oftentimes in a highly predictable manner.[34,35]

The third feature which has led to the flourishing of metal-coordination driven self-assembly is that the nature of the ligand, its topicity, denticity, size and flexibility, can all be controlled and tailored. The ability to customise the ligands has enabled the formation of broad range of self-assembled species, each with distinct properties, such as size,[36] binding ability[37,38] and fluorescence.[39]

In Figure 1.2, a tritopic tripyridyl building block is combined with a Pd^{II} source and 2,2'-bipyridine.[40] The square planar coordination environment preferred by the Pd^{II} results in the organising of the tripodal ligands into a *pseudo*-octahedral structure, with the coordination sphere of each of the Pd^{II} centres completed by 2,2'-bipyridine.

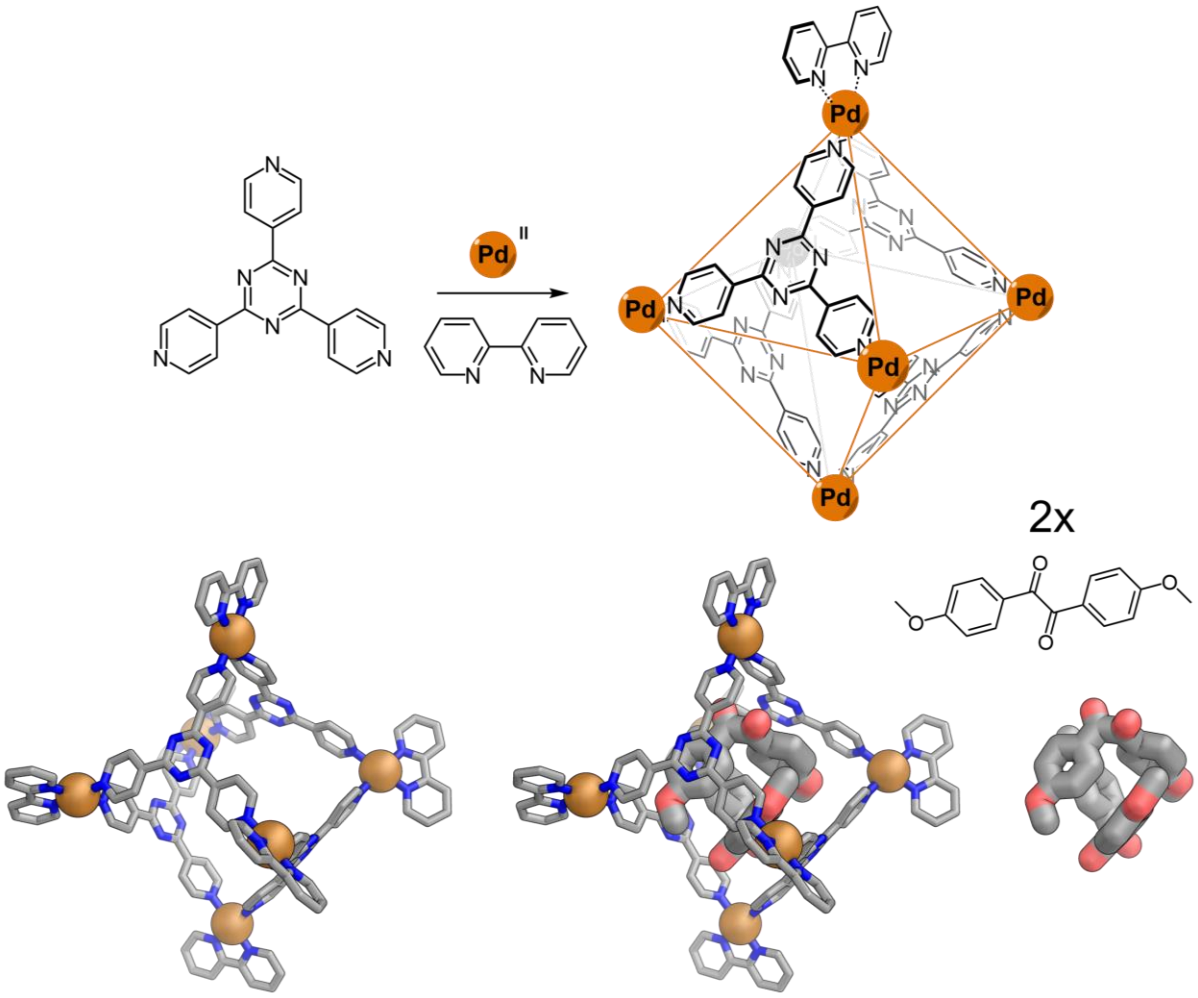

Figure 1.2 | A metal-organic cage formed with a tritopic pyridine containing ligand. Solid state evidence of the binding of 4,4'-dimethoxybenzil inside the cavity of the octahedron.[41]

These metal-organic structures have found applications in a range of different areas, most noticeable in host-guest chemistry.[42] In the example shown in Figure 1.2, the space defined by the three-dimensional architecture is chemically distinct from that of the bulk solution.[41] As such, it can act as a receptor for a range of different substrates. Here, two molecules of 4,4'-dimethoxybenzil are observed to bind within the cavity. These host-guest interactions can be driven by a number of different effects. In this case, guest uptake is attributed to both the π–π interactions between the electron-poor walls of the cage and the relatively electron-rich guest and to the minimisation of repulsive hydrophobic interactions between the guest and the external, aqueous environment. This is enhanced by the repulsion of high-energy water molecules occupying the cavity of the host.[43–45]

1.4 Subcomponent Self-Assembly

The ability of transition metals to push the equilibrium toward the imine, and away from the amine and carbonyl functionalities, was first reported by Busch[46,47] and Curtis[48] in the 1960s. The roots of the subcomponent self-assembly approach lie in this template synthesis strategy, used in the creation of a range of different macrocycles (Figure 1.3a).

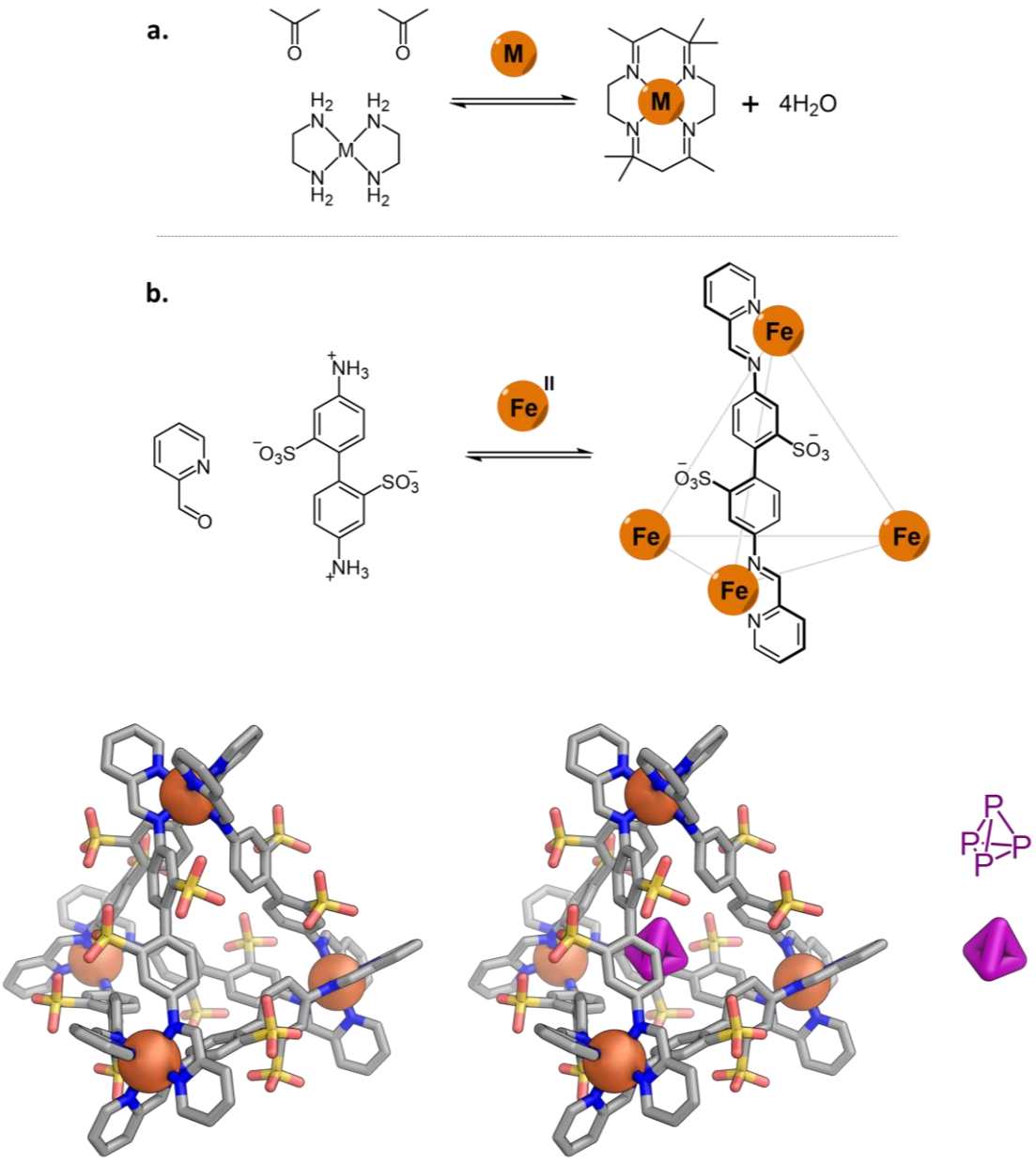

Figure 1.3 | a. Metal template synthesis of a 14-membered macrocycle.[49] **b.** Formation of an M_4L_6 tetrahedral cage via a subcomponent self-assembly approach.[50] The cage is observed to bind the pyrophoric phosphorus allotrope P_4.

Several decades later, the utility of the approach in self-assembly was explored more thoroughly. The preparation of a Borromean link by Stoddart *et al.*[51] and, later, a Solomon link[52] stand out as two particularly noteworthy examples. Leigh and coworkers have successfully employed this type of chemistry in the synthesis of different knots.[53,54]

These self-assembly processes involve the formation of covalent (carbon-heteroatom) and dative (metal-heteroatom) bonds. As such, the process brings both the ligand and the metal-organic structure into being. The utility of such an approach is apparent. The synthesis of the system's building blocks is simplified. Complex self-assembled structures can be accessed without the need for as much synthetic effort. The idea that the components used in the self-assembly process are formed in the same pot as that in which the self-assembly occurs led to the coining of the term subcomponent self-assembly,[55] with both the amine- and carbonyl-containing species acting as precursors to the eventual building blocks.

Late stage diversification of structures is also possible.[56] Rather than requiring the synthesis of new derivatives of the original building blocks, different subcomponents can be selected. Further to this, the substitution and metathesis reactions described in Section 1.2 allow for the exchange of subcomponents after the formation of the self-assembled structure.

Another defining feature of the subcomponent self-assembly approach, seen particularly in the work of the Nitschke group, is its propensity to form a broad array of geometrically and topologically interesting architectures from simple building blocks.[36,57] This tendency typically arises from a combination of several factors. The first is a stereochemical consideration.[58] Each of the metal vertices of the tetrahedron, shown in Figure 1.4, can adopt one of two configurations, Λ or Δ. If each of the subcomponents is achiral, or a racemic mixture of enantiomers, then an equal distribution of the two configurations across all corners will necessarily form in any self-assembled system. The two tetrahedra shown are enantiomers of each other, with each tetrahedron being homochiral. All four vertices are of the same handedness.

This may not always be the case, however. In fact three structures composed of the same building blocks are possible, each differing only in their stereochemistry and symmetry. For example, the $\Lambda\Lambda\Lambda\Delta$ isomer, which has C_3 symmetry, and the $\Lambda\Lambda\Delta\Delta$ isomer, with S_4 symmetry, differ only in the handedness of their vertices.

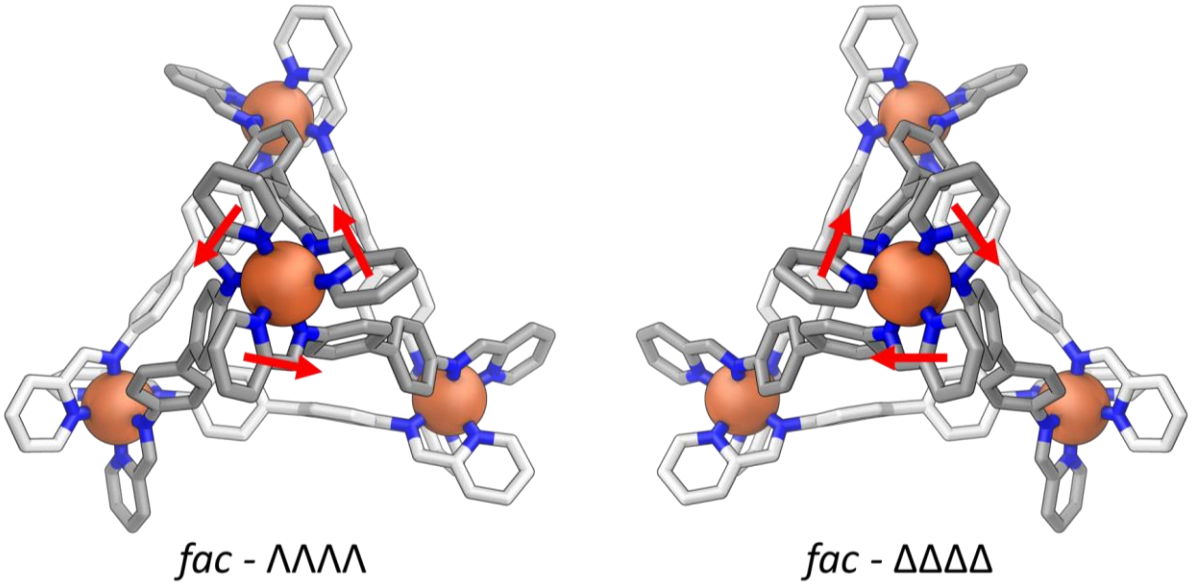

Figure 1.4 | Λ and Δ vertices in two M_4L_6 tetrahedra. The tetrahedra, which are both homochiral, are enantiomers of each other.

In the case of these M_4L_6 tetrahedral stereoisomers, this distinction can appear trivial from a structural perspective. While it may lead to slight variations in the cavity of cage, these changes have not been demonstrated to significantly affect other properties of the cages, such as host-guest affinity.

However, in other cases this phenomenon has given rise to interesting effects. The assembly of a $M_{12}L_6$ cuboctahedron from its fourfold-symmetric porphyrin building block produces a highly symmetric structure which has chiral octahedral point symmetry (Figure 1.5).[59] Each of its vertices are of the same handedness. When treated with C_{60} this cage undergoes a stereochemical transformation, producing the S_6 symmetric isomer which can encapsulate two equivalents of the fullerene. Both Λ and Δ handed vertices are present, in a 1:1 ratio. This response is most likely due to the system maximising favourable interactions between the host and its guests.

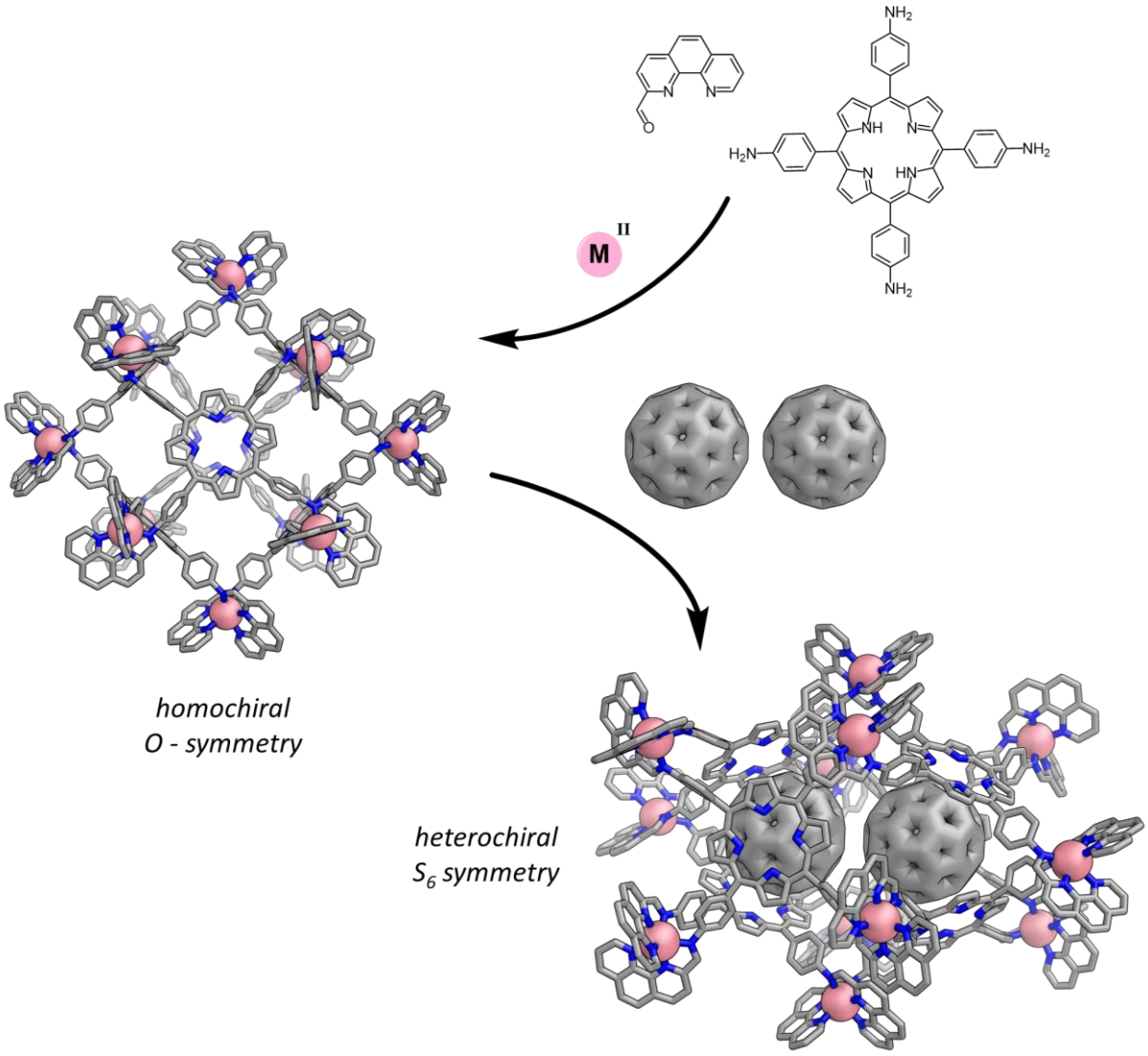

Figure 1.5 | Assembly of a $M_{12}L_6$ cuboctahedral cage which maintains the symmetry of its fourfold-symmetric building blocks. Encapsulation of two fullerenes leads to a stereochemical rearrangement of the architecture, rendering it a better binder of the two guest molecules.[59]

Another factor is that each metal complex may adopt one of two geometrically distinct configurations, either *mer* or *fac* (Figure 1.6).[60,61] The *fac* isomer, where each of the identical donors (for example the imine donors, highlighted as spheres in Figure 1.6) occupy one face of the octahedron defining the metal's coordination sphere, often leads to the formation of smaller structures.[62–64] This is a consequence of the angles at which the ligands radiate out from the metal centres. In contrast, the *mer* isomer, where the identical ligands sit on a plane which passes through the metal centre, tends to result in larger structures as a result of the splayed angles at which the ligands emanate from the metal centres.[57,61,65] Mixtures of the two configurations have also been observed in several cases.[36,66]

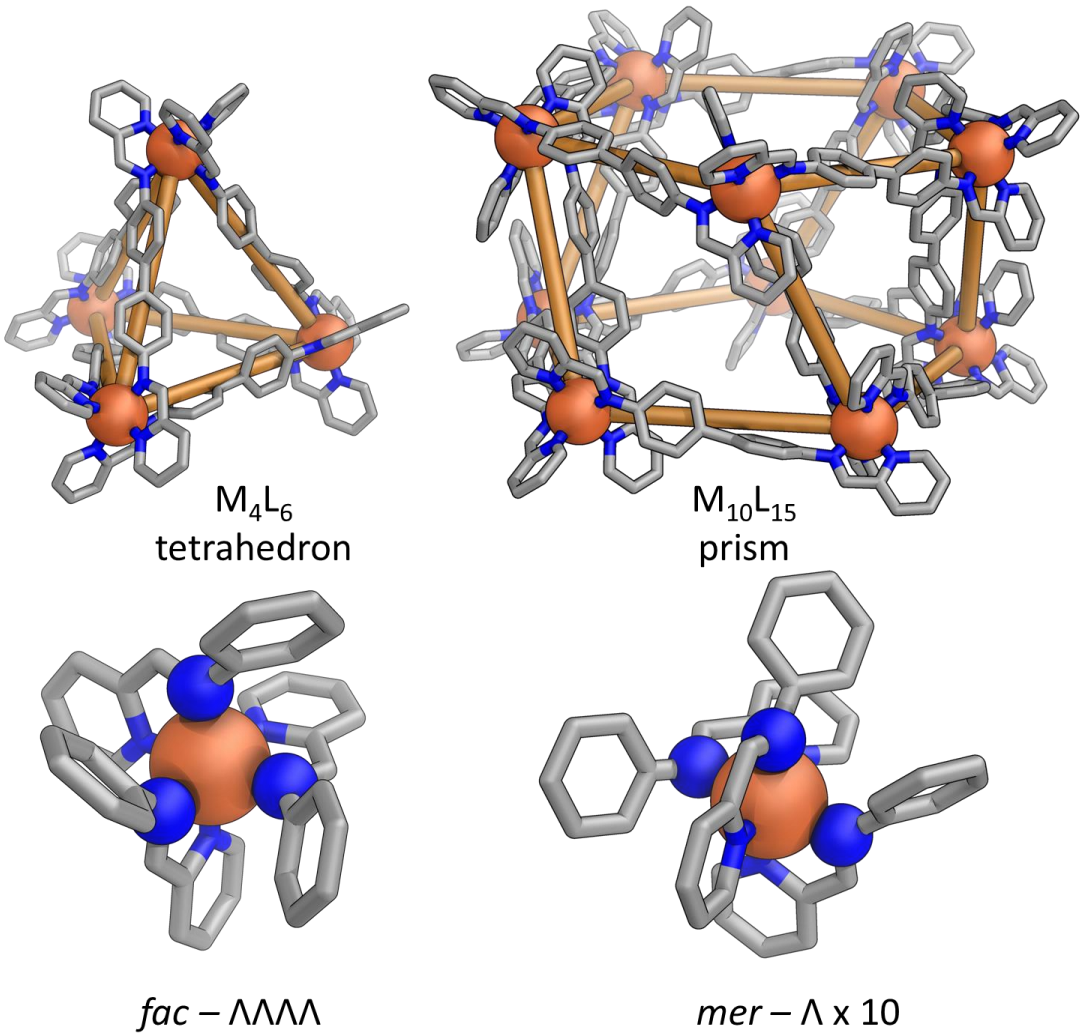

Figure 1.6 | Tetrahedral and pentagonal prismatic structures formed from the same dianiline subcomponent. Substituents on the biaryl dianiline residue have been omitted for clarity. Isolated vertices from each of the structures, showing their distinct ligand configurations. Imine nitrogen atoms are represented as spheres.

It is interesting to note that these two structural phenomena, Λ/Δ mixtures and *mer*/*fac* isomers, can occur for any combination of aldehyde- and amine-based subcomponents when coupled with a transition metal. Certain combinations may be more likely to produce one set of outcomes, but this is not predictable. This ability to generate structural diversity is derived almost entirely from the metal complexes, rather than flexibility inherent to the organic ligand.

1.5 Ligand Flexibility

Building flexibility into the organic component of metal-organic assemblies has also led to the creation of a variety of new architectures. One of the best known examples comes from the work of Lehn and coworkers (Figure 1.7).[26,67] Flexible tris-bipyridine containing ligands, when treated with different transition metal salts lead to the formation of a series of different planar grid structures. Each of the grids is built around a different number of metal centres. Which structure forms is a consequence of both the ligands linker groups and anion templation effects.

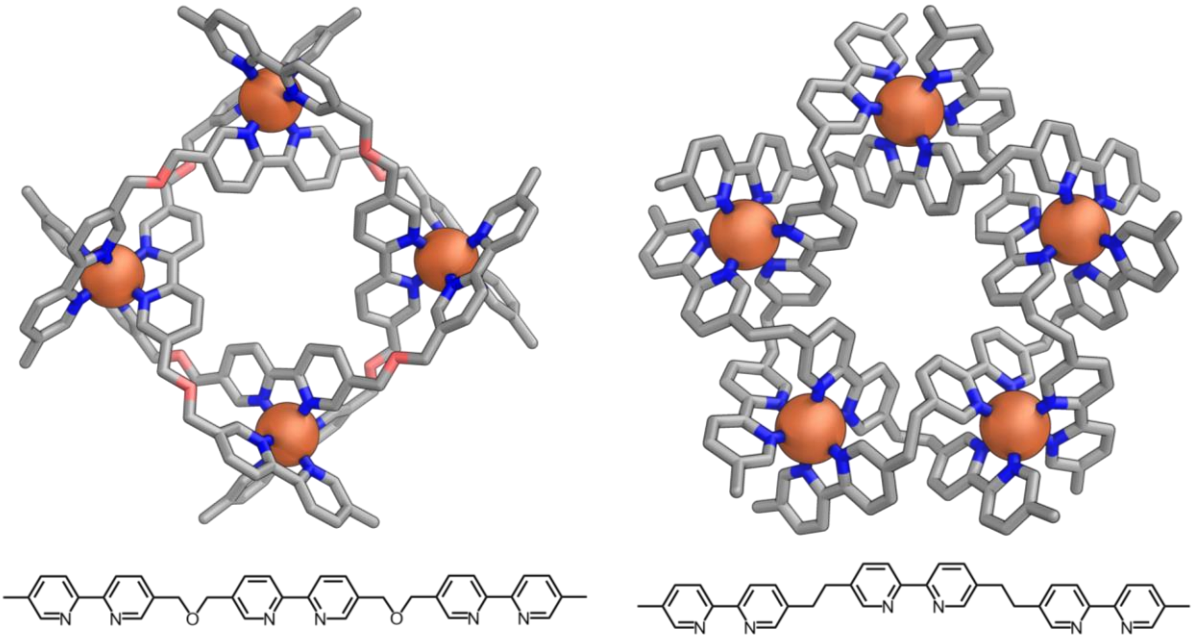

Figure 1.7 | A tetrameric and pentameric circular helicate formed from flexible organic building blocks. A hexameric relative has also been reported.[26,68]

The Ward group have developed a range of different metal-organic structures.[69] Many of these large polyhedral structures are constructed with flexible ligands. Among these structures are a octanuclear cubic cage (Figure 1.8a),[70] a heteroleptic dodecanuclear cuboctahedron (Figure 1.8b),[71] and two-dimensional coordination networks.[72]

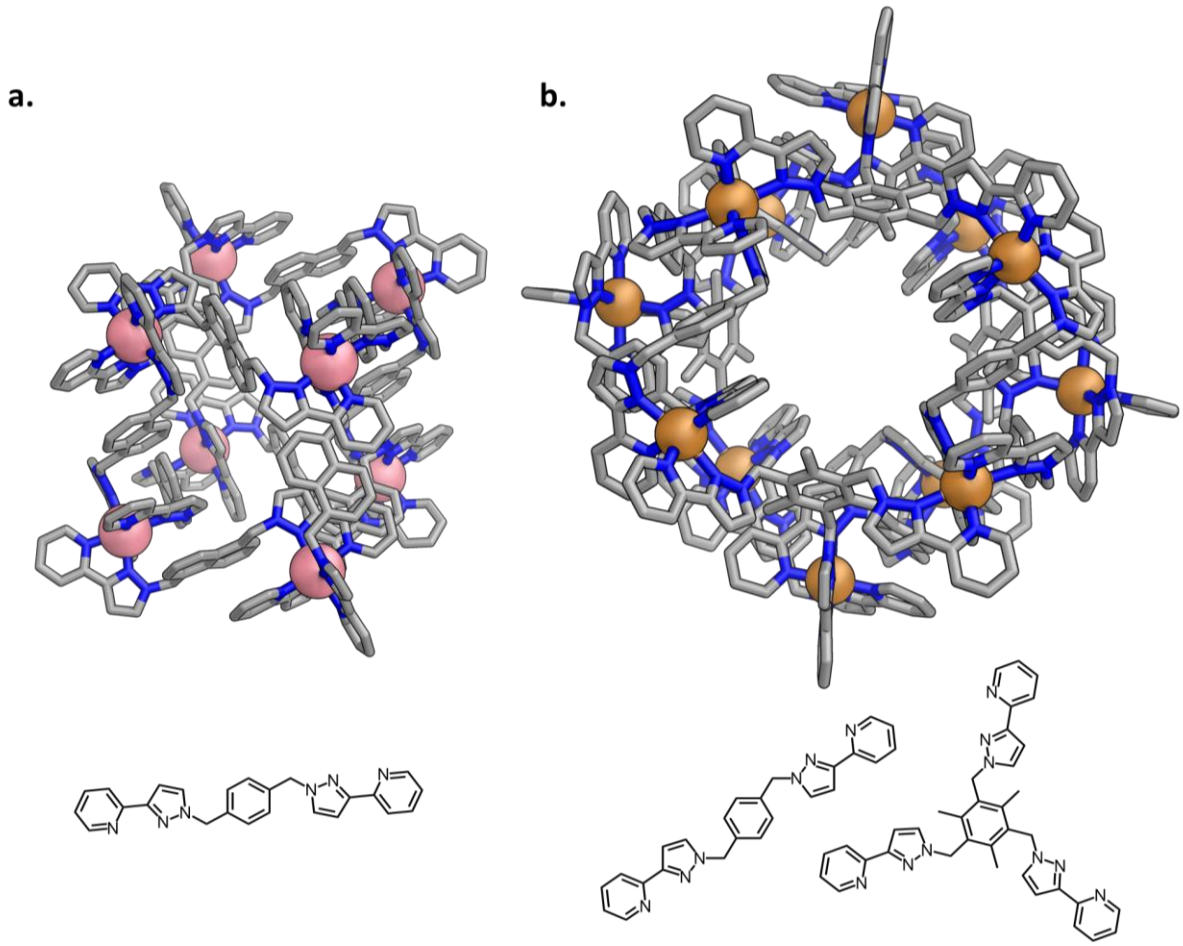

Figure 1.8 | a. An octanuclear cubic cage based assembled from a flexible bis-bidentate ligand.[70] **b**. A twelve metal centre cage formed with two flexible components.[71]

These architectures have found a range of applications particularly in the areas of host-guest chemistry[73] and catalysis.[74] The positively charged cage centre results in a high effective concentration of hydroxide anions around the faces of the cube in aqueous media. This phenomenon has been used to catalyse the Kemp elimination reaction of benzisoxazole within the cavity of the cage. [75]

1.6 Bimetallic Complexes in Metal-Organic Cages

Bimetallic complexes that contain two metal ions in close proximity are an area of active interest, particularly in catalysis.[76,77] In molecular self-assembly they have been employed as structural elements in a range of metal-organic cages (Figure 1.9)

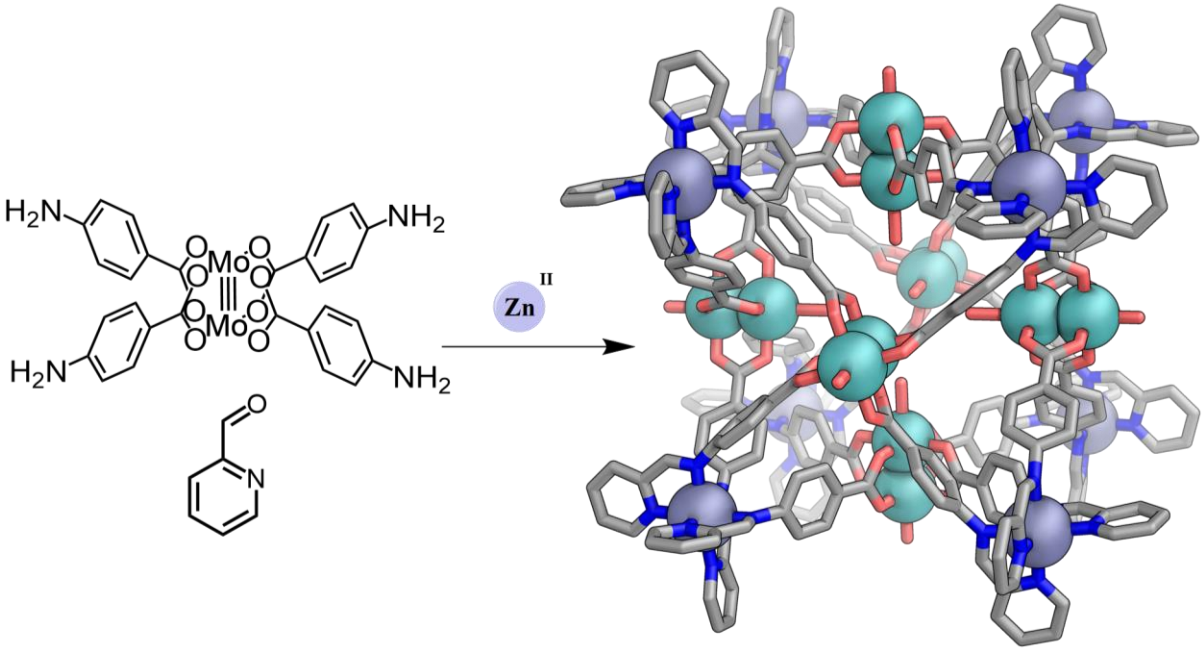

Figure 1.9 | Assembly of a metal-organic cube, the *C4* faces of which are based around Mo^{II} paddle-wheel complexes.[78]

One particularly common bimetallic motif is the paddle-wheel complex.[79] In Figure 1.9, the bimetallic unit is used to form a *C4* symmetric subcomponent which can be assembled into a cubic structure which incorporates twelve Mo^{II} and eight Fe^{II} centres.[78] In this example the paddle-wheel is formed in advance of the self-assembly step and doesn't play an active role in the assembly process. In other cases, the paddle-wheel complex can act as the point at which reversible bond forming and breaking occurs, enabling the self-assembly.

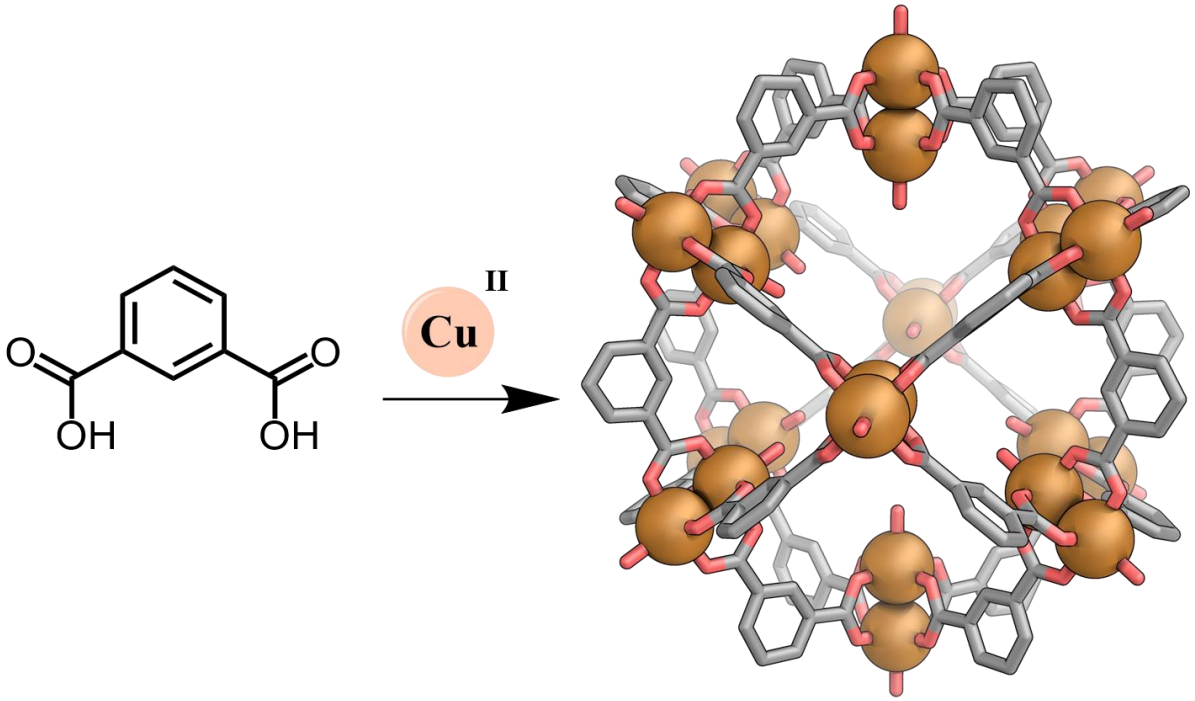

Figure 1.10 | Formation of a large truncated cuboctahedron formed with isophthalic acid and $Cu^{II}(NO_3)_2$.[80]

The truncated cuboctahedron reported by Yaghi demonstrated how the bimetallic paddle-wheel motif could operate as an alternative to the metal-pyridine linkages most commonly used at the time (Figure 1.10).[80] The two examples in Figures 1.9 and 1.10 use the bimetallic unit as a relatively rigid motif, about which the organic building blocks can be organised in a predictable manner.

Utilising these types of coordination complexes as flexible units has been less well studied, however. We envisaged that if bimetallic units which are capable of adopting a number of different coordination modes were employed, a range of interesting polyhedral structures may result. This could be in a manner which is analogous to the outcomes occasionally observed with flexible organic building blocks, as described in Section 1.5.

Further introduction to the types of coordination complexes we have chosen to study is available at the beginning of Chapters 3 and 4. Similarly, material and discussion pertaining to molecular knots, topology and chirality are discussed in detail at the beginning of Chapters 5 and 6.

1.7 Aims and Outline

The aforementioned strategies have been used to form regular polygons and polyhedra. Along the way a number of phenomena, such as heterochirality and *fac*/*mer* distributions in metal-organic cages, have led to interesting and oftentimes unprecedented structures forming. Many other interesting examples of geometrically complex structures have been observed when flexible ligands were employed.

Flexibility at the metal centres has been less well studied. It was reasoned that these sites could function in a manner analogous to the flexible ligands described above. The work in the first part of this thesis, comprising Chapters 3 and 4, focuses on the use of bimetallic complexes in molecular self-assembly, utilising a subcomponent self-assembly approach.

Chapter 3 details the use of 6-(diphenylphosphino)formylpyridine, a subcomponent which enforces the formation of bimetallic complexes by having proximal donor atoms whose coordination vectors do not converge. The formation of two homo-bimetallic $M^{I}_{12}L_4$ *pseudo*-octahedral cages is described. This Chapter also explores the use of this subcomponent in the formation of hetero-bimetallic based cages. In particular, a new class of $Cd_4Cu_4L_4$ tetrahedral cages is described.

Chapter 4 describes the formation of a trigonal antiprism based on a tritopic building block, the first such reported structure. Again, it is based on a new type of bimetallic complex, this time formed using a 1,8-naphthyridine-based subcomponent. The cage assembles around a pair of anionic templates, which are shown to bind internally by crystallographic and solution-phase data. A range of structurally distinct anions can serve as competent templates, and the cage can adapt its shape to allow for this.

Chapter 5 explores the synthesis of a topologically complex, eight crossing molecular knot formed using a subcomponent self-assembly approach. The 8_{19} knot possesses D_2 symmetry and is geometrically distinct from that reported by Leigh *et al*.[81] while remaining topologically equivalent. Characterisation of both the paramagnetic Fe^{II} and diamagnetic Zn^{II} congeners, in the solution-phase and solid-state, is reported.

Chapter 6 details efforts toward the enantioselective synthesis of a purely topologically chiral molecular knot. Employing an enantiopure dianiline subcomponent, diastereoselective

synthesis of a closely related knot is achieved. Efforts to displace this chiral dianiline with an achiral dianiline, while maintaining the integrity of the knotted structure and therefore the topological chirality of the knot, are also described.

Finally, Chapter 7 describes how three-dimensional architectures might be used to form a range of topologically complex catenanes and knots. A series of possible targets is outlined and discussed, with particular attention given to one of the targets, a fifteen crossing $15n_{41185}$ molecular knot. This future work builds directly on the work described in Chapters 5 and 6. The Chapter details several conclusions drawn from the work detailed in this thesis.

1.8 References

(1) Whitesides, G. M.; Boncheva, M. Beyond Molecules: Self-Assembly of Mesoscopic and Macroscopic Components. *Proc. Natl. Acad. Sci. U. S. A.* **2002**, *99*, 4769–4774.

(2) Zhou, J.; Yang, Y.; Yang, Y.; Kim, D. S.; Yuan, A.; Tian, X.; Ophus, C.; Sun, F.; Schmid, A. K.; Nathanson, M.; et al. Observing Crystal Nucleation in Four Dimensions Using Atomic Electron Tomography. *Nature* **2019**, *570*, 500–503.

(3) Bahcall, N. A. Large-Scale Structure in the Universe Indicated by Galaxy Clusters. *Annu. Rev. Astron. Astrophys.* **1988**, *26*, 631–686.

(4) Lehn, J.-M. Toward Self-Organization and Complex Matter. *Science* **2002**, *295*, 2400–2403.

(5) Philp, D.; Stoddart, J. F. Self-Assembly in Natural and Unnatural Systems. *Angew. Chem. Int. Ed. English* **1996**, *35*, 1154–1196.

(6) Lehn, J.-M. Toward Complex Matter: Supramolecular Chemistry and Self-Organization. *Proc. Natl. Acad. Sci. U. S. A.* **2002**, *99*, 4763–4768.

(7) Lehn, J.-M. Supramolecular Chemistry—Scope and Perspectives Molecules, Supermolecules, and Molecular Devices (Nobel Lecture). *Angew. Chem. Int. Ed. English* **1988**, *27*, 89–112.

(8) Müller-Dethlefs, K.; Hobza, P. Noncovalent Interactions: A Challenge for Experiment and Theory. *Chem. Rev.* **2000**, *100*, 143−167

(9) Hunter, C. A.; Sanders, J. K. M. The Nature of π-π Interactions. *J. Am. Chem. Soc.* **1990**, *112*, 5525–5534.

(10) Lehn, J.-M. From Supramolecular Chemistry towards Constitutional Dynamic Chemistry and Adaptive Chemistry. *Chem. Soc. Rev.* **2007**, *36*, 151–160.

(11) Li, J.; Nowak, P.; Otto, S. Dynamic Combinatorial Libraries: From Exploring Molecular Recognition to Systems Chemistry. *J. Am. Chem. Soc.* **2013**, *135*, 9222–9239.

(12) Corbett, P. T.; Leclaire, J.; Vial, L.; West, K. R.;Wietor, J. –L.; Sanders, J. K. M.; Otto, S. Dynamic Combinatorial Chemistry. *Chem. Rev*. **2006**, *106*, 3652−3711

(13) Briggs, M. E.; Cooper, A. I. A Perspective on the Synthesis, Purification, and Characterization of Porous Organic Cages. *Chem. Mater.* **2017**, *29*, 149–157.

(14) Mitra, T.; Jelfs, K. E.; Schmidtmann, M.; Ahmed, A.; Chong, S. Y.; Adams, D. J.; Cooper, A. I. Molecular Shape Sorting Using Molecular Organic Cages. *Nat. Chem.* **2013**, *5*, 276–281.

(15) Wood, C. S.; Ronson, T. K.; Belenguer, A. M.; Holstein, J. J.; Nitschke, J. R. Two-Stage Directed Self-Assembly of a Cyclic [3]Catenane. *Nat. Chem.* **2015**, *7*, 354–358.

(16) Al-Rasbi, N. K.; Tidmarsh, I. S.; Argent, S. P.; Adams, H.; Harding, L. P.; Ward, M. D. Mixed-Ligand Molecular Paneling: Dodecanuclear Cuboctahedral Coordination Cages Based on a Combination of Edge-Bridging and Face-Capping Ligands. *J. Am. Chem. Soc.* **2008**, *130*, 11641–11649.

(17) Rizzuto, F. J.; Carpenter, J. P.; Nitschke, J. R. Multisite Binding of Drugs and Natural Products in an Entropically Favorable, Heteroleptic Receptor. *J. Am. Chem. Soc*. **2019**, *141*, 9087−9095

(18) Sawada, T.; Yamagami, M.; Ohara, K.; Yamaguchi, K.; Fujita, M. Peptide [4]Catenane by Folding and Assembly. *Angew. Chem. Int. Ed.* **2016**, *55*, 4519–4522.

(19) McConnell, A. J.; Wood, C. S.; Neelakandan, P. P.; Nitschke, J. R. Stimuli-Responsive Metal–Ligand Assemblies. *Chem. Rev.* **2015**, *115*, 7729–7793.

(20) Baxter, E. W.; Reitz, A. B. Reductive Aminations of Carbonyl Compounds with Borohydride and Borane Reducing Agents. In *Organic Reactions*; John Wiley & Sons, Inc.: Hoboken, NJ, USA, **2002**; 1–714.

(21) Abdel-Magid, A. F.; Carson, K. G.; Harris, B. D.; Maryanoff, C. A.; Shah, R. D. Reductive Amination of Aldehydes and Ketones with Sodium Triacetoxyborohydride. Studies on Direct and Indirect Reductive Amination Procedures. *J. Org. Chem*. **1996**, *61*, 3849-3862

(22) Gomez, S.; Peters, J. A.; Maschmeyer, T. The Reductive Amination of Aldehydes and Ketones and the Hydrogenation of Nitriles: Mechanistic Aspects and Selectivity Control. *Adv. Synth. Catal.* **2002**, *344*, 1037–1057.

(23) Peters, A. J.; Chichak, K. S.; Cantrill, S. J.; Stoddart, J. F. Nanoscale Borromean Links for Real. *Chem. Commun.* **2005**, 27, 3394.

(24) Mosquera, J.; Zarra, S.; Nitschke, J. R. Aqueous Anion Receptors through Reduction of Subcomponent Self-Assembled Structures. *Angew. Chem. Int. Ed.* **2014**, *53*, 1556–1559.

(25) Sun, Q.-F.; Sato, S.; Fujita, M. An M18L24 Stellated Cuboctahedron through Post-Stellation of an $M_{12}L_{24}$ Core. *Nat. Chem.* **2012**, *4*, 330–333.

(26) Hasenknopf, B.; Lehn, J.-M.; Boumediene, N.; Dupont-Gervais, A.; Van Dorsselaer, A.; Kneisel, B; Fenske, D. Self-Assembly of Tetra- and Hexanuclear Circular Helicates. *J. Am. Chem. Soc*. **1997**, *119*, 10956–10962.

(27) Khlobystov, A. N.; Blake, A. J.; Champness, N. R.; Lemenovskii, D. A.; Majouga, A. G.; Zyk, N. V.; Schröder, M. Supramolecular Design of One-Dimensional Coordination Polymers Based on Silver(I) Complexes of Aromatic Nitrogen-Donor Ligands. *Coord. Chem. Rev.* **2001**, *222*, 155–192.

(28) Danon, J. J.; Krüger, A.; Leigh, D. A.; Lemonnier, J.-F.; Stephens, A. J.; Vitorica-Yrezabal, I. J.; Woltering, S. L. Braiding a Molecular Knot with Eight Crossings. *Science* **2017**, *355*, 159–162.

(29) Lehn, J.-M. Toward Complex Matter: Supramolecular Chemistry and Self-Organization. *Proc. Natl. Acad. Sci. U. S. A.* **2002**, *99*, 4763–4768.

(30) Helm, L.; Merbach, A. E. Inorganic and Bioinorganic Solvent Exchange Mechanisms. *Chem. Rev*. **2005**, *105*, 1923−1959

(31) Fujita, D.; Ueda, Y.; Sato, S.; Mizuno, N.; Kumasaka, T.; Fujita, M. Self-Assembly of Tetravalent Goldberg Polyhedra from 144 Small Components. *Nature* **2016**, *540*, 563–566.

(32) Olenyuk, B.; Whiteford, J. A.; Fechtenkötter, A.; Stang, P. J. Self-Assembly of Nanoscale Cuboctahedra by Coordination Chemistry. *Nature* **1999**, *398*, 796–799.

(33) Cook, T. R.; Zheng, Y.-R.; Stang, P. J. Metal–Organic Frameworks and Self-Assembled Supramolecular Coordination Complexes: Comparing and Contrasting the Design, Synthesis, and Functionality of Metal–Organic Materials. *Chem. Rev.* **2013**, *113*, 734–777.

(34) Li, D.; Zhou, W.; Landskron, K.; Sato, S.; Kiely, C. J.; Fujita, M.; Liu, T. Viral-Capsid-Type Vesicle-Like Structures Assembled from $M_{12}L_{24}$ Metal-Organic Hybrid Nanocages. *Angew. Chem. Int. Ed.* **2011**, *50*, 5182–5187.

(35) Fujita, M. Metal-Directed Self-Assembly of Two- and Three-Dimensional Synthetic Receptors. *Chem. Soc. Rev.* **1998**, *27*, 417.

(36) Riddell, I. A.; Hristova, Y. R.; Clegg, J. K.; Wood, C. S.; Breiner, B.; Nitschke, J. R. Five Discrete Multinuclear Metal-Organic Assemblies from One Ligand: Deciphering the Effects of Different Templates. *J. Am. Chem. Soc.* **2013**, *135*, 2723–2733.

(37) Preston, D.; Lewis, J. E. M.; Crowley, J. D. Multicavity $[Pd_nL_4]^{2n+}$ Cages with Controlled Segregated Binding of Different Guests. *J. Am. Chem. Soc.* **2017**, *139*, 2379–2386.

(38) Rizzuto, F. J.; von Krbek, L. K. S.; Nitschke, J. R. Strategies for Binding Multiple Guests in Metal–Organic Cages. *Nat. Rev. Chem.* **2019**, *3*, 204–222.

(39) Wang, J.; He, C.; Wu, P.; Wang, J.; Duan, C. An Amide-Containing Metal–Organic Tetrahedron Responding to a Spin-Trapping Reaction in a Fluorescent Enhancement Manner for Biological Imaging of NO in Living Cells. *J. Am. Chem. Soc.* **2011**, *133*, 12402–12405.

(41) Kusukawa, T.; Fujita, M. Self-Assembled M_6L_4-Type Coordination Nanocage with 2,2‘-Bipyridine Ancillary Ligands. Facile Crystallization and X-Ray Analysis of Shape-Selective Enclathration of Neutral Guests in the Cage. *J. Am. Chem. Soc.* **2002**, *124*, 13576-13582

(41) Kusukawa, T.; Fujita, M. Self-Assembled M_6L_4-Type Coordination Nanocage with 2,2‘-Bipyridine Ancillary Ligands. Facile Crystallization and X-Ray Analysis of Shape-Selective Enclathration of Neutral Guests in the Cage. *J. Am. Chem. Soc.* **2002**, *124*, 13576-13582

(42) Yoshizawa, M.; Klosterman, J. K.; Fujita, M. Molecular Flasks Functional Molecular Flasks: New Properties and Reactions within Discrete, Self-Assembled Hosts. *Angew. Chem. Int. Ed.* **2009**, *48*, 3418 – 3438

(43) Turega, S.; Cullen, W.; Whitehead, M.; Hunter, C. A.; Ward, M. D. Mapping the Internal Recognition Surface of an Octanuclear Coordination Cage Using Guest Libraries. *J. Am. Chem. Soc.* **2014**, *136*, 8475–8483.

(44) Ward, M. D.; Hunter, C. A.; Williams, N. H. Guest Binding and Catalysis in the Cavity of a Cubic Coordination Cage. *Chem. Lett.* **2017**, *46*, 2–9.

(45) Yamashina, M.; Sartin, M. M.; Sei, Y.; Akita, M.; Takeuchi, S.; Tahara, T.; Yoshizawa, M. Preparation of Highly Fluorescent Host–Guest Complexes with Tunable Color upon Encapsulation. *J. Am. Chem. Soc.* **2015**, *137*, 9266–9269.

(46) Thompson, M. C.; Busch, D. H. Reactions of Co√∂rdinated Ligands. II. Nickel(II) Complexes of Some Novel Tetradentate Ligands. *J. Am. Chem. Soc.* **1962**, *84*, 1762–1763.

(47) Hubin, T. J.; Busch, D. H. Template Routes to Interlocked Molecular Structures and Orderly Molecular Entanglements. *Coord. Chem. Rev.* **2000**, *200–202*, 5–52.

(48) House, D. A.; Curtis, N. F. Transition Metal Complexes with Aliphatic Schiff Bases. VI. Compounds Formed by the Reaction of Copper(II) and Nickel(II) Ethylenediamine and Triethylenetetramine Complexes with Some Aliphatic Aldehydes. *J. Am. Chem. Soc.* **1964**, *86*, 1331–1334.

(49) Melson, G. A.; Busch, D. H. Reactions of Coordinated Ligands. XI. The Formation and Properties of a Tridentate Macrocyclic Ligand Derived from o-Aminobenzaldehyde. *J. Am. Chem. Soc.* **1965**, *87*, 1706–1710.

(50) Mal, P.; Breiner, B.; Rissanen, K.; Nitschke, J. R. White Phosphorus Is Air-Stable within a Self-Assembled Tetrahedral Capsule. *Science* **2009**, *324*, 1697–1699.

(51) Chichak, K. S.; Cantrill, S. J.; Pease, A. R.; Chiu, S.-H.; Cave, G. W. V; Atwood, J. L.; Stoddart, J. F. Molecular Borromean Rings. *Science* **2004**, *304*, 1308–1312.

(52) Pentecost, C. D.; Chichak, K. S.; Peters, A. J.; Cave, G. W. V.; Cantrill, S. J.; Stoddart, J. F. A Molecular Solomon Link. *Angew. Chem. Int. Ed.* **2007**, *46*, 218–222.

(53) Ayme, J.-F.; Beves, J. E.; Leigh, D. A.; McBurney, R. T.; Rissanen, K.; Schultz, D. A Synthetic Molecular Pentafoil Knot. *Nat. Chem.* **2012**, *4*, 15–20.

(54) Zhang, L.; August, D. P.; Zhong, J.; Whitehead, G. F. S.; Vitorica-Yrezabal, I. J.; Leigh, D. A. Molecular Trefoil Knot from a Trimeric Circular Helicate. *J. Am. Chem. Soc.* **2018**, *140*, 4982–4985.

(55) Nitschke, J. R. Construction, Substitution, and Sorting of Metallo-Organic Structures via Subcomponent Self-Assembly. *Acc. Chem. Res.* **2007**, *402*, 103-112

(56) Schultz, D.; Nitschke, J. R. Designing Multistep Transformations Using the Hammett Equation: Imine Exchange on a Copper(I) Template. *J. Am. Chem. Soc.* **2006** *128*, 9887-9892

(57) Bilbeisi, R. A.; Ronson, T. K.; Nitschke, J. R. A Self-Assembled [$Fe^{II}_{12}L_{12}$] Capsule with an Icosahedral Framework. *Angew. Chem. Int. Ed.* **2013**, *52*, 9027–9030.

(58) Ousaka, N.; Grunder, S.; Castilla, A. M.; Whalley, A. C.; Stoddart, J. F.; Nitschke, J. R. Efficient Long-Range Stereochemical Communication and Cooperative Effects in Self-Assembled Fe_4L_6 Cages. *J. Am. Chem. Soc.* **2012**, *134*, 15528–15537.

(59) Rizzuto, F. J.; Nitschke, J. R. Stereochemical Plasticity Modulates Cooperative Binding in a CoII12L6 Cuboctahedron. *Nat. Chem.* **2017**, *9*, 903–908.

(60) Kieffer, M.; Pilgrim, B. S.; Ronson, T. K.; Roberts, D. A.; Aleksanyan, M.; Nitschke, J. R. Perfluorinated Ligands Induce Meridional Metal Stereochemistry to Generate M_8L_{12} , $M_{10}L_{15}$, and $M_{12}L_{18}$ Prisms. *J. Am. Chem. Soc.* **2016**, *138*, 6813–6821.

(61) Zarra, S.; Clegg, J. K.; Nitschke, J. R. Selective Assembly and Disassembly of a Water-Soluble $Fe_{10}L_{15}$ Prism. *Angew. Chem. Int. Ed.* **2013**, *52*, 4837–4840.

(62) Zarra, S.; Smulders, M. M. J.; Lefebvre, Q.; Clegg, J. K.; Nitschke, J. R. Guanidinium Binding Modulates Guest Exchange within an [M_4L_6] Capsule. *Angew. Chem. Int. Ed.* **2012**, *51*, 6882–6885.

(63) Davis, A. V.; Fiedler, D.; Seeber, G.; Zahl, A.; van Eldik, R.; Raymond, K. N. Guest Exchange Dynamics in an M_4L_6 Tetrahedral Host. *J. Am. Chem. Soc.* **2006**, *128*, 1324-1333

(64) Symmers, P. R.; Burke, M. J.; August, D. P.; Thomson, P. I. T.; Nichol, G. S.; Warren, M. R.; Campbell, C. J.; Lusby, P. J. Non-Equilibrium Cobalt(III) “Click” Capsules. *Chem. Sci.* **2015**, *6*, 756–760.

(65) Riddell, I. A.; Ronson, T. K.; Clegg, J. K.; Wood, C. S.; Bilbeisi, R. A.; Nitschke, J. R. Cation- and Anion-Exchanges Induce Multiple Distinct Rearrangements within Metallosupramolecular Architectures. *J. Am. Chem. Soc.* **2014**, *136*, 9491–9498.

(66) Sham, K.-C.; Yiu, S.-M.; Kwong, H.-L. Dodecanuclear Hexagonal-Prismatic $M_{12}L_{18}$ Coordination Cages by Subcomponent Self-Assembly Scheme 1. Subcomponent Self-Assembly of Manganese and Cadmium Complexes. *Inorg. Chem* **2013**, *52*, 39.

(67) Lehn, J.-M.; Rigault, A. Helicates: Tetra- and Pentanuclear Double Helix Complexes of CuI and Poly(Bipyridine) Strands. *Angew. Chem. Int. Ed. English* **1988**, *27*, 1095–1097.

(68) Hasenknopf, B.; Lehn, J.-M.; Kneisel, B. O.; Baum, G.; Fenske, D. Self-Assembly of a Circular Double Helicate. *Angew. Chem. Int. Ed. English* **1996**, *35*, 1838–1840.

(69) Fleming, J. S.; Mann, K. L. V.; Carraz, C.-A.; Psillakis, E.; Jeffery, J. C.; McCleverty, J. A.; Ward, M. D. Anion-Templated Assembly of a Supramolecular Cage Complex. *Angew. Chem. Int. Ed.* **1998**, *37*, 1279–1281.

(70) Tidmarsh, I. S.; Faust, T. B.; Adams, H.; Harding, L. P.; Russo, L.; Clegg, W.; Ward, M. D. Octanuclear Cubic Coordination Cages. *J. Am. Chem. Soc.* **2008**, *130*, 15167–15175.

(71) Al-Rasbi, N. K.; Tidmarsh, I. S.; Argent, S. P.; Adams, H.; Harding, L. P.; Ward, M. D. Mixed-Ligand Molecular Paneling: Dodecanuclear Cuboctahedral Coordination Cages Based on a Combination of Edge-Bridging and Face-Capping Ligands. *J. Am. Chem. Soc.* **2008**, *130*, 11641–11649.

(72) Ronson, T. K.; Adams, H.; Ward, M. D. Coordination Chemistry of a Tris-Bidentate Bridging Ligand: A 2-D Coordination Network and a T-Symmetry Hexanuclear Coordination Cage. *CrystEngComm.* **2006**, *8*, 497-501.

(73) Turega, S.; Cullen, W.; Whitehead, M.; Hunter, C. A.; Ward, M. D. Mapping the Internal Recognition Surface of an Octanuclear Coordination Cage Using Guest Libraries. *J. Am. Chem. Soc.* **2014**, *136*, 8475–8483.

(74) Cullen, W.; Metherell, A. J.; Wragg, A. B.; Taylor, C. G. P.; Williams, N. H.; Ward, M. D. Catalysis in a Cationic Coordination Cage Using a Cavity-Bound Guest and

Surface-Bound Anions: Inhibition, Activation, and Autocatalysis. *J. Am. Chem. Soc.* **2018**, *140*, 2821–2828.

(75) Cullen, W.; Misuraca, M. C.; Hunter, C. A.; Williams, N. H.; Ward, M. D. Highly Efficient Catalysis of the Kemp Elimination in the Cavity of a Cubic Coordination Cage. *Nat. Chem.* **2016**, *8*, 231–236.

(76) Desai, S. P.; Ye, J.; Zheng, J.; Ferrandon, M. S.; Webber, T. E.; Platero-Prats, A. E.; Duan, J.; Garcia-Holley, P.; Camaioni, D. M.; Chapman, K. W.; et al. Well-Defined Rhodium–Gallium Catalytic Sites in a Metal–Organic Framework: Promoter-Controlled Selectivity in Alkyne Semihydrogenation to *E* -Alkenes. *J. Am. Chem. Soc.* **2018**, *140*, 15309–15318.

(77) Buchard, A.; Kember, M. R.; Sandeman, K. G.; Williams, C. K. A bimetallic iron(III) catalyst for CO_2 /epoxide coupling. *Chem. Commun.* **2011**, *47*, 212–214.

(78) Ramsay, W. J.; Rizzuto, F. J.; Ronson, T. K.; Caprice, K.; Nitschke, J. R. Subtle Ligand Modification Inverts Guest Binding Hierarchy in $M^{II}_8L_6$ Supramolecular Cubes. *J. Am. Chem. Soc.* **2016**, *138*, 56.

(79) Rowland, C. A.; Lorzing, G. R.; Gosselin, E. J.; Trump, B. A.; A Yap, G. P.; Brown, C. M.; Bloch, E. D. Methane Storage in Paddlewheel-Based Porous Coordination Cages. *J. Am. Chem. Soc.* **2018**, *140*, 18.

(80) Eddaoudi, M.; Kim, J.; Wachter, J. B.; Chae, H. K.; O'Keeffe, M.; Yaghi, O. M. Porous Metal−Organic Polyhedra: 25 Å Cuboctahedron Constructed from 12 $Cu_2(CO_2)_4$ Paddle-Wheel Building Blocks. *J. Am. Chem. Soc.* **2001**, *123*, 4368-4369

(81) Danon, J. J.; Krüger, A.; Leigh, D. A.; Lemonnier, J.-F.; Stephens, A. J.; Vitorica-Yrezabal, I. J.; Woltering, S. L. Braiding a Molecular Knot with Eight Crossings. *Science* **2017**, *355*, 159–162.

2

Materials and Methods

2.1 General

Unless otherwise specified, all reagents were purchased from commercial sources and used as received. Tris(4-aminophenyl)amine (TAPA) **3.7** was purchased from TCI. 6-(diphenylphosphino)formylpyridine **3.1**,[1] 6,6′-diformyl-3,3′-bipyridine **5.8**,[2] 4,4'-(((ethane-1,2-diylbis(oxy))bis(ethane-2,1-diyl))bis(oxy))dianiline **5.10**[3] were synthesised following literature procedures. **6.1** and **6.2** were synthesised by Dr Charlie McTernan of the University of Cambridge.

2.2 Nuclear Magnetic Resonance (NMR) Spectroscopy

NMR spectra were recorded using a 400 MHz Avance III HD Smart Probe (routine and wide-sweep ^{1}H NMR), DCH 500 MHz dual cryoprobe (high-resolution ^{13}C and 2D experiments), DPX S5 500 MHz BB ATM (variable temperature NMR) and 500 MHz TCI-ATM cryo (1D selective NOESY and ROESY experiments, performed by Derrick Roberts and Roy Lavendomme at the University of Cambridge) NMR spectrometers.

Chemical shifts for ^{1}H, ^{13}C and ^{19}F are reported in ppm on the δ scale; ^{1}H and ^{13}C were referenced to the residual solvent peak and ^{19}F was referenced to an internal standard of C_6F_6 in CD_3CN at −164.9 ppm. Coupling constants (J) are reported in hertz (Hz). The following abbreviations are used to describe signal multiplicity for ^{1}H NMR spectra: s: singlet, d: doublet, t: triplet, dd: doublet of doublets; dt: doublet of triplets; m: multiplet, br: broad. All proton signals of diamagnetic compound were assigned with the aid of 2D NMR spectra.

Wide sweep paramagnetic NMR spectra were recorded in the analogue digitisation mode with a spectral width (SW) of 372.98 ppm, a transmitter frequency offset (O1P) of 100.00 ppm and the line width set to 10.0 Hz. Due to the experimental difficulties associated with collecting NMR data for ^{1}H nuclei with vastly different relaxation times, differences between measured and theoretical integration values were in some cases observed. While the paramagnetic nature of the complexes precluded complete assignment of the proton environments, it is proposed that through-bond proximity of the proton environment to each high-spin metal centre dictates the extent of downfield shifting of each signal, as observed in previous reports.[3,4]

DOSY NMR experiments were performed on a Bruker 500 MHz TCI-ATM cryo-NMR spectrometer or 500 MHz DPX S5 500 MHz BB ATM spectrometer. Maximum gradient strength was 6.57 G/cm A. The standard Bruker pulse program, ledbpgp2s, employing a stimulated echo and longitudinal eddy-current delay (LED) using bipolar gradient pulses for diffusion using 2 spoil gradients was utilised. Rectangular gradients were used with a total duration of 1.5 ms. Gradient recovery delays were 875 –1400 μs. Individual rows of the S4 quasi-2D diffusion databases were phased and baseline corrected. DOSY experiments in Chapter 4 were carried out by Dr Charlie McTernan of the University of Cambridge.

2.3 Mass Spectrometry

Low resolution electrospray ionisation mass spectrometry (LR-ESI-MS) was undertaken on a Micromass Quattro LC mass spectrometer (cone voltage 10-30 eV; desolvation temperature 313 K; ionisation temperature 313 K) infused from a Harvard syringe pump at a rate of 10 μL min^{-1}. High resolution electrospray ionisation mass spectrometry (HRMS-ESI) was performed on a Waters LCT Premier Mass Spectrometer featuring a Z spray source with electrospray ionisation and modular LockSpray interface.

2.4 X-ray Crystallography

X-ray crystallographic data were solved and refined by Dr Tanya K. Ronson or Dr Felix J. Rizzuto. Data were collected at Beamline I19 of Diamond Light Source employing silicon double crystal monochromated synchrotron radiation (0.6889 Å) with ω and ψ scans at 100(2) K. Data integration and reduction were undertaken with Xia2. Subsequent computations were carried out using the WinGX-32 graphical user interface. Multi-scan empirical absorption corrections were applied to the data using the AIMLESS tool in the CCP4 suite. The structures were solved by dual space methods using SHELXT or charge-flipping using SUPERFLIP then refined and extended with SHELXL. In general, non-hydrogen atoms with occupancies greater than 0.5 were refined anisotropically. Carbon-bound hydrogen atoms were included in idealised positions and refined using a riding model. Disorder was modelled using standard crystallographic methods including constraints, restraints and rigid bodies where necessary. CIF files are available on request from the author.

2.5 Molecular Modelling

Molecular model simulations (MM2 and MM3 force fields) of supramolecular complexes were performed using CAChe Worksystems Pro (Fujitsu Ltd., Beaverton, Oregon, 2000–2006) and SCIGRESS version FJ 2.6 (EU 3.1.9) Build 5996.8255.20141202.

2.5 Circular Dichroism (CD) Spectroscopy

Circular Dichroism was performed on an Applied-Photophysics Chirascan qCD spectrometer using a 1 mm path-length cuvette. Experiments were recorded at 298 K, maintained with a Peltier temperature control. Measurements were background subtracted from blank solvent in an identical cuvette. The sample concentrations were adjusted to maintain a HV below 700 Volts. A minimum sample integration time of 1 second was used. The data was smoothed using a 5 pts Savitzky-Golay algorithm and the residuals checked for distortions. Solutions for the CD measurements were made using dry degassed solvents and filtered through 0.2 μm PTFE membrane filters.

2.6 References

(1) Dry, E. F. V.; Clegg, J. K.; Breiner, B.; Whitaker, D. E.; Stefak R.; Nitschke, J. R. Reversible anion-templated self-assembly of [2+2] and [3+3] metallomacrocycles containing a new dicopper(I) motif. *Chem. Commun*., **2011**, *47*, 6021.

(2) Pilgrim, B. S.; Roberts, D. A.; Lohr, T. G.; Ronson, T. K.; Nitschke, J. R. Signal transduction in a covalent post-assembly modification cascade. *Nat. Chem*., **2017**, *9*, 1276–1281.

(3) Wood, C. S.; Ronson, T. K.; Belenguer, A. M.; Holstein J. J.; Nitschke, J. R. Two-stage directed self-assembly of a cyclic [3]catenane. *Nat. Chem*., **2015**, *7*, 354–358.

(4) Riddell, I. A.; Smulders, M. M. J.; Clegg, J. K.; Hristova, Y. R.; Breiner, B.; Thoburn J. D.; and Nitschke, J. R. Anion-induced reconstitution of a self-assembling system to express a chloride-binding $Co_{10}L_{15}$ pentagonal prism. *Nat. Chem*., **2012**, *4*, 751–756.

(5) Allan, D.; Nowell, H.; Barnett, S.; Warren, M.; Wilcox, A.; Christensen, J.; Saunders, L.; Peach, A.; Hooper, M.; Zaja, L.; Patel, S.; Cahill, L.; Marshall, R.; Trimnell, S.; Foster, A.; Bates, T.; Lay, S.; Williams, M.; Hathaway, P.; Winter, G.; Gerstel, M.; Wooley, R., A Novel Dual Air-Bearing Fixed-χ Diffractometer for Small-Molecule Single-Crystal X-ray Diffraction on Beamline I19 at Diamond Light Source. *Crystals*, **2017**, *7*, 336.

(6) Collaborative Computational Project, N., The CCP4 suite: programs for protein crystallography. *Acta Cryst*. **1994**, *50*, 760-763.

(7) Evans, P., Scaling and assessment of data quality. *Acta Cryst*. **2006**, *62*, 72-82.

(8) Winter, G., xia2: an expert system for macromolecular crystallography data reduction. *J. Appl. Crystallogr*. **2010**, *43*, 186-190.

(9) Farrugia, L., WinGX and ORTEP for Windows: an update. *J. Appl. Crystallogr*. **2012**, *45*, 849-854.

(10) Evans, P. R.; Murshudov, G. N., How good are my data and what is the resolution? *Acta Cryst.* **2013**, *69*, 1204-1214.

(11) Winn, M. D.; Ballard, C. C.; Cowtan, K. D.; Dodson, E. J.; Emsley, P.; Evans, P. R.; Keegan, R. M.; Krissinel, E. B.; Leslie, A. G. W.; McCoy, A.; McNicholas, S. J.; Murshudov, G. N.; Pannu, N. S.; Potterton, E. A.; Powell, H. R.; Read, R. J.; Vagin, A.; Wilson, K. S., Overview of the CCP4 suite and current developments. *Acta Cryst*. **2011**, *67*, 235-242.

(12) Sheldrick, G., SHELXT - Integrated space-group and crystal-structure determination. *Acta. Cryst*. **2015**, *71*, 3-8.

(13) Palatinus, L.; Chapuis, G., SUPERFLIP - a computer program for the solution of crystal structures by charge flipping in arbitrary dimensions. *J. Appl. Crystallogr*. **2007**, *40*, 786-790.

(14) Sheldrick, G. M., Crystal structure refinement with SHELXL. *Acta. Cryst*. **2015**, *71*, 3-8.

3

Self-Assembled Polyhedra With Bimetallic Vertices

This chapter reports on the self-assembly of a series of new metal-organic cage which employ a 2-formyl-6-diphenylphosphine-pyridine subcomponent **3.1**. This coordination motif, which has proximal N and P donor atoms with parallel coordination vectors, acts to hold metal ions in close proximity, resulting in the formation of bimetallic complexes.

Among the structures formed is a $Cu^{I}_{12}L_4$ *pseudo*-octahedral cage **3.9**, based on a new form of dicopper(I) motif, a hitherto unreported head-to-head conformation which contrasts with the previously reported head-to-tail conformation. **3.9** holds its two Cu^{I} cations in chemically distinct environments, unlike all previously reported structures involving **3.1**. Its disilver(I) congener **3.10** is also reported and characterised. With Ag being NMR active, this structural analogue allowed us to probe the solution-state structure of **3.10**, and confirm that it resembles that in the solid-state.

Building on these results, we show that subcomponent **6.1** can be utilised to hold different metal cations in close proximity to one another. Two $Cd^{II}_4Cu^{I}_4L_4$ tetrahedral cages, **3.11** and **3.14**, are reported. Again, these assemblies are based upon another unprecedented coordination complex.

3.1 Introduction

Previously, we have described the assembly of a series of bimetallic complexes, assembled utilising a 2-formyl-6-diphenylphosphine-pyridine unit **3.1**,[1] rather than the 2-formylpyridine typically used in the subcomponent self-assembly process.[2]

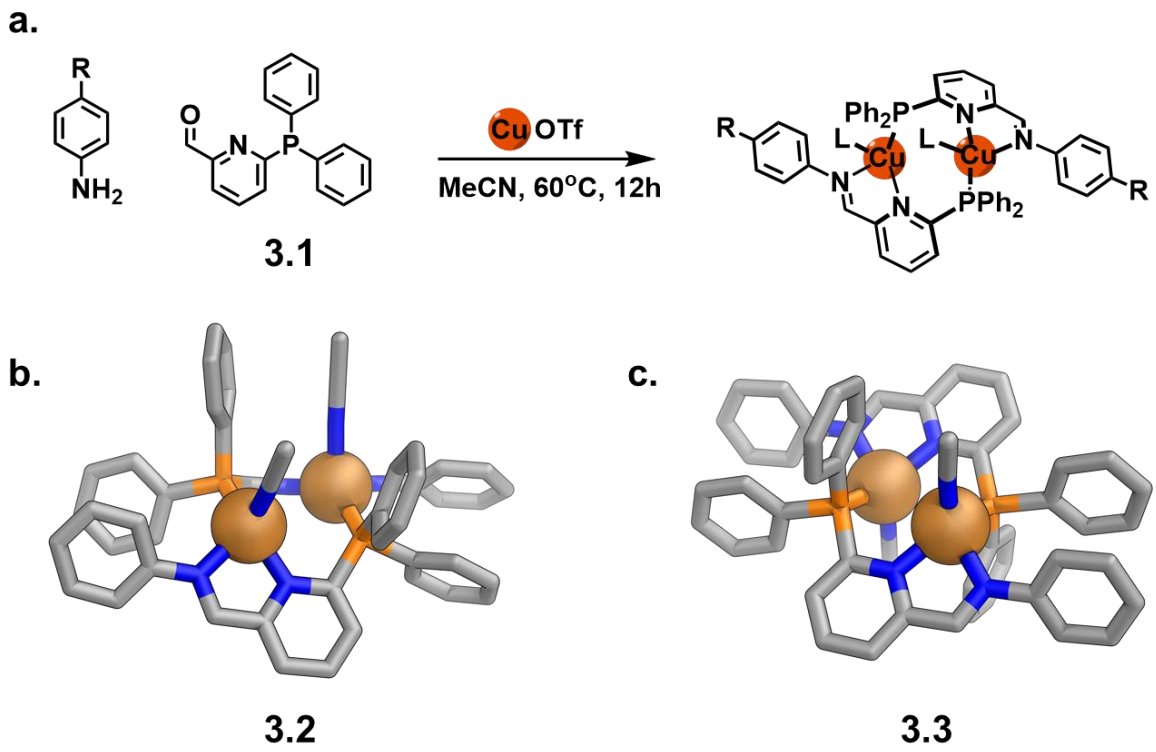

Figure 3.1 | a. Synthesis of dicopper(I) complexes **3.2** and **3.3** which both have a $Cu^{I}_{2}L_{2}$ stoichiometry. **b.** Crystal structure of **3.2** which adopts a *cis*-conformation. **c.** Crystal structure of **3.3** which adopts a *trans*-conformation. The para-substituents, non-coordinating solvents and anions have been omitted for clarity.

The two resulting structures, **3.2** and **3.3** are isomeric and rapidly interconvert on the NMR chemical shift timescale. It has also been shown that these complexes are capable of binding a diverse set of anions, carboxylates, phosphates, halides to name but a few. Affinities range from 10^4 for phosphate up to 10^{10} for iodide, as shown by a series of competitive guest binding experiments (Figure 3.2).

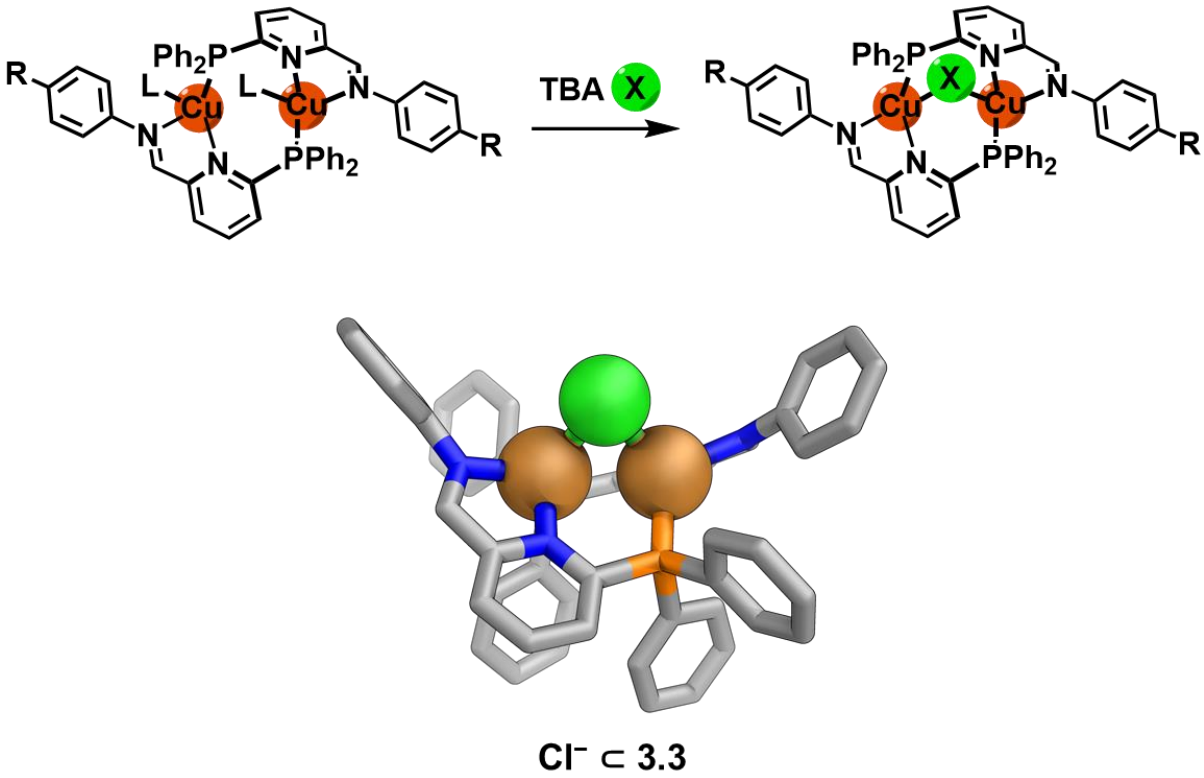

Figure 3.2 | Anion binding with complexes like **3.2** result in the formation of a $Cu^{I}_{2}X$ bridge-head, where X is an anion. The crystal structure is that of a Cl^{-} host-guest complex. Solvent molecule, non-binding anions and substituents on the aniline residues have been omitted for clarity.

Further to this it has been demonstrated that these dinuclear complexes can act as the labile units in a self-assembling system of molecules, which allows for error-checking to occur. In Figure 3.3a, it can be seen how a bis-anion such as terephthalic acid can be used to hold two dicopper(I) complexes in close proximity to each other, yielding **3.5**.

If subcomponent **3.1** is treated with a flexible dianiline (as in Figure 3.3b) and a source of Cu^{I}, it was found that no discrete species assembled, but rather a mixture of metallomacrocycles of different sizes and other ill-defined oligomers. However, subsequent templation of the mixture with terephthalic acid leads to quantitative formation of one architecture, metallomacrocycle **3.6**. It was also found that tridentate carboxylates are capable of templating even larger macrocycles.[1]

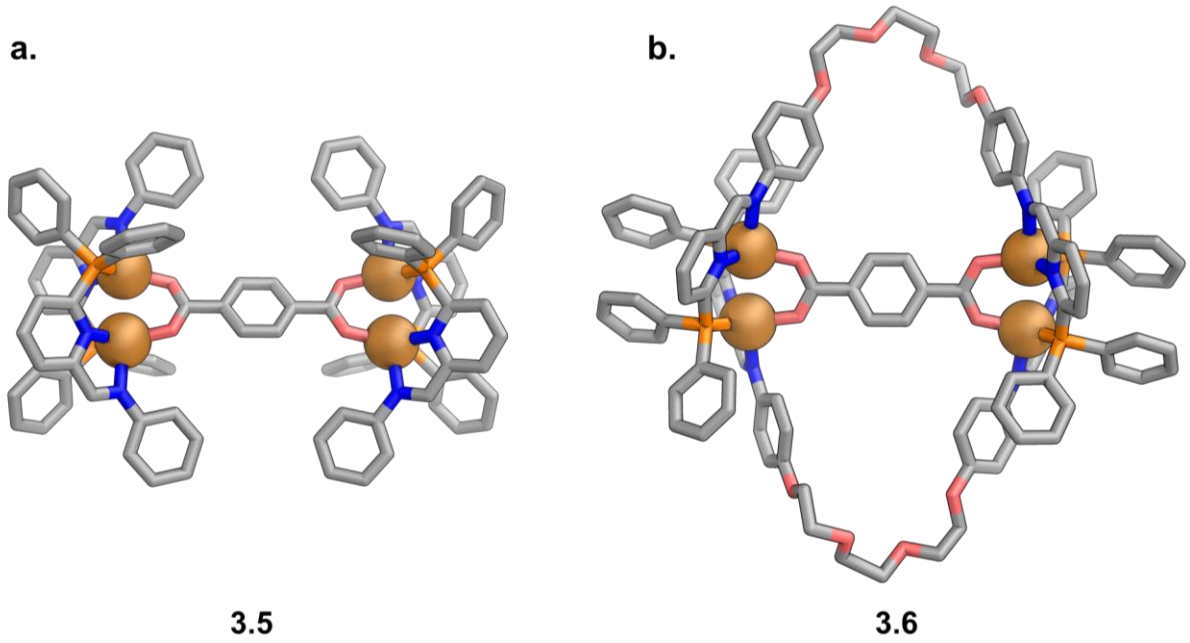

Figure 3.3 | a. Solid state structure of tetranuclear complex **3.5**. **b**. Anion templation for leads to the formation of metallomacrocycle **3.6**.[1]

As in the simpler dinuclear complexes **3.2** and **3.3**, a head-to-tail conformation is observed in both **3.5** and **3.6**. Each of the Cu^{I} centres is coordinated by an pyridyl-imine motif, a phosphine and either a solvent molecule or anionic species. The two metal centres are symmetry equivalent.

The subtly different configurations adopted by the ligands in each of the complexes described above also suggested that this motif may be able to offer a degree of flexibility which could allow for the formation of new and unexpected polyhedral structures, as outlined in the Chapter 1 of this thesis.

It was therefore reasoned that subcomponent **3.1** could serve as a useful building block which holds two aniline residues in proximity to one another at the vertex of a polyhedron. The nature of the polyhedron is dependent on the topicity of the aniline-containing subcomponent.[3,4] This is distinct from what occurs when self-assembly is carried out with 2-formylpyridine, where three aniline residues are held together at the vertex of the polyhedron.[5,6] In the simplest three-dimensional case, a tritopic aniline residue will give rise to a *pseudo*-octahedron (Figure 3.4a), where four of the eight faces are occupied by a ligand, the four remaining faces are empty. This contrasts with what our group has observed for assembly with 2-formylpyridine where, with a tritopic aniline, a face-capped tetrahedron is expected (Figure 3.4b).

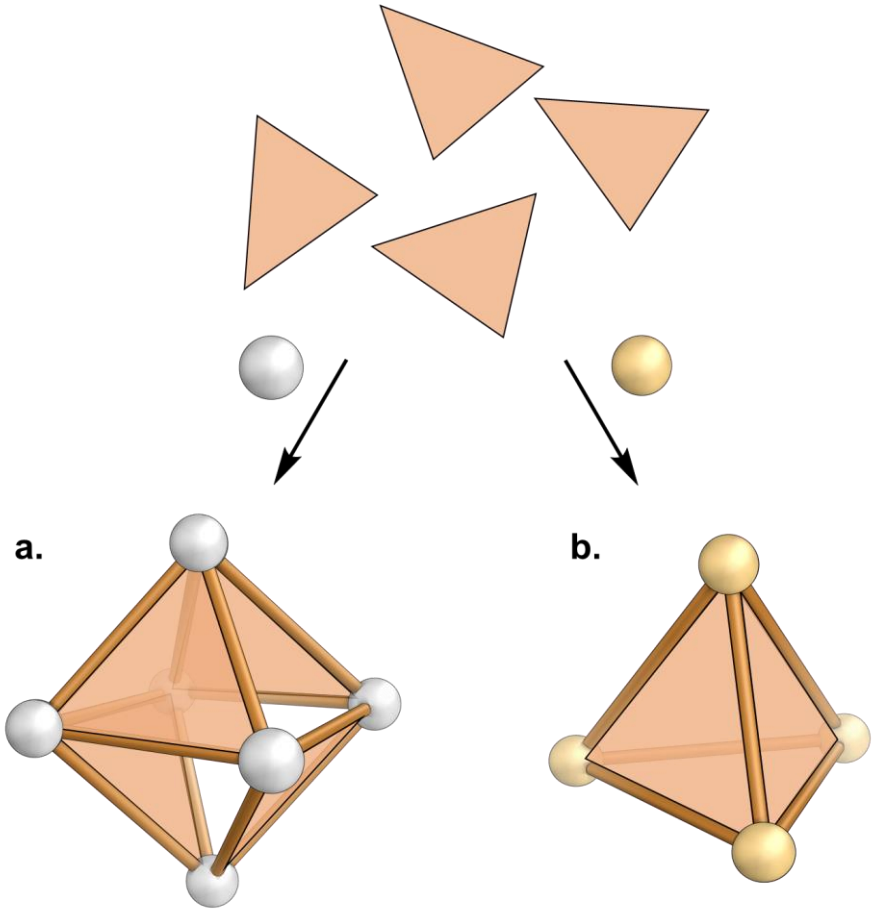

Figure 3.4 | a. Schematic representation of a *pseudo*-octahedron with four occupied and four empty faces, with each vertex bringing together two triangular building blocks **b.** A tetrahedron with four occupied faces, each vertex brings together three triangular building blocks.

We envisaged that combining a suitable tritopic aniline, such as **3.7**, could result in the formation of a large octahedral cage **3.8** (Figure 3.5). As described above, four of the faces of the octahedron are occupied, four are empty. The vertices of the proposed cage are isostructural to those observed in **3.2**, the *cis* conformer of the dinuclear complex, with each Cu^{I} cation occupying a chemically equivalent position within the cage. As in the bimetallic complexes and the metallomacrocycles, two coordinating solvent molecules are required to complete the tetrahedral coordination sphere of the metal centres.

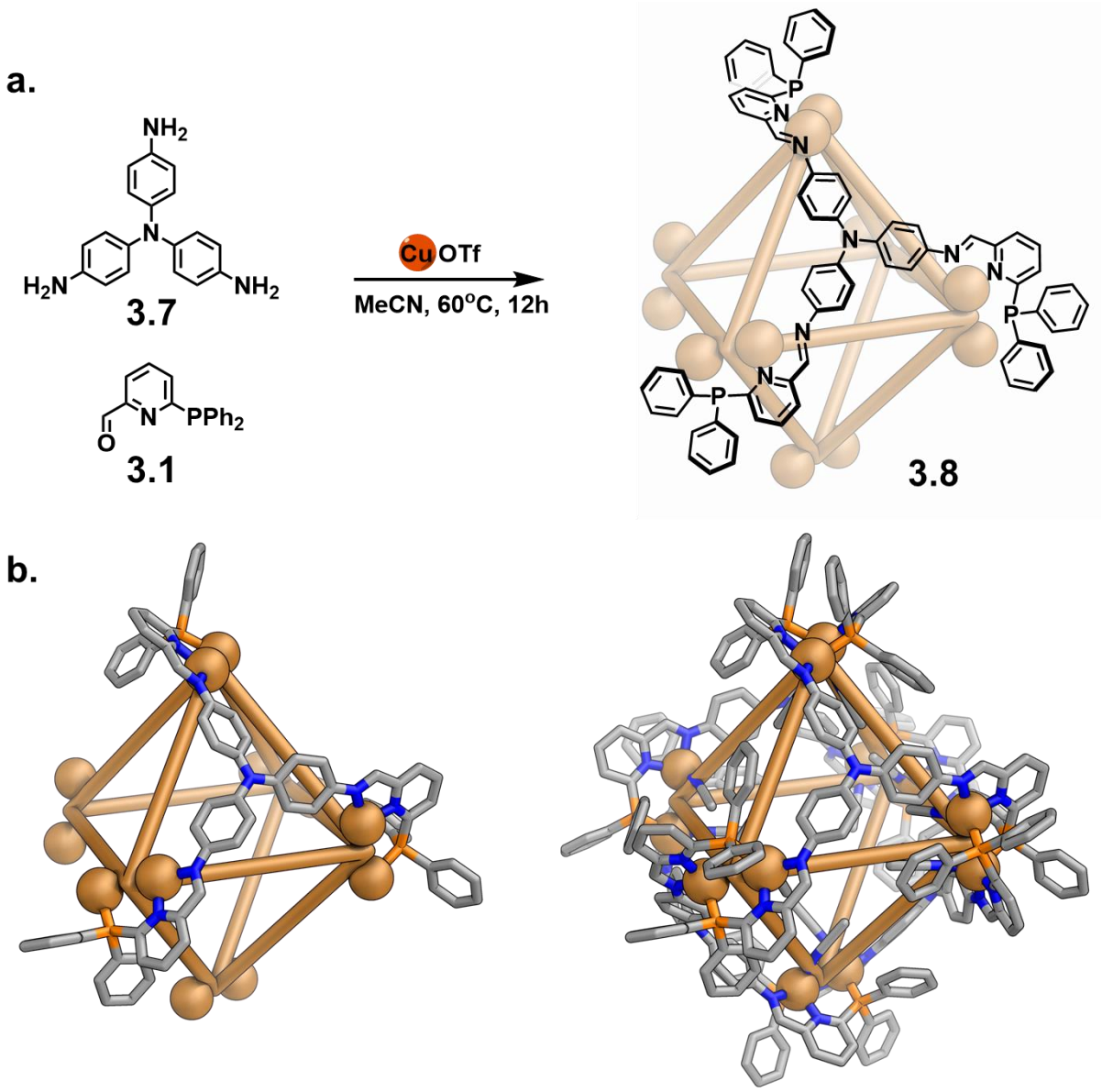

Figure 3.5 | a. Proposed synthetic route to a new octahedral cage **3.8**. **b.** Molecular model (MM3) of the proposed structure, with one ligands isolated on the left and all ligands included on the right. Coordinating solvent molecules, which point into the cavity of the cage are omitted. Each of the vertices are based on a crystal structure of **3.2**.

3.2 Synthesis of a Dicopper(I)-Based Octahedron

The assembly of tris(4-aminophenyl)amine **3.7** (4 equiv.) and 2-formyl-6-diphenylphosphine-pyridine **3.1** (12 equiv.) with copper(I) trifluoromethanesulfonate (triflate, OTf^-) was observed by ESI-MS to form $Cu^{I}_{12}L_4$ cage **3.9** following heating at 60 °C overnight (Figure 3.6). ^{1}H and DOSY NMR spectroscopy revealed the product to be highly symmetric, indicating the symmetry of each of the ligands had been maintained. A diffusion coefficient of of 3.72×10^{-6} cm^2 s^{-1} was measured, corresponding to a hydrodynamic radius of 15 Å. One broad peak was observed via ^{31}P NMR spectroscopy at 7.52 ppm, occurring at a similar chemical shift to those observed in related smaller architectures.[1] This evidence suggests that each of the three arms of the tripodal ligand are in chemically equivalent positions, which is consistent with proposed structure **3.8**, as outlined in Figure 3.5.

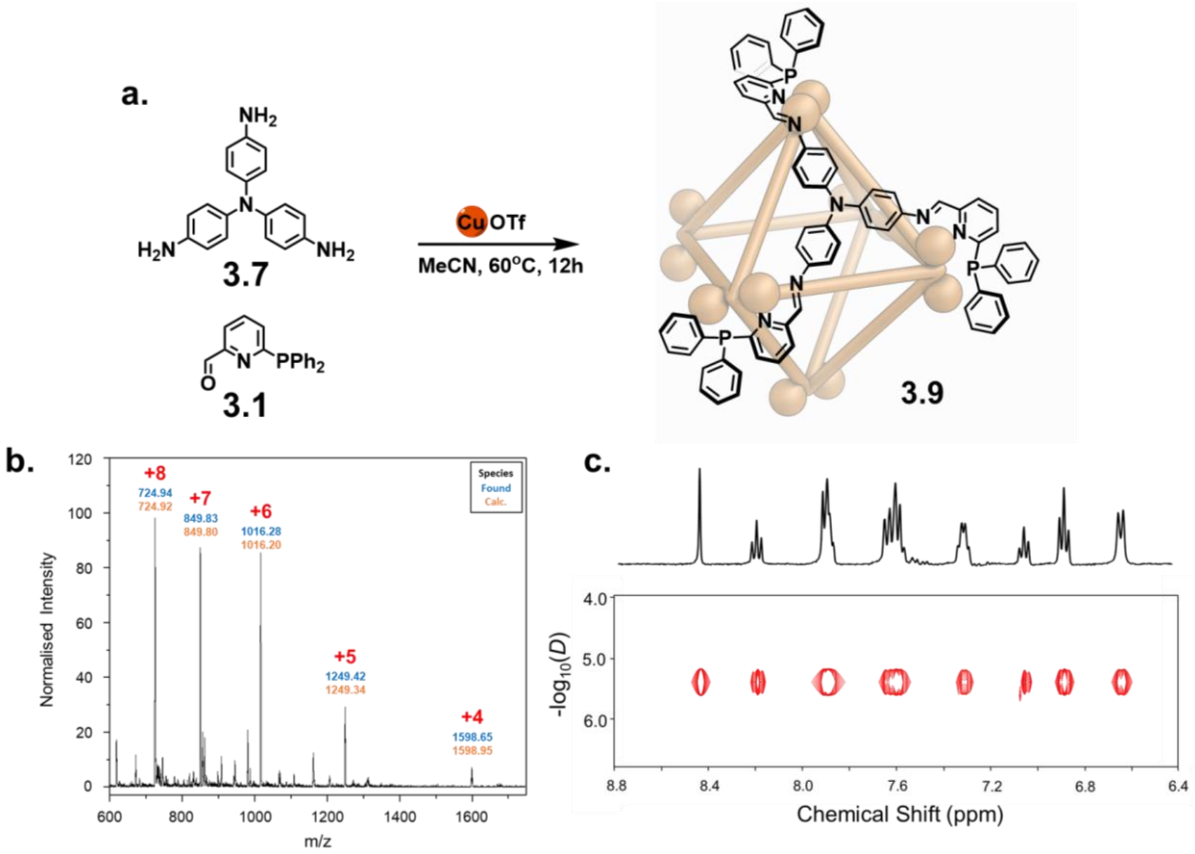

Figure 3.6 | a. Synthesis of $Ag^{I}_{12}L_4$ *pseudo*-octahedron **3.9**. **b.** ESI-MS of **3.9**. **c.** ^{1}H and DOSY NMR spectra of **3.9**. The units of *D* are cm^2 s^{-1}.

Slow diffusion of diethyl ether into an acetonitrile solution of **3.9** provided crystals of sufficient quality for X-ray diffraction analysis. This revealed the cage to be *pseudo*-octahedral, as expected.

Four of the polyhedron's faces are occupied by ligands while the remaining faces are vacant. However, there was one key difference. Rather than adopting the expected head-to-tail configuration previously observed for these complexes, the cage is based on a new and thus far unreported coordination mode.

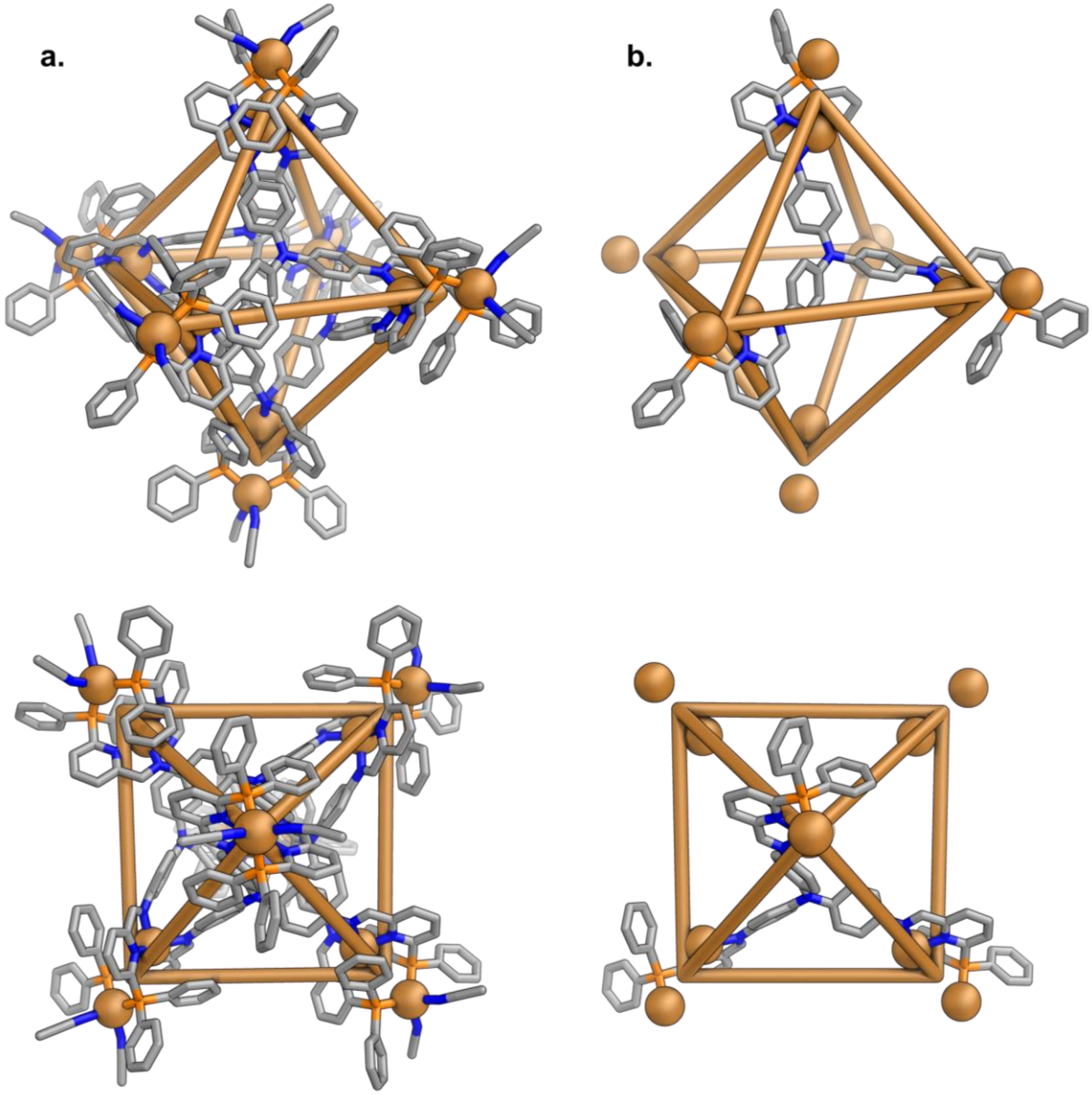

Figure 3.7 | a. Crystal structure of dicopper(I) cage **3.9** with each of the four ligands and coordinating solvent molecules included, with a side-on and top-down view. **b.** One ligand of **3.9** for clarity, with a side-on and top-down view.

The internal Cu^{I} cation is coordinated in a tetrahedral environment by two pyridyl-imine units, with the proximal phosphine moieties coordinated to the second, more peripheral Cu^{I} cation. The

coordination sphere of this second cation is then completed by two coordinating acetonitrile molecules.

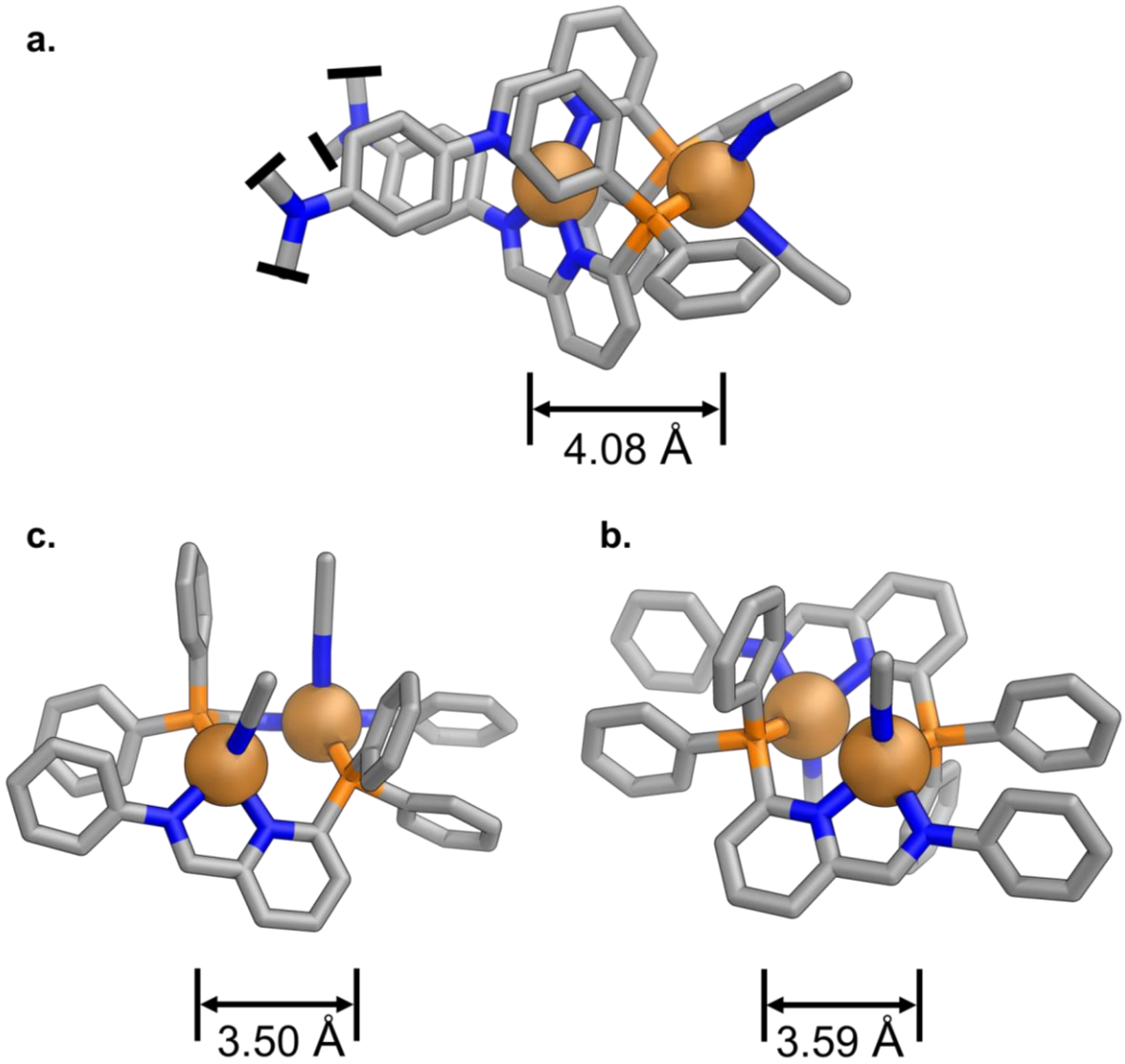

Figure 3.8 | a. One of the vertices of **3.9**, isolated from the cage. The internal Cu^{I} centre is coordinated by two pyridyl-imine motifs, the peripheral Cu^{I} centre is coordinated by two phosphines and two acetronitriles in solution. **b**. The *cis* and **c**. *trans* conformers **3.2** and **3.3**, with aniline substituents omitted for clarity. Metal-metal distances are included.

An average metal-metal distance of 4.08 ± 0.05 Å was measured for each of the symmetry equivalent vertices of the cage (Figure 3.8a). This is significantly larger than the sum of the ionic radii of the two cations (approximately 1.4 Å each).[1] It is also a larger metal-metal distances than that measured for both the *cis* and *trans* conformers **3.2** and **3.3** of the small molecule analogues (Figure 3.8b–c).

This result was entirely unexpected and completely changes the cage's shape from that of the expected architecture **3.8**. The volume of the cage's internal cavity is significantly reduced. The nature of the complexes around which the architecture is built also results in the two Cu^{I} cations of the vertices being in chemically distinct positions. In **3.8** the metal centres are symmetry equivalent.

At this point it was noted that the ^{1}H NMR and ESI-MS data collected thus far could in fact be consistent with both the originally proposed structure and that observed in the solid state. One possibility is that the two conformers could exist, with the two rapidly interconverting on the ^{1}H NMR chemical shift timescale. To ascertain that the structure observed in the solid state corresponds to that observed in solution the Ag^{I} congener of **3.9**, whose metal centres should be NMR active, was prepared.

3.3 Synthesis of a Disilver(I) Octahedron

In a similar manner to **3.9**, the disilver(I) analogue **3.10** could be formed by treating **3.7** (4 equiv.) with **3.1** (12 equiv.) and silver(I) triflate (12 equiv.) (Figure 3.9a). It has a $Ag^{I}_{12}L_6$ structure as determined by ESI- and HR-MS, analogous to that of **3.9**. ^{1}H NMR spectroscopy revealed **3.10** to be highly symmetric, with maintenance of the threefold symmetry of the ligands. A diffusion coefficient of 5.03×10^{-6} cm^2 s^{-1} was measured, corresponding to a hydrodynamic radius of 11 Å (Figure 3.9b). This is noticeably smaller than that of **3.9** (15 Å).

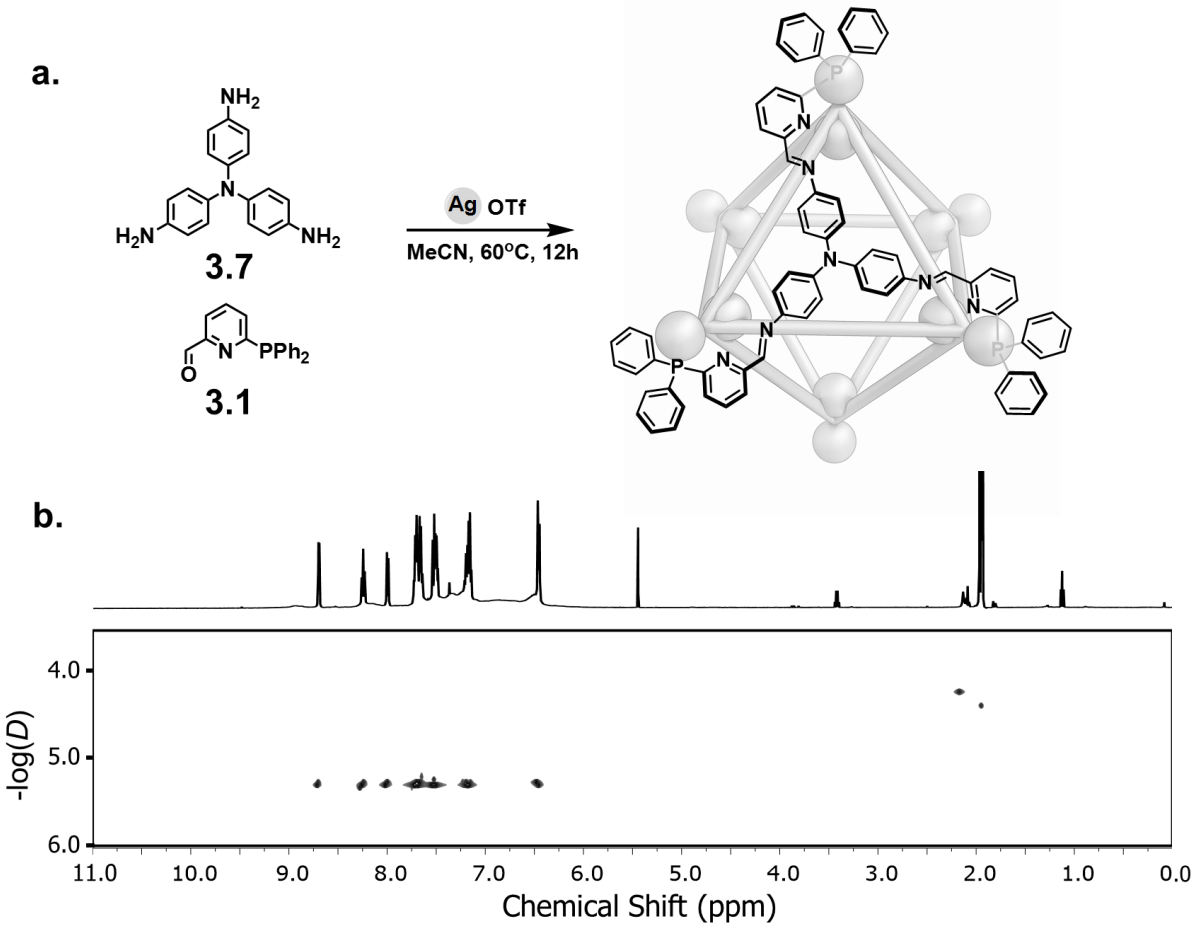

Figure 3.9 | a. Synthesis of $Ag^{I}_{12}L_4$ *pseudo*-octahedron **3.10**. **b**. ^{1}H and DOSY NMR spectra of **3.10**. The units of *D* are cm^2 s^{-1}.

Slow diffusion of diethyl ether into an acetonitrile solution of **3.10**, containing an excess of $TBAPF_6$ provided crystals suitable for analysis by X-ray diffraction. This confirmed the solid-state structure to be equivalent to that of **3.9** (Figure 3.10). An average radius of 12 ± 1 Å was found in the solid state, which matches closely with the hydrodynamic radius of 11 Å measured in solution by DOSY. Metal-

to-metal distances within the disilver(I) complex of 3.38 ± 0.02 Å were measured. This is significantly shorter than the 4.08 ± 0.05 Å observed in **3.9**, as well is that seen in dinuclear complexes **3.2** and **3.3**.

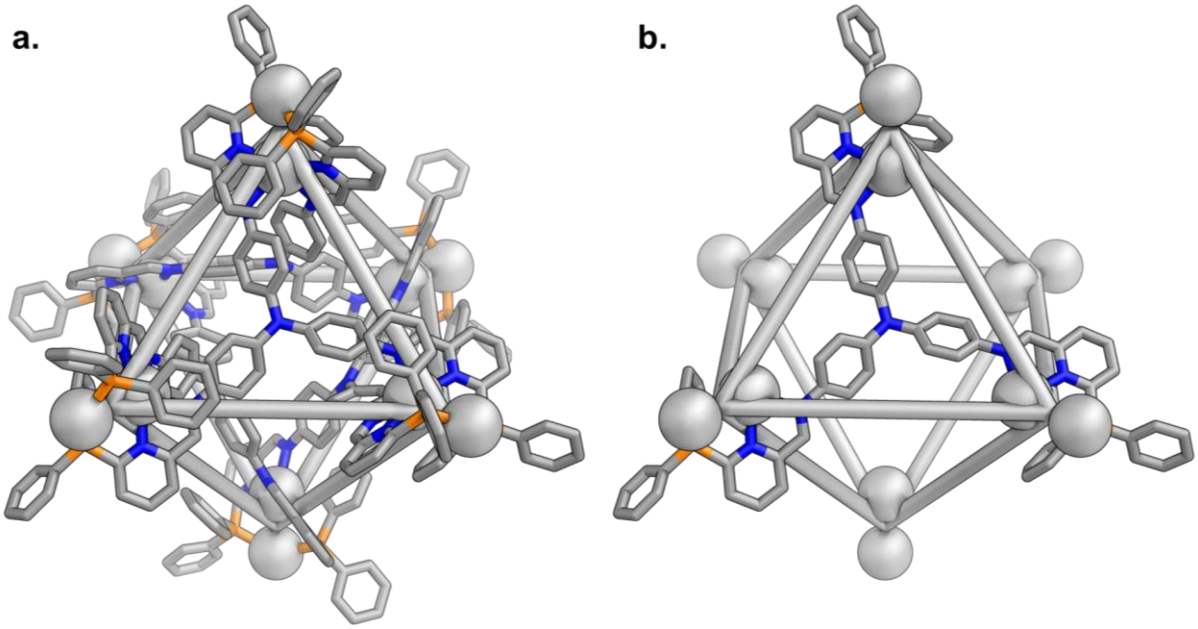

Figure 3.10 | a. Solid state structure of **3.10**. Coordinating solvents have been omitted for clarity. **b**. One ligand of **3.10** highlighted within the octahedral framework.

Returning to the question of which configuration these octahedra exist as in solution, we thought about how these species would be expected to behave if monitored by ^{31}P NMR. Ag atoms mainly exists as two isotopes, ^{107}Ag and ^{109}Ag (approximately 51.8% and 48.2%, respectively), which are both spin ½ and therefore NMR active. It was therefore reasoned that these cations, along with the phosphorus atoms of the cage's ligands could be used as handles to determine the conformation adopted by the cage in solution. If **3.10** adopts a structure similar to that originally proposed for **3.8** in solution, one would expect a single ^{109}Ag chemical shift. This assumption comes from the fact that in **3.8** both of the cations in the vertices are in chemically (and magnetically) identically positions, with each vertex being symmetry equivalent. Therefore, if we could identify two ^{109}Ag resonance frequencies we could conclude that the solid-state structure is reflective of what occurs in solution.

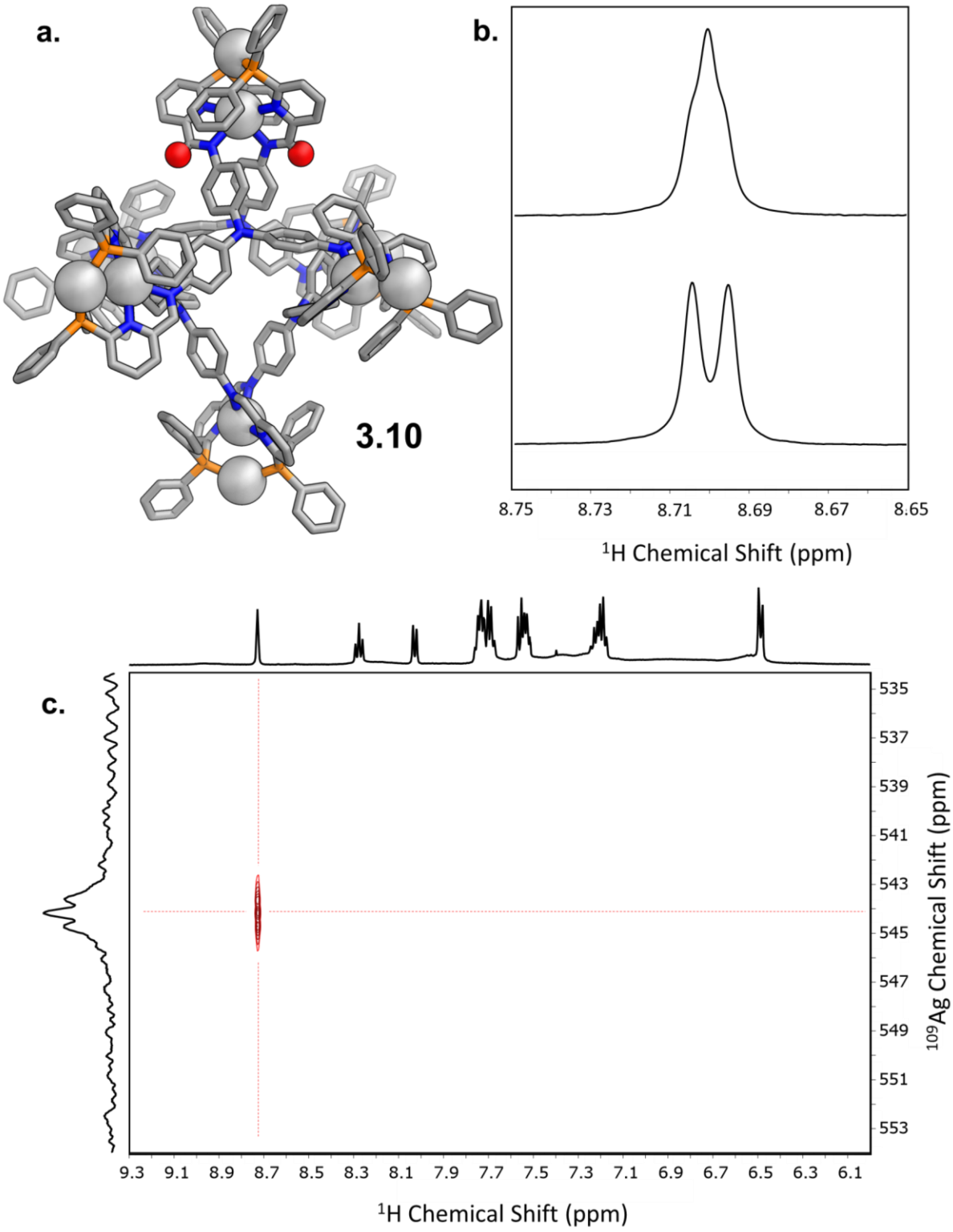

Figure 3.11 | a. Crystal structure of **3.10** with the imine protons highlighted as red spheres. **b**. Coalescence of the imine signal observed by ^{1}H NMR spectroscopy with irradiation of ^{109}Ag at 544 ppm. **c**. ^{1}H – ^{109}Ag HMBC of **3.10**, revealing a strong correlation between the imine resonance and a ^{109}Ag species, resonating at 544 ppm.

Attempts to acquire the ^{109}Ag NMR spectrum we unsuccessful, presumably because of the insensitivity of this isotope. To circumvent this issue a series of ^{1}H and ^{31}P experiments were devised to investigate the effects of the coupling between the protons and phosphines of **3.10** and its Ag^{I} cations. It was noted that in contrast to **3.9**, the imine signal of **3.10** was split, presumably as a result of coupling with a Ag^{I} cation (Figure 3.11b). A ^{1}H – ^{109}Ag HMBC revealed strong coupling between this proton resonance and a Ag^{I} species with a chemical shift of 544 ppm (Figure 3.11c). It was therefore inferred that this Ag signal corresponds to the internal Ag^{I} centre of the cage.

Turning to the ^{31}P NMR spectrum of **3.10** (^{1}H decoupled), several couplings were observed, again consistent with coupling to a Ag^{I} centre (Figure 3.12). The splitting pattern was too complex to be entirely explained by coupling with just the most external Ag^{I} cation (both the ^{107}Ag and ^{109}Ag isotope) as had been expected. Further fine splitting of the signals was also observed (Figure 3.12b). We hypothesised that this fine splitting in the ^{31}P spectra is the result of coupling between the internal Ag^{I} centre and the phosphine.

Irradiation of the ^{109}Ag at 544 ppm resulted in significant changes in the ^{31}P spectrum acquired, with partial collapse of the fine coupling. The fine coupling is not entirely eliminated, only that caused by the ^{109}Ag. Coupling resulting from the ^{107}Ag is still present.

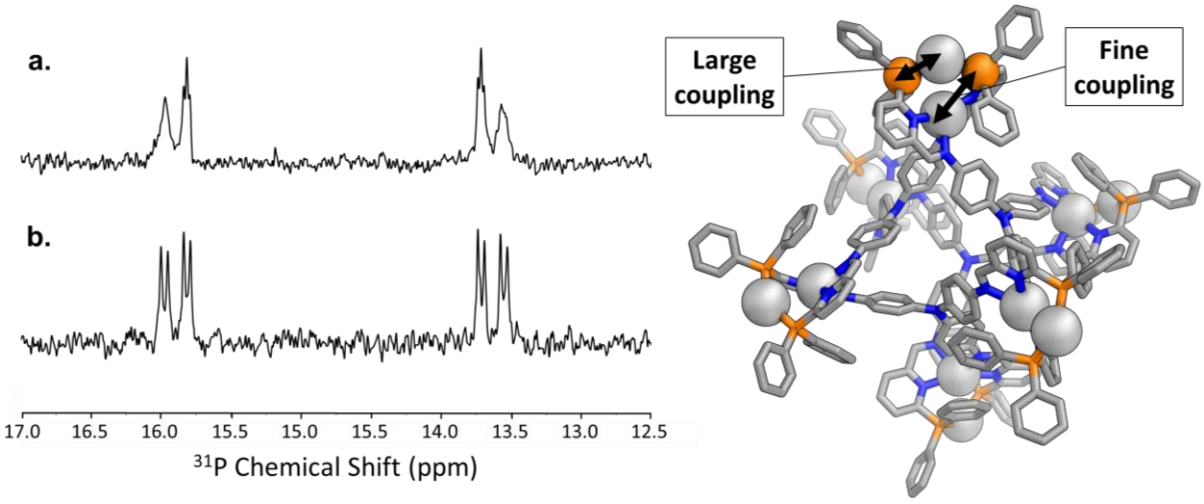

Figure 3.12 | ^{31}P NMR spectra of **3.10**. We propose larger coupling results from interactions with the closer, coordinated Ag^{I} centres. The fine coupling comes from interactions with the internal Ag^{I} centre. **a.** Irradiation of ^{109}Ag at 544 ppm partially eliminates the fine coupling. **b.** ^{31}P NMR spectrum with no irradiation of the ^{109}Ag.

As both ^{31}P and ^{109}Ag are relatively insensitive, analysis by HMBC proved ineffective. Instead of this, the ^{109}Ag was excited over a relatively broad window (approximately 50 ppm increments) from 300–1000 ppm (Figure 3.13). From this experiment it was possible to identify a second ^{109}Ag species

which was strongly interacting with the phosphine of the ligand. In this case, with irradiation at 950 ppm, rather than causing a collapse in the fine coupling, one of the doublets collapsed to give a singlet. This resultant signal appears to retain its fine coupling.

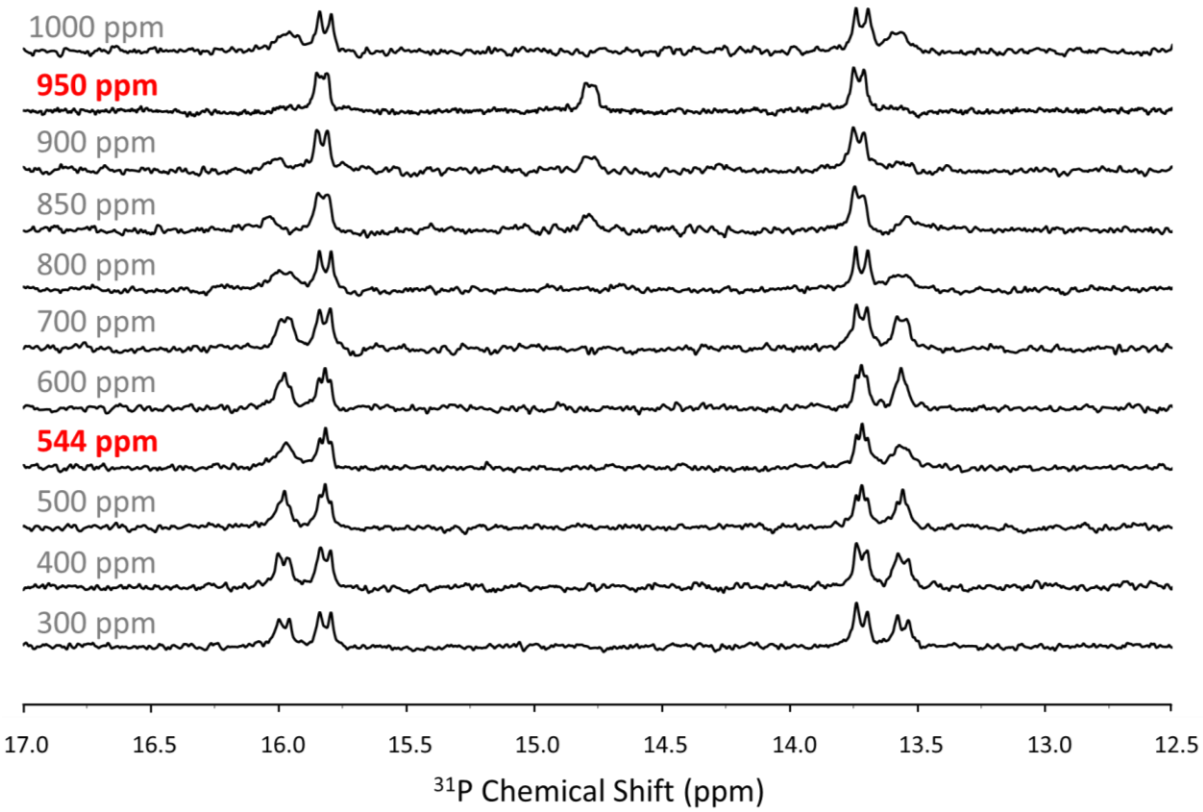

Figure 3.13 | A series of ^{31}P NMR spectra, each with irradiation of ^{109}Ag at a different chemical shift. Collapse of the fine coupling with irradiation of ^{109}Ag and of the larger coupling with irradiation at 950 ppm are highlighted.

These results, when taken together with the ^{1}H – ^{109}Ag HMBC experiment described above, provide strong evidence that the structure occurring in solution has two distinct Ag^{I} centres. This is consistent with the observations made in the solid state. As the proposed cage **3.8** would hold all of its metal centres in chemically equivalent positions, it is not consistent with these NMR results.

This new and unprecedented coordination mode led us to question whether this type of coordination motif, with proximal but non-converging coordination vectors, can be employed to form other architectures. In particular, it was noted that the formation of **3.9** and **3.10** leads to two distinct coordination environments coming into existence. One has two pyridyl-imine motifs, the other with two phosphine units. This suggested that subcomponent **3.1** may be capable of stabilising hetero-bimetallic complexes, which, to date, have been a challenging class of molecules to synthesise.

3.4 Forming Hetero-Bimetallic Structures

Control over the placement of metal centres in hetero-bimetallic complexes presents even greater challenges than their homo-bimetallic analogues. Several strategies have been explored, many of which utilise a mixture of different donor atoms which may be hard or soft and will therefore have a different affinity for hard and soft metals.[7] Coordination of metal cations with relatively similar affinities for different donors is more challenging with either statistical mixtures of different complexes or the homo-bimetallic complexes forming exclusively.[8]

Preliminary experiments were carried out to explore whether hetero-bimetallic complexes could be formed using **3.1** and proved largely unsuccessful. Treatment of trianiline **3.7** (4 equiv.) and **3.1** (12 equiv.) with equimolar amounts of Cu^{I} and Ag^{I} triflate (6 equiv. each) led to the formation of a broad distribution of products. While most peaks correspond to $M_{12}L_4$ species, similar to that of **3.9** and **3.10**, a statistical distribution of Ag^{I} and Cu^{I} is also observed (Figure 3.14). Significant broadening was also observed by ^{1}H NMR spectroscopy, consistent with a wide array of structures forming. Similar results were obtained when pre-formed **3.9** and **3.10** were mixed together and heated.

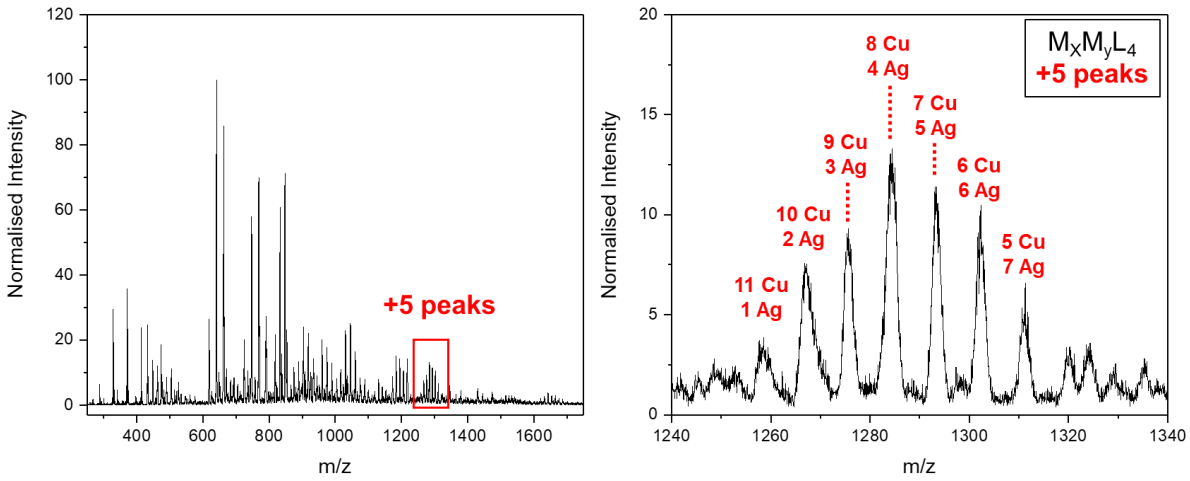

Figure 3.14 | ESI-MS of the mixture of products resulting from the mixing and subsequent heating of **3.9** with **3.10**. A statistical distribution of peaks was observed. The distribution associated with the +5 charge state is highlighted on the right.

This result indicates that while **3.9** and **3.10** do have a pair of chemically distinct coordination environments, they are incapable of discriminating between these two cationic species and addressing them selectively to either coordination environment.

Attention then turned to transition metals with significantly different electronic configurations, particularly Cd^{II}, which has a much more diffuse electron cloud. It was reasoned that the use of softer metal centres would lead to better discrimination between the different donors. It was anticipated that Cd^{II} should interact more favourably with the softer phosphine donors at the periphery of the hypothesised octahedral cage.

The assembly of **3.7** (4 equiv.) and **3.1** (12 equiv.) with copper(I) triflate (4 equiv.) and cadmium(II) triflate (4 equiv.) was observed by ESI-MS to form a $Cd^{II}_4Cu^{I}_4L_4$ cage **3.11** following heating at 60 °C overnight (Figure 3.15). This was another entirely unexpected result, given the 1:1:1 ratio of Cd^{II}, Cu^{I} and subcomponent **3.7**. ^{1}H NMR spectroscopy revealed the product to be highly symmetric with 9 distinct proton signals, indicating the symmetry of the ligands had been maintained. As with **3.9**, one broad peak was observed at 13.21 ppm by the ^{31}P NMR spectroscopy.

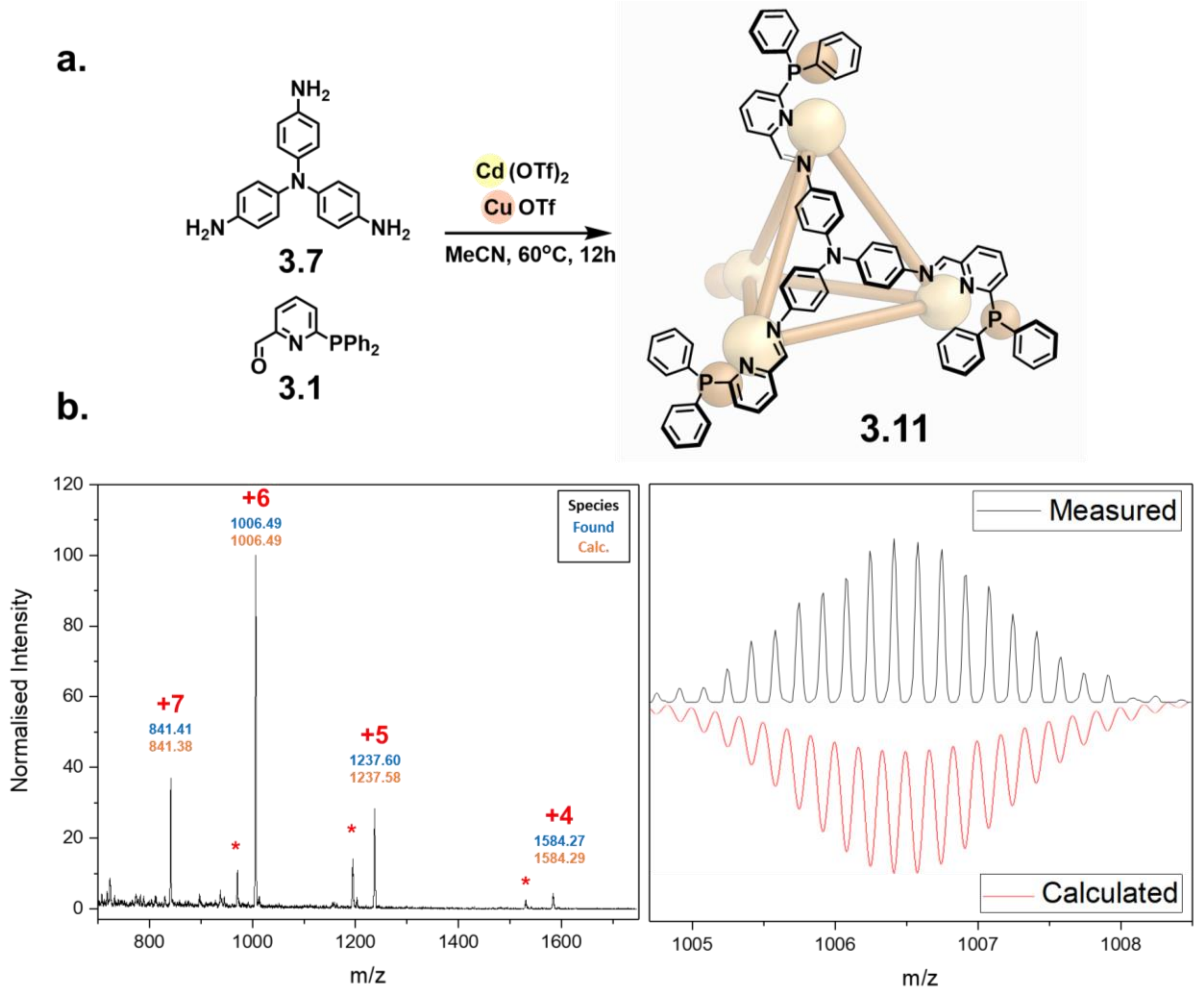

Figure 3.15 | a. Synthesis of $Cd^{II}_4Cu^{I}_4L_4$ tetrahedron **3.11**. **b**. ESI-MS of **3.11**. HRMS of the +5 peaks of the overall +12 charged cage. The asterisks indicate signals corresponding to **3.11** with the loss of one Cu^{I} cation.

Slow diffusion of diethyl ether into an acetonitrile solution of **3.11** resulted in crystals of sufficient quality for analysis by X-ray diffraction (Figure 3.16). The cage is tetrahedral and in terms of its connectivity it is structurally similar to a number of different M_4L_4 structures formed with 2-formylpyridine.[9]

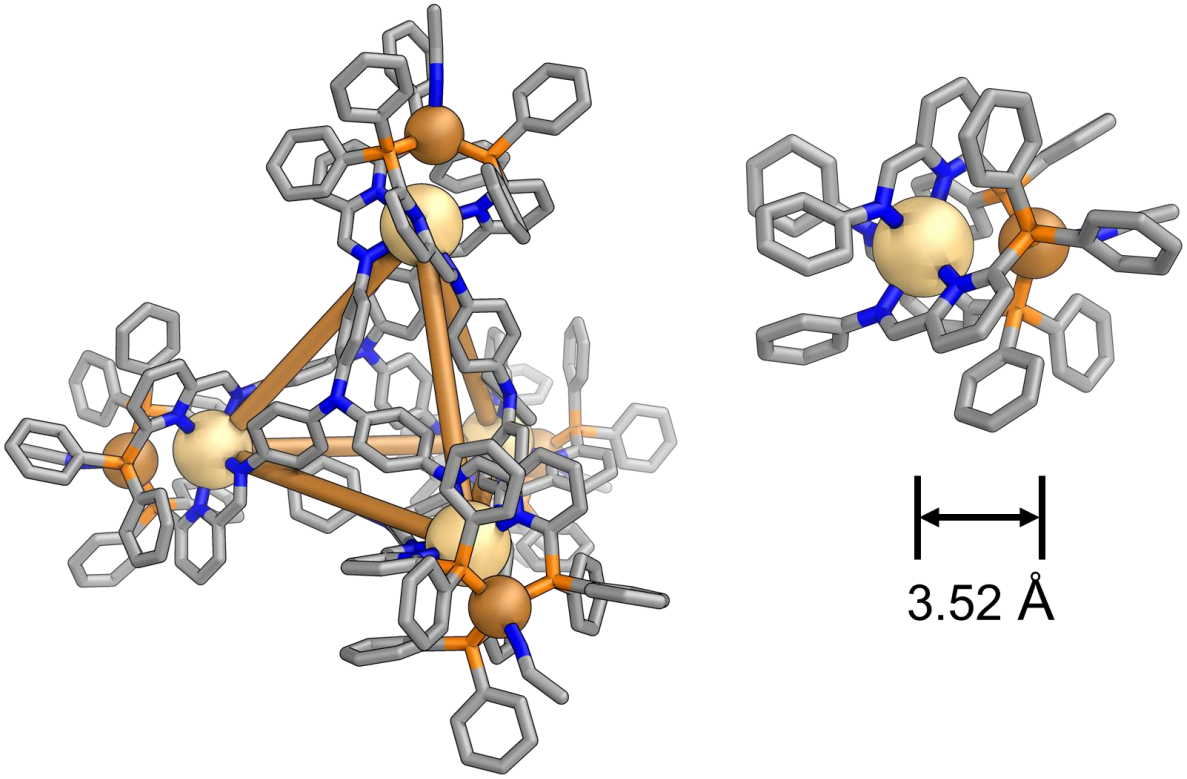

Figure 3.16 | Solid-state structure of **3.11**. A hetero-bimetallic vertex of the polyhedron has been isolated.

Counterintuitively, the softer Cd^{II} cations are coordinated by the relatively hard N donors of the pyridyl-imine motif. An average metal-metal distance of 3.52 ± 0.03 Å was measured for each of the symmetry equivalent vertices of the cage (Figure 3.16). This is significantly shorter than the metal-metal distance of 4.08 ± 0.05 Å measured for **3.9**, and longer than that of **3.10** (3.38 ± 0.03 Å).

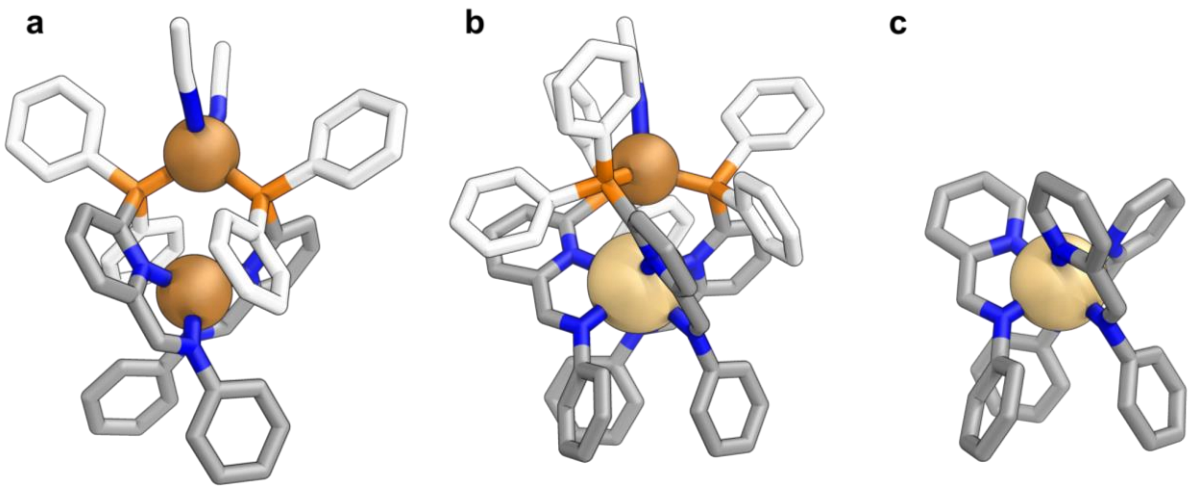

Figure 3.17 | Vertices of **a.** dicopper(I) based octahedron **3.9**, **b.** Cd^{II}-Cu^{I} based tetrahedron **3.11** and **c.** a Fe^{II} based tetrahedron we have previously reported.[9]

Structurally, **3.11** is similar to a previously reported Fe^{II} templated cage, formed with 2-formyl pyridine and the same tripodal amine ligand.[9] The phosphine-Cu^{I} appendages being the main distinguishing feature. The vertices **3.9** and **3.11** are compared with this previously reported structure **3.12** in Figure 3.17. In b. and c. it can be seen how each of the metal centres act to hold three ligands in close proximity, unlike in **3.9** where two ligands are held together. This results in the formation of geometrically distinct species, namely octahedra and tetrahedra.

3.5 A Larger Hetero-Bimetallic Tetrahedron

In order to probe whether this approach is generally applicable, a variety of different multitopic aniline ligands which are known to assemble into different polyhedral upon reaction with 2-formylpyridine and different transition metal salts where tested. Among them was ligand **3.13**, a tritopic ligand which, when reacted with 2-formylpyridine and a range of transition metal salts, produces a tetrahedron with rich host-guest chemistry.[10] The following synthetic work was carried out by Théophile Heliot at the University of Cambridge, under my supervision. Treatment of **3.13** (4 equiv.) with **3.1** (12 equiv.), $Cd(OTf)_2$ (4 equiv.) and $Cu(OTf)(MeCN)_4$ (4 equiv.) at 60° yielded a structure **3.14** with a $Cd_4Cu_4L_4$ structure, as confirmed by HR-MS (Figure 3.18 and Experimental Section). ^{1}H NMR spectroscopy revealed **3.14** to be highly symmetric, with maintenance of the symmetry of the threefold-symmetric ligand **3.13**.

Slow vapour diffusion of diisopropyl ether into an acetonitrile solution of **3.14** provided crystals of suitable quality for analysis by X-ray diffraction. These studies confirmed **3.14** to be isostructural to **3.11** (Figure 3.18b). The internal Cd^{II} cations are separated from one another by an average distance of 16.30 ± 0.08 Å, significantly greater than that of **3.11**, where they are separated by 12.6 ± 0.1 Å. The average distance between the Cd^{II} and Cu^{I} cations within the hetero-bimetallic vertices was measured to be 3.48 ± 0.01 Å, which is comparable to that of **3.11**. Surprisingly, the crystal structure revealed a bound cyclohexane molecule inside the cavity of **3.14**. We suspect that this may have occurred as a result of a contaminant in the diisopropyl ether used in the process of crystallising **3.14**.

This binding of the cyclohexane not unprecedented. The Fe^{II} congener **3.12** is known to bind cyclohexane and numerous other small aliphatic and aromatic guests.[10] This final result suggests that these new hetero-bimetallic assemblies may retain many of the well-characterised properties of their previously reported monometallic congeners. Given the breadth of structures formed with a multitude of ligands with different symmetries and physico-chemical properties, there remains a lot of room to explore with this new method of synthesising metal-organic cages.

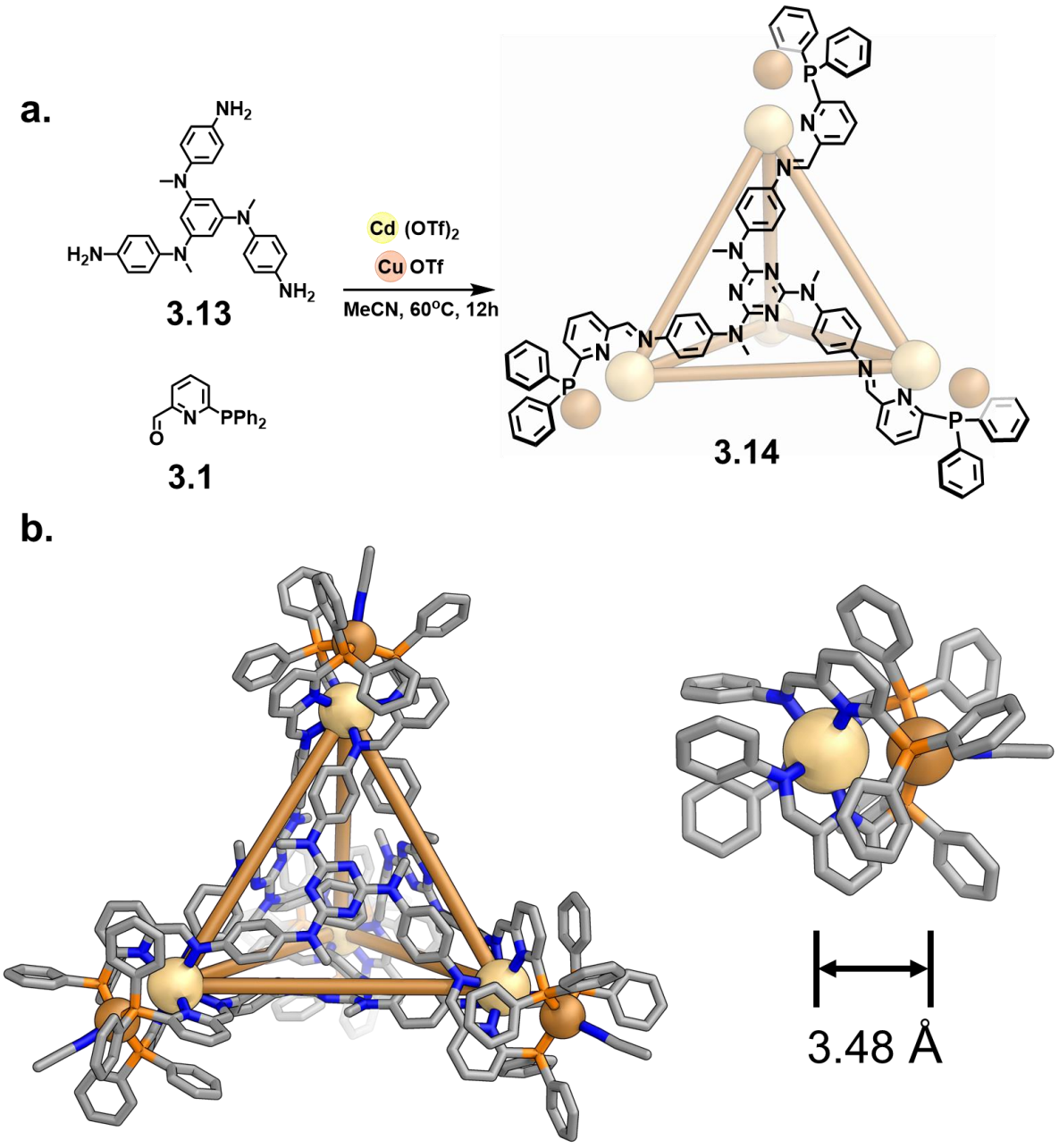

Figure 3.18 | Synthesis of $Cd^{II}_4Cu^{I}_4L_4$ tetrahedron **3.14** from subcomponents **3.1** and **3.13**. **b**. Solid-state structure with one vertex isolate for clarity.

3.6 Future Work

Developing new cages for the sake of incorporating bimetallic or hetero-bimetallic vertices, while synthetically interesting, is not a worthwhile pursuit. Preliminary studies of the host chemistry of cages **3.11** (which binds several small anions) and **3.14** in solution has shown that their host-guest affinities are relatively similar to those of the monometallic analogues. Differentiation of the cages in this regard appears unlikely.

Future work will look into whether the labile coordination sites, occupied by acetonitrile molecules in the solid state, could be used as points at which the cages could be functionalised. The ability to attach new moieties to the periphery of already assembled cage could enable it to achieve an otherwise difficult task. Phase-transfer could be triggered with the attachment of a suitable molecule. Fluorescent tags could be used to label the cages, which may have be useful in a biological context.

In conclusion, this Chapter has introduced the use of a subcomponent which has proximal, but non-converging, donor groups which enforce the formation of both homo- and hetero-bimetallic vertices in the synthesis of polyhedral cages. The same subcomponent, with same trianiline ligand, can be used to form very distinct architectures, a *pseudo*-octahedron and a tetrahedron in particular, with the use of different metal cations with different coordination preferences. Each of the structures formed are based on novel and unprecedented coordination modes.

3.7 Experimental Section

*Synthesis of **3.9***

Tris(4-aminophenyl)amine (7.74 mg, 27 µmol, 4 equiv.), copper(I) triflate (30.35 mg, 81 µmol, 12 equiv.) and 6-(diphenylphosphino)formylpyridine (23.30 mg, 80 µmol, 12 equiv.) were stirred in CD_3CN (5 mL) at 60 °C for 12 h in a sealed vessel under a nitrogen atmosphere, yielding a dark red solution. The reaction mixture was then filtered through a glass fibre filter (0.7 µm pore size). The acetonitrile was concentrated under a stream of N_2 to a volume of 1 mL. Addition of diethyl ether (5 mL) resulted in the precipitation of a dark red powder. The suspension was then centrifuged (10 min, 3000 RPM), the eluent decanted. Further diethyl ether (5 mL) was added, the powder was resuspended by sonication and then centrifuged. Again, the eluent was decanted. The residue was then dried *in vacuo* to afford the solid product as a fine dark red powder (51 mg, 83%).

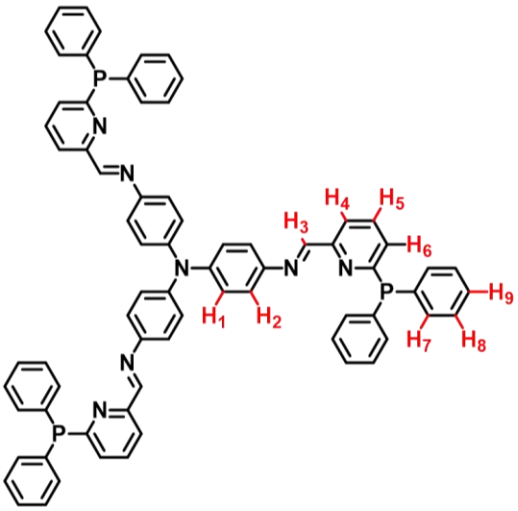

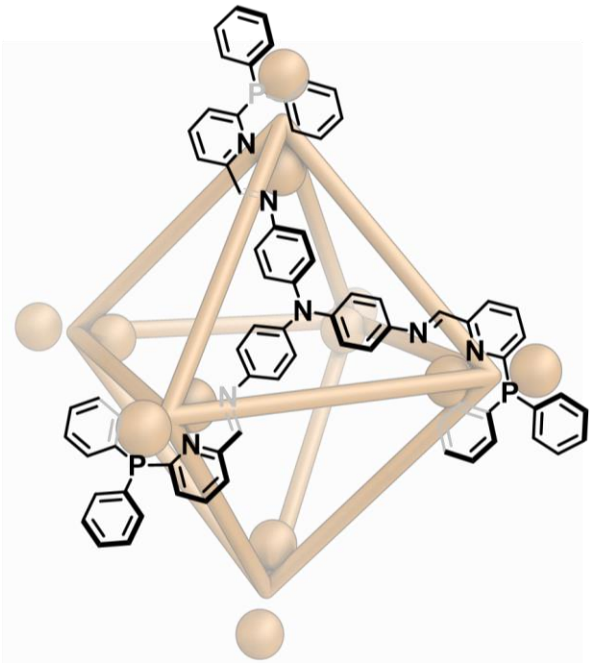

^{1}H NMR (500 MHz, 298 K, CD_3CN) δ: 8.42 (H_3, s, 12H), 8.18 (H_5, t, J = 7.9 Hz, 1H), 7.89 (H_6, d, J = 7.4 Hz, 3H), 7.87 (H_2, m, 3H), 7.63 (H_4, d, J = 8.8 Hz, 2H), 7.30 (H_7, dd, J = 7.6, 6.5 Hz, 2H), 7.04 (H_9, t, J = 7.5 Hz, 1H), 6.87 (H_8, t, J = 7.6 Hz, 2H), 6.63 (H_1 d, J = 8.4 Hz, 2H).

^{31}P NMR (162 MHz, 298 K, CD_3CN) δ: 7.52 (br s).

HRMS (ESI-LTQ Orbitrap XL, CH_3CN) m/z found 1249.3436, calculated 1249.3433 for +5 species.

*Synthesis of **3.10***

Tris(4-aminophenyl)amine (7.76 mg, 27 µmol, 4 equiv.), silver(I) triflate (20.6 mg, 82 µmol, 12 equiv.) and 6-(diphenylphosphino)formylpyridine (23.2 mg, 79 µmol, 12 equiv.) were stirred in CD_3CN (5 mL) at 60 °C for 12 h in a sealed vessel under a nitrogen atmosphere and in the dark, yielding a light red solution. The reaction mixture was then filtered through a glass fibre filter (0.7 µm pore size). The acetonitrile was concentrated under a stream of N_2 to a volume of 1 mL. Addition of diethyl ether (4 mL) resulted in the precipitation of a dark powder. The suspension was then centrifuged (10 min, 3000 RPM), the eluent decanted. Further diethyl ether (5 mL) was added, the powder was resuspended by sonication and then centrifuged. Again, the eluent was decanted. The residue was then dried *in vacuo* to afford the solid product as a fine bright red powder (45 mg, 89%).

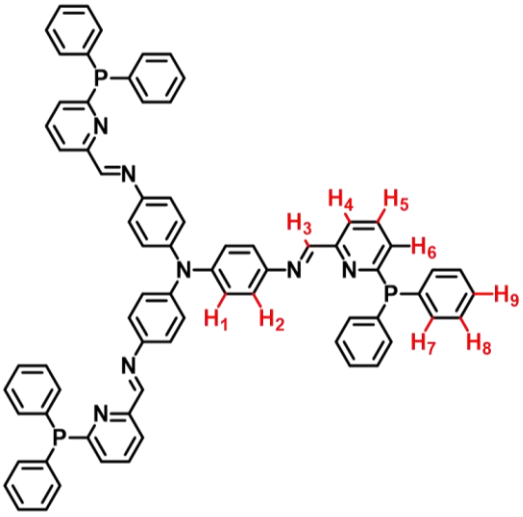

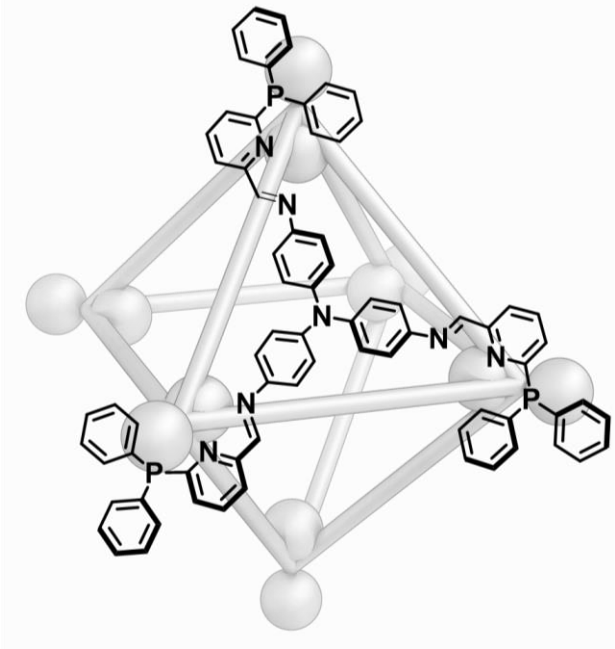

^{1}H NMR (500 MHz, 298 K, CD_3CN) δ: 8.42 (H_3, s, 12H), 8.18 (H_5, t, J = 7.9 Hz, 12H), 7.89 (H_6, d, J = 7.4 Hz, 12H), 7.87 (m, 3H), 7.63 (H_4, d, J = 8.8 Hz, 12H), 7.58 (H_2, d, J = 7.8 Hz, 24H), 7.30 (H_7, q, J = 6.5 Hz, 24H), 7.04 (H_9, t, J = 7.5 Hz, 24H), 6.87 (H_8, t, J = 7.6 Hz, 24H), 6.63 (H_1, d, J = 8.4 Hz, 24H). Proton was assigned according to ^{1}H-^{1}H COSY and NOESY experiments.

^{13}C NMR (125 MHz, 298 K, CD_3CN) δ: 160.2, 154.0, 152.7 147.7, 141.6, 136.8, 134.9, 133.1, 132.1, 130.9, 130.0, 129.3 128.5, 126.0, 124.5, 123.4, 120.9.

^{13}P NMR (125 MHz, 298 K, CD_3CN) δ: 14.78 (multiplet)

HRMS (ESI-LTQ Orbitrap XL, CH_3CN) m/z found 1355.5970, calculated 1355.5979 for +5 species.

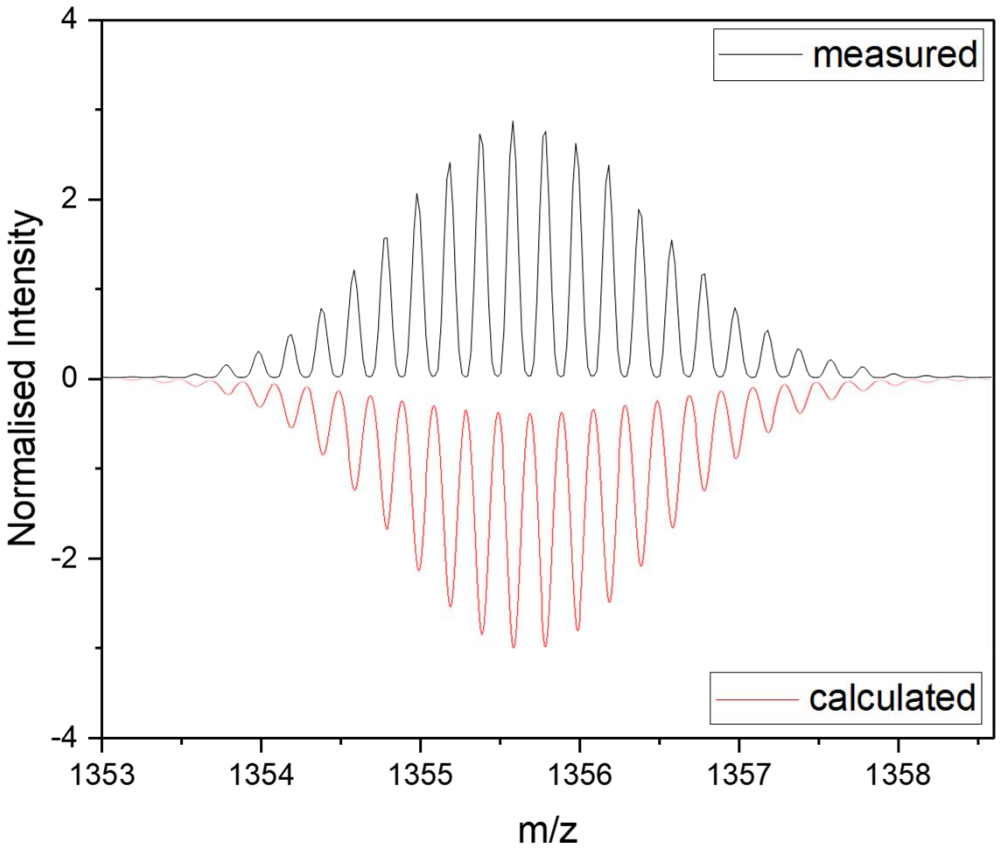

*Synthesis of **3.11***

Tris(4-aminophenyl)amine (3.9 mg, 13.4 µmol, 4 equiv.), copper(I) triflate (5.05 mg, 13.3 µmol, 4 equiv.), cadmium(II) triflate (5.76 mg, 13.37 µmol, 4 equiv.) and 6-(diphenylphosphino)formylpyridine (11.65 mg, 40.2 µmol, 12 equiv.) were stirred in CD_3CN (3 mL) at 60 °C for 12 h in a sealed vessel under a nitrogen atmosphere and in the dark, yielding a light red solution. The reaction mixture was then filtered through a glass fibre filter (0.7 µm pore size). The acetonitrile was concentrated under a stream of N_2 to a volume of 1 mL. Addition of diethyl ether (5 mL) resulted in the precipitation of a dark red powder. The suspension was then centrifuged (10 min, 3000 RPM), the eluent decanted. Further diethyl ether (5 mL) was added, the powder was resuspended by sonication and then centrifuged. Again, the eluent was decanted. The residue was then dried *in vacuo* to afford the solid product as a red powder (19.1 mg, 73%).

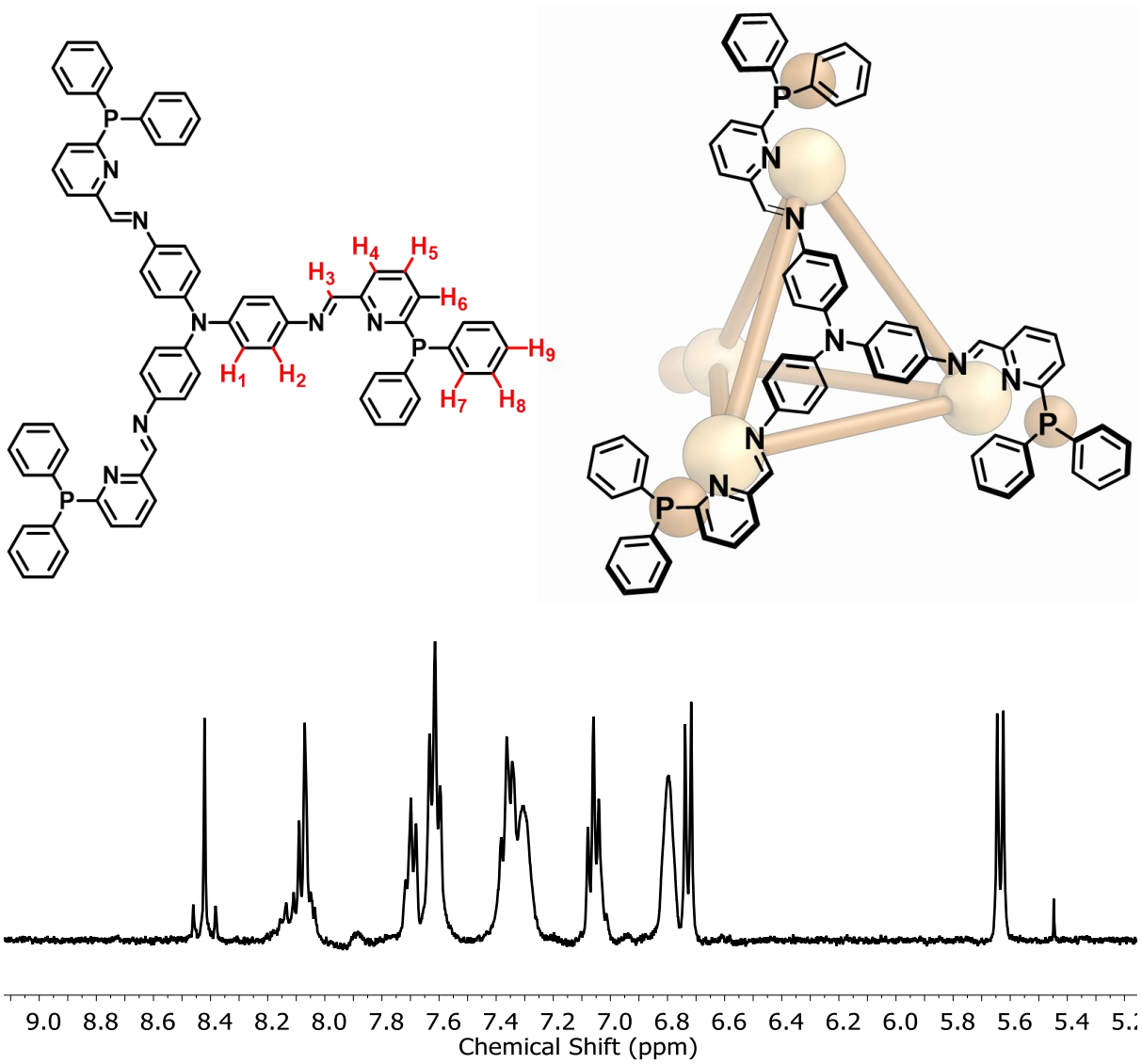

^{1}H NMR (500 MHz, 298 K, CD_3CN) δ: 8.42 (H_3, s, 12H), 8.07 (H_5, t, J = 7.9 Hz, 12H), 7.70 (H_6, d, J = 7.4 Hz, 12H), 7.63 (H_2, m, 3H), 7.61 (H_4, d, J = 8.8 Hz, 2H), 7.36 (H_7, q, J = 6.5 Hz, 2H), 7.27 (H_{10}, q, J = 6.5 Hz, 2H), 7.04 (H_9, t, J = 7.5 Hz, 1H), 6.87 (H_8, t, J = 7.6 Hz, 2H), 6.63 (H_1 d, J = 8.4 Hz, 2H).

^{13}C NMR (125 MHz, 298 K, CD_3CN) δ: 168.3, 152.9, 149.1 148.1, 145.1, 139.2, 134.1, 133.9, 133.1, 131.0, 130.5, 128.3 127.5, 126.9, 125.5, 124.1, 122.9.

^{31}P NMR (162 MHz, 298 K, CD_3CN) δ: 13.21 (br, s)

HRMS (ESI-LTQ Orbitrap XL, CH_3CN) m/z found 1006.4883, calculated 1006.4880 for +6 species.

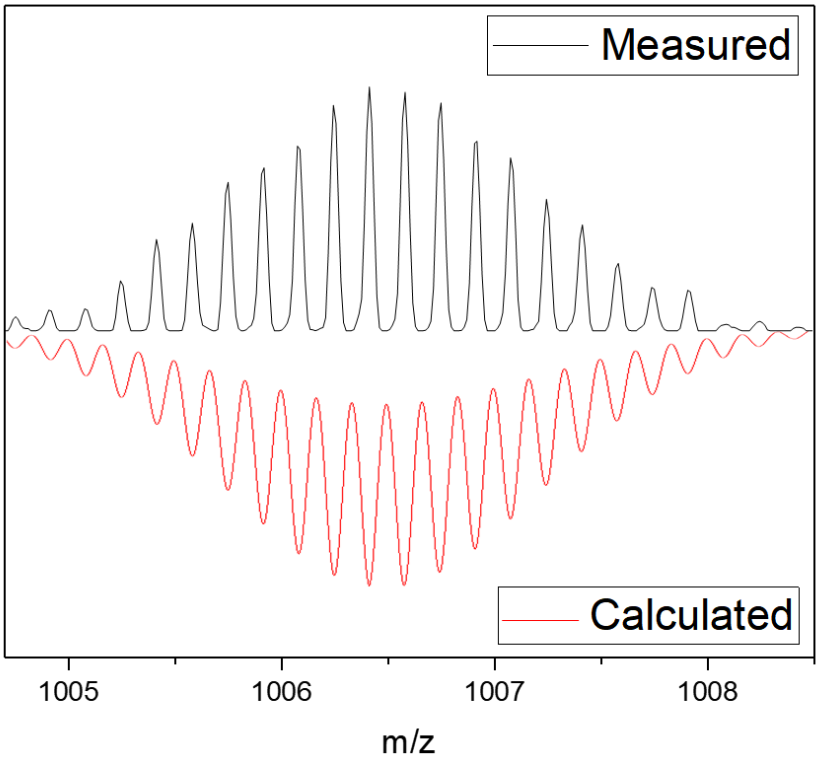

*Synthesis of **3.14***

$Cd^{II}_4Cu^{I}_4L_4$ was synthesised by Théophile Heliot at the Univeristy of Cambridge, under my supervision.

Trianiline subcomponent **3.13** (5.89 mg, 13.4 µmol, 4 equiv.), 5.05 mg, 13.3 µmol, 4 equiv.), cadmium(II) triflate hydrate (4.5 equiv. H_2O) (5.76 mg, 13.37 µmol, 4 equiv.) and 6-(diphenylphosphino)formylpyridine (11.65 mg, 40.2 µmol, 12 equiv.) were stirred in CD_3CN (3 mL) at 60 °C for 12 h in a sealed vessel under a nitrogen atmosphere and in the dark, yielding a pale yellow solution. The reaction mixture was then filtered through a glass fibre filter (0.7 µm pore size). The acetonitrile was concentrated under a stream of N_2 to a volume of 1 mL. Addition of diethyl ether (4 mL) resulted in the precipitation of a dark purple powder. The suspension was then centrifuged (10 min, 3000 RPM), the eluent decanted. Further diethyl ether (4 mL) was added, the powder was resuspended by sonication and then centrifuged. Again, the eluent was decanted. The residue was then dried *in vacuo* to afford the solid product as a fine dark purple powder (21 mg, 63%).

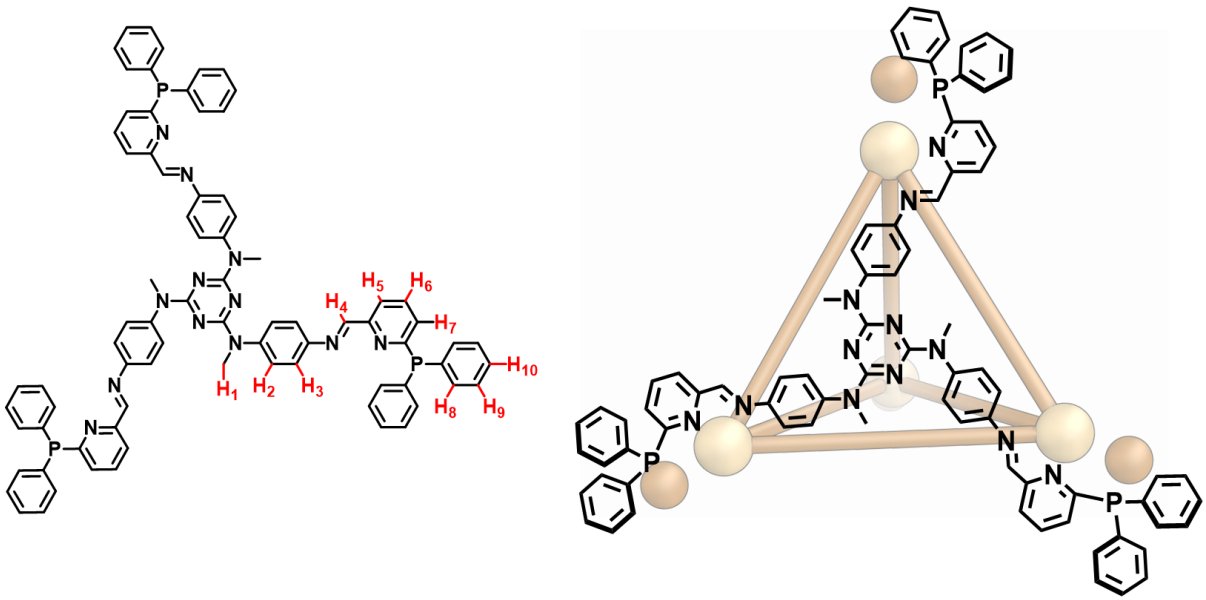

^{1}H NMR (500 MHz, 298 K, CD_3CN) δ: 8.23 (H_6, t, J = 7.8 Hz, 12H), 8.10 (H_4, s, 12H), 7.82 (H_5, d, J = 7.7 Hz, 12H), 7.74 (H_9, t, J = 7.4 Hz, 24H), 7.66 (H_7, br d, J = 7.7 Hz, 1H), 7.45 (H_3, d, J = 7.9 Hz, 1H), 7.42 – 7.32 (H_8 and H_{10}, m, 48H), 7.09 (H_2, d, J = 7.8 Hz, 24H), 6.85 (s, 2H), 3.37 (H_1, s, 36H).

^{31}P NMR (162 MHz, 298 K, CD_3CN) δ: 10.21 (br, s)

HRMS (ESI-LTQ Orbitrap XL, CH_3CN) m/z found 1358.5350, calculated 1358.5354 for +5 species.

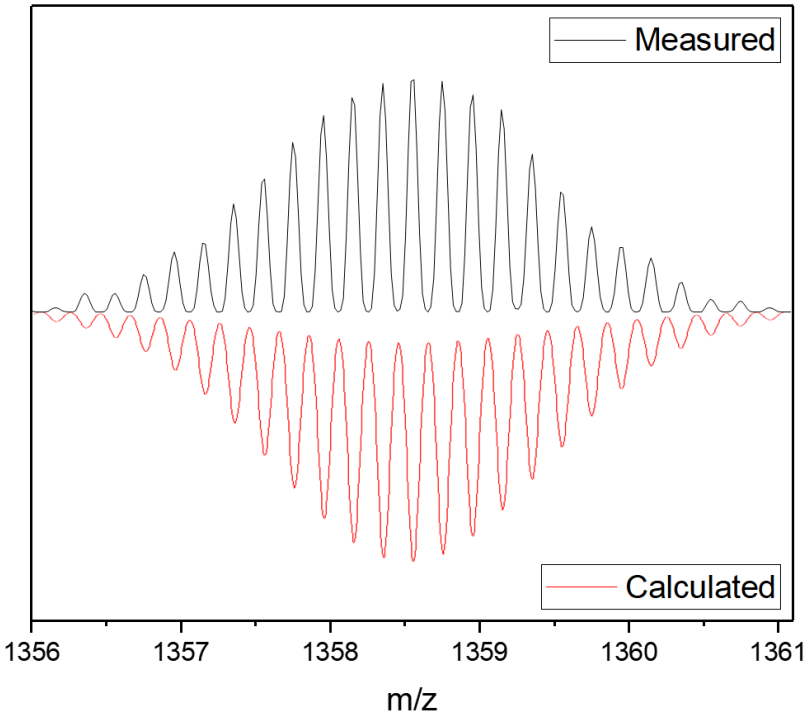

3.8 Crystallography

Data were for all structures except $[Cu_{12}L_4(MeCN)_{12}]\cdot OTf\cdot 11ClO_4\cdot 0.5MeCN$ were collected at Beamline I19 of Diamond Light Source employing silicon double crystal monochromated synchrotron radiation (0.6889 Å) with ω and ψ scans at 100(2) K. Data integration and reduction were undertaken with Xia2 and multi-scan empirical absorption corrections were applied to the data using the AIMLESS tool in the CCP4 suite. Data for $[Cu_{12}L_4(MeCN)_{12}]\cdot OTf\cdot 11ClO_4\cdot 0.5MeCN$ were collected using a Bruker D8 VENTURE equipped with high-brilliance IμS Cu-Kα radiation (1.54178 Å), with ω and ψ scans at 180(2) K. Data integration and reduction were undertaken with SAINT and XPREP and a multi-scan empirical absorption corrections were applied to the data using SADABS. In all cases subsequent computations were carried out using the WinGX-32 graphical user interface. The structures were solved by dual space methods using SHELXT or charge-flipping using SUPERFLIP then refined and extended with SHELXL. In general, non-hydrogen atoms with occupancies greater than 0.5 were refined anisotropically. Carbon-bound hydrogen atoms were included in idealised positions and refined using a riding model. Disorder was modelled using standard crystallographic methods including constraints, restraints and rigid bodies where necessary. Crystallographic data along with specific details pertaining to the refinement follow.

Three data sets were collected for the complex $Cu_{12}L_4(MeCN)_{12}$, from three different samples, grown in the presence of different counterions. The crystallographic data for all three are presented here but only the highest resolution data set, obtained for $[Cu_{12}L_4(MeCN)_{12}]\cdot 11.7OTf\cdot 0.3ReO_4\cdot 2MeCN\cdot 1.5{}^{i}Pr_2O$, is discussed in detail in the main text. All three data sets are isomorphous with respect to the $Cu_{12}L_4(MeCN)_{12}$ cations.

$[Cu_{12}L_4(MeCN)_{12}]\cdot 11.7OTf\cdot 0.3ReO_4\cdot 2MeCN\cdot 1.5{}^{i}Pr_2O$ [+ solvent]

Formula $C_{336.70}H_{279}Cu_{12}F_{35.10}N_{42}O_{37.80}P_{12}Re_{0.30}S_{11.70}$, M 7750.18, Cubic, space group P 2_1 3 (#198), a 43.215(5), b 43.215(5), c 43.215(5) Å, V 80705(28) $Å^3$, D_c 1.276 g cm^{-3}, Z 8, crystal size 0.040 by 0.030 by 0.030 mm, colour brown, habit prism, temperature 100(2) Kelvin, λ(Synchrotron) 0.6889 Å, μ(Synchrotron) 0.827 mm^{-1}, $T(\text{Analytical})_{min,max}$ 0.924445967991, 1.0, $2\theta_{max}$ 47.80, *hkl* range -50 50, -50 50, -50 50, N 983792, N_{ind} 45877(R_{merge} 0.0551), N_{obs} 43473(I > 2σ(I)), N_{var} 2725, residuals* $R1(F)$ 0.0401, $wR2(F^2)$ 0.1028, GoF(all) 1.016, $\Delta\rho_{min,max}$ -0.244, 0.634 e^- $Å^{-3}$.

*$R1 = \Sigma||F_o| - |F_c||/\Sigma|F_o|$ for $F_o > 2\sigma(F_o)$; $wR2 = (\Sigma w(F_o^2 - F_c^2)^2/\Sigma(wF_c^2)^2)^{1/2}$ all reflections

$w=1/[\sigma^2(F_o^2)+(0.0827P)^2]$ where $P=(F_o^2+2F_c^2)/3$

Specific refinement details:

The crystals of $[Cu_{12}L_4(MeCN)_{12}]\cdot 11.7OTf\cdot 0.3ReO_4\cdot 2MeCN\cdot 1.5{}^iPr_2O$ [+ solvent] were grown by diffusion of diethyl ether into an acetonitrile solution of $[Cu_{12}L_4(MeCN)_{12}]\cdot 12OTf$ containing Bu_4NReO_4. The crystals employed immediately lost solvent after removal from the mother liquor and rapid handling prior to flash cooling in the cryostream was required to collect data. Data were obtained to 0.85 Å resolution. The asymmetric unit was found to contain one third each of two separate $Cu_{12}L_4$ assemblies and associated counterions and solvent molecules. The structure was refined as both a merohedral twin (twin law 0 1 0 1 0 0 0 0 -1) and a racemic twin with the BASF parameters refining to 0.21493/0.20971/0.29022.

Bond lengths and angles within pairs of chemically identical organic ligand arms were restrained to be similar to each other (SAME) and some aromatic rings were refined with rigid body constraints (AFIX 66). Thermal parameter restraints (SIMU, RIGU) were applied to all atoms except for copper and rhenium to facilitate anisotropic stable refinement. Two of the coordinated acetonitrile molecules were modelled as disordered over two locations and a further one shows evidence of thermal motion or minor unresolved disorder. These acetonitrile molecules were modelled with isotropic thermal parameters and bond length restraints (DFIX) were applied to all coordinated acetonitrile molecules.

The anions within the structure also show evidence of disorder. One triflate anion was modelled as disordered over two locations. One lattice site (on a special position) was modelled as a disordered mixture of triflate and perrhenate. A further triflate anion was modelled as disordered over a special position using a rigid group and another triflate was modelled with partial occupancy. The occupancies of the disordered anions were allowed to refine freely and in some cases were then fixed at the obtained values. Some disordered anions could not be located in the electron density map and were not included in the model resulting in a discrepancy of 4.28 anions per $Cu_{12}L_4$ assembly; these anions are included as triflate in the formula given above. Some lower occupancy disordered atoms were modelled with isotropic thermal parameters and bond length and thermal parameter restraints were applied to facilitate realistic modelling of the disordered anions.

Further reflecting the solvent loss there is a significant amount of void volume in the lattice containing smeared electron density from disordered solvent the unresolved anions. Consequently the SQUEEZE function of PLATON was employed to remove the contribution of the electron density

associated with these highly disordered solvents and anions which gave a potential solvent accessible void of 19970 Å^3 per unit cell (a total of approximately 5351 electrons). Since the diffuse solvent molecules could not be assigned conclusively to acetonitrile or diisopropyl ether they were not included in the formula. Consequently, the molecular weight and density given above are likely to be slightly underestimated.

CheckCIF gives one B level alert, resulting from isotropic refinement of some of the coordinated acetonitrile molecules.

$[Ag_{12}L_4(MeCN)_{12}]\cdot 11.7OTf\cdot 0.3ReO_4\cdot 2MeCN\cdot 1.5{}^{i}Pr_2O$ [+ solvent]

$C_{300}H_{234}Ag_{12}F_{72}N_{34}P_{24}$, *M* 7720.92, Cubic, Fd–3 (#203), *a* 43.208(5), *b* 43.208(5), *c* 43.208(5) Å, *V* 80669(28) Å^3, D_c 1.271 g cm^{-3}, *Z* 8, crystal size 0.150 by 0.120 by 0.100 mm, colour purple, habit block, temperature 100(2) Kelvin, λ(Synchrotron) 0.6889 Å, μ(Synchrotron) 0.674 mm^{-1}, T(Analytical)$_{min,max}$ 0.9915, 1.0, 2θ_{max} 36.46, *hkl* range -38 39, -39 39, -39 39, *N* 49148, N_{ind} 2657(R_{merge} 0.1386), N_{obs} 1688(I > 2σ(I)), N_{var} 379, residuals* *R*1(*F*) 0.1008, *wR*2(F^2) 0.3140, GoF(all) 1.088, $\Delta\rho_{min,max}$ -0.605, 1.104 e$^-$ Å^{-3}.

*$R1 = \Sigma||F_o| - |F_c||/\Sigma|F_o|$ for $F_o > 2\sigma(F_o)$; $wR2 = (\Sigma w(F_o^2 - F_c^2)^2/\Sigma(wF_c^2)^2)^{1/2}$ all reflections

$w=1/[\sigma^2(F_o^2)+(0.1500P)^2+2000.0000P]$ where $P=(F_o^2+2F_c^2)/3$

Specific refinement details:

In general, non-hydrogen atoms with occupancies greater than 0.5 were refined anisotropically. Carbon-bound hydrogen atoms were included in idealised positions and refined using a riding model. The molecular formula was determined firstly from the required number of charge-balancing anions, and then confirmed from the number of electrons identified in the disordered portion of the crystal by SQUEEZE. Crystallographic data along with specific details pertaining to the refinements follow.

Crystals of **3.10·12PF$_6$** were grown by slow diffusion of diethyl ether into a CD_3CN solution of **3.10**. The crystals employed in this study rapidly lost solvent after removal from the mother liquor and rapid handling prior to flash cooling in the cryostream was required to collect data. Despite the use of high intensity synchrotron radiation, few reflections at greater than 1.1 Å resolution were observed. Nevertheless, the quality of the data is more than sufficient to establish the connectivity of the structure.

The SQUEEZEd portion of the cell totals 2,672 electrons per unit cell, with a solvent accessible void volume of 16,600 Å^3 per unit cell. This equates to 334 electrons per structure, where $Z = 8$. As all the anions were identified in the electron density map, we attribute this residual density to unresolved solvent molecules.

CheckCIF produces 1 Level A and 3 Level B alerts. All these alerts are due to the high thermal motion of some atoms, leading to the less than ideal resolution of the data.

Efforts to complete the refinement of **3.11** are ongoing. Metal-to-metal distances reported in this thesis should be reliable.

[C_6H_{12}⊂$Cu_4Cd_4L_4$(MeCN)$_4$]·12OTf·3.75MeCN [+ solvent]

Formula $C_{345.50}H_{287.25}Cd_4Cu_4F_{36}N_{55.75}O_{36}P_{12}S_{12}$, M 7940.16, Monoclinic, space group P 21/n (#14), a 20.229(4), b 47.904(10), c 40.646(8) Å, β 90.58(3), V 39386(14) Å^3, D_c 1.339 g cm^{-3}, Z 4, crystal size 0.010 by 0.010 by 0.010 mm, colour orange, habit block, temperature 100(2) Kelvin, λ(Synchrotron) 0.6889 Å, μ(Synchrotron) 0.565 mm^{-1}, T(Analytical)$_{min,max}$ 0.942873565376, 1.0, $2\theta_{max}$ 40.30, *hkl* range -20 20, -47 47, -40 40, N 194036, N_{ind} 40805(R_{merge} 0.0913), N_{obs} 28502(I > 2σ(I)), N_{var} 4529, residuals* $R1(F)$ 0.1340, $wR2(F^2)$ 0.3948, GoF(all) 1.062, $\Delta\rho_{min,max}$ -1.525, 1.999 e$^-$ Å^{-3}.

*$R1 = \Sigma||F_o| - |F_c||/\Sigma|F_o|$ for $F_o > 2\sigma(F_o)$; $wR2 = (\Sigma w(F_o^2 - F_c^2)^2/\Sigma(wF_c^2)^2)^{1/2}$ all reflections

$w=1/[\sigma^2(F_o^2)+(0.1946P)^2+491.1736P]$ where $P=(F_o^2+2F_c^2)/3$

Specific refinement details:

The crystals of $[C_6H_{12}\subset Cu_4Cd_4L_4(MeCN)_4]\cdot 12OTf\cdot 3.75MeCN$ [+ solvent] were grown by diffusion of diisopropyl ether into an acetonitrile solution of the complex. The crystals employed immediately lost solvent after removal from the mother liquor and rapid handling prior to flash cooling in the cryostream was required to collect data. Despite these measures and the use of synchrotron radiation few reflections at greater than 1.0 Å resolution were observed and the data were trimmed accordingly. The crystals were small and were subject to beam damage during data collection using synchrotron radiation; consequently the quality of the integration is less than ideal with relatively high residuals. Nevertheless, the quality of the data is far more than sufficient to establish the connectivity of the structure.

Bond lengths and angles within pairs of chemically identical organic ligands were restrained to be similar to each other (SAME) and some aromatic rings were refined with rigid body constraints (AFIX 66). Thermal parameter restraints (SIMU, RIGU) were applied to all atoms except for copper and cadmium to facilitate anisotropic stable refinement. Even with these restraints some thermal parameters remain larger than ideal as a consequence of the high level of thermal motion or minor unresolved disorder present throughout the structure. The encapsulated cyclohexane molecule was modelled as disordered over two locations with opposite orientations of the chair conformation. Bond lengths and angles within the disordered cyclohexane were restrained (DFIX, DANG) in order to obtain a reasonable geometry.

The anions within the structure also show evidence of substantial disorder. Seven triflate anions were modelled as disordered over two or three locations and several others were modelled with partial occupancy. The occupancies of the all the located anions were allowed to refine freely and then fixed at the obtained values. Some additional minor occupancy positions of the anions could not be located in the electron density map and were not included in the model resulting in a discrepancy of 4.55 anions per $Cu_4Cd_4L_4$ assembly; these anions are assigned as triflate in the formula given above. Some lower occupancy disordered atoms were modelled with isotropic thermal parameters and substantial bond length and thermal parameter restraints were required to facilitate realistic modelling of the disordered anions. Some acetonitrile solvent molecules were also modelled as disordered and/or with partial occupancy. The hydrogen atoms on some disordered acetonitrile molecules could not be resolved and were thus not included in the model.

Further reflecting the solvent loss there is a significant amount of void volume in the lattice containing smeared electron density from disordered solvent (and potentially the unresolved anions). Consequently, the SQUEEZE function of PLATON was employed to remove the contribution of the electron density associated with this highly disordered solvent which gave a potential solvent accessible void of 6276 $Å^3$ per unit cell (a total of approximately 1895 electrons). Since the diffuse

solvent molecules could not be assigned conclusively to acetonitrile or diisopropyl ether they were not included in the formula. Consequently, the molecular weight and density given above are likely to be underestimated.

CheckCIF gives one A and four B level alerts. These alerts all result from the limited data resolution, beam damage, thermal motion or minor unresolved disorder present throughout the structure and the disordered acetonitrile molecules for which hydrogen atoms were not modelled as described above.

3.9 References

(1) Dry, E. F. V.; Clegg, J. K.; Breiner, B.; Whitaker, D. E.; Stefak, R.; Nitschke, J. R. Reversible Anion-Templated Self-Assembly of [2+2] and [3+3] Metallomacrocycles Containing a New Dicopper(i) Motif. *Chem. Commun*. **2011**, *47*, 6021.

(2) Nitschke, J. R. Construction, Substitution, and Sorting of Metallo-Organic Structures via Subcomponent Self-Assembly. *Acc. Chem. Res.* **2007**, *40*, 103-112

(3) Rizzuto, F. J.; Wu, W.-Y.; Ronson, T. K.; Nitschke, J. R. Peripheral Templation Generates an $M^{II}_6L_4$ Guest-Binding Capsule. *Angew. Chem. Int. Ed*. **2016**, *55*, 7958–7962.

(4) Rizzuto, F. J.; Nitschke, J. R. Stereochemical Plasticity Modulates Cooperative Binding in a CoII12L6 Cuboctahedron. *Nat. Chem*. **2017**, *9*, 903–908.

(5) Mal, P.; Breiner, B.; Rissanen, K.; Nitschke, J. R. White Phosphorus Is Air-Stable within a Self-Assembled Tetrahedral Capsule. *Science* **2009**, *324*, 1697–1699.

(6) Ronson, T. K.; Zarra, S.; Black, S. P.; Nitschke, J. R. Metal–Organic Container Molecules through Subcomponent Self-Assembly. *Chem. Commun*. **2013**, *49*, 2476.

(7) Liu, S.; Motta, A.; Mouat, A. R.; Delferro, M.; Marks, T. J. Very Large Cooperative Effects in Heterobimetallic Titanium-Chromium Catalysts for Ethylene Polymerization/Copolymerization. *J. Am. Chem. Soc*. **2014**, *136*, 10460−10469.

(8) Garden, J. A.; White, A. J. P.; Williams, C. K. Heterodinuclear Titanium/Zinc Catalysis: Synthesis, Characterization and Activity for CO2/Epoxide Copolymerization and Cyclic Ester Polymerization. *Dalton Trans*. **2017**, *46*, 2532.

(9) Bilbeisi, R. A.; Clegg, J. K.; Elgrishi, N.; Hatten, X. de; Devillard, M.; Breiner, B.; Mal, P.; Nitschke, J. R. Subcomponent Self-Assembly and Guest-Binding Properties of Face-Capped $Fe_4L_4^{8+}$ Capsules. *J. Am. Chem. Soc*. **2012**, *134*, 5110–5119.

(10) Bolliger, J. L.; Ronson, T. K.; Ogawa, M.; Nitschke, J. R. Solvent Effects upon Guest Binding and Dynamics of a Fe^{II}_4 L_4 Cage. *J. Am. Chem. Soc*. **2014**, *136*, 14545−14553

4

Anions Pairs Template a Trigonal Prism with Disilver(I) Vertices

This Chapter explores the formation of a $Ag^{I}_{12}L_6$ trigonal prismatic cage **4.2** which is formed utilising a 2-formyl-1,8-naphthyridine subcomponent **4.1**. This motif has coordination vectors which are similar to the 2-formyl-6-diphenylphosphine-pyridine subcomponent **3.1** described in Chapter 3 and can bind pairs of Ag^{I} cations in close proximity to one another. The coordination mode adopted in cage **4.2** is distinct from those observed in Chapter 3 and is, to the best of our knowledge, unreported in the literature.

The cage self-assembles around a pair of anionic templates, which are shown by crystallographic and solution-phase data to bind within the central cavity of the structure. Many different anions serve as competent templates and guests. Elongated dianions, such as the strong oxidising agent peroxysulfate, also serve to template and bind within the cavity of the prism.

The work builds upon that described in Chapter 3 to show that using subcomponents that have more than one spatially close, but non-chelating, binding site may allow access to other complex and unexpected structures with multi-metallic vertices.

4.1 Introduction

The non-converging coordination vectors of commercially-available 1,8-naphthyridine have been utilised to produce a diverse array of transition metal complexes with highly distinct configurations and stoichiometries.[1,2] Depending on the nature of its ancillary groups and of the metal, it can act as a monodentate, bidentate or bidentate bridging ligand (Figure 4.1a-c).[3,4] Importantly, while the two N-donors are proximal (separated by 2.2 Å) their coordination vectors are parallel to one another. This prevents the formation of chelate complexes except in the case of metal cations with large, diffuse orbitals such as cadmium(II) (Figure 4.1b).

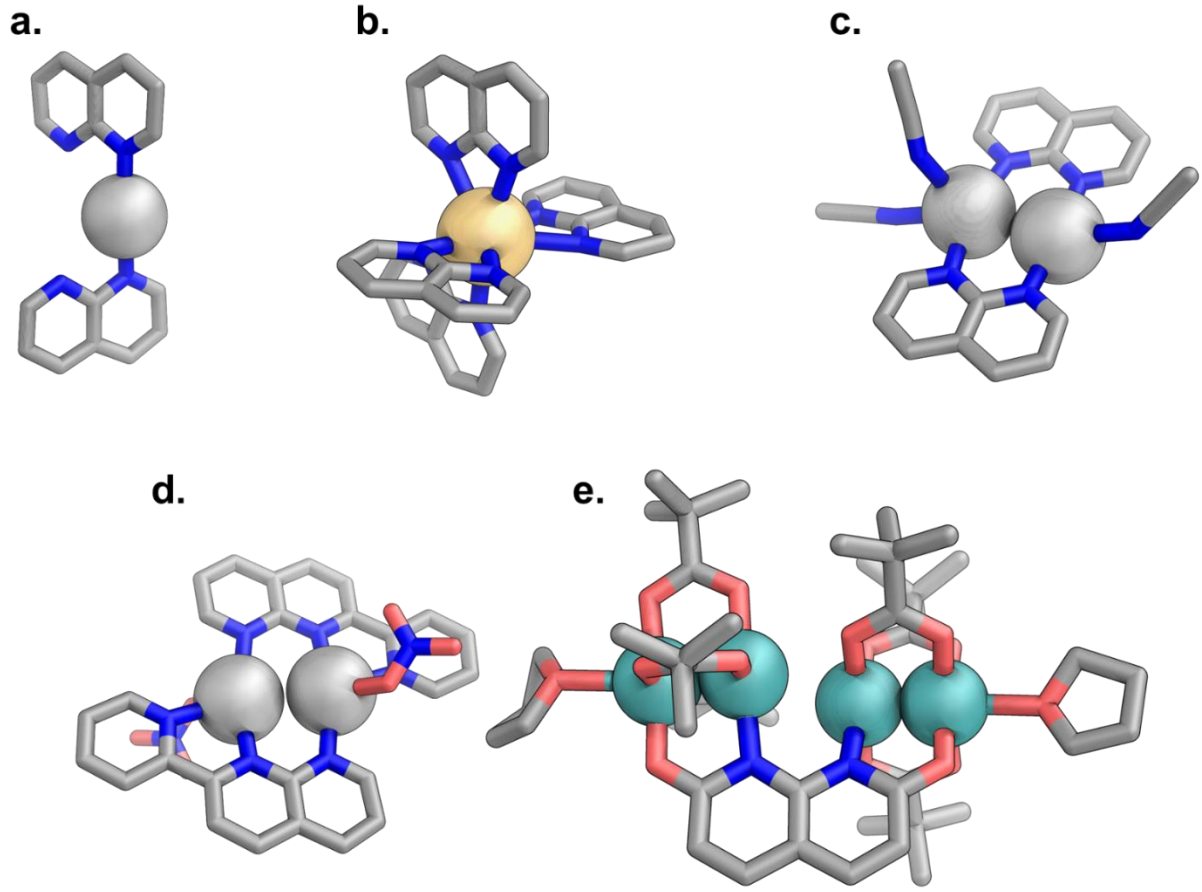

Figure 4.1 | Crystal structures of a selection of coordination complex which can be formed using the 1,8-naphthyridine motif. Anions and non-coordinating solvent molecules have been omitted for clarity. Metals are **a.** Ag^{I} **b.** Cd^{II} **c.** Ag^{I} **d.** Ag^{I} and **e.** Mo^{II}

If coordinating ancillaries are included different types of complexes are possible (Figure 4.1d-e).[5,6] In such cases, the N-donors of the naphthyridine often form a bridge with the ancillary ligand chelating to one of the metals.

In supramolecular chemistry, and particularly in coordination-driven self-assembly, many unprecedented and unexpected architectures have been obtained through the use of flexible organic building blocks.[7,8] Many systems that incorporate such species form unexpected and often structurally complex assemblies, including a range of intricate cages and grids,[9-11] which have been used for catalysis,[12] guest binding[13] and molecular knot formation.[14,15]

Normally, the coordination motif is considered to be the rigid part of the metal-organic architecture, rigidifying it and holding the organic ligands in set configurations relative to one another which enables the formation of larger structures. Indeed this is generally true, and has been used to great effect in the assembly of a wide array of polyhedral structures, with octahedral[16,17] and square planar[18,19] transition metals acting in this role.

Given the propensity of these 1,8-naphthyridine derivatives for forming such a vast array of coordination complexes and the flexible coordination sphere of Ag^{I},[20-22] it was hypothesised that this coordination motif could be used in an analogous way to the flexible organic ligands described above. In particular, the commercially available 2-formyl-1,8-naphthyridine, coupled with a subcomponent self-assembly approach,[23,24] was targeted.

4.2 Synthesis of a Trigonal Prism Using Bimetallic Vertices

The reaction of tris(4-aminophenyl)amine **3.7** (6 equiv.) and 1,8-naphthyridine-2-carbaldehyde **4.1** (12 equiv.) with silver(I) perchlorate ($AgClO_4^-$, 12 equiv.), at room temperature and in the dark yielded $Ag^I_{12}L_6$ cage **4.2** (Figure 4.2), whose composition was confirmed by both ESI- and HR-MS (Figure 4.3). ^{1}H NMR spectroscopy revealed 28 signals, consistent with a distinct environment for each ligand arm, and with two of the phenyl rings undergoing rapid rotation on the NMR chemical shift timescale (Figure 4.3a).

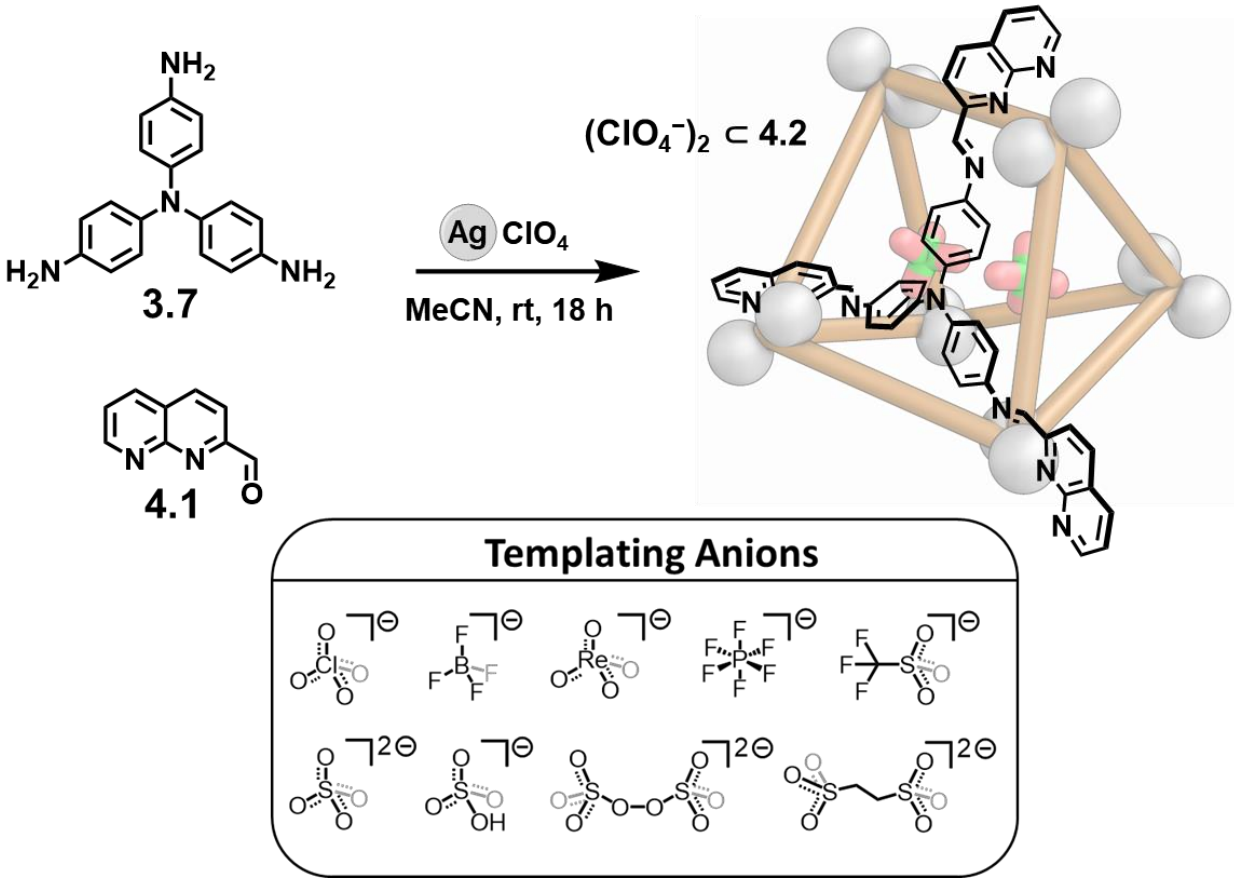

Figure 4.2 | Synthesis of $Ag^I_{12}L_6$ trigonal prism **4.2** from tris(4-aminophenyl)amine **3.7**, 1,8-naphthyridine-2-carbaldehyde **4.1** and silver(I) perchlorate. The assembly of the architecture requires an appropriate template anion, examples of which are tabulated.

Further analysis by diffusion ordered spectroscopy (DOSY) supported the formation of a single product structure in solution, with an observed diffusion coefficient of 4.8×10^{-6} cm^2 s^{-1}, corresponding to a hydrodynamic radius of 12 Å (Figure 4.3a).

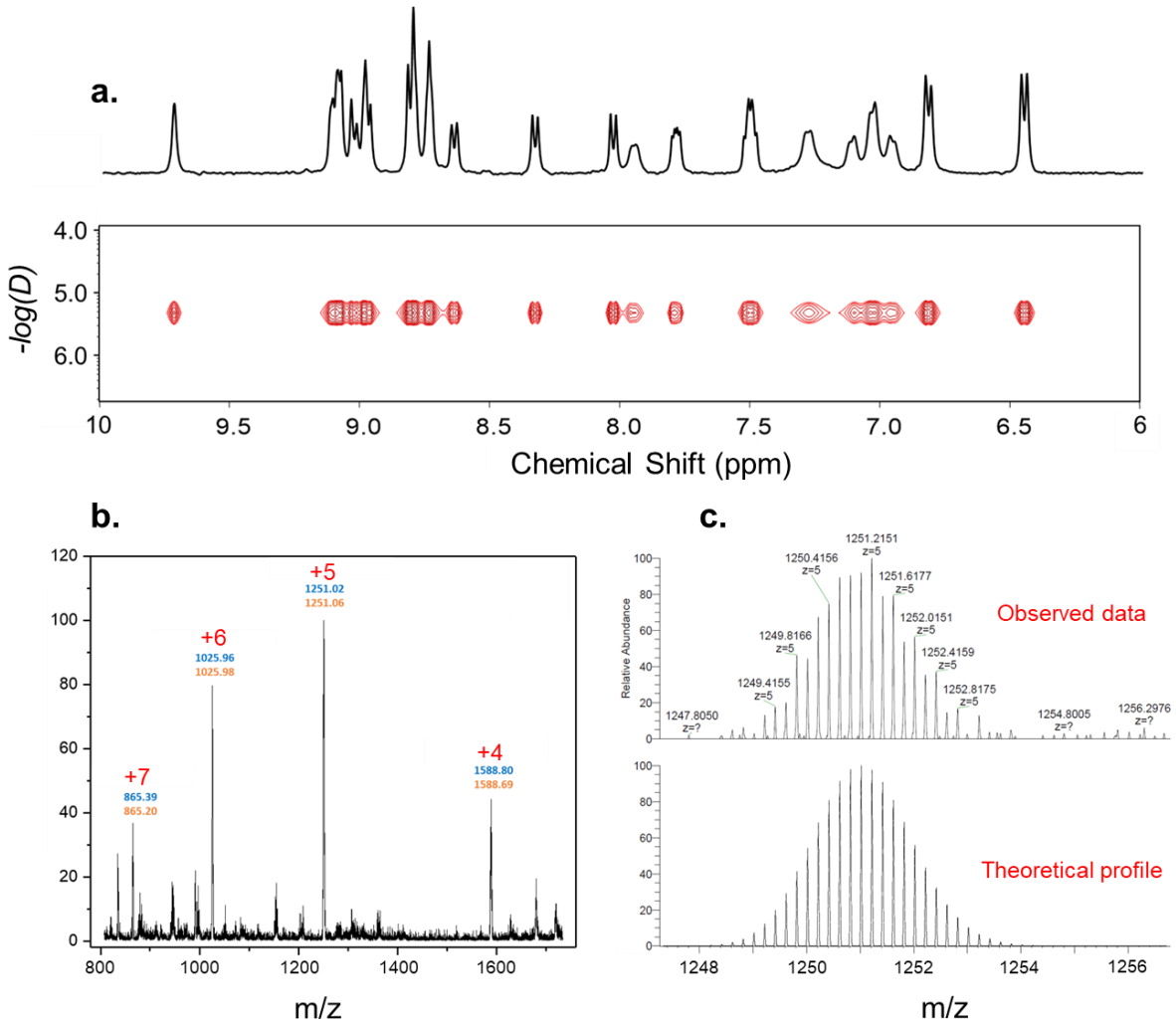

Figure 4.3 | a. ^{1}H NMR spectrum and diffusion ordered NMR spectrum of **$(ClO_4^-)_2 \subset$ 4.2** showing threefold desymmetrisation of the cage's ligands. The units of *D* are 10^{-6} cm^2 s^{-1}. **b.** ESI-MS of **$(ClO_4^-)_2 \subset$ 4.2** and **c.** HR-MS of the +5 charge state of **$(ClO_4^-)_2 \subset$ 4.2**.

Vapor diffusion of diisopropyl ether (iPr_2O) into an acetonitrile solution of **4.2** provided crystals suitable for analysis by X-ray diffraction. The cationic portion of **4.2** was revealed to have a twisted trigonal prismatic structure (Figure 4.4a-b) with a pair of Ag^I centres at each vertex of the prism.

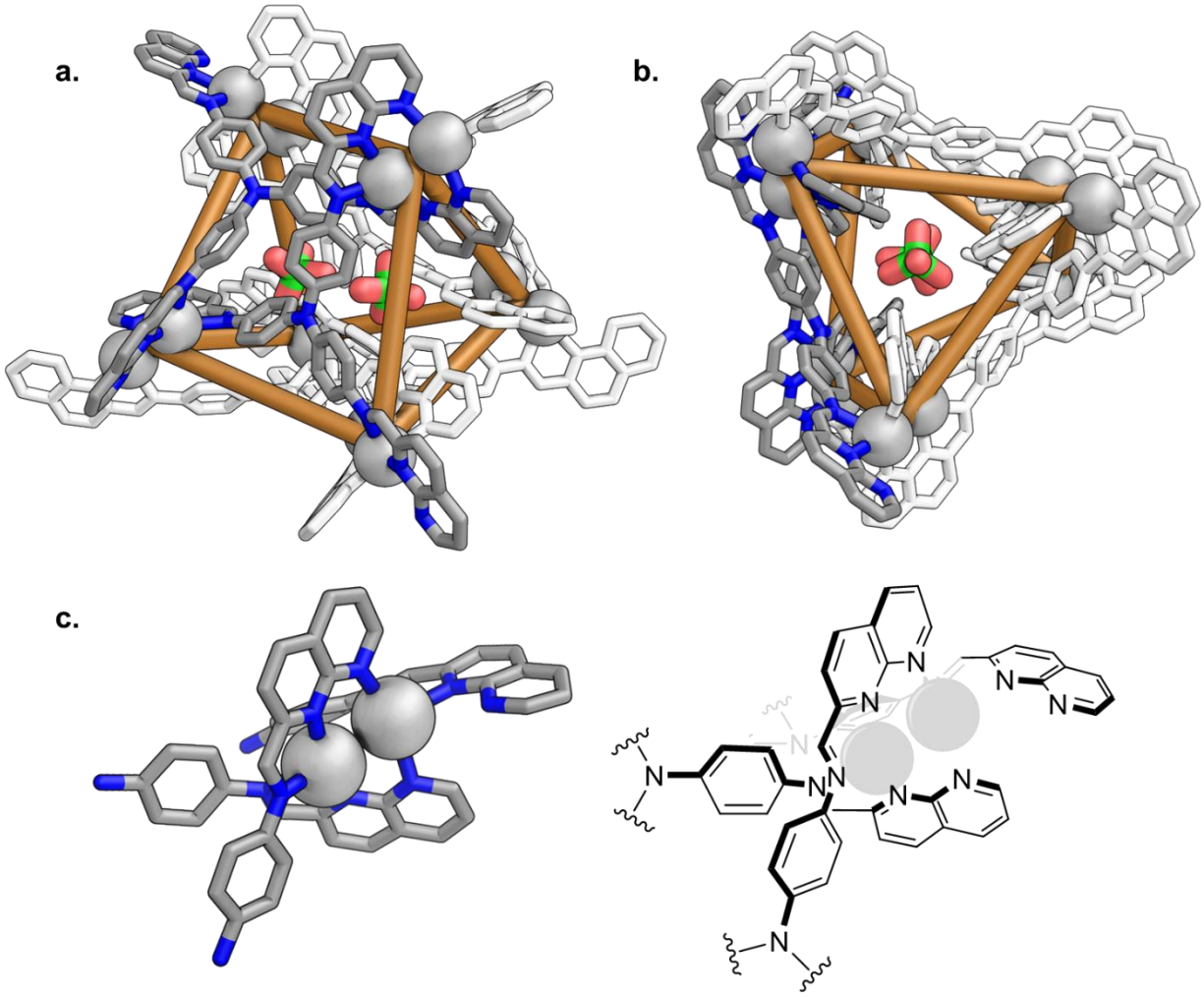

Figure 4.4 | a. X-ray crystal structure of $(ClO_4^-)_2 \subset$ **4.2** with the two templating anions included. Two ligands belonging to a single rectangular face of the prism have been highlighted to show the three-fold desymmetrisation of each ligand. Disorder, non-bound anions and solvent molecules have been omitted for clarity. **b.** Top-down view depicting the central, elongated void of $(ClO_4^-)_2 \subset$ **4.2**. **c.** One of the six identical bimetallic vertices of $(ClO_4^-)_2 \subset$ **4.2** isolated from the rest of the structure.

The vertices of the structure were observed to adopt a new mode of coordination (Figure 4.4c). The two Ag^I cations at each vertex are coordinated by three distinct naphthyridine-imine arms from different ligands. Two of the arms bridge between Ag^I centres, using all three N-donors. The third naphthyridine-imine arm only coordinates to the outermost Ag^I centre *via* two of its N-donors. The bidentate bridging mode of the napthyridines forces the Ag^I centres into close proximity with $Ag^I \cdots Ag^I$ distances of 2.816(2) – 2.861(3) Å, within the range reported for other naphthyridine bridged silver(I) complexes.[1,3] All Ag^I centres are coordinated by four N-donor atoms, with Ag-N bond lengths ranging from 2.227(5) – 2.520(7) Å.

The two triangular faces of the trigonal prism, as defined by the locations of the centroids of the disilver(I) centres of each vertex, are twisted by 30 ± 1° with respect to each other. Two tritopic ligands define each rectangular face of the prism, each bridging between three vertices. Two naphthyridine-imine arms of each ligand connect vertices belonging to the same triangular face, while the third arm bridges to a vertex of the opposing triangular face, through the interior of the structure. The connectivity of the structure is thus similar to a D_4-symmetric $Cd^{II}_8L_8$ tetragonal prism with a larger internal cavity and single-metal vertices.[25] In the present case, the overall architecture has D_3 symmetry, as well as a much smaller internal cavity.

The three arms of each tritopic ligand thus experience different environments within the overall structure. Further analysis by COSY and NOESY NMR, both 1D and 2D, allowed us to unambiguously assign each of the proton environments in solution. Each of the arms of the tritopic ligand can be separated into the phenylene unit of the triamine precursor, an imine and the naphthyridine section (green, red and blue in Figure 4.5). Assignment within each of these sections is possible with a COSY experiment. In order to elucidate which phenylene and naphthyridine resonances correspond to each other NOE correlations with the imine proton were instructive.

The diffusion coefficient of 4.8×10^{-6} cm^2 s^{-1} described above is also consistent with the average cross-section of the cationic cage measured from the solid-state structure. A hydrodynamic radius of 12 Å is calculated, which compares to solid-state measurements of 10–16 Å. This wide range is a consequence of the anisotropic nature of **4.2**. All solution-state structural characterisation data for **4.2** were consistent with the crystal structure.

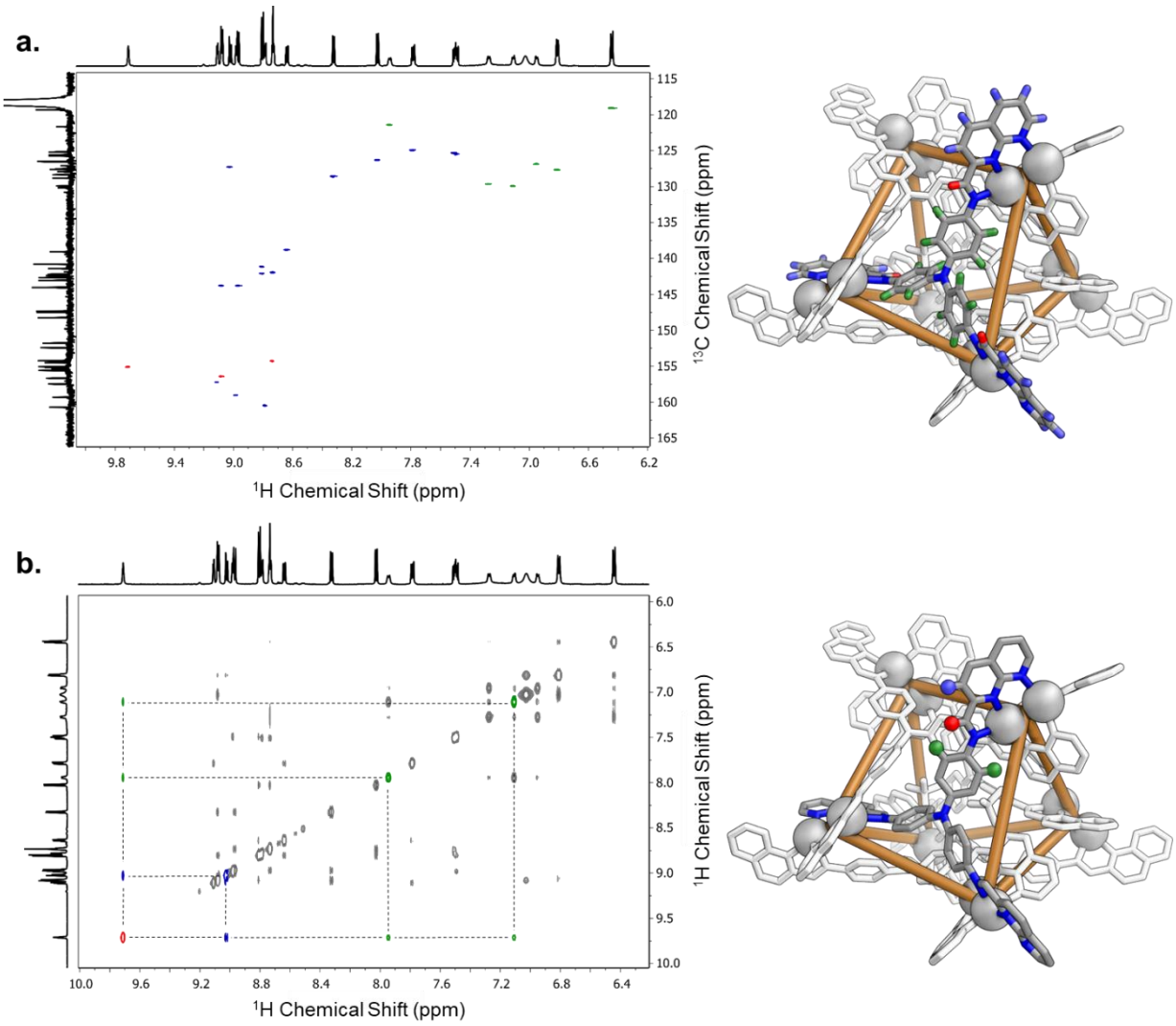

Figure 4.5 | a. ^{1}H-^{13}C HSQC of **$(ClO_4^-)_2 \subset$ 4.2** (500 MHz, 298 K, CD_3CN) with each of the phenylene, naphthyridine and imine cross-peaks shaded in green, blue and red, respectively. **b.** ^{1}H-^{1}H NOESY of **$(ClO_4^-)_2 \subset$ 4.2** (500 MHz, 298 K, CD_3CN) highlighting the NOE correlations used in the assignment of each ligand arm.

The crystal structure revealed that the triangular prism bound a pair of ClO_4^- anions within its elongated cavity. Both encapsulated anions benefit from non-classical hydrogen bonding interactions with internally directed protons of the cage, with CH···anion distances in the range 2.4–2.7 Å. Several other ClO_4^- anions were found to associate with the periphery of the cage. From this, it was inferred that anions may play a crucial role in templating the formation of this architecture.

4.3 Templation of the Prism by Two Anions

To further probe the scope of this phenomenon, a series of anion templation experiments were carried out. Silver bis(trifluoromethanesulfonyl)imide ($AgNTf_2$) was used as the silver(I) source in all cases. Following treatment of this salt with subcomponents **3.7** and **4.1**, it was found that no well-defined structure formed in the absence of a competent template ion (Figure 4.6, bottom-most spectrum). No discrete assembly was observed even after heating the mixture to 60 °C in an inert atmosphere in the dark for several days. Molecular modelling, starting from the crystal structure of **$(ClO_4^-)_2 \subset$ 4.2**, indicated that the cavity is too small to accommodate two NTf_2^- anions, rendering NTf_2^- an ineffective template for **4.2**.

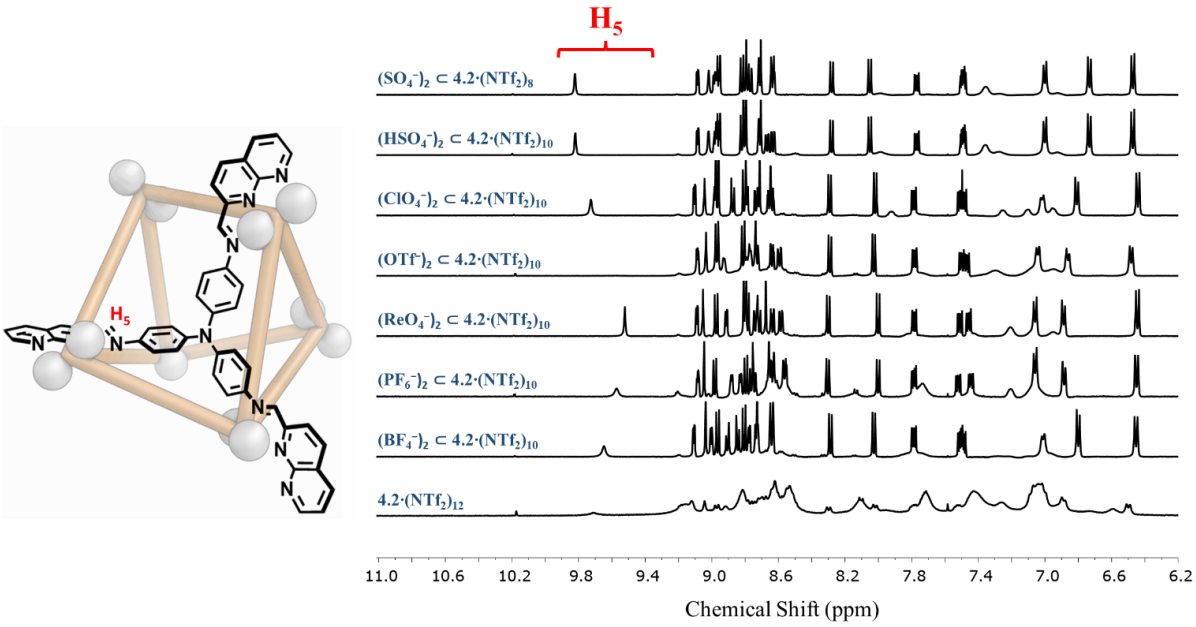

Figure 4.6 | Aromatic region of the ^1H NMR spectra (500 MHz, 298 K, CD_3CN) of **$(X^-)_2 \subset$ 4.2·$(NTf_2)_{10}$** after equilibration at room temperature for 18 h (X^- = BF_4^-, PF_6^-, ReO_4^-, OTf^-, ClO_4^-, HSO_4^-, SO_4^{2-}). Each sample was prepared by addition of two equivalents of the appropriate TBA salt to a DCL formed with $AgNTf_2$. The bottom spectrum is the untemplated mixture of subcomponents **3.7** and **4.1** with $AgNTf_2$.

Templation of **$(X^-)_2 \subset$ 4.2** occurred following the addition of two equivalents of trifluoromethanesulfonate (OTf^-), tetrafluoroborate (BF_4^-), perrhenate (ReO_4^-), hexafluorophosphate (PF_6^-), ClO_4^-, sulfate (SO_4^{2-}) and bisulfate (HSO_4^-) as their tetrabutylammonium salts to the untemplated mixture of **3.7**, **4.1**, and $AgNTf_2$. Cage **$(X^-)_2 \subset$ 4.2** also formed directly when $AgPF_6$, $AgClO_4$ or $AgBF_4$ were used as the silver(I) source.

$AgReO_4$ and Ag_2SO_4 were not sufficiently soluble in acetonitrile to allow for the reaction to proceed.

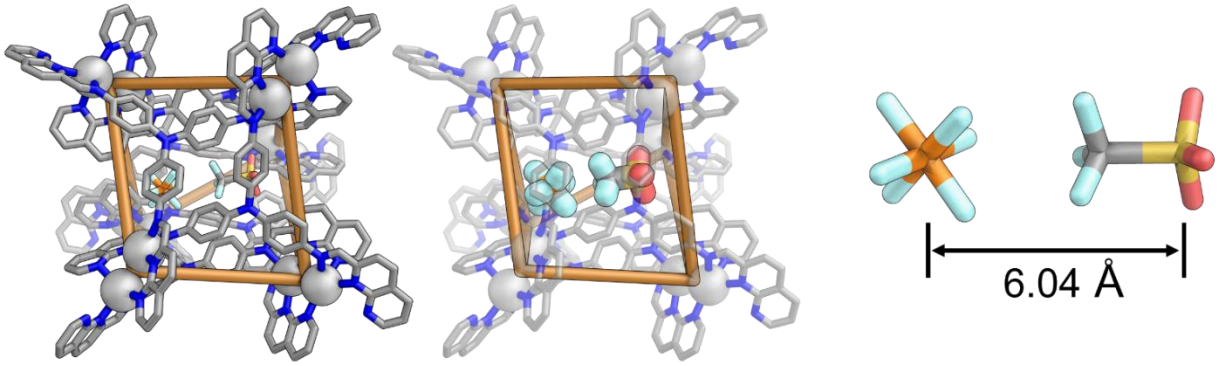

Figure 4.7 | X-ray crystal structure of (**OTf^- + PF_6^-)$_2$ ⊂ 4.2**. The OTf^- site is also occupied by a PF_6 anion (65%/35% occupancy, respectively). The distance was measured from the phosphorus atom of $PF6^-$ to the sulfur atom of OTf^-.

The diffusion of diethyl ether into a solution of **(OTf^-)$_2$ ⊂ 4.2** containing excess $TBAPF_6$ furnished crystals of sufficient quality for analysis by X-ray diffraction, confirming formation of a $Ag^I_{12}L_6$ cage isostructural to **(ClO_4^-)$_2$ ⊂ 4.2**. A clearly-resolved hexafluorophosphate (PF_6^-) anion was observed in one internal site, while the second site contained a disordered mixture of OTf^- and PF_6^- (65%/35% occupancy respectively, Figure 4.7). This result, whereby two distinct anions can be seen to occupy the cavity of **4.2**, hints that it may be possible to form hetero-anion host-guest complexes in solution. This has proven challenging to probe, as all of the anions described in this Chapter bind in fast exchange on the NMR chemical shift timescales.

Crystals of **(HSO_4^-)$_2$ ⊂ 4.2** formed following the diffusion of iPr_2O into a concentrated acetonitrile solution, and the structure was analysed by single-crystal X-ray diffraction. The distance between the two encapsulated anions was found to be 4.150(2) Å, measured between the two sulfur atoms. This value is similar to the 4.112(1) Å distance observed by Flood and co-workers, where a pair of HSO_4^- anions is stabilised by two tricarbazole macrocycles (TCMs) (Figure 4.8).[26,27]

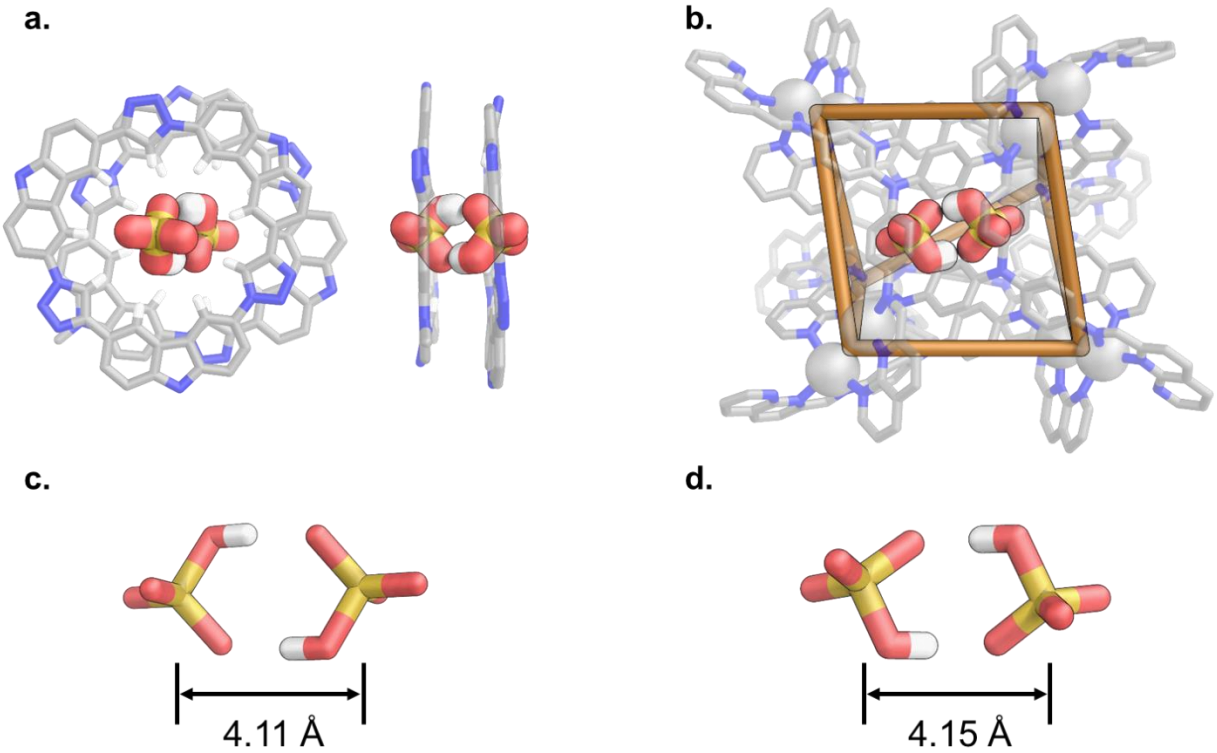

Figure 4.8 | X-ray crystal structures of **a.** $(\mathbf{HSO_4^-})_2 \subset (\mathbf{TCM})_2$, **b.** $(\mathbf{HSO_4^-})_2 \subset \mathbf{4.2}$, **c.** the isolated anion pair from the TCM host-guest complex and **d.** from cage **4.2**.

In the case of $\mathbf{(ClO_4^-)_2 \subset 4.2}$, the distance between the chlorine atoms was found to be 4.88(2) Å (Figure 4.9). These results suggest that hydrogen bonding between the two HSO_4^- anions within the cage cavity, coupled with interactions between the internally directed protons of the cage and the HSO_4^-, facilitates close proximity between bisulfate anions.

It should be noted that substantial disorder of the oxygen atoms of the encapsulated HSO_4^- anions was observed for $\mathbf{(HSO_4^-)_2 \subset 4.2}$. Despite the high resolution (0.77 Å), this disorder precluded accurate resolution of the hydrogen atom of the anions. The proton was placed on one of the disordered locations based on a peak in the electron density map but its exact location is subject to a high degree of uncertainty. The observed distance between the disordered HSO_4^- anions, measured from their sulfur atoms, which are not disordered, is consistent with the presence of a hydrogen bonded dimer.

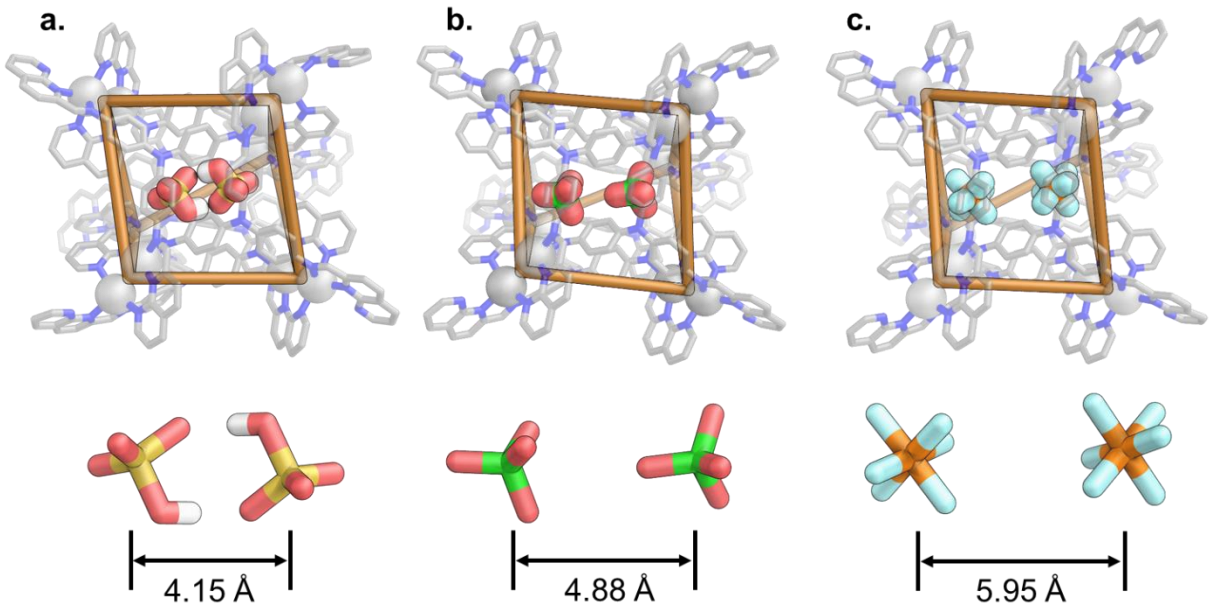

Figure 4.9 | X-ray crystal structures of **a.** $(\mathbf{HSO_4^-})_2 \subset \mathbf{4.2}$, **b.** $(\mathbf{ClO_4^-})_2 \subset \mathbf{4.2}$ and $(\mathbf{PF_6^-})_2 \subset \mathbf{4.2}$, with side-views of the isolated anion dimers.

Noting that each crystal structure obtained contained two bound anions, whether two anions were required to template the framework of **4.2** in solution was explored. Titration of two equivalents of $TBAHSO_4$ into an untemplated mixture of **3.7**, **4.1**, and $AgNTf_2$ revealed complete formation of $(\mathbf{HSO_4^-})_2 \subset \mathbf{4.2}$, as measured against an internal standard of known concentration. Complete formation of $(\mathbf{HSO_4^-})_2 \subset \mathbf{4.2}$ was observed after addition of approximately 1.5 equivalents.

Addition of further HSO_4^- led to no appreciable changes (Figure 4.10). Further procedural details are available in the Experimental Section of this Chapter. This result, coupled with the crystallographic evidence, suggests that **4.2** hosts more than one anion within its central void in solution.

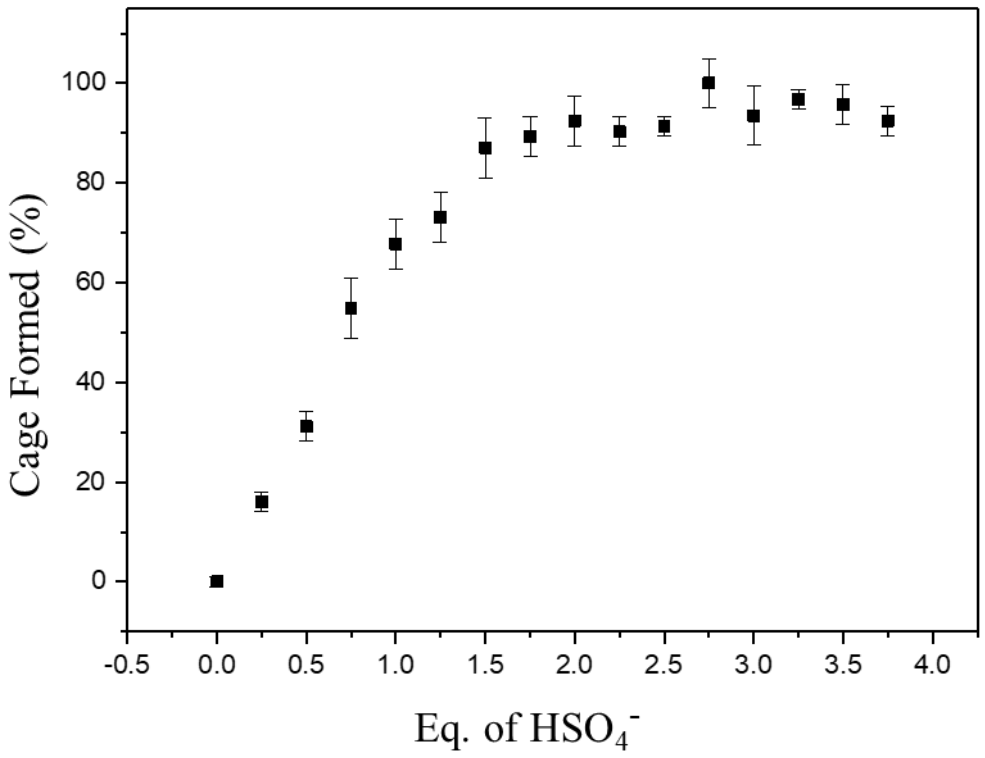

Figure 4.10 | Titration of 4 equiv. of $TBAHSO_4^-$ into a solution of **3.7** (6 equiv.), **4.1** (18 equiv.) and $AgNTf_2$ (12 equiv.). The formation of $(\mathbf{HSO_4^-})_2 \subset$ **4.2** was monitored by integration of several ^1H resonances against an internal standard of 1,3,5-trimethoxybenzene (10 equiv.).

Having observed these supramolecular interactions holding anions in close proximity within **4.2**, we questioned whether linear, covalently-linked dianions could also serve as guests and templates for this host. There are few reported examples of such dianions bound inside cage structures.[28,29] Addition of sodium 1,2-ethanedisulfonate ($\mathbf{EDS^{2-}}$) was found to lead to formation of the templated cage. Crystallisation by diffusion of iPr_2O into an acetonitrile solution of ($\mathbf{EDS^{2-}}$) $\subset$ **4.2**, followed by X-ray analysis, unambiguously confirmed the formation of a 1:1 host guest complex (Figure 4.11a), as opposed to the 2:1 host-guest complexes described above.

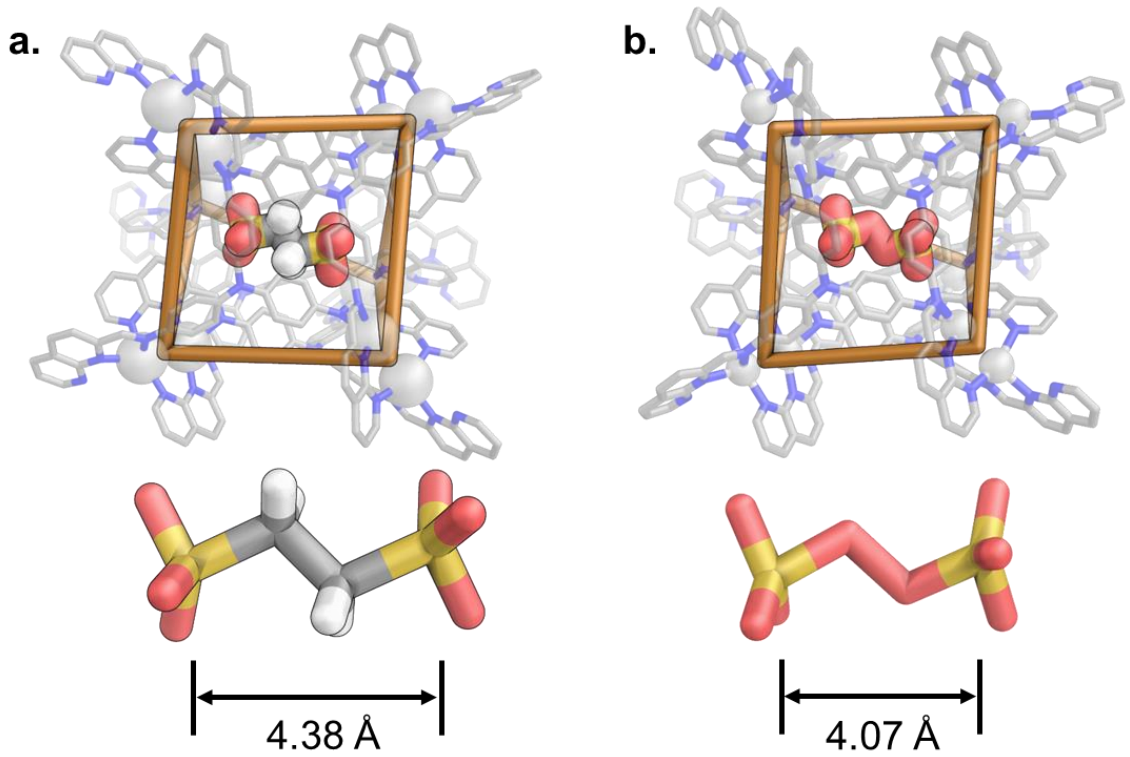

Figure 4.11 | X-ray crystal structures of **a.** (**EDS^{2-}) ⊂ 4.2** and **b.** (**S$_2$O$_8^{2-}$) ⊂ 4.2**, with side-views of the isolated anion dimers.

We also found that the addition of potassium persulfate ($S_2O_8^{2-}$), which is known to oxidise Ag^I to Ag^{II} in acetonitrile solution,[30] led to the formation of cage (**S$_2$O$_8^{2-}$) ⊂ 4.2**. Diffusion of iPr_2O into a solution of (**S$_2$O$_8^{2-}$) ⊂ 4.2** in acetonitrile produced X-ray quality crystals, which revealed a single $S_2O_8^{2-}$ anion bound in the centre of the cage's cavity (Figure 4.11b). A sulfur-sulfur distance of 4.070(3) Å was measured, shorter than that of the hydrogen-bonded HSO_4^- dimer.

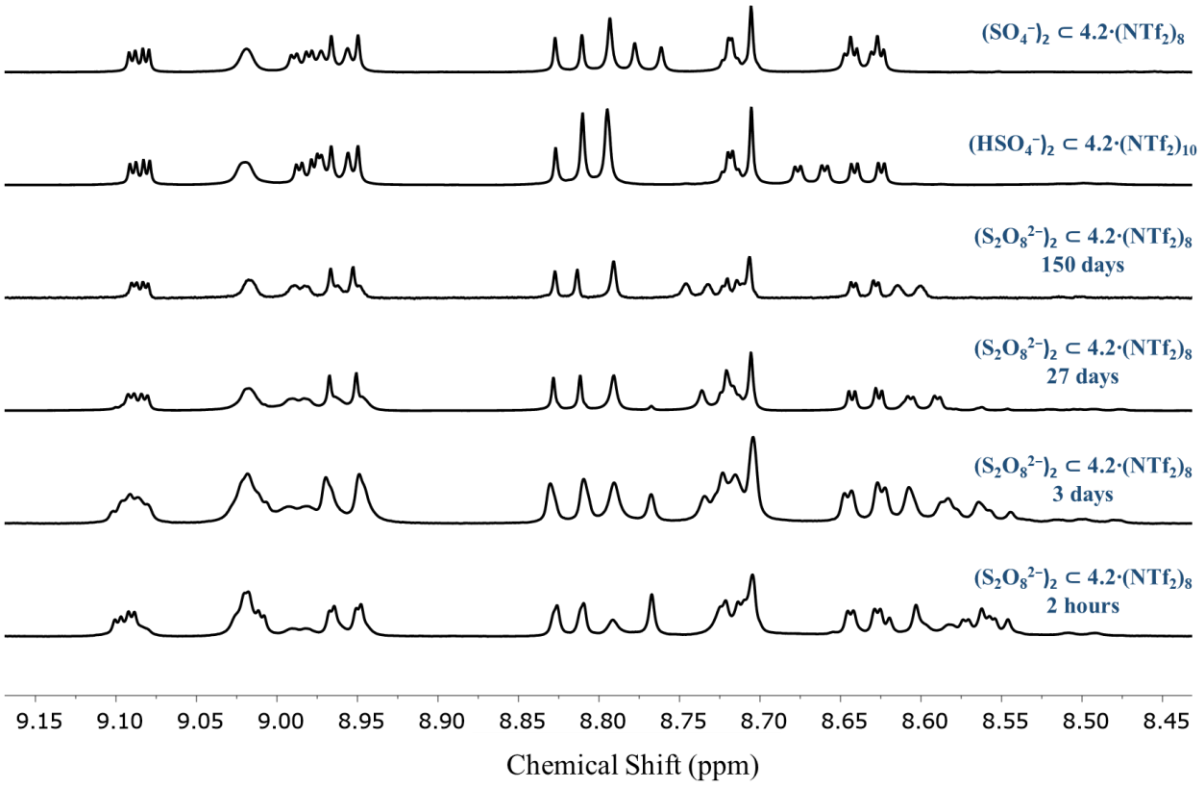

Figure 4.12 | Part of the aromatic region of the ^{1}H NMR spectra (500 MHz, 298 K, CD_3CN) of **$(S_2O_8^{2-}) \subset 4.2\cdot(NTf_2^{-})_{10}$** at various time points. The ^{1}H NMR spectra of **$(SO_4^{2-})_2 \subset 4.2\cdot(NTf_2^{-})_8$** and **$(HSO_4^{-})_2 \subset 4.2\cdot(NTf_2^{-})_{10}$** are included for comparison.

Over the course of 150 days at room temperature, changes in the ^{1}H NMR spectrum of (**$S_2O_8^{2-}$**) **$\subset$ 4.2** were observed, consistent with the formation of a new host-guest complex. We thus inferred that the $S_2O_8^{2-}$ was ultimately reduced to other anionic species, which also templated the prism. The ^{1}H NMR spectra of the resulting host-guest species did not match those templated solely by SO_4^{2-} or HSO_4^{-} (Figure 4.12).

4.4 Structural Adaption of the Prism

The shape and size of cage **4.2** was observed to adapt to accommodate the different guest anions, as evidenced in the crystallographic data. The volumes of these anions vary from 53 $Å^3$ (for BF_4^-) to 85 $Å^3$ (for OTf^-).[31]

Measuring between the centroids of the disilver(I) vertices, significant changes in the conformation of the cage were noted, depending on the guest. While the length of the cage did not vary (< 2% change), the apertures at the ends of the cage were found to contract by up to 12 ± 2 % (66.9 ± 0.3 $Å^2$ for **$(EDS^{2-}) \subset$ 4.2** to 76.3 ± 0.5 $Å^2$ for **$(PF_6^-)_2 \subset$ 4.2**) (Figure 4.13).

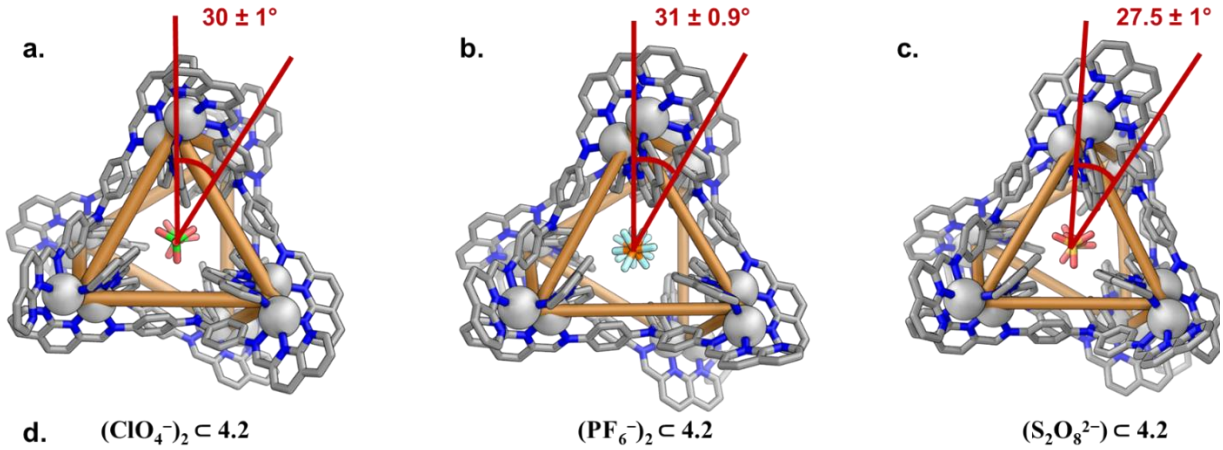

$(X^{m-})_n \subset 4.2$	Ag···Ag in disilver centre (Å)	Ag···Ag in triangular face (Å)	Ag···Ag along length (Å)	Torsion angle (°)	Triangular Aperture Area ($Å^2$)
$(PF_6^-)_2 \subset 4.2$	2.84 ± 0.01	13.3 ± 0.2	11.86 ± 0.06	31.1 ± 0.9	76.3 ± 0.5
$(ClO_4^-)_2 \subset 4.2$	2.83 ± 0.02	12.7 ± 0.1	11.98 ± 0.06	30.0 ± 1.0	70.2 ± 0.5
$(HSO_4^-)_2 \subset 4.2$	2.85 ± 0.02	12.6 ± 0.1	11.96 ± 0.09	28.2 ± 2.0	68.4 ± 0.4
$(EDS^{2-}) \subset 4.2$	2.85 ± 0.02	12.4 ± 0.1	12.04 ± 0.05	27.9 ± 0.8	66.9 ± 0.3
$(S_2O_8^{2-}) \subset 4.2$	2.86 ± 0.03	12.6 ± 0.2	11.9 ± 0.07	27.5 ± 1.0	68.5 ± 0.4

Figure 4.13 | Crystal structures of **a. $(ClO_4^-)_2 \subset$ 4.2**, **b. $(PF_6^-)_2 \subset$ 4.2**, and **c. $(S_2O_8^{2-}) \subset$ 4.2** with measurements of the angle defining the prisms' twist overlaid. **d.** Tabulated measurements of the adaptions of cage **4.2** for different encapsulated anions.

The twist angle between the two triangular faces of the prism was also found to vary (Figure 4.13a-c). With a twist angle of 0° defining a trigonal prism and 60° defining a trigonal antiprism, **4.2** varied between 27.5 ± 1.0° (for **$(S_2O_8^{2-}) \subset$ 4.2**) and 31 ± 0.9° (for **$(OTf^-/PF_6^-)_2$**

⊂ **4.2**). These twist angles indicate that the geometry of **4.2** is approximately halfway between an idealised trigonal prism and antiprism.

These changes in the structure of **4.2** are attributed to two factors - structural tuning of **4.2** to maximise favorable interactions with the internalised anions, and crystal packing effects. Smaller anions led to a contraction of the apertures of the cage, whereas larger anions required the cage to expand to accommodate them. A greater contraction of the triangular apertures corresponds to a greater distortion of the twist angle from that of an ideal prism. These results go some way toward explaining how it is possible for such a broad range of anions to template cage **4.2**.

4.5 Conclusion

This work thus demonstrated the formation of a desymmetrised trigonal prismatic cage from bimetallic motifs using subcomponent self-assembly. The use of 2-formyl-1,8-naphthyridine allowed the formation of the disilver(I) corners of cage **4.2**, permitting access to this new structure type. The self-assembly process was template-driven, with either two mono-anions, or an elongated dianion, occupying the central, tubular cavity defined by the cage. The cage flexed and adapted in order to accommodate a broad range of anionic species, including strong oxidants.

Further work will look to explore this system in aqueous media and examine the potential uses of its unusual binding pocket. As cage **4.2** has two open pores at each end of its binding pocket, we are currently investigating whether it is capable of binding a negatively charged thread-like molecule such as ATP. This type of host-guest interaction may pave the way toward a new class of rotaxanes based on metal-organic cages.

New structures and structure types may also become accessible through the use of other subcomponents that contain spatially close, but non-chelating, binding sites for bimetallic motifs at the vertices of polyhedral. In particular, it would be interesting to establish whether larger trigonal prisms can be formed from extended trianiline subcomponents which would have larger cavities for binding poly-anionic aromatic species.

Given the propensity of these coordination motifs described in Chapters 3 and 4 to produce new and unexpected coordination modes, it is of course reasonable to assume that assemblies with other ligands will produce further unanticipated results. As such, one should not limit their imagination when it comes to the design of other polyhedral architectures from these exciting, new building blocks.

4.6 Experimental Section

Synthesis of $(ClO_4^-)_2 \subset$ **4.2**

Tris(4-aminophenyl)amine (11.6 mg, 40 µmol, 6 equiv.), silver(I) perchlorate (16.6 mg, 80 µmol, 12 equiv.) and 1,8-naphthyridine-2-carbaldehyde (19.0 mg, 121 µmol, 18 equiv.) were stirred in CD_3CN (3.00 mL) at room temperature for 18 h in a sealed vessel under a nitrogen atmosphere and in the dark, yielding a dark purple solution. The reaction mixture was then filtered through a glass fibre filter (0.7 µm pore size). The acetonitrile was concentrated under a stream of N_2 to a volume of 1 mL. Addition of diethyl ether (10 mL) resulted in the precipitation of a dark purple powder. The suspension was then centrifuged (10 min, 3000 RPM), the eluent decanted. Further diethyl ether (10 mL) was added, the powder was resuspended by sonication and then centrifuged. Again, the eluent was decanted. The residue was then dried *in vacuo* to afford the solid product as a fine dark purple powder (44 mg, 94%).

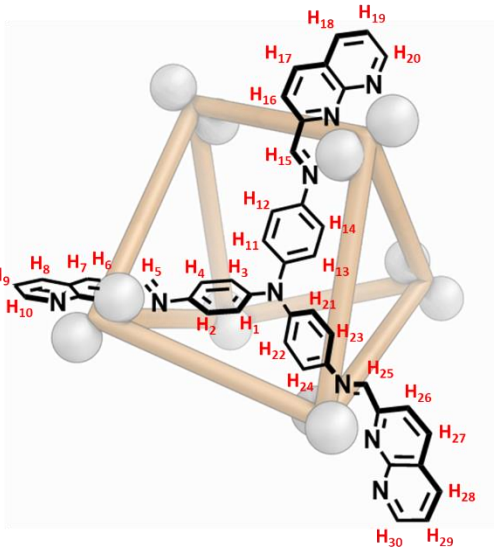

^{1}H NMR (500 MHz, 298 K, CD_3CN) δ: 9.71 (H_5, s, 6H), 9.10 (H_{30}, dd, *J* = 4.2, 1.88 Hz, 6H), 9.08 (H_{15}, s, 6H), 9.07 (H_7, d, *J* = 8.1 Hz, 6H), 9.02 (H_6, d, *J* = 8.2 Hz, 6H), 8.98 (H_{20}, dd, *J* = 4.6, 1.74 Hz, 6H), 8.97 (H_{17}, d, *J* = 8.4 Hz, 6H), 8.80 (H_{27}, d, *J* = 8.3 Hz, 6H), 8.80 (H_8, br, 6H), 8.79 (H_{10}, dd, *J* = 4.8, 1.76 Hz, 6H), 8.73 (H_{25}, s, 6H), 8.73 (H_{18}, dd, *J* = 8.2, 1.79 Hz, 6H), 8.64 (H_{28}, dd, *J* = 8.4, 1.87 Hz, 6H), 8.32 (H_{16}, d, *J* = 8.3 Hz, 6H), 8.02 (H_{26}, d, *J* = 8.3 Hz, 6H), 7.95 (H_4 or H_2, d, *J* = 7.4 Hz, 6H), 7.78 (H_{29}, dd, *J* = 8.3, 4.3 Hz, 6H), 7.51 (H_{19}, dd, *J* = 8.2, 4.8 Hz, 6H), 7.49 (H_9, dd, *J* = 8.3, 4.7 Hz, 6H), 7.27 (H_3 or H_1, d, *J* = 7.8 Hz, 6H), 7.11 (H_4 or H_2, d, *J* = 8.1 Hz, 6H), 7.06 (H_{23} and H_{21}, br, 12H), 7.03 (H_{14} and H_{12}, br s, 12H), 6.96 (H_3 or H_1, d, *J* = 7.7 Hz, 6H), 6.81 (H_{13} and H_{11}, d, *J* = 8.8 Hz, 12H), 6.44 (H_{24} and H_{22}, d, *J* = 9.1 Hz, 12H)

^{13}C NMR (125 MHz, 298 K, CD_3CN) δ: 160.5 (imine), 159.6 (naphthyridine), 157.5 (imine), 156.4 (imine), 156.2 (naphthyridine), 155.6 (naphthyridine), 155.5 (naphthyridine), 155.1

(naphthyridine), 154.4 (naphthyridine), 154.1 (naphthyridine), 152.3 (naphthyridine), 151.8 (naphthyridine), 148.8 (naphthyridine), 147.5 (naphthyridine), 147.4 (naphthyridine), 144.1 (naphthyridine), 143.6 (naphthyridine), 143.1 (naphthyridine), 142.8 (naphthyridine), 142.4 (naphthyridine), 142.2 (naphthyridine), 141.2 (naphthyridine), 140.6 (naphthyridine), 139.1 (naphthyridine), 129.7 (aniline), 128.6 (aniline), 128.4 (aniline), 127.7 (aniline), 127.5 (aniline), 127.5 (aniline), 126.6 (aniline), 126.5 (aniline), 125.8 (aniline), 125.7 (aniline), 125.2 (aniline), 124.7 (aniline), 122.2 (aniline), 120.0 (aniline), 119.6 (aniline), 117.1 (aniline)

HRMS (ESI-LTQ Orbitrap XL, CH_3CN) m/z found 1251.0181, calculated 1251.0185 for $C_{270}H_{180}Ag_{12}N_{60}(ClO_4)_7^{5+}$

*Anion Templation of **4.2***

Tris(4-aminophenyl)amine (11.6 mg, 40 µmol, 6 equiv.), silver(I) bis(trifluoromethane)sulfonimide (40.0 mg, 100 µmol, 15 equiv.) and 1,8-naphthyridine-2-carbaldehyde (19.0 mg, 121 µmol, 18 equiv.) were stirred in CD_3CN (10 mL) at room temperature for 2 h or until all of the material was in solution. Aliquots of this stock solution (500 µL) were then added to J-Young tubes followed by two equivalents of template anion (0.67 µmol) from the salts of $TBABF_4$, $TBAPF_6$, $TBAReO_4$, TBAOTf, $TBAClO_4$, $TBAHSO_4$, Na_2SO_4, $K_2S_2O_8$, ethane-1,2-disulfonate disodium salt (EDS) and propane-1,3-disulfonate disodium salt (PDS). The reaction mixture was stirred at room temperature under nitrogen and in the dark for 18 hours. The resulting purple solutions were used directly for characterisation.

4.7 Crystallography

Data were collected at Beamline I19 of Diamond Light Source employing silicon double crystal monochromated synchrotron radiation (0.6889 Å) with ω and ψ scans at 100(2) K.[32] Data integration and reduction were carried out by Dr. Tanya Ronson of the University of Cambridge and undertaken with Xia2.[33-35] Subsequent computations were carried out using the WinGX-32 graphical user interface.[36] Multi-scan empirical absorption corrections were applied to the data using the AIMLESS[37] tool in the CCP4 suite.[38] The structures were solved by direct methods using SHELXT[39] then refined and extended with SHELXL.[40] In general, non-hydrogen atoms with occupancies greater than 0.5 were refined anisotropically. Carbon-bound hydrogen atoms were included in idealised positions and refined using a riding model. Disorder was modelled using standard crystallographic methods including constraints, restraints and rigid bodies where necessary. Crystallographic data along with specific details pertaining to the refinement follow. Crystallographic data have been deposited with the CCDC (1913631 - 1913635).

$[(PF_6)_{1.65}(OTf)_{0.35} \subset Ag_{12}L_6]\cdot 9.35PF_6\cdot 0.65OTf\cdot 2.25MeCN$ [+ solvent]

Formula $C_{275.50}H_{186.75}Ag_{12}F_{69}N_{62.25}O_3P_{11}S$, *M* 7395.28, Triclinic, space group P -1 (#2), *a* 23.3103(3), *b* 27.5339(3), *c* 34.0879(4) Å, α 87.7970(10), β 79.3500(10), γ 70.8740(10)°, *V* 20308.9(4) Å^3, D_c 1.209 g cm^{-3}, *Z* 2, crystal size 0.050 by 0.040 by 0.030 mm, color purple, habit block, temperature 100(2) Kelvin, λ(Synchrotron) 0.6889 Å, μ(Synchrotron) 0.628 mm^{-1}, T(Analytical)$_{min,max}$ 0.97689755547, 1.0, $2\theta_{max}$ 48.42, *hkl* range -27 27, -29 32, -40 38, *N* 192935, N_{ind} 69422(R_{merge} 0.0607), N_{obs} 38737(I > 2σ(I)), N_{var} 3934, residuals* *R*1(*F*) 0.0845, *wR*2(F^2) 0.2943, GoF(all) 1.030, $\Delta\rho_{min,max}$ -1.303, 1.274 e- Å^{-3}.

*$R1 = \Sigma||F_o| - |F_c||/\Sigma|F_o|$ for $F_o > 2\sigma(F_o)$; $wR2 = (\Sigma w(F_o^2 - F_c^2)^2/\Sigma(wF_c^2)^2)^{1/2}$ all reflections

$w=1/[\sigma^2(F_o^2)+(0.1860P)^2]$ where $P=(F_o^2+2F_c^2)/3$

Specific refinement details:

The crystals of $[(PF_6)_{1.65}(OTf)_{0.35}\subset Ag_{12}L_6]\cdot 9.35PF_6\cdot 0.65OTf\cdot 2.25MeCN$ were grown by diffusion of diethyl ether into an acetonitrile solution of $[Ag_{12}L_6]\cdot 12OTf$ containing excess Bu_4NPF_6. The crystals employed immediately lost solvent after removal from the mother liquor and rapid handling prior to flash cooling in the cryostream was required to collect data. Data

were obtained to 0.84 Å resolution. The asymmetric unit was found to contain one complete $Ag_{12}L_6$ assembly and associated counterions and solvent molecules.

Bond lengths and angles within pairs of chemically identical organic ligands were restrained to be similar to each other and additional bond length restraints (DFIX) were applied to some sections of the organic ligands. Thermal parameter restraints (SIMU, RIGU) were applied to all atoms except for silver to facilitate anisotropic stable refinement.

One of the encapsulated anions was modelled as a full occupancy PF_6^-. The other one was modelled as a disordered mixture of PF_6^- and OTf^- with occupancies of 0.65 and 0.35 respectively; these occupancies were initially refined and then fixed at the obtained values. The other anions within the structure also show evidence of substantial disorder. A further anion lattice site was modelled as a disordered mixture of PF_6^- and OTf^- and three PF_6^- anions were modelled as disordered over two locations. The occupancies of the all the located anions were allowed to refine freely and then fixed at the obtained values. Some additional minor occupancy positions of the anions could not be located in the electron density map and were not included in the model resulting in a discrepancy of 2.5 anions per $Ag_{12}L_6$ assembly; these anions are given as PF_6^- in the formula given above. Some lower occupancy disordered atoms were modelled with isotropic thermal parameters bond length and thermal parameter restraints were applied to facilitate realistic modelling of the disordered anions. Some acetonitrile solvent molecules were also modelled with partial occupancy.

Further reflecting the solvent loss there is a significant amount of void volume in the lattice containing smeared electron density from disordered solvent (and potentially the unresolved anions). Consequently the SQUEEZE[41] function of PLATON[42] was employed to remove the contribution of the electron density associated with this highly disordered solvent which gave a potential solvent accessible void of 7729 $Å^3$ per unit cell (a total of approximately 2273 electrons). Since the diffuse solvent molecules could not be assigned conclusively to acetonitrile or diethyl ether they were not included in the formula. Consequently, the molecular weight and density given above are likely to be slightly underestimated. The remaining electron density peaks and holes (up to 1.274 or −1.303 $e^-Å^3$) are close to the silver centres reflecting absorption effects or a small amount of unresolved disorder.

CheckCIF gives thirteen B level alerts, all resulting from thermal motion and/or unresolved disorder of the anions as described above.

[$(ClO_4)_2$⊂$Ag_{12}L_6$]·10NTf_2·2.5MeCN [+ solvent]

Formula $C_{295}H_{187.50}Ag_{12}Cl_2F_{60}N_{72.50}O_{48}S_{20}$, *M* 8662.20, Triclinic, space group P -1 (#2), *a* 24.5951(5), *b* 25.8919(4), *c* 33.0285(4) Å, α 82.2940(10), β 80.7880(10), γ 67.0800(10)°, *V* 19063.0(6) Å^3, D_c 1.509 g cm^{-3}, *Z* 2, crystal size 0.050 by 0.040 by 0.030 mm, colour purple, habit block, temperature 100(2) Kelvin, λ(Synchrotron) 0.6889 Å, μ(Synchrotron) 0.748 mm^{-1}, *T*(Analytical)$_{min,max}$ 0.976600983573, 1.0, $2\theta_{max}$ 42.52, *hkl* range -25 25, -27 27, -33 31, *N* 105710, N_{ind} 44821(R_{merge} 0.0701), N_{obs} 23407(I > 2σ(I)), N_{var} 3556, residuals* *R*1(*F*) 0.0919, *wR*2(F^2) 0.3151, GoF(all) 1.010, $\Delta\rho_{min,max}$ -0.894, 0.902 e- Å^{-3}.

*$R1 = \Sigma||F_o| - |F_c||/\Sigma|F_o|$ for $F_o > 2\sigma(F_o)$; $wR2 = (\Sigma w(F_o^2 - F_c^2)^2/\Sigma(wF_c^2)^2)^{1/2}$ all reflections

$w=1/[\sigma^2(F_o^2)+(0.2000P)^2]$ where $P=(F_o^2+2F_c^2)/3$

Specific refinement details:

The crystals of [$(ClO_4)_2$⊂$Ag_{12}L_6$]·10NTf_2·2.5MeCN were grown by diffusion of diisopropyl ether into an acetonitrile solution of the complex formed via the procedure described above. The crystals employed immediately lost solvent after removal from the mother liquor and rapid handling prior to flash cooling in the cryostream was required to collect data. Despite these measures and the use of synchrotron radiation few reflections at greater than 0.95 Å resolution were observed and the data were trimmed accordingly. Nevertheless, the quality of the data is far more than sufficient to establish the connectivity of the structure. The asymmetric unit was found to contain one complete $Ag_{12}L_6$ assembly and associated counterions and solvent molecules.

Due to the limited resolution, bond lengths and angles within pairs of chemically identical organic ligands were restrained to be similar to each other and additional restraints (DFIX, FLAT) were applied to some sections of the organic ligands. Thermal parameter restraints (SIMU, RIGU) were applied to all atoms except for silver to facilitate anisotropic stable refinement. Even with these restraints some thermal parameters remain larger than ideal as a consequence of the high level of thermal motion or minor unresolved disorder present throughout the structure.

Both encapsulated ClO_4^- anions were modelled as disordered over two locations. These disordered ClO_4^- anions were restrained to have an idealised tetrahedral geometry and the disordered oxygen atoms were modelled with isotropic thermal parameters. The other resolved anions within the structure were all identified as triflimide and also show evidence of

substantial disorder. Two triflimide anions were modelled as disordered over two locations and all triflimide anions were modelled with partial occupancy. The occupancies of the triflimide anions were allowed to refine freely and then fixed at the obtained values. These anions were modelled with isotropic thermal parameters and bond length and thermal parameter restraints were applied to facilitate realistic modelling of the disordered anions. Some acetonitrile solvent molecules were also modelled with partial occupancy.

A further 8.3 anions per $Ag_{12}L_6$ assembly remain unaccounted for and no satisfactory model for these anions could be obtained despite numerous attempts at modelling, including with rigid bodies. Therefore the SQUEEZE[41] function of PLATON[42] was employed to account for the highly disordered anions and further disordered solvent molecules, which gave a potential solvent accessible void of 7120 $Å^3$ per unit cell (a total of approximately 2727 electrons). These anions are included as triflimide in the formula given above. Since the diffuse solvent molecules could not be assigned conclusively to acetonitrile or diethyl ether they were not included in the formula. Consequently, the molecular weight and density given above are likely to be underestimated.

CheckCIF gives three A and five B level alerts. These alerts (both A and B level) all result from the limited data resolution, thermal motion and/or unresolved disorder of some anions and solvent molecules and the generally high level of thermal motion present throughout the structure as described above.

$[(SO_4H)_2 \subset Ag_{12}L_6] \cdot 10NTf_2 \cdot 13MeCN \cdot 1.5iPr_2O$ [+ solvent]

Formula $C_{325}H_{242}Ag_{12}F_{60}N_{83}O_{49.50}S_{22}$, *M* 9241.76, Monoclinic, space group C 2/c (#15), *a* 43.3421(4), *b* 32.8367(2), *c* 27.6735(2) Å, *β* 93.2690(10), *V* 39321.2(5) $Å^3$, *D*c 1.561 g cm^{-3}, *Z* 4, crystal size 0.030 by 0.020 by 0.010 mm, colour purple, habit block, temperature 100(2) Kelvin, λ(Synchrotron) 0.6889 Å, μ(Synchrotron) 0.729 mm^{-1}, $T(\text{Analytical})_{min,max}$ 0.973805583854, 1.0, $2\theta_{max}$ 53.15, *hkl* range -52 56, -41 42, -35 33, *N* 143905, N_{ind} 42439(R_{merge} 0.0446), N_{obs} 26507(I > 2σ(I)), N_{var} 2742, residuals* *R*1(*F*) 0.0888, *wR*2(F^2) 0.3047, GoF(all) 1.117, $\Delta\rho_{min,max}$ -1.989, 1.565 e- $Å^{-3}$.

*$R1 = \Sigma||F_o| - |F_c||/\Sigma|F_o|$ for $F_o > 2\sigma(F_o)$; $wR2 = (\Sigma w(F_o^2 - F_c^2)^2/\Sigma(wF_c^2)^2)^{1/2}$ all reflections

$w=1/[\sigma^2(F_o^2)+(0.2000P)^2]$ where $P=(F_o^2+2F_c^2)/3$

Specific refinement details:

The crystals of $[(SO_4H)_2 \subset Ag_{12}L_6] \cdot 10NTf_2 \cdot 13MeCN \cdot 1.5iPr_2O$ were grown by diffusion of diisopropyl ether into an acetonitrile solution of the complex. The crystals employed immediately lost solvent after removal from the mother liquor and rapid handling prior to flash cooling in the cryostream was required to collect data. Even so data were obtained to 0.77 Å resolution by employing synchrotron radiation. The asymmetric unit was found to contain one half of a $Ag_{12}L_6$ assembly and associated counterions and solvent molecules.

Bond lengths and angles within pairs of chemically identical organic ligands were restrained to be similar to each other. Thermal parameter restraints (SIMU, RIGU) were applied to all atoms except for silver to facilitate anisotropic stable refinement. One naphthyridine arm was modelled as disordered over two locations with bond length (DFIX) and FLAT restraints were applied to the disordered parts to ensure a stable refinement.

The oxygen atoms of the central HSO_4^- anion were modelled as disordered over three locations with refined occupancies of 0.35108/0.31593/0.33299. Soft bond length and angle restraints were applied to the disordered atoms to achieve a reasonable refinement. While the distance between the disordered HSO_4^- anion and its symmetry equivalent is consistent with the presence of a hydrogen bonded dimer,[43] the hydrogen atom of the HSO_4^- could not be adequately resolved due to the extensive disorder. One hydrogen atom was placed on one of the disordered locations based on a peak in the electron density map; however the position of this hydrogen is subject to a high degree of uncertainty.

The other anions within the structure, all modelled as triflimide, also show evidence of substantial disorder. All five triflimide anions were modelled as disordered over two or three locations. The occupancies of the disordered anions were allowed to refine freely and then fixed at the obtained values. Some additional minor occupancy positions of the anions could not be located in the electron density map and were not included in the model resulting in a discrepancy of 1.1 counterions per asymmetric unit. Some lower occupancy disordered atoms were modelled with isotropic thermal parameters and bond length and thermal parameter restraints were applied to facilitate realistic modelling of the disordered anions. Some acetonitrile solvent molecules were also modelled with as disordered over multiple locations and/or with partial occupancy. The hydrogen atoms of some disordered acetonitrile molecules could not be located in the electron density map and were not included in the model.

Further reflecting the solvent loss there is a significant amount of void volume in the lattice containing smeared electron density from disordered solvent (and potentially the unresolved anions). Consequently the SQUEEZE[41] function of PLATON[42] was employed to remove the

contribution of the electron density associated with this highly disordered solvent which gave a potential solvent accessible void of 1132 $Å^3$ per unit cell (a total of approximately 401 electrons). Since the diffuse solvent molecules could not be assigned conclusively to acetonitrile or diisopropyl ether they were not included in the formula. Consequently, the molecular weight and density given above are likely to be slightly underestimated. The remaining electron density peaks and holes (up to 1.565 or −1.990 $e^{-}Å^3$) are close to the silver centres reflecting absorption effects or a small amount of unresolved disorder.
CheckCIF gives six B level alerts, all resulting from acetonitrile solvent molecules for which hydrogens were not modelled as described above.

[(EDS)⊂$Ag_{12}L_6$]·10NTf_2·18MeCN·1.5iPr_2O·0.5H_2O

Formula $C_{337}H_{260}Ag_{12}F_{60}N_{88}O_{48}S_{22}$, *M* 9450.07, Monoclinic, space group C 2/c (#15), *a* 43.6194(3), *b* 32.4028(3), *c* 27.3509(2) Å, *β* 92.5640(10), *V* 38618.8(5) $Å^3$, D_c 1.625 g cm^{-3}, *Z* 4, crystal size 0.050 by 0.040 by 0.040 mm, colour purple, habit block, temperature 100(2) Kelvin, λ(Synchrotron) 0.6889 Å, μ(Synchrotron) 0.744 mm^{-1}, $T(\text{Analytical})_{min,max}$ 0.939023710754, 1.0, $2\theta_{max}$ 58.95, *hkl* range -51 62, -42 43, -36 39, *N* 157325, N_{ind} 53025(R_{merge} 0.0452), N_{obs} 32723(I > 2σ(I)), N_{var} 3188, residuals* *R*1(*F*) 0.0666, *wR*2(F^2) 0.2239, GoF(all) 1.014, $\Delta\rho_{min,max}$ -1.134, 0.937 e- $Å^{-3}$.
*$R1 = \Sigma||F_o| - |F_c||/\Sigma|F_o|$ for $F_o > 2\sigma(F_o)$; $wR2 = (\Sigma w(F_o^2 - F_c^2)^2/\Sigma(wF_c^2)^2)^{1/2}$ all reflections
$w=1/[\sigma^2(F_o^2)+(0.1443P)^2]$ where $P=(F_o^2+2F_c^2)/3$

Specific refinement details:
The crystals of [(EDS)⊂$Ag_{12}L_6$]·10NTf_2·18MeCN·1.5iPr_2O·0.5H_2O were grown by diffusion of diisopropyl ether into an acetonitrile solution of the complex formed via the procedure described above. The crystals employed immediately lost solvent after removal from the mother liquor and rapid handling prior to flash cooling in the cryostream was required to collect data. Even so data were obtained to 0.7 Å resolution by employing synchrotron radiation. The asymmetric unit was found to contain one half of a $Ag_{12}L_6$ assembly and associated counterions and solvent molecules.
Bond lengths and angles within pairs of chemically identical organic ligands were restrained to be similar to each other. Thermal parameter restraints (SIMU, RIGU) were applied to all atoms except for silver to facilitate anisotropic stable refinement. One naphthyridine arm was

modelled as disordered over two locations with bond length (DFIX) and FLAT restraints were applied to the disordered parts to ensure a stable refinement; one of the silver centres coordinated to the disordered ligand arm was also modelled as disordered over two locations. The carbon atoms of the encapsulated ethanedisulfonate anion were modelled as disordered over a special position with symmetry enforced half occupancy. The other anions within the structure, all modelled as triflimide, also show evidence of substantial disorder. All triflimide anions were modelled as disordered over two or three locations. Some lower occupancy disordered atoms were modelled with isotropic thermal parameters and bond length and thermal parameter restraints were applied to facilitate realistic modelling of the disordered anions. Some acetonitrile solvent molecules were also modelled with as disordered over multiple locations and/or with partial occupancy. The hydrogen atoms of some disordered acetonitrile molecules and the water molecule could not be located in the electron density map and were not included in the model.

CheckCIF gives sixteen B level alerts, all resulting from thermal motion and/or unresolved disorder of the anions and solvent molecules and solvent molecules for which hydrogens were not modelled as described above.

[(S_2O_8)⊂$Ag_{12}L_6$]·10NTf_2·12MeCN [+ solvent]

Formula $C_{314}H_{216}Ag_{12}F_{60}N_{82}O_{48}S_{22}$, *M* 9045.44, Monoclinic, space group C 2/c (#15), *a* 42.8029(7), *b* 32.7310(4), *c* 27.8538(5) Å, *β* 93.4120(10), *V* 38953.5(11) $Å^3$, D_c 1.542 g cm^{-3}, *Z* 4, crystal size 0.100 by 0.100 by 0.030 mm, colour purple, habit block, temperature 100(2) Kelvin, *λ*(Synchrotron) 0.6889 Å, *μ*(Synchrotron) 0.734 mm^{-1}, $T(\text{Analytical})_{min,max}$ 0.966892968533, 1.0, $2\theta_{max}$ 47.81, *hkl* range -50 50, -38 36, -32 31, *N* 128026, N_{ind} 32151(R_{merge} 0.1067), N_{obs} 20558(I > 2σ(I)), N_{var} 2633, residuals* *R*1(*F*) 0.0872, *wR*2(F^2) 0.2907, GoF(all) 1.044, $\Delta\rho_{min,max}$ -1.064, 1.340 e- $Å^{-3}$.

*$R1 = \Sigma||F_o| - |F_c||/\Sigma|F_o|$ for $F_o > 2\sigma(F_o)$; $wR2 = (\Sigma w(F_o^2 - F_c^2)^2/\Sigma(wF_c^2)^2)^{1/2}$ all reflections

$w=1/[\sigma^2(F_o^2)+(0.1970P)^2]$ where $P=(F_o^2+2F_c^2)/3$

Specific refinement details:

The crystals of [(S_2O_8)⊂$Ag_{12}L_6$]·10NTf_2·12MeCN [+ solvent] were grown by diffusion of diisopropyl ether into an acetonitrile solution of the complex formed via the procedure described above. The crystals employed immediately lost solvent after removal from the

mother liquor and rapid handling prior to flash cooling in the cryostream was required to collect data. Even so data were obtained to 0.85 Å resolution by employing synchrotron radiation. The asymmetric unit was found to contain one half of a $Ag_{12}L_6$ assembly and associated counterions and solvent molecules.

Bond lengths and angles within pairs of chemically identical organic ligands were restrained to be similar to each other. Thermal parameter restraints (SIMU, RIGU) were applied to all atoms except for silver to facilitate anisotropic stable refinement. One napthyridine arm was modelled as disordered over two locations with bond length (DFIX) and FLAT restraints were applied to the disordered parts to ensure a stable refinement.

The central O-O linkage of the encapsulated peroxydisulfate anion was modelled as disordered over a special position with symmetry enforced half occupancy. The remaining oxygen atoms of this peroxydisulfate anion also show evidence of thermal motion or minor unresolved disorder which could not be adequately modelled with discrete atom positions. The other anions within the structure, all modelled as triflimide, also show evidence of substantial disorder. Four triflimide anions were modelled as disordered over two or three locations and the remaining triflimide was modelled with partial occupancy. The occupancies of the disordered anions were allowed to refine freely and then fixed at the obtained values. Some additional minor occupancy positions of the anions could not be located in the electron density map and were not included in the model resulting in a discrepancy of 1.45 counterions per asymmetric unit. Some lower occupancy disordered atoms were modelled with isotropic thermal parameters and bond length and thermal parameter restraints were applied to facilitate realistic modelling of the disordered anions. Some acetonitrile solvent molecules were also modelled with as disordered over multiple locations and/or with partial occupancy. The hydrogen atoms of some disordered acetonitrile molecules could not be located in the electron density map and were not included in the model.

Further reflecting the solvent loss there is a significant amount of void volume in the lattice containing smeared electron density from disordered solvent (and potentially the unresolved anions). Consequently the SQUEEZE[41] function of PLATON[42] was employed to remove the contribution of the electron density associated with this highly disordered solvent which gave a potential solvent accessible void of 4358 $Å^3$ per unit cell (a total of approximately 1130 electrons). Since the diffuse solvent molecules could not be assigned conclusively to acetonitrile or diethyl ether they were not included in the formula. Consequently, the molecular weight and density given above are likely to be slightly underestimated.

CheckCIF gives one A level and six B level alerts, all resulting from thermal motion and/or unresolved disorder of the anions and solvent molecules.

4.8 References

(1) Bera, J. K.; Sadhukhan, N.; Majumdar, M. 1,8-Naphthyridine Revisited: Applications in Dimetal Chemistry. *Eur. J. Inorg. Chem*. **2009**, *27*, 4023–4038.

(2) Giordana, A.; Priola, E.; Bonometti, E.; Benzi, P.; Operti, L.; Diana, E. Structural and Spectroscopic Study of the Asymmetric 2-(2′-Pyridyl)-1,8-Naphthyridine Ligand with Closed-Shell Metals. *Polyhedron* **2017**, *138*, 239–248.

(3) Tanaka, K.; Koizumi, T. Synthesis and crystal structures of mono- and dinuclear silver(I) complexes bearing 1,8-naphthyridine ligand. *Inorganica Chim. Acta*. **2004**, *357*, 3666–3672.

(4) Epstein, J. M.; Dewan, J. C.; Kepert, D. L.; White, A. H. Crystal structures of tris(1,8-naphthyridine)(perchlorato)mercury(II) perchlorate and tetrakis(1,8-naphthyridine)cadmium(II) bis(perchlorate). *Dalton Trans*. **1974**, *18*, 1949–1954.

(5) Giordana, A.; Priola, E.; Bonomettia, E.; Benzi, P.; Operti, L.; Diana, E. Structural and spectroscopic study of the asymmetric 2-(20-pyridyl)-1,8-naphthyridine ligand with closed-shell metals. *Polyhedron*. **2017**, *138*, 239–248.

(6) Cayton, R. H.; Chisholm, M. H.; Huffman, J. C.; and Lobkovsky E. B. Metal-metal multiple bonds in ordered assemblies. 1. Tetranuclear molybdenum and tungsten carboxylates involving covalently linked metal-metal quadruple bonds. Molecular models for subunits of one-dimensional stiff-chain polymers. *J. Am. Chem. Soc*. **1991**, *113*, 8709–8724.

(7) Rizzuto, F. J.; Pröhm, P.; Plajer, A. J.; Greenfield, J. L.; Nitschke, J. R. Hydrogen-Bond-Assisted Symmetry Breaking in a Network of Chiral Metal–Organic Assemblies. *J. Am. Chem. Soc*. **2019**, *141*, 1707–1715.

(8) Song, B.; Kandapal, S.; Gu, J.; Zhang, K.; Reese, A.; Ying, Y.; Wang, L.; Wang, H.; Li, Y.; Wang, M.; Lu, S.; Hao, X.-Q.; Li, X.; Xu, B.; Li, X. Self-Assembly of Polycyclic Supramolecules Using Linear Metal-Organic Ligands. *Nat. Commun*. **2018**, *9*, 4575.

(9) Hasenknopf, B.; Lehn, J.-M.; Boumediene, N.; Dupont-Gervais, A.; Van Dorsselaer, A.; Kneisel, B; Fenske, D. Self-Assembly of Tetra- and Hexanuclear Circular Helicates. *J. Am. Chem. Soc*. **1997**, *119*, 10956–10962.

(10) Hasenknopf, B.; Lehn, J.-M.; Kneisel, B. O.; Baum, G.; Fenske, D. Self-Assembly of a Circular Double Helicate. *Angew. Chem. Int. Ed*. **1996**, *35*, 1838–1840.

(11) Hasenknopf, B.; Lehn, J.-M.; Boumediene, N.; Leize, E.; Van Dorsselaer, A. Kinetic and Thermodynamic Control in Self-Assembly: Sequential Formation of Linear and Circular Helicates. *Angew. Chem. Int. Ed*. **1998**, *37*, 3265–3268.

(12) Cullen, W.; Metherell, A. J.; Wragg, A. B.; Taylor, C. G. P.; Williams, N. H.; Ward, M. D. Catalysis in a Cationic Coordination Cage Using a Cavity-Bound Guest and Surface-Bound Anions: Inhibition, Activation, and Autocatalysis. *J. Am. Chem. Soc*. **2018**, *140*, 2821–2828.

(13) Tidmarsh, I. S.; Faust, T. B.; Adams, H.; Harding, L. P.; Russo, L.; Clegg, W.; Ward, M. D. Octanuclear Cubic Coordination Cages. *J. Am. Chem. Soc*. **2008**, *130*, 15167–15175.

(14) Ayme, J.-F.; Beves, J. E.; Leigh, D. A.; McBurney, R. T.; Rissanen, K.; Schultz, D. A. Synthetic Molecular Pentafoil Knot. *Nat. Chem*. **2012**, *4*, 15–20.

(15) Danon, J. J.; Krüger, A.; Leigh, D. A.; Lemonnier, J.-F.; Stephens, A. J.; Vitorica-Yrezabal, I. J.; Woltering, S. L. Braiding a Molecular Knot with Eight Crossings. *Science* **2017**, *355*, 159–162.

(16) Argent, S. P.; Adams, H.; Riis-Johannessen, T.; Jeffery, J. C.; Harding, L. P.; Ward, M. D. High-Nuclearity Homoleptic and Heteroleptic Coordination Cages Based on Tetra-Capped Truncated Tetrahedral and Cuboctahedral Metal Frameworks. *J. Am. Chem. Soc*. **2006**, *128*, 72–73.

(17) Riddell, I. A.; Hristova, Y. R.; Clegg, J. K.; Wood, C. S.; Breiner, B.; Nitschke, J. R. Five Discrete Multinuclear Metal-Organic Assemblies from One Ligand: Deciphering the Effects of Different Templates. *J. Am. Chem. Soc*. **2013**, *135*, 2723–2733.

(18) Jansze, S. M.; Wise, M. D.; Vologzhanina, A. V.; Scopelliti, R.; Severin, K. $Pd^{II}_2L_4$-Type Coordination Cages up to Three Nanometers in Size. *Chem. Sci*. **2017**, *8*, 1901–1908.

(19) Sun, Q.-F.; Sato, S.; Fujita, M. An M18L24 Stellated Cuboctahedron through Post-Stellation of an $M_{12}L_{24}$ Core. *Nat. Chem*. **2012**, *4*, 330–333.

(20) Dong, Y.-B.; Geng, Y.; Ma, J.-P.; Huang, R.-Q. Organometallic Silver(I) Supramolecular Complexes Generated from Multidentate Furan-Containing Symmetric and Unsymmetric Fulvene Ligands and Silver(I) Salts. *Inorg. Chem*. **2005**, *44*, 1693–1703.

(21) Yue, N. L. S.; Jennings, M. C.; Puddephatt, R. J. Disilver(I) Macrocycles: Variation of Cavity Size with Anion Binding. *Inorg. Chem*. **2005**, *44*, 1125–1131.

(22) Beauchamp, D. A.; Loeb, S. J. Molecular Squares, Rectangles and Infinite Helical Chains Utilising the Simple 'Corner' Ligand 4-(2-Pyridyl)-Pyrimidine. *Chem. Commun*. **2002**, 2484–2485.

(23) Wiley, C. A.; Holloway, L. R.; Miller, T. F.; Lyon, Y.; Julian, R. R.; Hooley, R. J. Electronic Effects on Narcissistic Self-Sorting in Multicomponent Self-Assembly of Fe-Iminopyridine Meso-Helicates. *Inorg. Chem*. **2016**, *55*, 9805–9815.

(24) Ronson, T. K.; Zarra, S.; Black, S. P.; Nitschke, J. R. Metal–organic Container Molecules through Subcomponent Self-Assembly. *Chem. Commun*. **2013**, *49*, 2476–2490.

(25) Mosquera, J.; Ronson, T. K.; Nitschke, J. Subcomponent Flexibility Enables Conversion between D4-Symmetric CdII8L8 and T-Symmetric $Cd^{II}_4L_4$ Assemblies. *J. Am. Chem. Soc*. **2016**, *138*, 1812–1815.

(26) Fatila, E. M.; Twum, E. B.; Karty, J. A.; Flood, A. H. Ion Pairing and Co-Facial Stacking Drive High-Fidelity Bisulfate Assembly with Cyanostar Macrocyclic Hosts. *Chem. Eur. J*. **2017**, *23*, 10652–10662.

(27) Dobscha, J. R.; Debnath, S.; Fadler, R. E.; Fatila, E. M.; Pink, M.; Raghavachari, K.; Flood, A. H. Host-Host Interactions Control Self-Assembly and Switching of Triple and Double Decker Stacks of Tricarbazole Macrocycles Co-Assembled with Anti-Electrostatic Bisulfate Dimers. *Chem. Eur. J*. **2018**, *24*, 9841–9852.

(28) Bravin, C.; Guidetti, A.; Licini, G.; Zonta, C. Supramolecular Cages as Differential Sensors for Dicarboxylate Anions: Guest Length Sensing Using Principal Component Analysis of ESI-MS and ^{1}H-NMR Raw Data. *Chem. Sci*. **2019**, *10*, 3523–3528.

(29) Clever, G. H.; Kawamura, W.; Shionoya, M. Encapsulation versus Aggregation of Metal–Organic Cages Controlled by Guest Size Variation. *Inorg. Chem*. **2011**, *50*, 4689–4691.

(30) Minisci, F.; Citterio, A.; Giordano, C. Electron-Transfer Processes: Peroxydisulfate, a Useful and Versatile Reagent in Organic Chemistry. *Acc. Chem. Res.* **1983**, *16*, 27–32.

(31) Zhang, D.; Ronson, T. K.; Mosquera, J.; Martinez, A.; Guy, L.; Nitschke, J. R. Anion Binding in Water Drives Structural Adaptation in an Azaphosphatrane-Functionalized $Fe^{II}_4L_4$ Tetrahedron. *J. Am. Chem. Soc*. **2017**, *139*, 6574–6577.

(32) Allan, D.; Nowell, H.; Barnett, S.; Warren, M.; Wilcox, A.; Christensen, J.; Saunders, L.; Peach, A.; Hooper, M.; Zaja, L.; Patel, S.; Cahill, L.; Marshall, R.; Trimnell, S.; Foster, A.; Bates, T.; Lay, S.; Williams, M.; Hathaway, P.; Winter, G.; Gerstel, M.; Wooley, R. A Novel Dual Air-Bearing Fixed-χ Diffractometer for Small-Molecule

Single-Crystal X-ray Diffraction on Beamline I19 at Diamond Light Source. *Crystals.* **2017**, *7*, 336–359.

(33) Collaborative Computational Project, N., The CCP4 suite: programs for protein crystallography. *Acta Cryst*. **1994**, *D50*, 760–763.

(34) Evans, P. Scaling and assessment of data quality. *Acta Cryst*. **2006**, *D62*, 72–82.

(35) Winter, G., xia2: an expert system for macromolecular crystallography data reduction. *J. Appl. Crystallogr*. **2010**, *43*, 186–190.

(36) Farrugia, L. WinGX and ORTEP for Windows: an update. *J. Appl. Crystallogr*. **2012**, *45*, 849–854.

(37) Evans, P. R.; Murshudov, G. N. How good are my data and what is the resolution? *Acta Cryst*. **2013**, *D69*, 1204–1214.

(38) Winn, M. D.; Ballard, C. C.; Cowtan, K. D.; Dodson, E. J.; Emsley, P.; Evans, P. R.; Keegan, R. M.; Krissinel, E. B.; Leslie, A. G. W.; McCoy, A.; McNicholas, S. J.; Murshudov, G. N.; Pannu, N. S.; Potterton, E. A.; Powell, H. R.; Read, R. J.; Vagin, A.; Wilson, K. S. Overview of the CCP4 suite and current developments. *Acta Cryst*. **2011**, *D67*, 235–242.

(39) Sheldrick, G. SHELXT - Integrated space-group and crystal-structure determination. *Acta. Cryst*. **2015**, *A71*, 3–8.

(40) Sheldrick, G. M. Crystal structure refinement with SHELXL. *Acta. Cryst*. **2015**, *C71*, 3–8.

(41) van der Sluis, P.; Spek, A. L. BYPASS: an effective method for the refinement of crystal structures containing disordered solvent regions. *Acta Cryst*. **1990**, *A46*, 194–201.

(42) Spek, A. L. PLATON: A Multipurpose Crystallographic Tool. Utrecht University: Utrecht, The Netherlands, **2008**.

(43) Fatila, E. M.; Twum, E. B.; Sengupta, A.; Pink, M.; Karty, J. A.; Raghavachari, K.; Flood, A. H. Anions Stabilize Each Other inside Macrocyclic Hosts. *Angew. Chem. Int. Ed*. **2016**, *55*, 14057–14062.

5

A New Eight Crossing Molecular Knot

This Chapter provides a brief overview of the different strategies adopted by supramolecular chemists to synthesise topologically complex molecular knots. This introductory material is only concerned with the synthesis of molecular knots by metal-templated synthesis, one of several different strategies.

The formation of a new type of 8_{19} molecular knot is then discussed. The knot is formed using a subcomponent self-assembly strategy. The knot consists of a single organic molecule which weaves a path about six templating metal centres. The knot exhibits D_2 point symmetry. This contrasts with a previously reported, but topologically identical, molecular knot which has D_4 symmetry. Characterisation of the knot, both the paramagnetic Fe^{II} templated and the diamagnetic Zn^{II} templated congeners, **5.11** and **5.12**, respectively, is described, in solution and in the solid state.

This work builds upon chemistry developed in the Nitschke group into the synthesis of a range of geometrically complex extended circular helicate and cage molecules, as well as strategies developed in the synthesis of a topologically complex [3]catenane, but extends it to enable the synthesis of an eight-crossing molecular knot.

5.1 Knot Theory

Originating in the works of Vandermonde in the 18th century, and further developed by Gauss in the 19th century, knot theory describes the embedding of circles in three-dimensional space. It has interested mathematicians ever since. The systematic classification of knots remains an outstandingly difficult task in modern mathematics.

The fields of chemistry and knot theory have long been entwined. It was Lord Kelvin's theory that atoms were knots in the aether, with each element being a distinct knot, which led to the first connection between the two fields in the 1860s.[1] This theory led Tait, a close collaborator of Lord Kelvin, to create the first knot table which allowed for the systematic classification of a subset of the known knots with up to ten crossings.

This ill-conceived theory of Lord Kelvin was ultimately proven false by the Michelson-Morley experiment of 1887. Despite this, the work of Tait, and particularly the Tait conjectures, motivated early knot theorists. Eventually knot theory went on to become an important part of the emerging subject of topology. This field concerns itself with the study of shapes and space which are maintained under continuous deformation.

5.2 The Linear Double Helicate Strategy

It wasn't for nearly another century that chemistry and knot theory would cross paths again. Key contributors to this renaissance were Frisch and Wasserman,[2] with Schill and Lüttringhaus developing the first synthetic route to a mechanically interlocked molecular link, or catenane as this class of molecule became known as.[3] The group of Jean-Pierre Sauvage pioneered many advances in the synthesis of mechanically interlocked molecules, and were the first to report the synthesis of such molecules by template methods.[4] The tetrahedral Cu^{I} cation organises two coordinating ligands in close proximity to each other. The geometry of the ligands is such that it is then possible to link the two opposing ends together, via a condensation reaction. Demetallation can then be carried out to yield the metal-free catenane **5.1**.

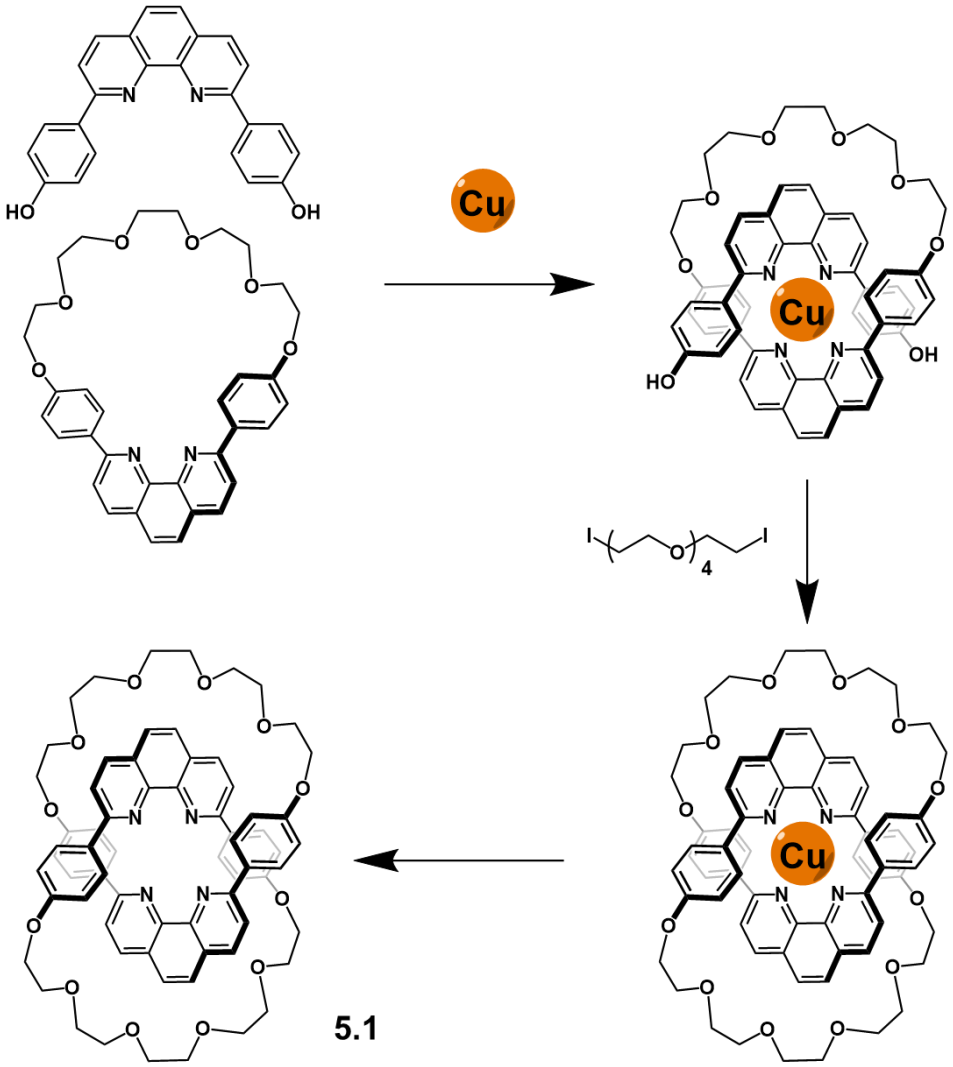

Figure 5.1 | Synthesis of [2]catenane **5.1** using a metal-templation strategy.[4]

Building on this seminal work, they realised that with the appropriate molecular weaving and linking patterns it would be possible to create one continuous and interwoven organic molecule, a molecular trefoil knot **5.2** (Figure 5.2).[5] The trefoil knot may also be referred to as a 3_1 knot in Alexander Briggs notation, a system for distinguishing topologically distinct knots.[6] The 3 denotes the number of crossing points, the subscripted 1 distinguishes the knot from others with the same crossing number. For the trefoil knot there are no other knots to distinguish it from with three crossings, but this is no longer true for more complex knotted structures.

This was the first example of the linear helicate strategy for molecular knot synthesis. Organising two ligands around two Cu^{I} cations to form a linear double helicate, followed by the linking of each ligand end to the most proximal and correctly oriented ligand end, resulted in formation of the trefoil knot. Subsequent adaption of the linking strategy led to increased yields, up to 74%.

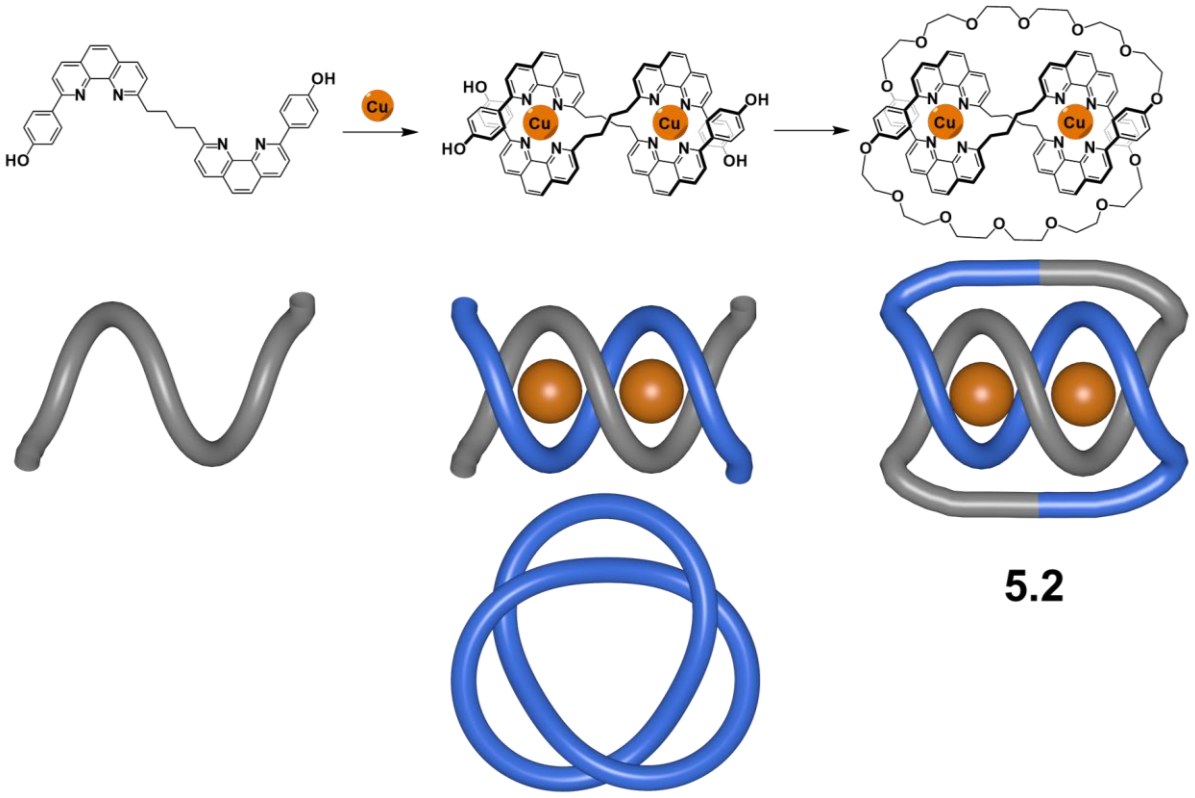

Figure 5.2 | Synthesis of a molecular trefoil knot, the first example of a molecular knot synthesised using the linear helicate approach.[5] A schematic representation is included for clarity. The bottommost representation is the symmetric torus representation, which is discussed in greater detail in Section 5.6 of this Chapter.

Most importantly, this work laid out the intellectual groundwork, later adopted by many research groups, for forming such structures. In order to construct these topologically complex molecules the organisation of molecular components into certain restricted configurations is required. The geometry of these fragments relative to one another then leads to the formation of a given knot, if the linking process can be controlled.

It is important to note that not all strategies to form molecular knots and links have relied on metal-templation effects. Work by Stoddart,[7] Hunter,[8] Vögtle[9] and Feigel[10] have demonstrated the utility of π-π and hydrogen-bonding interactions for directing the formation of knots. Dynamic combinatorial chemistry has also been utilised by Sanders and coworkers to form a trefoil knot in aqueous solution.[11] In this case, the main driving force for the formation of the knot is likely to be the minimisation of exposure of the hydrophobic surfaces of the NDI fragments.

5.3 The Circular Double Helicate Strategy

Returning to the metal templated strategies, successfully employed to form the 3_1 knot, it remained to be seen if more complex topologies could be obtained. Extending the linear double helicates to incorporate three metal templates allowed for the synthesis of a Solomon link **5.3** (Figure 5.3).[12] Pushing this even further, with the incorporation of four templates, was envisaged to allow for the synthesis of the next torus knot after the trefoil knot, the pentafoil or 5_1 knot (Figure 5.3). However, significant effort by Sauvage and coworkers proved unfruitful.[13] It was found that as the length of the double helicate was extended, it became increasingly difficult to make the necessary connections to form the desired knot.

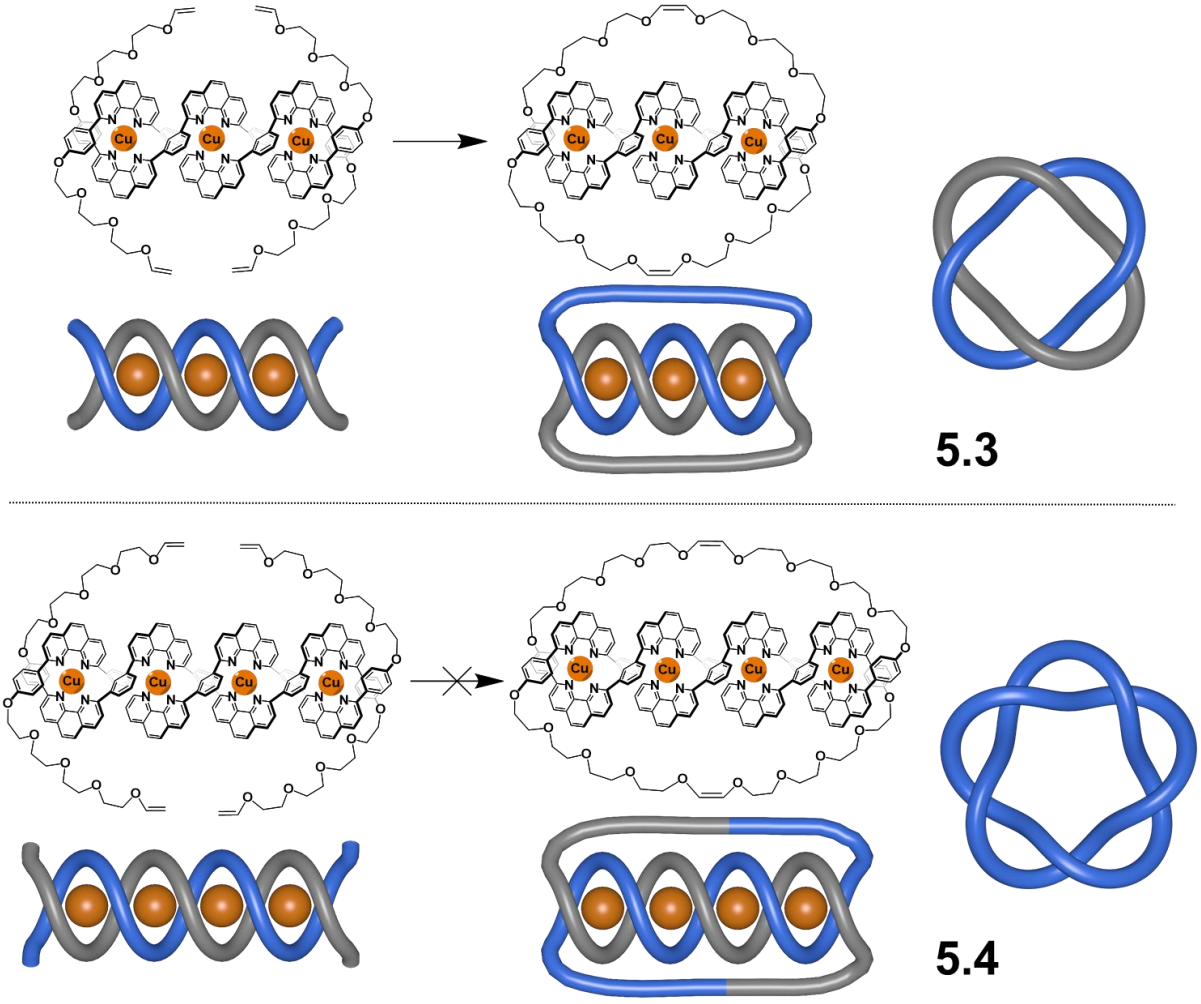

Figure 5.3 | Synthesis of a molecular Solomon link and attempted synthesis of a pentafoil knot using the linear helicate approach.

This inherent problem in the linear helicate strategy was overcome by Leigh and coworkers nearly two decades later. They recognised that by bringing the ends of the helicate closer together, it should be possible to make the desired connections, and thereby form more complex knots. This realisation led to the development of the circular helicate strategy for knot formation (Figure 5.4). This work built upon the chemistry developed by Jean-Marie Lehn in the 1990s which reported on the formation of a range of circular helicates with different numbers of metal centres built into the structure.[14,15]

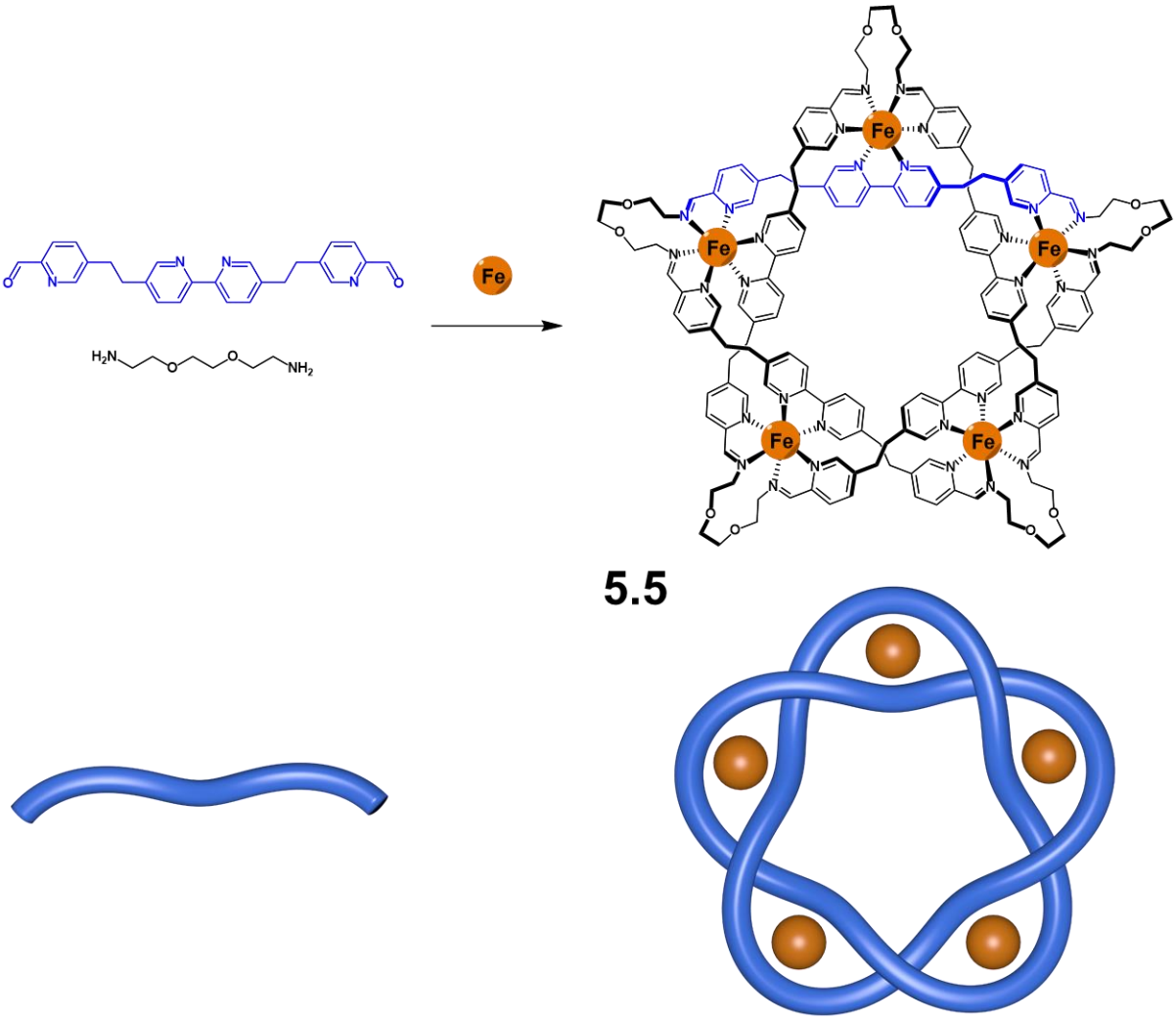

Figure 5.4 | Synthesis of a molecular pentafoil knot by Leigh, using the circular helicate approach. One of the five identical ligands in **5.5** is highlighted in blue for clarity.[16]

In the first reported example, they utilised this strategy to form the pentafoil knot.[16] The linear helicate approach required the formation of two connections, as outlined in Figure 5.3. While the new circular helicate strategy increased this number to five, the close proximity of the

ligand ends and their orientation in space relative to one another allowed for nearly quantitative yields of pentafoil knot **5.5**.

Higher order knots and links could also be obtained using this strategy. Incorporation of six metal centres into the circular helicate, which is an anion-templation driven effect (note that **5.5** and **5.6** are assembled from very similar ligands), followed by connection of ligand ends via olefin metathesis, led to the formation of a molecular Star of David, a triply interlocked [2]catenane (Figure 5.5).[17]

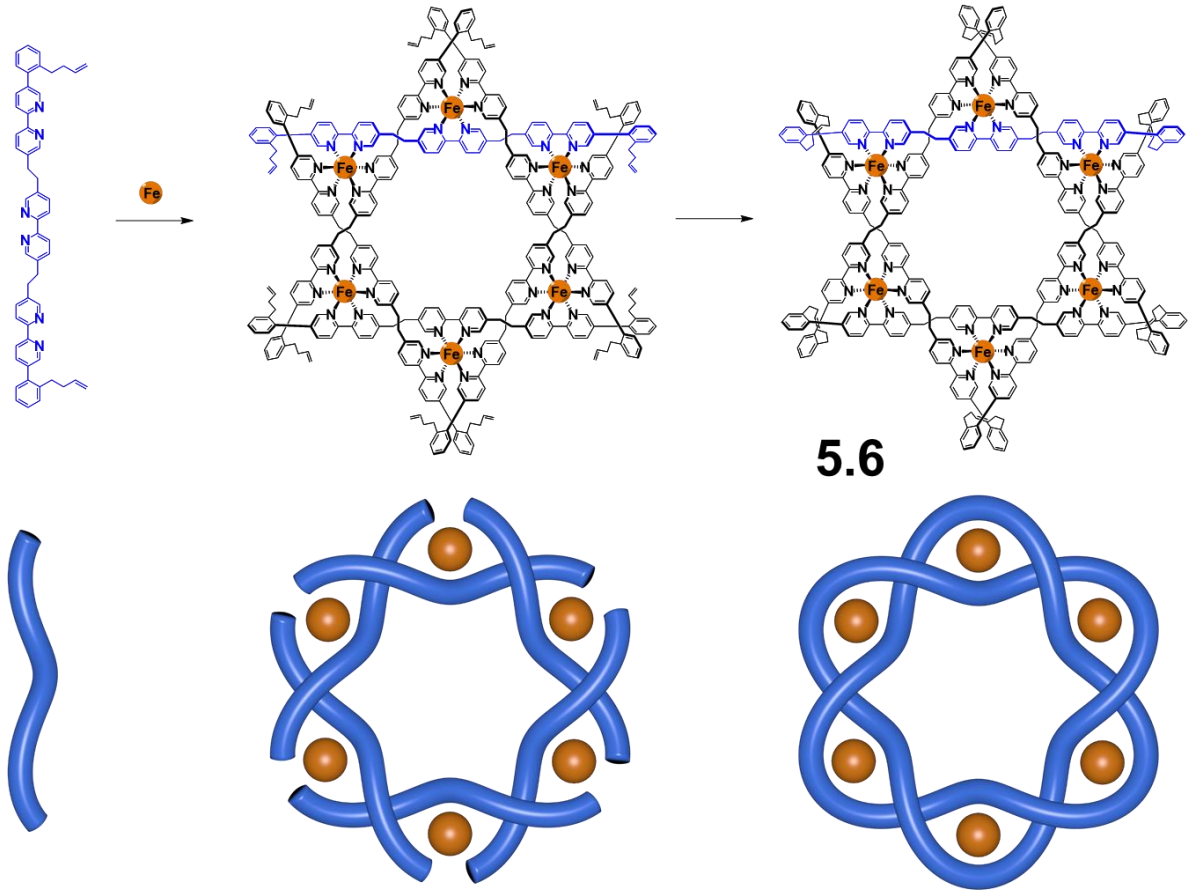

Figure 5.5 | Synthesis of a molecular Star of David. One of the five identical ligands in **5.6** is highlighted in blue for clarity. The overall structure is a triply-interlocked [2]catenane. The linking of ligand ends is achieved by means of olefin metathesis.[17]

5.4 The Circular Triple Helicate Strategy

In perhaps the most impressive piece of work on molecular topology by the Leigh group thus far, they realised that the circular helicate strategy could be used to form triple braid knots, in particular the 8_{19} knot. Adoption of the same connection strategy used in the synthesis of the pentafoil knot and the Star of David catenane (as in Figures 5.4 and 5.5) leads to the formation of a relatively simple doubly interlocked [2]catenane, or Solomon link, as had been previously reported.[18] In each of these cases, the connections are made between ligand ends which are coordinating to the same metal centre.

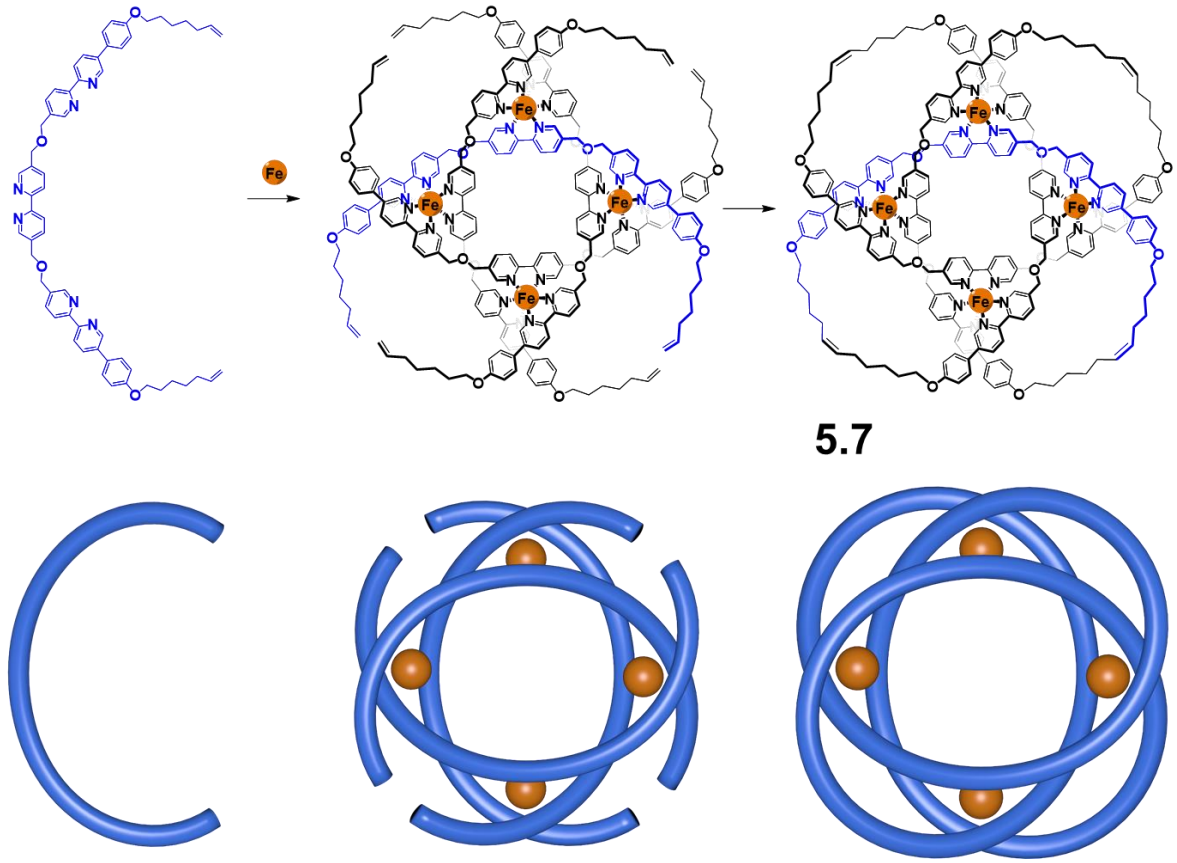

Figure 5.6 | Synthesis of a molecular knot with eight crossing points. In contrast to the pentafoil knot and Star of David described above, connections are made between ligand ends which are coordinated to different metal centres.

Leigh and coworkers recognised that if the connections were instead made between ligand ends which were attached to different metal centres in the parent helicate an eight crossing knot would result.[19]

This small but significant change in strategy showed how these circular helicates developed by Lehn can be treated as a circular triple helicate. It led to the synthesis of the most tightly knotted synthetic molecule at the time, a record since surpassed by the same group.[20] Application of the same concept to the six metal centre helicate, already used to form the Star of David **5.6**, led to the formation of a nine-crossing knot in a subsequent work.[21] A 10_{124} torus knot would result if the approach were to work with the five metal centre helicate used to form the pentafoil knot **5.5**. At the time of writing, this hasn't been achieved experimentally.

5.5 A Subcomponent Self-Assembled Circular Helicate

Previous work in the Nitschke group has demonstrated that treatment of the di-pyridylaldehyde subcomponent **5.8** with *p*-anisidine and a range of different metal salts can produce a range of supramolecular architectures.[22,23] One of these structures is an M_6L_8 quasi-planar, grid-like structure **5.9** (Figure 5.7). The eight bis-bidentate ligands weave about the metal centres, forming a type of extended circular helicate.

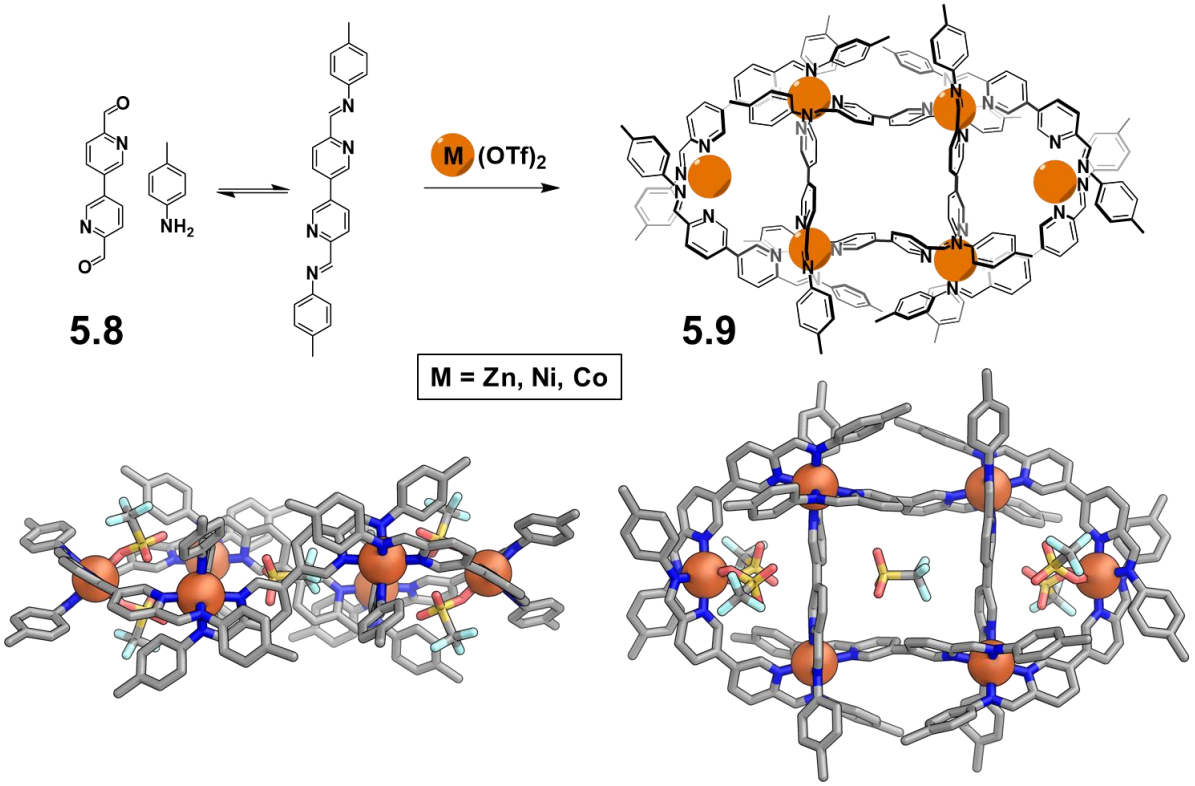

Figure 5.7 | The formation of M_6L_8 planar extended circular helicate **5.9**. The extended circular helicate can be formed cleanly with $Zn(OTf)_2$ and in equilibrium with several other supramolecular constructs with $Co(OTf)_2$ and $Ni(OTf)_2$. The crystal structure shown here was produced using $Ni(OTf)_2$.[23]

Extended circular helicate **5.9** has six metal centres. Two of these are peripheral and are coordinated by four N donors and two triflate anions in the solid-state. The others, referred to as the "core" metal centres in this thesis, are coordinated by six N donors.

Noting the proximity of the aniline residues within the structure, and that each of these proximal groups were attached to different metal centres, it was reasoned that connecting these fragments could yield a topologically interesting molecule. Previous work on a related structure, which led to the synthesis of a [3]catenane, provided the precedence for this idea.[24] It should be noted that for several weeks after the project was conceived it was not known which topology would arise, if the envisaged connections were successfully made.

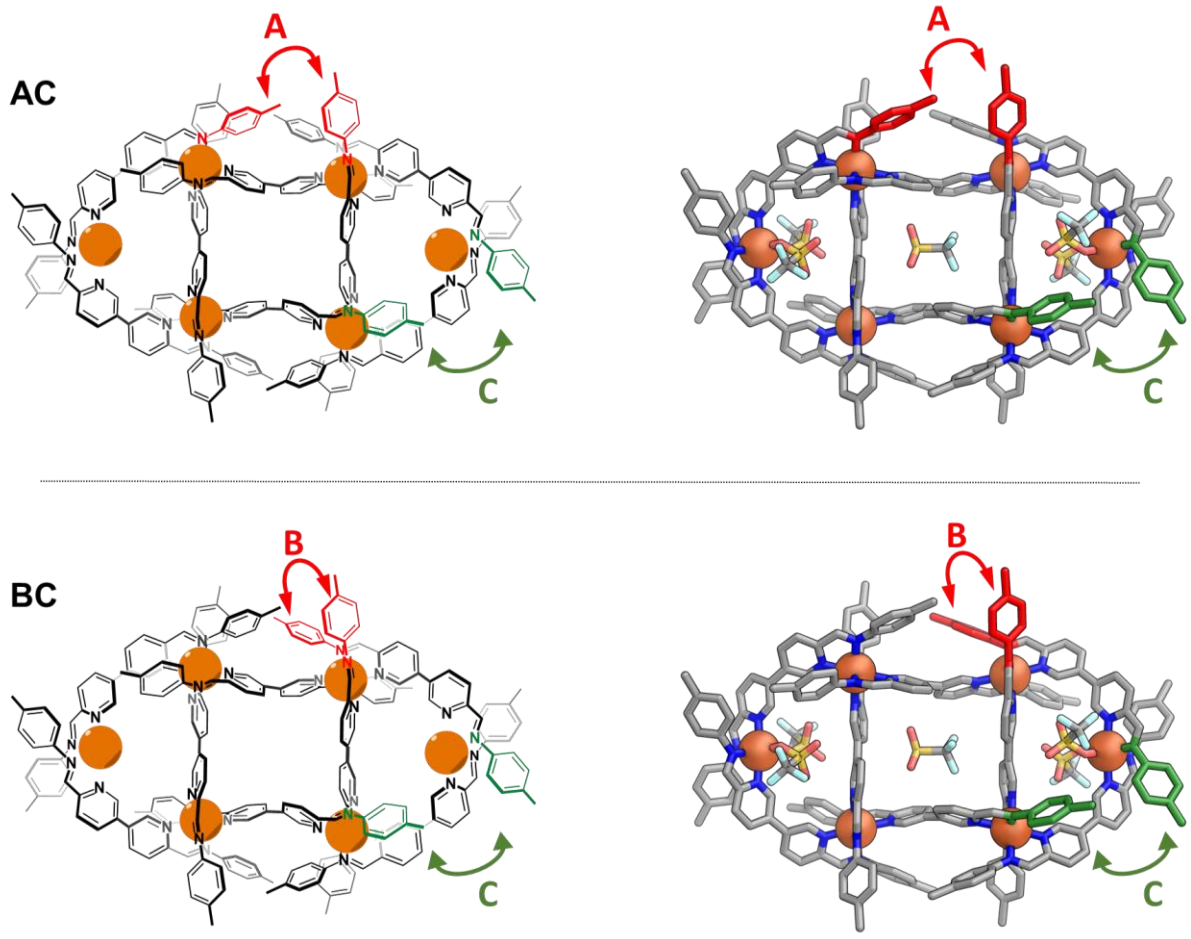

Figure 5.8 | Three types of connections between the aniline residues of the M_6L_8 extended circular helicate **5.9** are possible. This can be divided into two categories, connections between the four metal centres at the core of the extended circular helicate (type **A** and type **B**) and connections between the core metal centres and the peripheral metal centres (type **C**). **A** and **B** cannot occur together and so two combinations are possible, **AC** and **BC**.

Molecular modelling studies (MM3 level) were carried out to establish the feasibility of both the desired and the competing connections. From these studies it was concluded that two types of connection were required in order to form a closed ring system. In the first type of connection

there are two distinct options, connections **A** and **B**, both coloured in red in Figure 5.8. Both of these connect aniline residues which are coordinating to one of the core metal centres.

Connection **A** spans a distance of 4.91 ± 0.02 Å (as measured from the carbon atom of the methyl group of the aniline residues) while connection **B** spans 8.61 ± 0.02 Å. These values were measured from a Ni^{II} based extended helicate, previously published by our group.[23] Given this greater distance, and perhaps more importantly, the angles at which the aniline residues protrude from the extended circular helicate, it was reasoned that for dianilines with relatively short, flexible connectors and a *para*-substitution pattern, connection **A** should be favoured.

The second type of connection, labelled **C** and coloured green in Figure 5.8, spans between the core metal centres of the extended circular helicate and the two peripheral anion-coordinated metal centres. It spans a distance of 6.51 ± 0.03 Å and is, again, distinct from connections **A** and **B** in how it protrudes from the extended circular helicate.

These factors necessitate the judicious selection of connector, one which can readily bend or adopt a more elongated configuration, depending on the connection required. Competing connections must be taken into consideration, as they would lead to the formation of totally different structures.

Closer analysis of the structures which result from pairing connection **C** with either **A** or **B** revealed several interesting features. The first was that for both the **AC** and **BC** connection pattern, the resulting structures consist of one organic loop which incorporates each of the eight ligands of the parent extended circular helicate **5.8**. These two structures would therefore be expected to appear practically identical by both NMR and mass spectrometry.

The second interesting feature was revealed with the removal of the metal cations from the two models. This leaves behind two macrocyclic molecules, which we hypothesised to be topologically distinct. A series of rudimentary, sequential force-field energy minimisation calculations (MM3) indicated this to be true. Connection pattern **BC** was able to completely unravel, revealing itself to be a topologically trivial, if very large, unknot or macrocycle as it is commonly referred to in chemistry.

In contrast, connection pattern **AC** was never found to unravel. Of course, this does not necessarily mean that a knot has been formed, it could simply be an unknot which is very hard to untangle. Further to this, even if it were to be established that it is a knot, it still leaves open the question of what type of knot it is exactly.

In order to get a better understanding of this, a macroscopic version of the envisaged molecular knot, with connection pattern **AC**, was constructed using string as the ligand. Continuous deformation of the loop revealed a more symmetric D_4 form of the knot. This more symmetric form was reminiscent of the 8_{19} knot formed by Leigh and coworkers, as described in Figure 5.6. A similar procedure, with the **BC** pattern, confirmed it to be an unkot.

Starting from this point, we hypothesised that the extended circular helicate may be capable of supporting a topologically equivalent knot to that described by Leigh, but which is very geometrically distinct. The four core metal centres appear to adopt a similar role to the four metal centres in the 8_{19} knot described by Leigh and coworkers. The two peripheral metal cations do not play an active role in the entwining of the ligands but instead act to organise the ligand ends in an orientation such that the desired connection **C** is made feasible.

5.6 Synthesis of a Fe_6 - 8_{19} Knot

To synthesise the knot, subcomponent **5.8** (8 equivalents) was treated with flexible dianiline **5.10** (8 equivalents) and $Fe(OTf)_2$ (6 equivalents) in acetonitrile, leading to the formation of **5.11** in 52% isolated yield (Figure 5.9a). Experimental details are available in Experiment Section 5.9. Dianiline **5.10** was selected as molecular modelling indicated that it should be able to bridge the distance required for connection **C**, while favouring connection **A** over **B**. ESI-MS (Figure 5.9b) was consistent with the formation of either the undesired macrocycle or knot **5.11**, both of which have a Fe_6L_1 structure, where the ligand is one continuous organic loop which incorporates eight equivalents of both **5.8** and **5.10**.

Analysis by ^{1}H NMR (Figure 5.9c) revealed that **5.11** exhibits paramagnetism, indicating some of its metal centres are high-spin. This is consistent with previously reported results, such as the [3]catenane reported by our group.[24] Coordination of triflate, which is a low ligand field strength donor, to the two external Fe^{II} sites stabilises their high-spin state. This leads to the complex exhibiting paramagnetism. In contrast, the internal Fe^{II} centres, each coordinated by three pyridyl-imine ligands, are low-spin and therefore diamagnetic.

While this mixture of high-spin and low-spin metal centres makes the analysis of the NMR spectrum challenging, it is possible to say that the molecule or molecules formed have relatively low-symmetry, compared to the starting materials. It was not possible to accurately count the number of signals in the spectrum due to signal broadening and overlap.

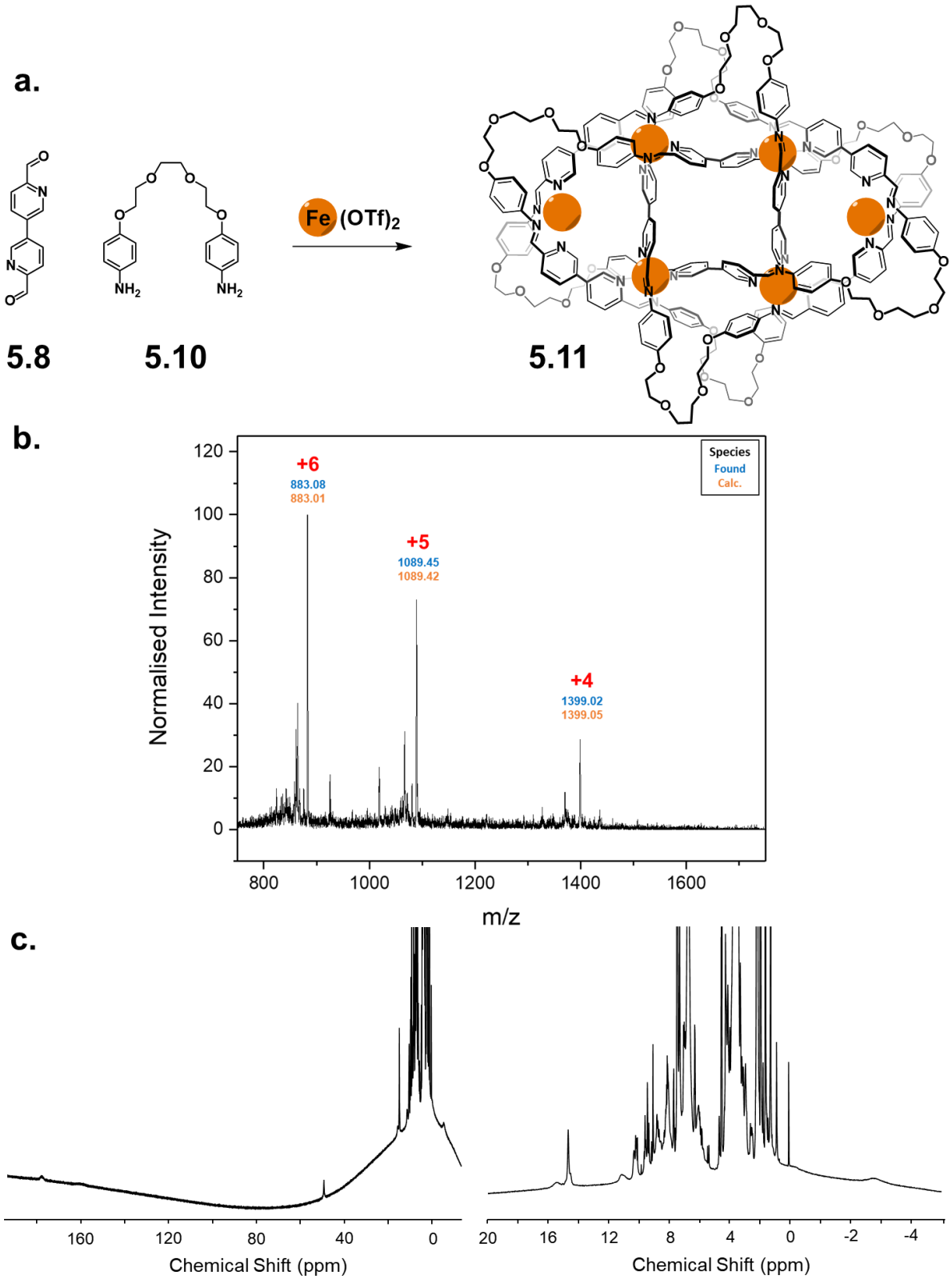

Figure 5.9 | a. Synthesis of Fe^{II} templated 8_{19} knot **5.11**. **b.** ESI- and HR-MS of **5.11**. **c.** Wide-sweep ^{1}H NMR spectrum of **5.11**, with the second spectrum focusing on the aromatic and aliphatic region, more clearly showing the desymmetrised nature of **5.11**.

Given that the treatment of **5.8** with *p*-anisidine and $Fe(OTf)_2$ was previously observed to lead to the formation of a M_4L_6 tetrahedron, this result is somewhat surprising. It was also found that if $Co(OTf)_2$ or $Ni(OTf)_2$, both of which form the parent M_6L_8 extended circular helicate with *p*-anisidine,[23] were used with dianiline **5.10** significant amounts of insoluble precipitate resulted. A small amount of the desired knots could be detected by ESI-MS for both $Co(OTf)_2$ and $Ni(OTf)_2$, but attempts to isolate the metallated knots proved unsuccessful.

Slow diffusion of diisopropyl ether into a concentrated solution of **5.11** gave dark green crystals suitable of analysis by single-crystal X-ray diffraction. The solid state structure (Figure 5.10) unambiguously confirmed the topology of **5.11** as being that of an 8_{19} knot, consistent with the **AC** connection pattern, as described in Figure 5.8.

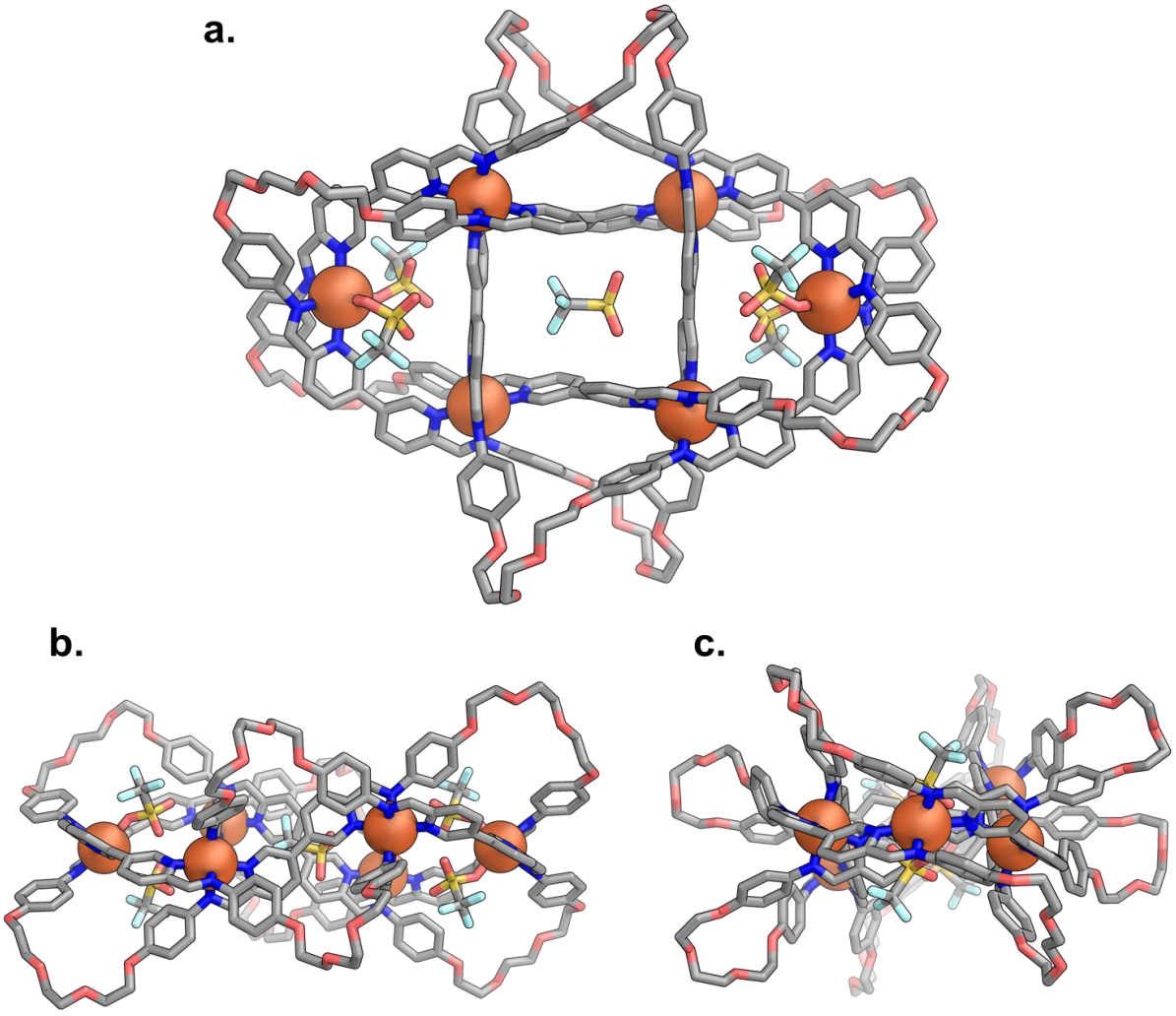

Figure 5.10 | a. Crystal structure of **5.11** which is revealed to be a 8_{19} knot. **b.** Side-on view of the knot showing the slight distortion away from planarity of the Fe^{II} centres. **c.** Side-on view of the knot focusing on a peripheral high-spin centre of the knot.

Several interesting structural features were noted. Owing to the different types of connections which dianiline **5.10** is required to make, two very distinct conformations for the ethylene glycol chains are observed to occur. In the case of connection **A**, ie. between the core metal centres, the ethylene glycol chains of the dianiline are observed to adopted a highly bent state where the *gauche* conformer predominates. Connections between the core metal centres and the peripheral high-spin metal centres (connection **C**) adopted a more elongated state, with the *anti*- conformer predominating. These distinct conformations highlight how important the nature of the dianiline linker is in this system.

As is the case with the original parent extended circular helicate **5.9** (which was formed with Ni^{II}), the metal centres are found to be quasi-planar, with slight distortion of the central Fe^{II} cations above and below the mean plane (Figure 5.11b-c). A torsion angle of 28.2 ± 0.4° was measured, 9° greater than that of **5.9**.

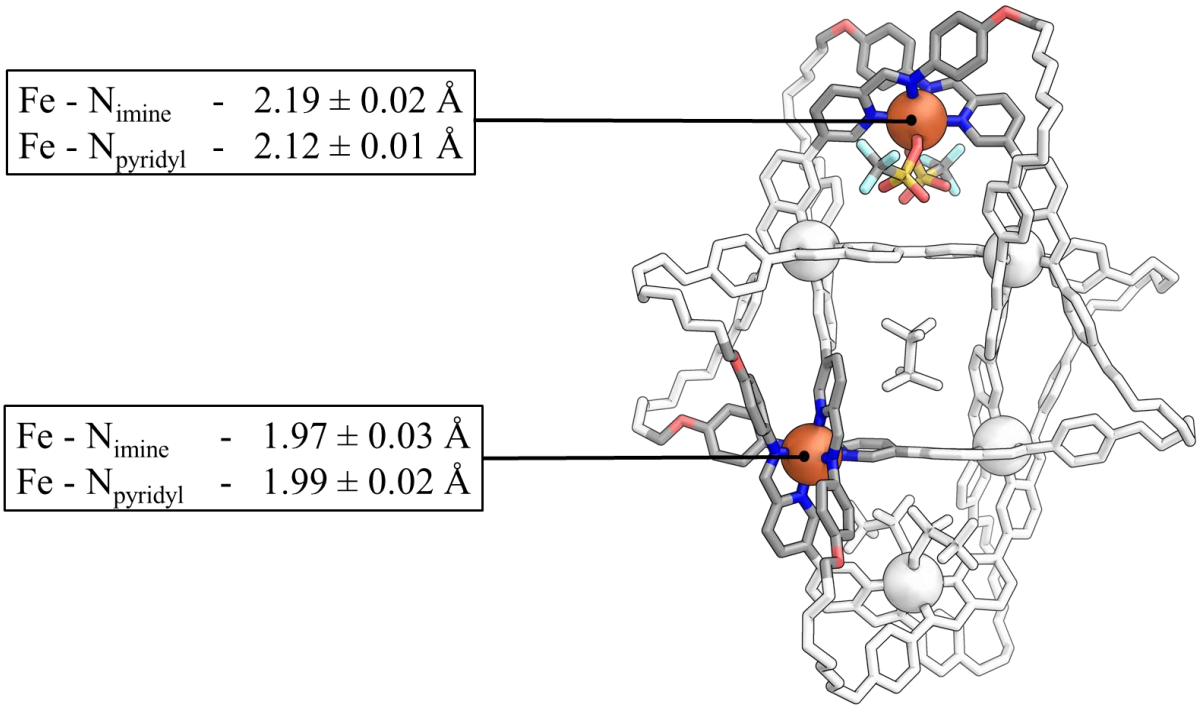

Figure 5.11 | Variation in the coordinative bond lengths for the four low-spin metal centres and the two peripheral, high-spin metal centres of **5.11**. Values reported are averaged for each of the metal centres.

Significant changes in the positions adopted by the ligands, as compared to **5.9**, were also noted. This can be seen in the variation of the distances spanned in connection **A** which was measured to be 4.37 ± 0.02 Å (compared to value of 4.91 ± 0.02 Å in **5.9**) and connection **C**, measured at 7.33 ± 0.5 Å (compared to a distance of 6.51 ± 0.03 Å for **5.9**). Measurements were taken between the phenolic oxygens of the dianiline linker. These changes probably arises from the distinct coordination preference of the two metal cations and crystallographic packing effects.

In order to probe whether the two peripheral Fe^{II} centres are high-spin at 100 K in the solid state, the average distances between the Fe^{II} cations and their N donors were measured. In the case of the core Fe^{II} centres, an average distance of 1.97 ± 0.03 Å was measured between the cations and their imine donors and 1.99 ± 0.02 Å between the cations and the pyridyl donors. For the peripheral centres, Fe^{II} to imine distances of 2.19 ± 0.02 Å and Fe^{II} to pyridyl donor distances of 2.12 ± 0.01 Å were measured.

The greater coordinative bond lengths, even at much lower temperatures, indicate that the peripheral centres are destabilised relative to the core metal centres. This is consistent with a reduction in the crystal field splitting energy of the octahedral metal centre, such that the splitting energy is now less than the energy of pairing the electrons. This effect leads to the unpairing of electrons and the knot exhibiting paramagnetism as a consequence.

It is noteworthy that while **5.11** is topologically equivalent to **5.7**, the 8_{19} knot reported by Leigh, it is geometrically distinct. **5.7** has overall D_4 point symmetry and a total of 8 crossings. In contrast, **5.11** has overall D_2 point symmetry. Furthermore, if viewed as in Figure 5.11, it has a total of 16 crossing points, 8 of which are nugatory. This means that they can be removed using simple deformations of the knot. The sole requirement of these deformations is that the knot does not pass through itself.

In particular, a type of deformation called a Reidmeister type II move is required. This move is defined as any deformation in which one loop passes completely over another (Figure 5.12). This results in either a reduction or increase in the apparent crossing number by two. It is important to note that these crossings are not true crossings, the true crossing number of any knot is invariant to deformation. It cannot be either increased or decreased by any type of loop move.

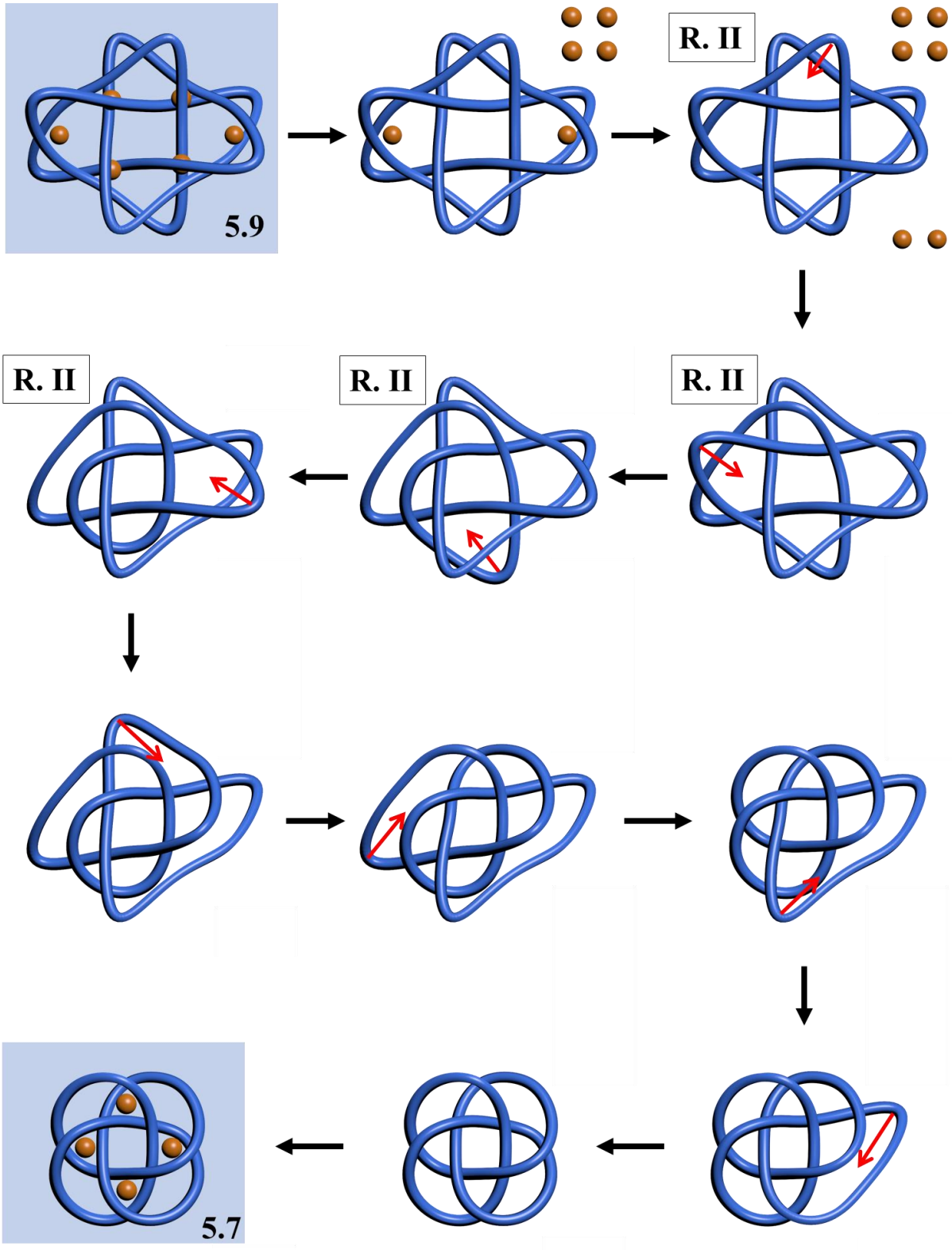

Figure 5.12 | Demetallation of the of 8_{19} knot **5.11**, followed by its continuous deformation through a series of four Reidmeister type 2 moves (labelled R. II) and four topologically trivial moves. The red arrows indicate the upcoming movement of a section of the knot. Remetallation would in principle yield the D_4 symmetric representation of the knot, as in **5.7**.

Figure 5.12 shows an idealised representation of **5.11**, generated from the crystal structure and showing only the organic portion of the knot with its metal templates. Demetallation, followed by a series of continuous deformations, which are described and labelled, show that this conformer of the 8_{19} knot can be converted into the D_4 symmetric representation which closely resembles that reported by Leigh and described above, **5.7**. This simplified representation involves the following steps: (a) the "demetallation" of the core metal centres of **5.11**, (b) the "demetallation" of the peripheral metal centres, (c) four Reidmeister II moves, (d) four topologically-trivial moves and finally (e) remetallation of the knot.

This new form of the 8_{19} knot is in fact its most symmetric representation. The 8_{19} knot can be generated by tracing along the surface of a torus (Figure 5.13). The ability to generate such topologies in geometrically distinct and desymmetrised configurations therefore constitutes a new development in molecular knot synthesis. To understand how these two knots are geometrically distinct but topologically equivalent, it is instructive to consider the torus about which the knot has been traced. The simplest knot, the trefoil knot, can be formed by tracing a line about the surface of a torus. Of course, there are various paths that one can trace about a torus.

As mentioned previously, all of the simpler knots (those with a crossing number ≤ 15) have been classified and tabulated by mathematicians. Alexander-Briggs notation is one strategy for assigning and distinguishing these topologically distinct species. However it doesn't encode any information about the structure of the knot, beyond its crossing number.

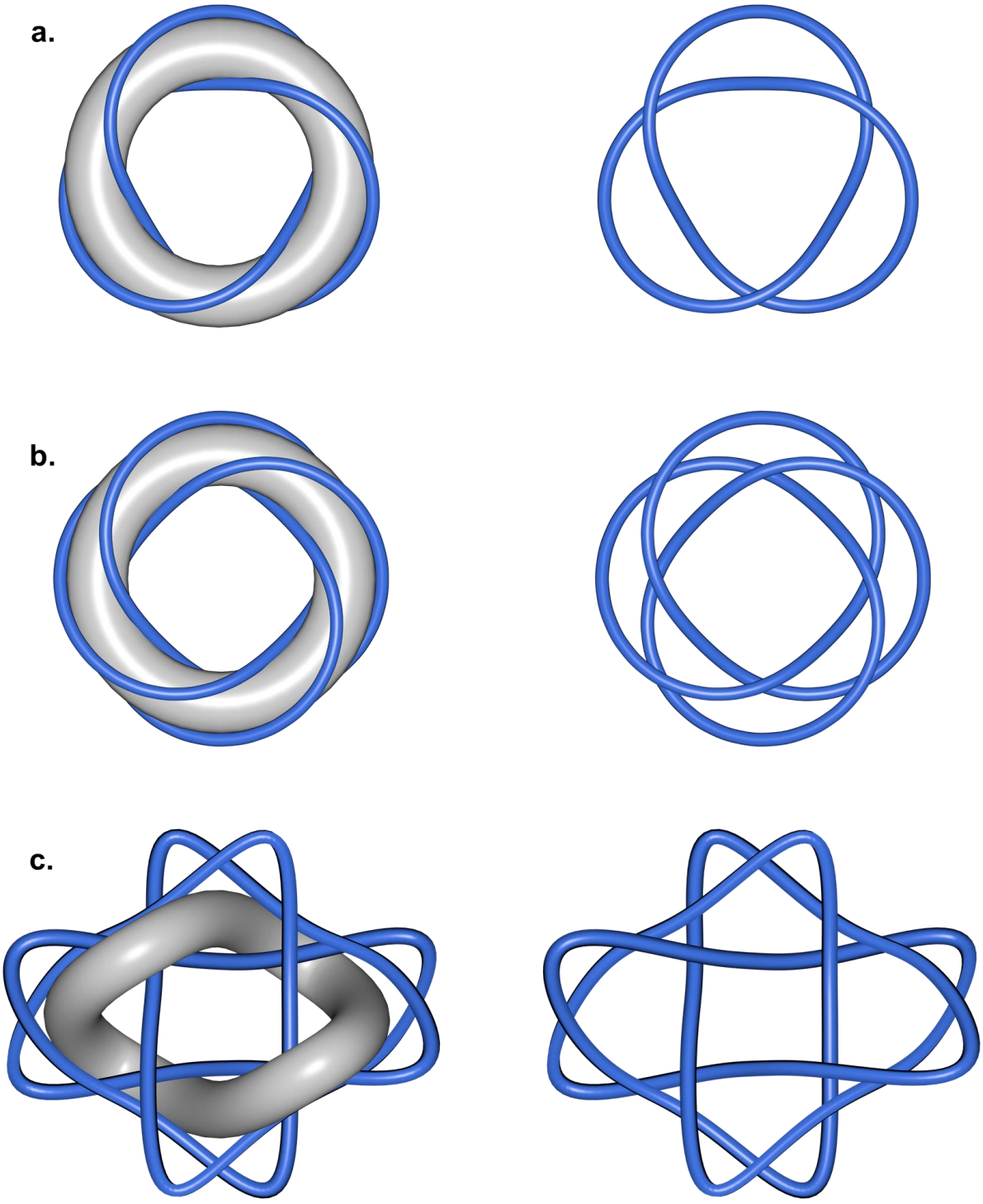

Figure 5.13 | Showing how torus knots lie on the surface of a torus. **a.** A trefoil knot (3_1 or T(3,2), refer to main text for further discussion of this nomenclature) on a torus. **b.** The D_4 symmetric representation of an 8_{19} knot (T(4,3)) on a torus. **c.** Idealised representation of **5.11** on a heavily distorted torus. This distortion of the torus leads to the geometric inequivalence of **5.7** and **5.11**, despite their topological equivalence.

In the case of the trefoil knot (3_1 in Alexander Briggs notation) an alternative form of nomenclature is T(3,2). In this case, the T signifies that the knot is a torus knot and the 3 and 2 are integers which carry information about the nature of the knot. For any torus knot these two integers must be coprime, or in other words their largest common divisor must be 1. If this condition is not met, the object is not a torus knot.

For the trefoil knot, the 3 indicates the number of times the knot winds about the torus itself. In Figure 5.13a this can be readily visualised by considering the number of times the knot passes by the outer edge of the torus (there are many other equally valid ways to consider this). The number of times one must cross the knot when travelling from the axis of rotational symmetry of the torus to the outside of the knot is encoded in the 2 of T(3,2).

This same system can be readily applied to the 8_{19} knot when it is in its most symmetric representation. In the T(4,3), the knot (Figure 5.13b) passes by the outer edge of the torus four times and to get from the axis of rotational symmetry to the outside of the knot one must pass over the knot three times.

Figure 5.13c shows how **5.11** is both topologically equivalent to, and geometrically distinct from, **5.7**. A torus is defined as the object formed upon rotation of a circle in three-dimensional space about an axis which is coplanar to the circle. This means that the torus is effectively flat (or rather it has three dimensional depth but can sit flat on a two-dimensional surface, as with a doughnut, or with the grey toruses in Figure 5.13a-b).

In order to fit **5.11** to a torus, the torus must first be heavily distorted. This new viewpoint can be seen as another way of understanding why **5.11** is geometrically distinct to **5.7**, while remaining topologically identical. Continuous deformation of the twisted torus defining the knot back to its more planar configuration would in fact lead to a much more regular and symmetric representation of the knot itself, like that in Figure 5.13b.

5.7 Synthesis of a Zn_6 - 8_{19} Knot

In contrast to the Fe^{II} templated knot **5.11** described above, the synthesis of the Zn^{II} templated knot proved challenging and highly dependent on stoichiometry, concentration and the purity of the precursors used (see the Experimental Section 5.9). Nonetheless, selective synthesis of the $Zn^{II}_6L_1$ knot could be achieved in a reproducible manner after extensive tuning of the reaction conditions.

Treatment of **5.8** (8 equivalents) with **5.10** (8 equivalents) and $Zn(OTf)_2$ (6 equivalents) in acetonitrile led to the formation of a single species, **5.12**, shown by ESI-MS to be consistent with a Zn_6L_1 structure (Figure 5.14a-c). Zn^{II} is d^{10}, which precludes the possibility of unpaired electrons. This means that **5.12** is diamagnetic unlike its Fe^{II} congener, **5.11**. This means that analysis by ^{1}H NMR spectroscopy becomes much more instructive. **5.12** was revealed to be highly desymmetrised, with 24 ^{1}H resonances in the aromatic region in total, consistent with the starting subcomponents adopting four chemically distinct environments (Figure 5.15b).

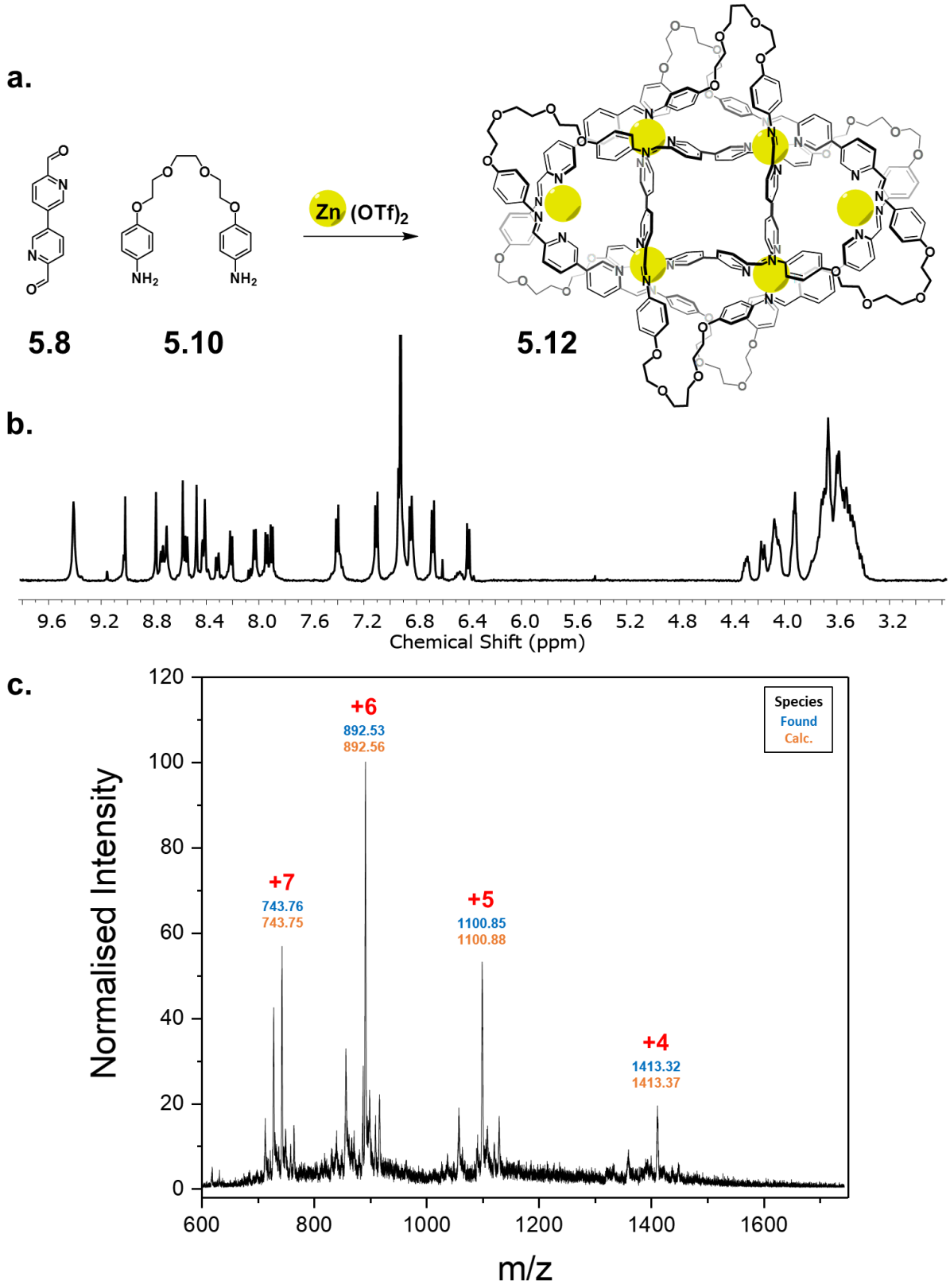

Figure 5.14 | a. Synthesis of Zn^{II} templated 8_{19} knot **5.12**. **b.** ^{1}H NMR spectrum of **5.12**, which exhibits four-fold desymmetrisation resulting in 24 aromatic resonances. **c.** ESI-MS of **5.12**.

This result is consistent with those observed for the parent extended circular helicate formed with Zn^{II}, described previously.[23] Inspection of aromatic region of the ^{1}H-^{13}C HSQC revealed distinct clustering of the 24 signals into six groups, with each having four signals of equal ^{1}H integration. At this point, it was possible to assign each of these groupings to a given proton environment. Complete assignment of the ^{1}H NMR spectrum was possible once the structure of **5.12** was elucidated in the solid state, and is detailed later in the Chapter.

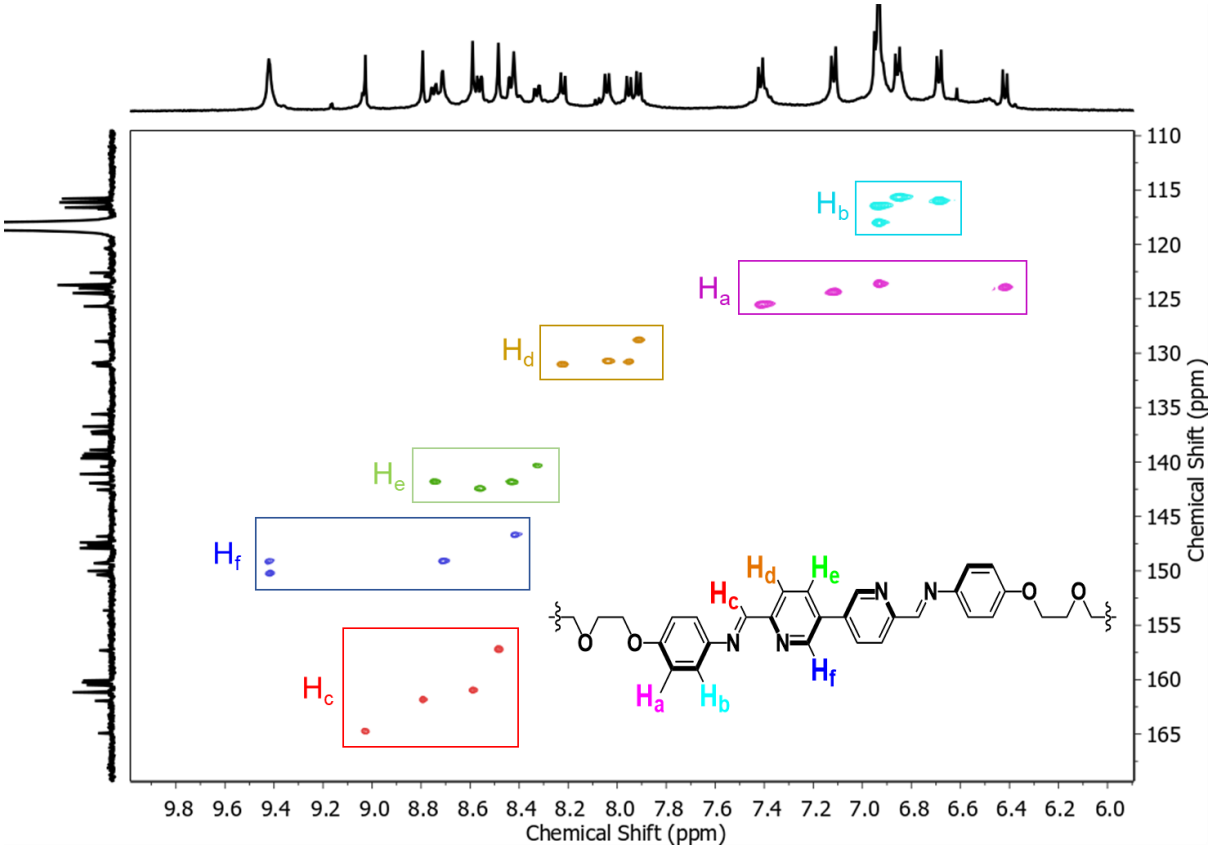

Figure 5.15 | ^{1}H-^{13}C HSQC of **5.12**. Each proton environment is four-fold desymmetrised as a result of their different positions in the overall knotted structure.

Vapour diffusion of diisopropyl ether into an acetonitrile solution of **5.12** furnished crystals of sufficient quality for analysis by X-ray diffraction. This revealed **5.12** to be isostructural with **5.11**, with a few noteworthy distinctions.

Firstly, there was no evidence for a well-resolved triflate anion being bound in the centre of the Zn^{II} knot (Figure 5.16a). While this may simply be a crystallographic packing effect, it does

call into question the assertion that the triflate anion is strictly required to template the structure in solution.[23]

Secondly, the metal centres of **5.12** are almost exactly coplanar (Figure 5.16b), which contrasts with the distortion from planarity observed in **5.11**, as well as in the Ni^{II} extended circular helicate **5.9**, described above. The torsion angle between the metal centres was found to be 3.2 ± 0.3°.

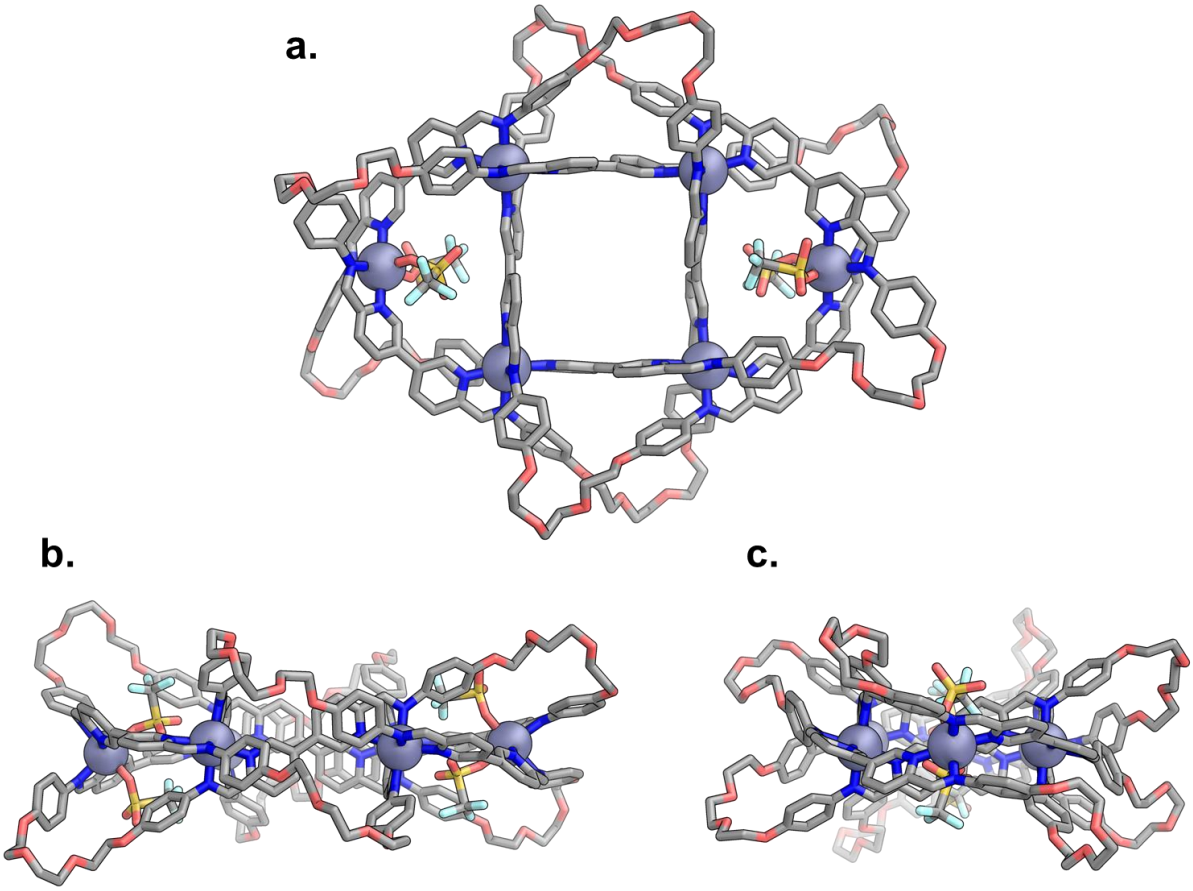

Figure 5.16 | a. Crystal structure of **5.12** which is revealed to be a 8_{19} knot. **b.** Side-on view of the knot, showing the slight distortion away from planarity of the Zn^{II} centres. **c.** Side-on view of the knot, focusing on the triflate coordinated metal centre of **5.12**.

Thirdly, unlike in the Fe^{II} knot, there was no significant variation in the distances between the Zn^{II} centres and their N donors throughout the knot. In the case of the core Zn^{II} centres, an average distance of 2.18 ± 0.03 Å was measured between the cations and their imine donors and 2.16 ± 0.02 Å between the cations and their pyridyl donors. For the peripheral centres, Zn^{II}

to imine distances of 2.20 ± 0.02 Å and Zn^{II} to pyridyl donor distances of 2.07 ± 0.01 Å were measured.

Each of these slight variations in the structure may shed light on why the knot is more readily synthesised with certain metal salts. Changes in the ionic radius of the metal centre can lead to significant variation in the ligands' preferred conformation, rendering some knots stable and others unstable. It should be noted that these variations may be entirely due to differences in crystal packing effects.

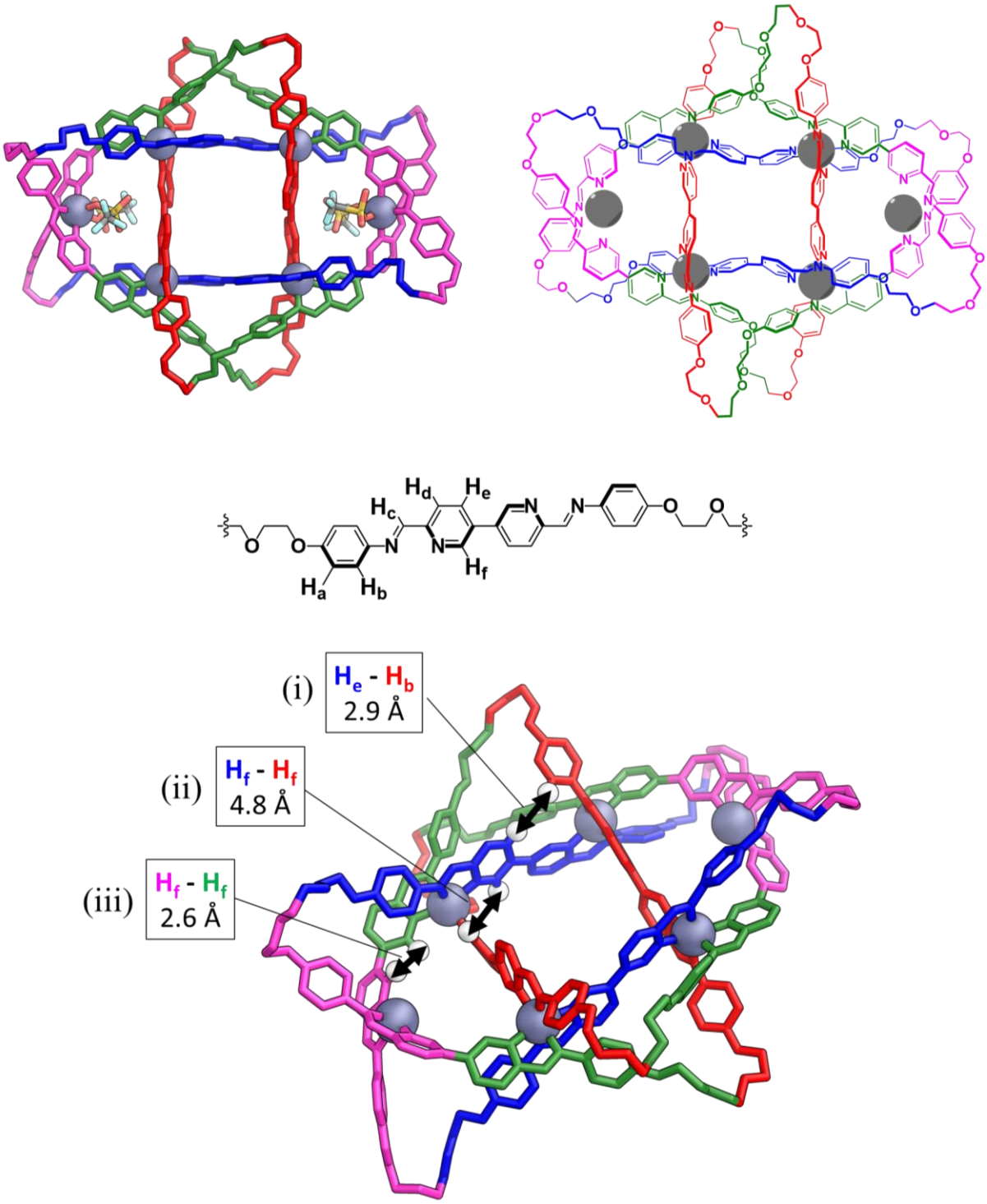

Figure 5.17 | The four chemically distinct ligand environments of **5.12** distinguished by colour-coding. Each of the four regions have six resonances in the aromatic region of the ^{1}H NMR spectrum, giving 24 resonances in total. Average distances between certain protons, which proved key to the complete assignment of **5.12** using NOE correlations, are highlighted. These important protons are shown as white spheres.

In order to fully assign the ^{1}H NMR spectrum, several important features of the solid-state structure were noted. The first was that each of the core Zn^{II} centres adopts a *mer* configuration. This results in each of the three coordinating ligands adopting a chemically distinct environment. Secondly, each of the ligands coordinating to the peripheral, triflate-coordinated Zn^{II} centres are desymmetrised along their length. These two factors alone explain the four-fold desymmetrisation observed in the ^{1}H NMR spectrum.

Another noteworthy feature of the knot's structure is that the different ligands comprising the structure adopt distinct conformations. In the red and blue shaded ligands in Figure 5.17, which form the central core of the knot, an *anti*- conformation is observed, whereby the two pyridyl rings defined a torsion angle of approximately 155° relative to one another. In contrast, the single ligand shaded in green and pink, which spans between the core metal centres and the peripheral metal centres adopts a *syn*- conformation with a torsion angle of approximately 50°. These two different configurations would be expected to produce different NOE correlations, particularly for the protons labelled H_f and H_e, which proves important in the assignment (green and blue NOE correlations in Figure 5.18).

Fourth and finally, it was noted that of the protons labelled H_f, only one (ligand shaded in blue in Figure 5.17) was spatially separated from the other distinct H_f protons. The H_f proton of the ligand shaded in blue (the proton is shaded in white to distinguish it from the carbon atoms) is particularly isolated from other H_f protons, the closest is shaded in red and they are separated by a distance of 4.84 ± 0.09 Å, as measured from the crystal structure. This is outside the range in which one would expect to see strong NOE correlations. It compares to values of 3.7 ± 0.1 Å and 2.6 ± 0.2 Å for red-to-green and green-to-pink, respectively.

This difference in distances is reflected in the ^{1}H-^{1}H NOESY with an absence of any strong NOE correlation to other H_f resonances for blue, unlike in the other cases. However, the absence of an NOE correlation is not definitive evidence, and so therefore it was also noted that the proton labelled H_e on the same aromatic ring as the isolated H_f (again, shaded in blue in Figure 5.17) is the only such proton in close proximity to a H_b proton (ligand shaded in red in Figure 5.17), with a separation of 2.9 ± 0.2 Å (red NOE correlation in Figure 5.18). These pieces of evidence allow us to confidently assign these proton resonances, which acts as the starting point for the complete assignment of **5.12**.

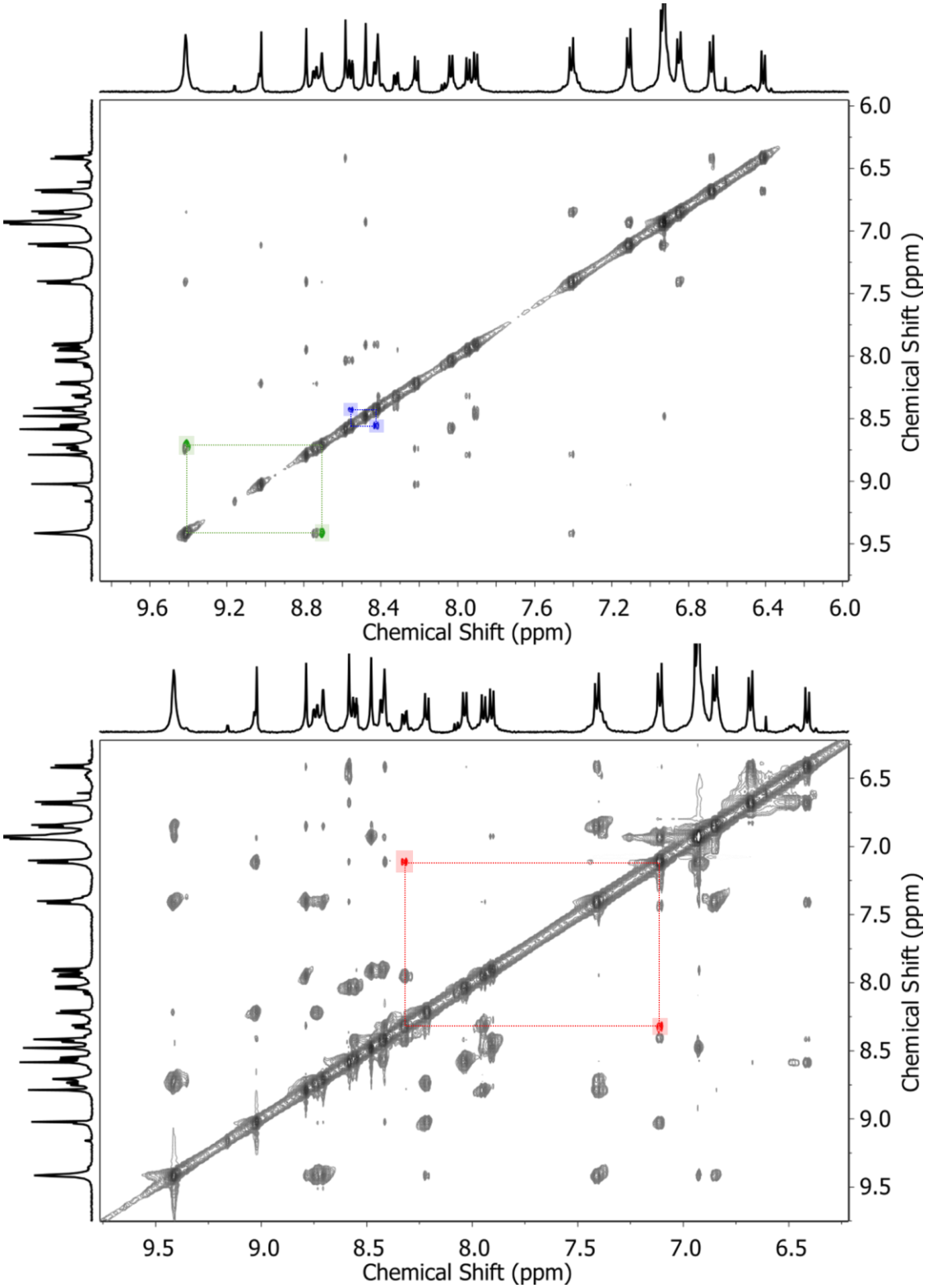

Figure 5.18 | ^{1}H-^{1}H NOESY of **5.12**. The second spectrum is zoomed in by a factor of 2 to allow resolution of weaker NOE correlations. The green cross-peak corresponds to the two proximal H_f protons in the ligand shaded in green and pink (marked (iii) in Figure 5.17). The blue cross-peak corresponds to the proximal H_e protons on the same ligand. The red cross-peak corresponds to the proximal H_e and H_b protons (marked (i) in Figure 5.17).

It was then possible to fully assign each of the 24 proton environments in the knotted structure by following a series of correlations in both the ^{1}H-^{1}H COSY and ^{1}H-^{1}H NOESY spectra. This assignment is consistent with each of the phenylene residues being in rapid rotation on the NMR timescale, as are the ^{1}H NMR resonances integrals.

Given the high-spin character of Fe^{II} knot **5.11** and the resulting paramagnetic shifting and line-broadening observed, the full NMR characterisation of Zn^{II} knot **5.12** provides solid evidence that the knot exists in solution. The use of a molecular knot which exhibits net diamagnetism also allows for greater insight into this supramolecular system and will prove useful for probing the chirality of other related knots, as described in Chapter 6 of this thesis.

5.8 Conclusions

This Chapter has detailed the formation of two 8_{19} molecular knots, one templated by Fe^{II}, the other by Zn^{II}. This new architecture is geometrically distinct from, but topologically equivalent to, the 8_{19} molecular knot described by Leigh and coworkers.

When it comes to the design of functionalised knotted molecules and materials, this new way of synthesising a desymmetrised knot may prove useful. In the assembly of **5.11** and **5.12**, only one type of dianiline was utilised, one which can bridge both of the connections required. However, one can readily imagine two different dianilines, one of which can form a particular bridge but not the other, to achieve the selective functionalisation of the knot at particular points but not others. This could be used to precisely control properties of the knot such as its tightness.[25] Alternatively, one could consider attaching two different moieties at these different points.

Given the current interest in the use of catenanes and molecular knots for the control of material properties,[26] such control over regio-chemistry which is not possible with more symmetric knots may be of further interest.

5.9 Experimental Section

*Synthesis of **5.11***

6,6´-diformyl-3,3´-bipyridine **5.8** (71.0 mg, 334 µmol, 8 equiv.),[27] 4,4'-(((ethane-1,2-diylbis(oxy))bis(ethane-2,1-diyl))bis(oxy))dianiline **5.10** (111.3 mg, 334 µmol, 8 equiv.) and $Fe(OTf)_2$ (89 mg, 250 µmol, 6 equiv.) were added to a Schlenk flask in a glovebox. Degassed and dried CH_3CN (40 mL) was added along with a Teflon-coated magnetic stir-bar. The sealed Schlenk flask was removed from the glovebox and left to stir at 80 °C for 54 hours. The dark green reaction mixture was allowed to cool to room temperature and was then filtered through a glass fibre filter (0. 7 µm pore size). The acetonitrile was concentrated under a stream of N_2 to a volume of 10 mL. Addition of diisopropyl ether (20 mL) resulted in the precipitation of a dark green solid. The suspension was then centrifuged (10 min, 3000 RPM) and the eluent decanted. Further diisopropyl ether (10 mL) was added, the powder was resuspended by sonication and then centrifuged. Again, the eluent was decanted. The residue was then dried *in vacuo* to afford the solid product as a fine dark green powder (137 mg, 52%).

^{1}H NMR (500 MHz, 298 K, CD_3CN) δ: 177.5, 159.8, 49.0, 15.4, 14.7, 14.5, 11.1, 10.3, 9.6, 9.4, 9.1, 8.8, 8.7, 8.2, 7.7, 7.5, 7.3, 7.0, 6.8, 6.8, 6.3, 6.0, 5.8, 4.7, 4.3, 4.1, 4.0, 3.7, 3.6, 3.4, 2.9, 2.5, 1.3, -5.5. Accurate peak peaking was not possible due to significant signal broadening and overlap.

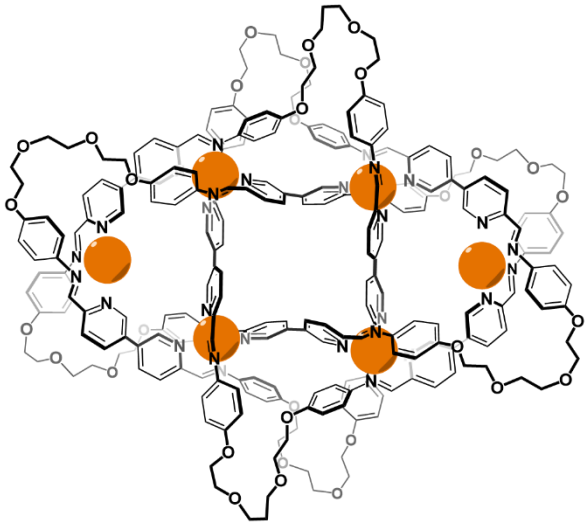

HRMS (ESI-LTQ Orbitrap XL, CH_3CN) m/z found 1398.9807, calculated for 1398.9801 for the +4 charged species.

*Synthesis of **5.12***

The synthesis of the Zn^{II} templated knot proved considerably more challenging than that of the Fe^{II} based knot. The purity of the $Zn(OTf)_2$ source and the concentration of the reaction mixture were found to be important. Furthermore, scaling up the reaction led to a significant reduction in yield. This type of behaviour is not unprecedented for the dialdehyde subcomponent **5.8** in particular, and may be a result of its ability to form a wide variety of structures, as will be described more fully in Chapter 7 of this thesis. Further to this, the reaction of dialdehyde and dianiline subcomponents may be leading to the formation of insoluble oligomers and polymers, a challenge which is not typically encountered in the synthesis of cages using a subcomponent self-assembly approach. Notwithstanding, a reliable synthesis of the Zn^{II} knot is described.

6,6´-diformyl-3,3´-bipyridine **5.8** (3.56 mg, 16.8 μmol, 8 equiv.), 4,4'-(((ethane-1,2-diylbis(oxy))bis(ethane-2,1-diyl))bis(oxy))dianiline **5.10** (5.60 mg, 16.8 μmol, 8 equiv.) and $Zn(OTf)_2$ (4.44 mg, 12.2 μmol, 6 equiv.) were added to a small Schlenk flask (total volume 4 mL). CH_3CN (1 mL) was added along with a Teflon-coated magnetic stir-bar. The sealed Schlenk flask was sonicated for 10 minutes at 70 °C and left to stir at 90 °C for 18 hours. The light yellow reaction mixture was allowed to cool to room temperature and was then filtered through a glass fibre filter (0. 7 μm pore size). Addition of diisopropyl ether (2 mL) resulted in the precipitation of a yellow solid. The suspension was then centrifuged (10 min, 3000 RPM), the eluent decanted. Further diisopropyl ether (2 mL) was added, the powder was resuspended by sonication and then centrifuged. Again, the eluent was decanted. The residue was then dried *in vacuo* to afford the solid product as a light yellow powder (9.9 mg, 72%).

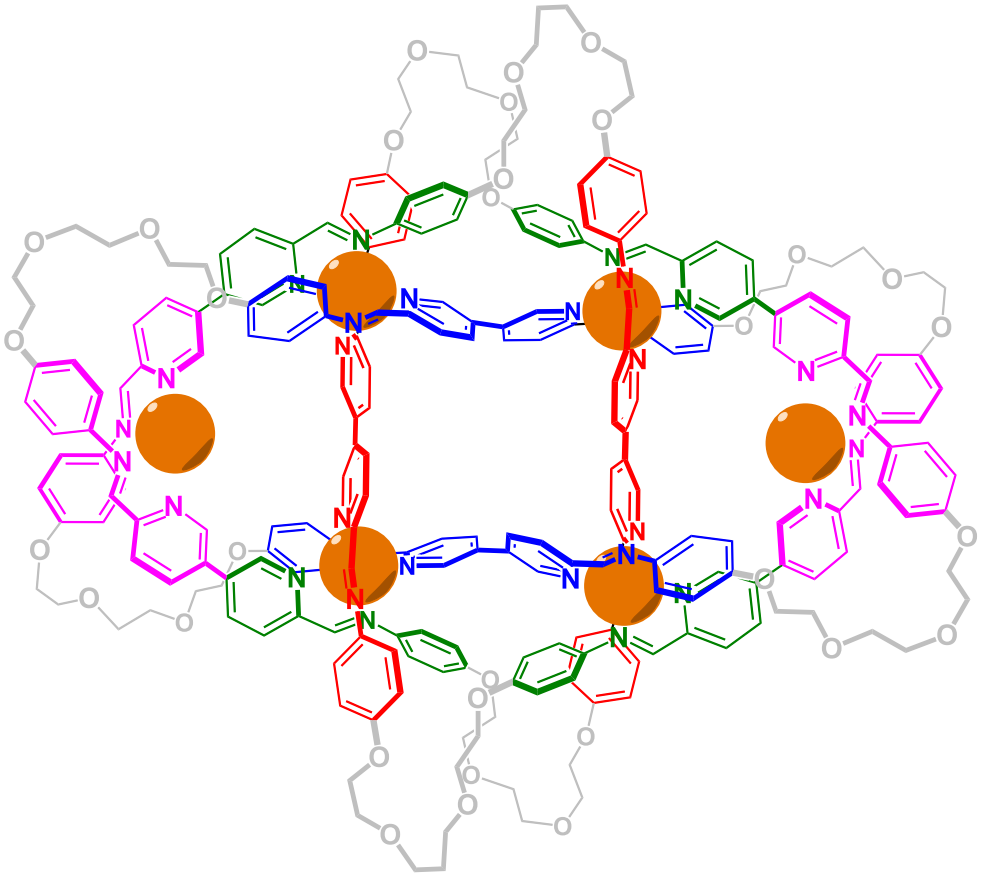

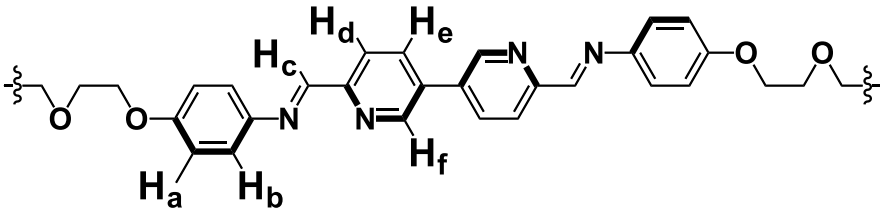

^{1}H NMR (500 MHz, 298 K, CD_3CN) δ: 9.42 (H_f, s, 4H), 9.41 (H_f, s, 4H), 9.02 (H_c, s, 1H), 8.79 (H_c, s, 1H), 8.74 (H_e, dd, J = 8.4, 2.2 Hz, 1H), 8.71 (H_f, d, J = 2.1 Hz, 4H), 8.58 (H_c, s, 1H), 8.56 (H_e, dd, J = 8.0, 2.0 Hz, 1H), 8.48 (H_c, s, 1H), 8.43 (H_e, dd, J = 8.0, 2.3 Hz, 1H), 8.42 (H_f, s, 4H), 8.32 (H_e, dd, J = 8.4, 2.4 Hz, 1H), 8.22 (H_d, d, J = 8.3 Hz, 1H), 8.04 (H_d, d, J = 7.9 Hz, 1H), 7.95 (H_d, d, J = 8.3 Hz, 1H), 7.91 (H_d, d, J = 8.0 Hz, 1H), 7.41 (H_b, d, J = 8.7 Hz, 1H), 7.11 (H_b, d, J = 8.9 Hz, 2H), 6.94 (H_b, d, 2H, overlapped), 6.93 (H_a, d, 2H, overlapped), 6.93 (H_a, d, 2H, overlapped), 6.85 (H_a, d, J = 8.8 Hz, 1H), 6.68 (H_a, d, J = 8.9 Hz, 1H), 6.41 (H_b, d, J = 8.8 Hz, 1H)

^{13}C NMR (125 MHz, 298 K, CD_3CN) δ: 164.9 (imine), 162.0 (imine), 161.2 (pyridine), 161.1 (imine), 160.5 (pyridine), 160.3 (pyridine), 160.1 (pyridine), 157.3 (imine), 153.6 (excess L_1), 150.4 (pyridine with proton H_f), 150.0 (pyridine), 149.3 (pyridine), 149.3 (pyridine), 147.9

(pyridine), 147.9 (pyridine), 147.6 (pyridine), 147.4 (pyridine), 146.8 (pyridine), 142.6 (pyridine), 141.9 (pyridine) , 141.9 (pyridine) , 141.1 (excess L_1), 140.4 (pyridine), 139.7 (pyridine), 139.4 (pyridine), 139.2 (pyridine), 138.9 (pyridine), 137.4 (pyridine), 137.3 (pyridine), 137.2 (pyridine), 136.7 (pyridine), 135.6 (pyridine), 131.2 (pyridine), 130.9 (pyridine), 130.9 (pyridine), 128.9 (pyridine), 125.7 (aniline), 124.5 (aniline), 124.0 (aniline), 123.7 (aniline), 122.6 (excess L_1), 118.2 (aniline) , 116.6 (aniline), 116.1 (aniline), 115.8 (aniline), 73.3 (ethylene glycol), 72.0 (ethylene glycol), 71.4 (ethylene glycol), 71.3 (ethylene glycol), 71.2 (ethylene glycol), 71.0 (ethylene glycol), 70.3 (ethylene glycol), 70.1 (ethylene glycol), 70.1 (ethylene glycol), 69.9 (ethylene glycol), 69.5 (ethylene glycol), 69.2 (ethylene glycol), 68.8 (ethylene glycol), 68.8 (ethylene glycol), 68.7 (ethylene glycol), 62.0 (ethylene glycol)

HRMS (ESI-LTQ Orbitrap XL, CH_3CN) m/z found 1100.7842, calculated for 1100.7845 for the +5 charged species.

5.10 Crystallography

Data were collected at Beamline I19 of Diamond Light Source employing silicon double crystal monochromated synchrotron radiation (0.6889 Å) with ω and ψ scans at 100(2) K.[28] Date was solved and refined by Dr Tanya Ronson. Data integration and reduction were undertaken with Xia2.[29-31] Subsequent computations were carried out using the WinGX-32 graphical user interface.[29] Multi-scan empirical absorption corrections were applied to the data using the AIMLESS[32] tool in the CCP4 suite.[31] The structure was solved by dual space methods using SHELXT[32] then refined and extended with SHELXL.[33] In general, non-hydrogen atoms with occupancies greater than 0.5 were refined anisotropically. Carbon-bound hydrogen atoms were included in idealised positions and refined using a riding model. Disorder was modelled using standard crystallographic methods including constraints, restraints and rigid bodies where necessary. Crystallographic data along with specific details pertaining to the refinement follow.

$[Fe_6L_8(OTf)_4]\cdot 8OTf\cdot CH_3CN$ [+ solvent]

Formula $C_{254}H_{227}F_{36}Fe_6N_{33}O_{68}S_{12}$, *M* 6233.49, Monoclinic, space group C 2/c (#15), *a* 46.0522(5), *b* 23.5033(2), *c* 28.5496(4) Å, β 94.9020(10), *V* 30788.4(6) $Å^3$, D_c 1.345 g cm^{-3}, *Z* 4, crystal size 0.070 by 0.070 by 0.020 mm, colour dark green, habit block, temperature 100(2) Kelvin, λ(Synchrotron) 0.6889 Å, μ(Synchrotron) 0.416 mm^{-1}, $T(\text{Analytical})_{min,max}$ 0.983761759095, 1.0, $2\theta_{max}$ 38.30, *hkl* range -43 43, -21 22, -26 27, *N* 43946, N_{ind} 13870(R_{merge} 0.0489), N_{obs} 7811(I > 2σ(I)), N_{var} 1828, residuals* *R*1(*F*) 0.1070, *wR*2(F^2) 0.3394, GoF(all) 1.199, $\Delta\rho_{min,max}$ -0.388, 0.596 e^- $Å^{-3}$.

*$R1 = \Sigma||F_o| - |F_c||/\Sigma|F_o|$ for $F_o > 2\sigma(F_o)$; $wR2 = (\Sigma w(F_o^2 - F_c^2)^2/\Sigma(wF_c^2)^2)^{1/2}$ all reflections

$w=1/[\sigma^2(F_o^2)+(0.2000P)^2]$ where $P=(F_o^2+2F_c^2)/3$

Specific refinement details:

Crystals of $[Fe_6L_8(OTf)_4]\cdot 8OTf\cdot CH_3CN$ [+ solvent] were grown by vapour diffusion of diisopropyl ether into an acetonitrile solution of an acetonitrile solution of the complex. The

crystals were small and weakly diffracting, immediately losing solvent after removal from the mother liquor. Rapid handling prior to flash cooling in the cryostream was required to collect data. Despite these measures and the use of synchrotron radiation few reflections at greater than 1.05 Å resolution were observed and the data were trimmed accordingly. Nevertheless, the quality of the data is far more than sufficient to establish the connectivity of the structure. The asymmetric unit was found to contain one half of a $Fe_6L_8(OTf)_4$ assembly and associated counterions and solvent molecules.

There is a significant amount of thermal motion in the structure and extensive thermal parameter and bond length restraints were required to facilitate realistic modelling for the organic parts of the structure. Bond lengths and angles within pairs of ligands in the rigid central core of the complex were restrained to be similar to each other and thermal parameter restraints (SIMU, RIGU) were applied to all atoms except for iron. In order to obtain a reasonable model for the flexible ethylene glycol chains the GRADE program[34] was employed using the GRADE Web Server[35] to generate a full set of bond distance and angle restraints (DFIX, DANG, FLAT) for these residues (including the attached aniline rings). One of the ethylene glycol chains was modelled as disordered over two locations and modelled with isotropic thermal parameters. The other ethylene glycol chains show evidence of substantial thermal motion or dynamic disorder which could not be adequately modelled with discrete atom positions. Consequently, the thermal parameters of these groups are larger than ideal, resulting in a large average Ueq value.

The anions within the structure show evidence of disorder. One triflate anion was modelled as disordered over two locations and another one was modelled with partial occupancy. The occupancies of the disordered anions were allowed to refine freely and then fixed at the obtained values. Some lower occupancy disordered atoms were modelled with isotropic thermal parameters and bond length restraints were applied to facilitate realistic modelling of the disordered triflate anions. A further triflate anion located in the centre of the complex was modelled as end for end disordered over a special position using a rigid group.

Further reflecting the solvent loss and poor diffraction properties there is a significant amount of void volume in the lattice containing smeared electron density from disordered solvent and 4 unresolved anions per Fe_6L_8 complex (assigned to triflate in the formula). Consequently the SQUEEZE[36] function of PLATON[37] was employed to remove the contribution of the electron density associated with this remaining anion and further highly disordered solvent, which gave

a potential solvent accessible void of 6460 $Å^3$ per unit cell (a total of approximately 2228 electrons). Since the diffuse solvent molecules could not be assigned to acetonitrile or diethyl ether they were not included in the formula. Consequently, the molecular weight and density given above are likely to be underestimated.

CheckCIF gives 3 A and 9 B level alerts. These alerts (both A and B level) result from the poor diffraction properties (low resolution, low bond precision, poor data / parameter ratio) and thermal motion and/or unresolved disorder of the ethylene glycol and some anions and solvent molecules (large average Ueqs, short contacts, isotropic refinement).

$[Zn_6L_8(OTf)_{3.5}(H_2O)_{0.5}]\cdot 8.5OTf\cdot 2.75CH_3CN\cdot 0.5H_2O$ [+ solvent]

Formula $C_{257.50}H_{234.25}F_{36}N_{34.75}O_{69}S_{12}Zn_6$, *M* 6380.47, Triclinic, space group P -1 (#2), *a* 13.5874(2), *b* 27.2027(2), *c* 45.8537(3) Å, α 98.9770(10), β 94.5960(10), γ 103.4220(10)°, *V* 16163.5(3) $Å^3$, D_c 1.311 g cm^{-3}, *Z* 2, crystal size 0.080 by 0.070 by 0.070 mm, colour Yellow, habit Block, temperature 100(2) Kelvin, λ(Synchrotron) 0.6889 Å, μ(Synchrotron) 0.560 mm^{-1}, *T*(Analytical)$_{min,max}$ 0.984979868456, 1.0, $2\theta_{max}$ 45.00, *hkl* range -15 15, -28 30, -50 50, *N* 137987, N_{ind} 45600(R_{merge} 0.0455), N_{obs} 21395($I > 2\sigma(I)$), N_{var} 3655, residuals* *R*1(*F*) 0. 1253, *wR*2(F^2) *wR*2(F^2) 0.3987, GoF(all) 1.287, $\Delta\rho_{min,max}$ -0.498, 0.897 $e^- Å^{-3}$.

*$R1 = \Sigma||F_o| - |F_c||/\Sigma|F_o|$ for $F_o > 2\sigma(F_o)$; $wR2 = (\Sigma w(F_o^2 - F_c^2)^2/\Sigma(wF_c^2)^2)^{1/2}$ all reflections

$w=1/[\sigma^2(F_o^2)+(0.2000P)^2]$ where $P=(F_o^2+2F_c^2)/3$

Specific refinement details:

Crystals of $[Zn_6L_8(OTf)_{3.5}(H_2O)_{0.5}]\cdot 8.5OTf\cdot 2.75CH_3CN\cdot 0.5H_2O$ [+ solvent] were grown by vapour diffusion of diisopropyl ether into an acetonitrile solution of the complex. The crystals were small and weakly diffracting, immediately losing solvent after removal from the mother liquor. Rapid handling prior to flash cooling in the cryostream was required to collect data.

Despite these measures and the use of synchrotron radiation few reflections at greater than 0.9 Å resolution were observed and the data were trimmed accordingly. Nevertheless, the quality of the data is far more than sufficient to establish the connectivity of the structure. The asymmetric unit was found to contain one complete Zn_6L_8 assembly and associated counterions and solvent molecules.

There is a significant amount of thermal motion in the structure and extensive thermal parameter and bond length restraints were required to facilitate realistic modelling for the organic parts of the structure. Bond lengths and angles within pairs of ligands in the rigid central core of the complex were restrained to be similar to each other and thermal parameter restraints (SIMU, RIGU) were applied to all atoms except for zinc. Similarly to the structure of $[Fe_6L_8(OTf)_4]\cdot 8OTf\cdot CH_3CN$, the GRADE Web Server[35] was employed to generate a full set of bond distance and angle restraints (DFIX, DANG, FLAT) for the flexible ethylene glycol chains (including the attached aniline rings). Three of the ethylene glycol chains were modelled as disordered over two locations and were modelled with isotropic thermal parameters. The other ethylene glycol chains show evidence of substantial thermal motion or dynamic disorder which could not be adequately modelled with discrete atom positions. Consequently, the thermal parameters of these groups are larger than ideal, resulting in some large Ueq values.

The anions within the structure show evidence of disorder. One of the coordinated triflate anions was modelled as disordered over two locations. Another coordination site was modelled as a disordered mixture of triflate and water (each with 50% occupancy). Four of the uncoordinated triflate anions were also modelled as disordered over two or three locations and the remaining located anion was modelled with partial occupancy. The occupancies of the disordered anions were allowed to refine freely and then fixed at the obtained values. Some lower occupancy disordered atoms were modelled with isotropic thermal parameters and bond length restraints were applied to facilitate realistic modelling of the disordered triflate anions. The acetonitrile solvent molecules were also modelled as disordered over multiple locations and/or with partial occupancy. The hydrogen atoms of the disordered acetonitrile molecules and the water molecules could not be located in the electron density map and were not included in the model.

Further reflecting the solvent loss and poor diffraction properties there is a significant amount of void volume in the lattice containing smeared electron density from disordered solvent and

5.05 unresolved anions per Zn_6L_8 complex (assigned to triflate in the formula). Consequently the SQUEEZE[36] function of PLATON[37] was employed to remove the contribution of the electron density associated with these highly disordered solvents and anions, which gave a potential solvent accessible void of 3338 $Å^3$ per unit cell (a total of approximately 1014 electrons). Since the diffuse solvent molecules could not be assigned to acetonitrile or diethyl ether they were not included in the formula. Consequently, the molecular weight and density given above are likely to be underestimated.

CheckCIF gives 2 A and 16 B level alerts. These alerts (both A and B level) result from the poor diffraction properties (low resolution, low bond precision, high wR2 value), thermal motion and/or unresolved disorder of the ethylene glycol chains (large Ueqs, short contacts, isotropic refinement) and acetonitrile molecules for which hydrogens were not modelled (singly bonded carbons).

5.10 References

(1) Thomson, W. 4. On Vortex Atoms. *Proc. R. Soc. Edinburgh* **1869**, 6, 94–105..

(2) Frisch, H. L.; Wasserman, E. Chemical Topology 1. *J. Am. Chem. Soc*. **1961**, *83*, 3789–3795.

(3) Schill, G.; Lüttringhaus, A. The Preparation of Catena Compounds by Directed Synthesis. *Angew. Chem. Int. Ed. English* **1964**, *3*, 546–547.

(4) Cesario, M.; Dietrich-Buchecker, C. O.; Guilhem, J.; Pascard, C.; Sauvage, J. P. Molecular Structure of a Catenand and Its Copper(I) Catenate: Complete Rearrangement of the Interlocked Macrocyclic Ligands by Complexation. *J. Chem. Soc. Chem. Commun*. **1985**, *5*, 244.

(5) Dietrich-Buchecker, C. O.; Sauvage, J. -P. A Synthetic Molecular Trefoil Knot. *Angew. Chee Int. Ed. English* **1989**, *28*, 189–192.

(6) Fielden, S. D. P.; Leigh, D. A.; Woltering, S. L. Molecular Knots. *Angew. Chem. Int. Ed.* **2017**, *56* , 11166–11194.

(7) Ashton, P. R.; Matthews, O. A.; Menzer, S.; Raymo, F. M.; Spencer, N.; Stoddart, J. F.; Williams, D. J. A Template-Directed Synthesis of a Molecular Trefoil Knot. Liebigs Ann. **1997**, *12*, 2485–2494.

(8) Carver, F. J.; Hunter, C. A.; Shannon, R. J. Directed Macrocyclisation Reactions. J. Chem. Soc. *Chem. Commun*. **1994**, *10*, 1277.

(9) Safarowsky, O.; Nieger, M.; Fröhlich, R.; Vögtle, F. A Molecular Knot with Twelve Amide Groups—One-Step Synthesis, Crystal Structure, Chirality. *Angew. Chem. Int. Ed.* **2000**, *39*, 1616–1618.

(10) Feigel, M.; Ladberg, R.; Engels, S.; Herbst-Irmer, R.; Fröhlich, R. A Trefoil Knot Made of Amino Acids and Steroids. *Angew. Chem. Int. Ed*. **2006**, *45*, 5698–5702.

(11) Ponnuswamy, N.; Cougnon, F. B. L.; Clough, J. M.; Pantoş, G. D.; Sanders, J. K. M. Discovery of an Organic Trefoil Knot. *Science* **2012**, *338*, 783–785.

(12) Nierengarten, J. F.; Dietrich-Buchecker, C. O.; Sauvage, J. P. Synthesis of a Doubly

Interlocked [2]-Catenane. *J. Am. Chem. Soc*. **1994**, *116*, 375–376.

(13) Dietrich-Buchecker, C.; Colasson, B.; Jouvenot, D.; Sauvage, J.-P. Synthesis of Multi-1,10-Phenanthroline Ligands with 1,3-Phenylene Linkers and Their Lithium Complexes. *Chem. - A Eur. J*. **2005**, *11*, 4374–4386.

(14) Hasenknopf, B.; Lehn, J.-M.; Boumediene, N.; Dupont-Gervais, A.; Van Dorsselaer, A.; Kneisel, B.; Fenske. D. Self-Assembly of Tetra- and Hexanuclear Circular Helicates *J. Am. Chem. Soc*. **1997**, *119*, 10956-10962.

(15) Hasenknopf, B.; Lehn, J.-M.; Boumediene, N.; Leize, E.; Van Dorsselaer, A. Kinetic and Thermodynamic Control in Self-Assembly: Sequential Formation of Linear and Circular Helicates. *Angew. Chem. Int. Ed*. **1998**, *37*, 3265–3268.

(16) Ayme, J.-F.; Beves, J. E.; Leigh, D. A.; McBurney, R. T.; Rissanen, K.; Schultz, D. A Synthetic Molecular Pentafoil Knot. *Nat. Chem*. **2012**, *4*, 15–20.

(17) Leigh, D. A.; Pritchard, R. G.; Stephens, A. J. A Star of David Catenane. *Nat. Chem*. 2014, *6*, 978–982.

(18) Beves, J. E.; Campbell, C. J.; Leigh, D. A.; Pritchard, R. G. Tetrameric Cyclic Double Helicates as a Scaffold for a Molecular Solomon Link. *Angew. Chem. Int. Ed*. **2013**, *52*, 6464–6467.

(19) Danon, J. J.; Krüger, A.; Leigh, D. A.; Lemonnier, J. F.; Stephens, A. J.; Vitorica-Yrezabal, I. J.; Woltering, S. L. Braiding a Molecular Knot with Eight Crossings. *Science* **2017**, *355*, 159-162.

(20) Zhang, L.; August, D. P.; Zhong, J.; Whitehead, G. F. S.; Vitorica-Yrezabal, I. J.; Leigh, D. A. Molecular Trefoil Knot from a Trimeric Circular Helicate. *J. Am. Chem. Soc*. **2018**, *140*, 4982–4985.

(21) Zhang, L.; Stephens, A. J.; Nussbaumer, A. L.; Lemonnier, J.-F.; Jurček, P.; Vitorica-Yrezabal, I. J.; Leigh, D. A. Stereoselective Synthesis of a Composite Knot with Nine Crossings. *Nat. Chem*. **2018**, *10*, 1083–1088.

(22) Riddell, I. A.; Smulders, M. M. J.; Clegg, J. K.; Hristova, Y. R.; Breiner, B.; Thoburn, J. D.; Nitschke, J. R. Anion-Induced Reconstitution of a Self-Assembling System to Express a Chloride-Binding $Co_{10}L_{15}$ Pentagonal Prism. *Nat. Chem*. **2012**, *4*, 751–756.

(23) Riddell, I. A.; Hristova, Y. R.; Clegg, J. K.; Wood, C. S.; Breiner, B.; Nitschke, J. R. Five Discrete Multinuclear Metal-Organic Assemblies from One Ligand: Deciphering the Effects of Different Templates. *J. Am. Chem. Soc*. **2013**, *135*, 2723–2733.

(24) Wood, C. S.; Ronson, T. K.; Belenguer, A. M.; Holstein, J. J.; Nitschke, J. R. Two-Stage Directed Self-Assembly of a Cyclic [3]Catenane. *Nat. Chem*. **2015**, *7*, 354–358.

(25) Zhang, L.; Lemonnier, J.-F.; Acocella, A.; Calvaresi, M.; Zerbetto, F.; Leigh, D. A. Effects of Knot Tightness at the Molecular Level. *Proc. Natl. Acad. Sci. U. S. A*. **2019**, *116*, 2452–2457.

(26) Zhang, M.; De Bo, G. Impact of a Mechanical Bond on the Activation of a Mechanophore. J. Am. Chem. Soc. **2018**, *140*, 12724–12727.

(27) Pilgrim, B. S.; Roberts, D. A.; Lohr, T. G.; Ronson, T. K.; Nitschke, J. R. Signal Transduction in a Covalent Post-Assembly Modification Cascade. *Nat. Chem*. **2017**, *9*, 1276–1281.

(28) Winter, G. xia2: an expert system for macromolecular crystallography data reduction. J. Appl. Crystallogr. **2010**, *43*, 186-190.

(29) Farrugia, L. WinGX and ORTEP for Windows: an update. *J. Appl. Crystallogr*. **2012**, *45*, 849-854.

(30) Evans, P. R.; Murshudov, G. N. How good are my data and what is the resolution? *Acta Crystallogr., Sect. D* **2013**, *69*, 1204-1214.

(31) Winn, M. D.; Ballard, C. C.; Cowtan, K. D.; Dodson, E. J.; Emsley, P.; Evans, P. R.; Keegan, R. M.; Krissinel, E. B.; Leslie, A. G. W.; McCoy, A.; McNicholas, S. J.; Murshudov, G. N.; Pannu, N. S.; Potterton, E. A.; Powell, H. R.; Read, R. J.; Vagin, A.; Wilson, K. S. Overview of the CCP4 suite and current developments. *Acta Crystallogr., Sect. D* **2011**, *67*, 235-242.

(32) Sheldrick, G. SHELXT - Integrated space-group and crystal-structure determination. *Acta. Cryst.* 2015, *71*, 3-8.

(33) Sheldrick, G. M. Crystal structure refinement with SHELXL. *Acta. Cryst.* **2015**, *71*, 3-8.

(34) Bricogne, G.; Blanc, E.; Brandle, M.; Flensburg, C.; Keller, P.; Paciorek, W.; Roversi, P.; Sharff, A.; Smart, O. S.; Vonrhein, C.; Womack, T. O.: BUSTER; 2.11.2 ed.; Global Phasing Ltd.: Cambridge, United Kingdom, **2011**.

(35) Smart, O. S.; Womack, T. O.: Grade Web Server; Global Phasing Ltd., **2014**.

(36) van der Sluis, P.; Spek, A. L. BYPASS: an effective method for the refinement of crystal structures containing disordered solvent regions. *Acta Cryst*. **1990**, *46*, 194-201.

(37) Spek, A. L.: PLATON: A Multipurpose Crystallographic Tool; Utrecht University: Utrecht, The Netherlands, **2008**.

6

Topological Chirality in a Knotted Molecule

This Chapter provides a brief overview of the different strategies developed for the diastereo- or enantio-selective synthesis of chiral interlocked and knotted molecules. Details on how topologically chiral knotted molecules have been separated by chiral stationary phase high performance liquid chromatography (HPLC) are discussed. Diastereoselective synthesis of knots is also detailed. Finally, the strategies developed by the Goldup group to synthesise enantiopure rotaxanes and catenanes where the only stereogenic unit is the mechanical bond are discussed.

The Chapter then reports on the synthesis of a new 8_{19} molecular knot which is assembled from a dianiline subcomponent which incorporates covalent stereogenic units. The structure forms in a diastereoselective manner, with one handedness of the dianiline favouring one handedness of the knot.

Ongoing efforts to displace this chiral dianiline with an achiral one, while maintaining the topological handedness of the knot, is detailed. To date, we have succeeded in displacing the chiral dianiline, however, the resulting knot appears to have racemised in the process. Directions being pursued to overcome this challenge are also discussed.

6.1 Topological Chirality

Chirality is one of the most important concepts in chemistry. In 1848, Louis Pasteur deduced that the rotation of plane polarised light by certain substances has a molecular basis. This was first observed by Biot in 1815. From this point forth, chemists have been interested in finding new ways in which chirality can manifest itself in a chemical system. The list now extends to those based on point, planar, axial and helical chirality. More recently, a further noteworthy example has been added to the list, chiral mechanically interlocked molecules.[1,2] In these examples, described in more detail later in the Chapter, the only stereogenic unit is the mechanical bond of the rotaxane or catenane.

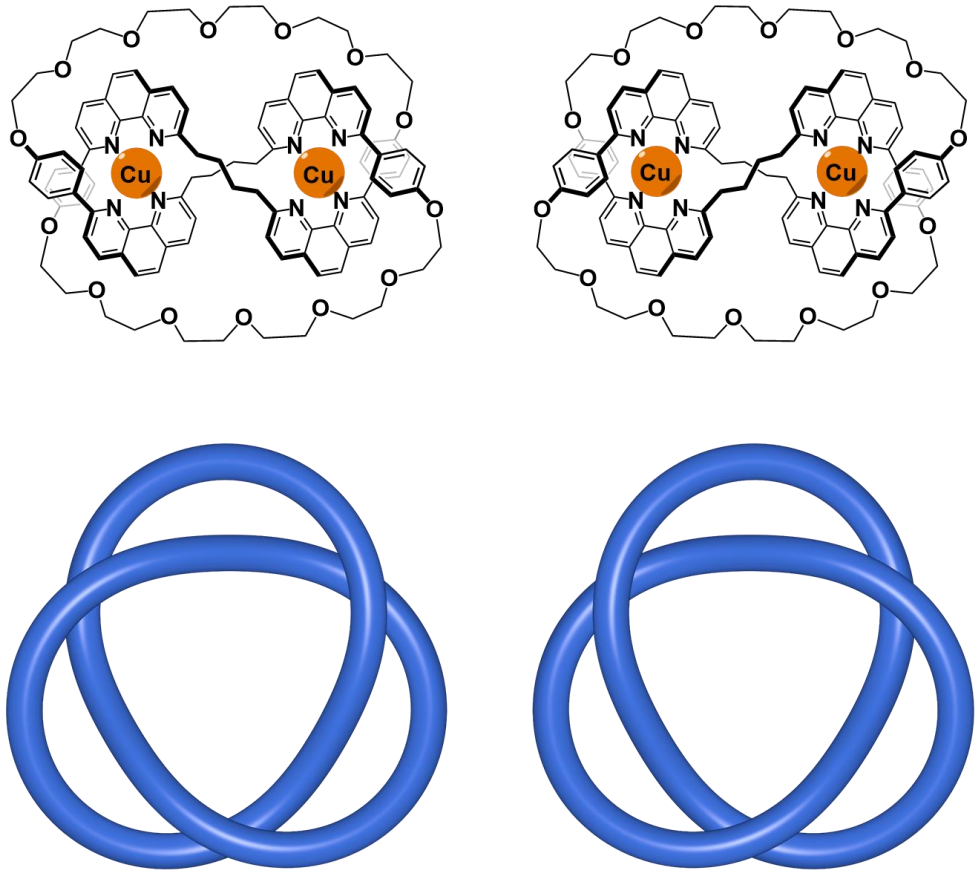

Figure 6.1 | The two topological enantiomers of the trefoil knot. No continuous deformation of the organic portion of the trefoil knot can be carried out which converts it from one enantiomer to the other.[3]

The natural progression of this work is the investigation of knotted molecules. Any close-loop graph embedded in three-dimensional space which can be continuously deformed to its mirror image is achiral. Otherwise it is topologically chiral. The only requirements of the deformation performed is that they do not involve the cutting of the continuous loop or it passing through itself.

In the simplest case, the trefoil or 3_1 knot, no continuous deformation is able to convert one of the enantiomers into the other (Figure 6.1). If it is not possible to reshape the knot so that it perfectly resembles its mirror image, the two are a pair of enantiomers. This is entirely independent of the components of the knot, rather it is a property of the whole system. In the case of the trefoil knot synthesised by Sauvage,[3] it can be seen how the handedness of the knot relates to the handedness of the helix used to form the knot.

Knot theory has shown that the majority of knots, but not all, behave in this manner. One exception to this is the 4_1 (or figure-eight) knot. Through continuous deformation, it is possible to convert this knot into its mirror image, meaning it is achiral.

To date, chemists have prepared these chiral knots as racemic mixture and resolved them into their enantiopure form by chiral stationary phase HPLC. This separation of knots, such as the trefoil[4] and more recently the 8_{19},[5] and their subsequent analysis by circular dichroism (CD) spectroscopy provides experimental evidence that these molecular knots do exist as pairs of enantiomers, even when they do not include covalent stereogenic units (Figure 6.2).

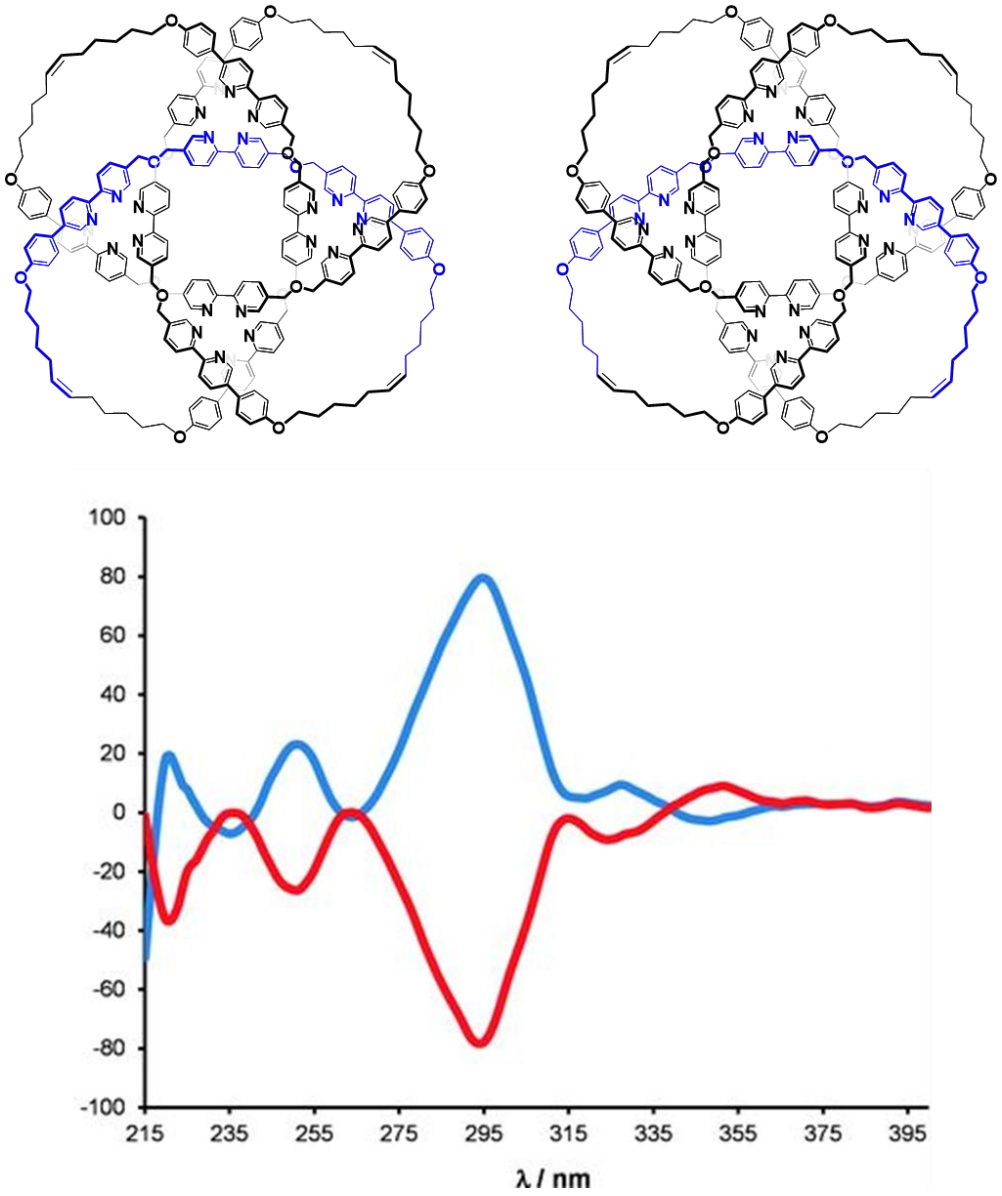

Figure 6.2 | Separation of the two topological enantiomers of an 8_{19} molecular knot by chiral stationary phase HPLC. The CD spectra of the two enantiomers.[5]

In other cases, there are examples where the incorporation of covalent stereogenic units can be used to influence the handedness of the knot.[6,7] This is because the two forms of the knot, if they incorporate the same handedness of building block, are in fact diastereomers. These diastereomers will tend to have different energies, largely due to steric effects. If this energetic difference is large enough, a significant biasing in the handedness of the knot will be observed (Figure 6.3).

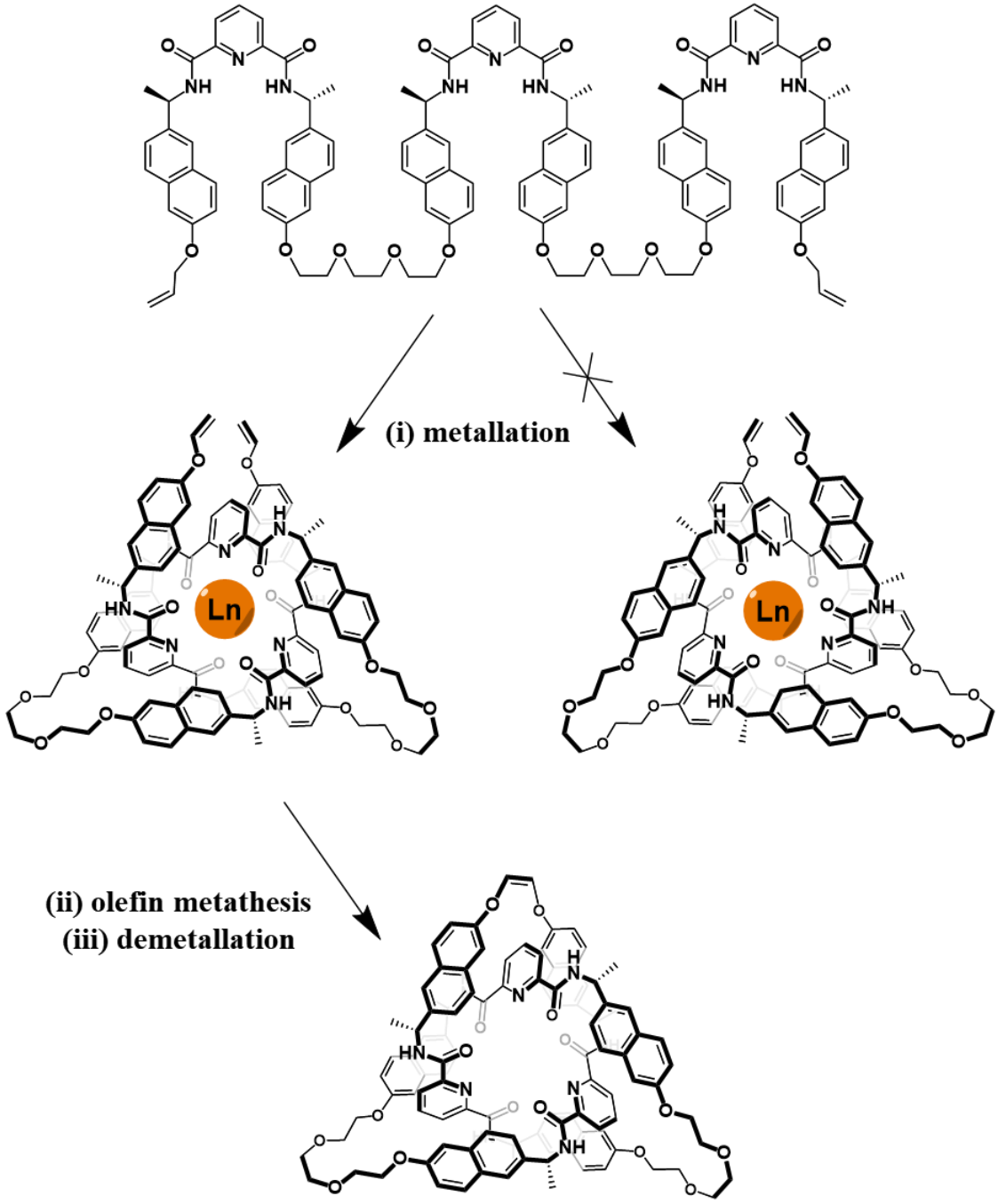

Figure 6.3 | Incorporation of covalent stereogenic units into the ligand, which coordinates to a lanthanide metal centre and is ultimately tied into a trefoil knot, leads to a preference for one diastereomer over the other.[7]

Various other knots which include such stereogenic units have been reported thus far. Sanders and coworkers formed a purely organic knot using dynamic combinatorial chemistry which only forms as a single diastereomer.[6] Feigel reported another trefoil knot composed entirely of amino acids and steroids whose formation is also diastereoselective.[8]

The preparation of enantio-enriched or enantiopure knots which contain no other chiral information has not been achieved thus far, at least without the use of chiral stationary phase HPLC. This form of chirality is not dependent on the chemical nature of the molecular knot, or on the spatial positioning of certain moieties relative to one another. Instead, it is an intrinsic property of the knot.

6.2 Chirality in Mechanically Interlocked Molecules

Recently, Goldup and coworkers have reported on the enantioselective synthesis of mechanically interlocked molecules. They have developed two distinct methods for achieving this. In one case, active metal templation is employed to couple alkyne and azide containing molecules together to form the thread through a tightly-fitting and desymmetrised macrocycle (Figure 6.4).[1] Importantly, the azide derivative used is an enantiopure chiral species derived from glucose.

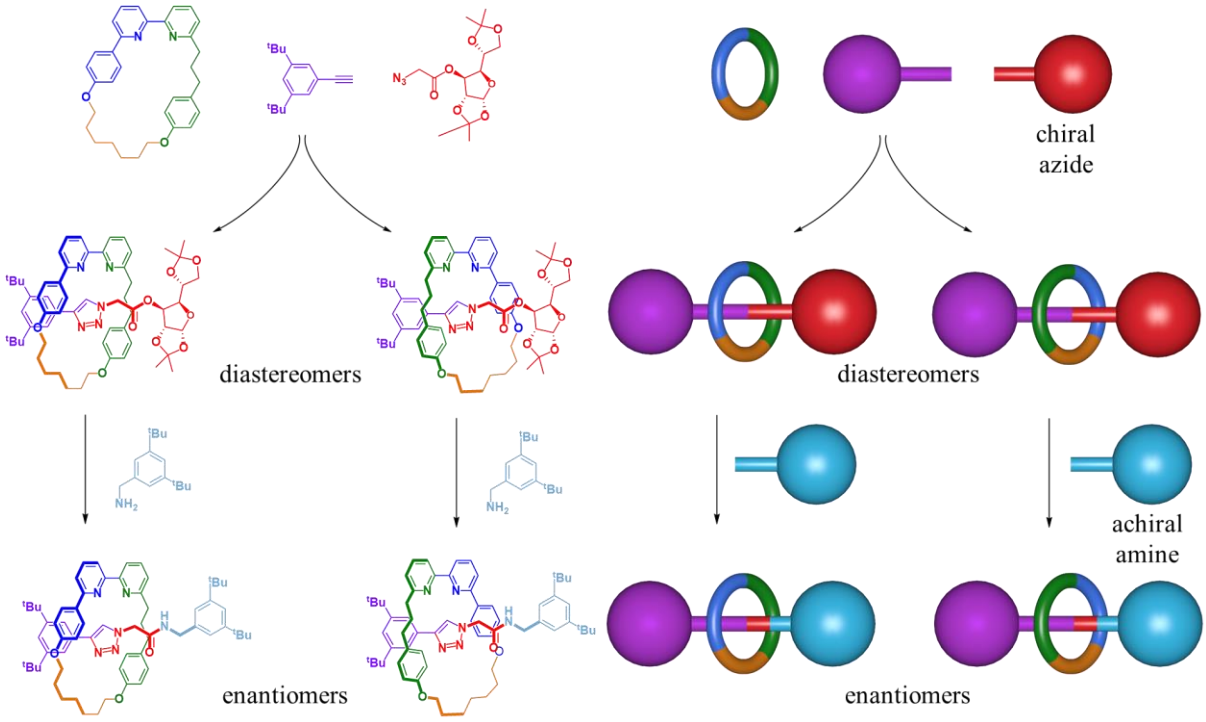

Figure 6.4 | Synthesis of the two possible diastereomers of an asymmetric rotaxane. These diastereomers can be separated by standard chromatographic techniques. Subsequent displacement of the chiral auxiliary yields a rotaxane where the chirality is encoded in the mechanical bond.[1]

This choice of precursors means that rotaxane formation produces two diastereomers (with little or no diastereoselectivity observed). The two diastereomers differ in how the axle of the rotaxane threads the oriented macrocycle. These diastereomers are separable by regular chromatographic techniques. Separation of the two, followed by substitution of the chiral glucose unit with an achiral amine yields a rotaxane in which the mechanical bond is the only

stereogenic element. This methodology therefore removes the need to employ chiral stationary-phase HPLC, making the synthesis of these enantiopure molecules far cheaper, easier and more scalable.

In the second approach, active metal templation is employed again. Procedurally, it is similar to the example described in Figure 6.4., however, because of a close steric fit between the reactants as they are coupled, diastereoselectivity is observed. Alkylation of the thread at the covalent stereocentre, a tetravalent carbon centre which is part of an amino acid derivative, symmetrises the thread and yields a rotaxane with up to 98:2 enantiomeric excess. All of this is achieved without the need for any purification of diastereromers or enantiomers. Again, the mechanical bond is the only stereogenic element in the system.[9]

It should be noted that this form of chirality in rotaxanes is not topological in the strict sense. This is because continuous deformation of the rotaxane can lead to the formation of the other enantiomer (Figure 6.5). Of course, such a process is only theoretical and is unlikely to occur in this chemical system.

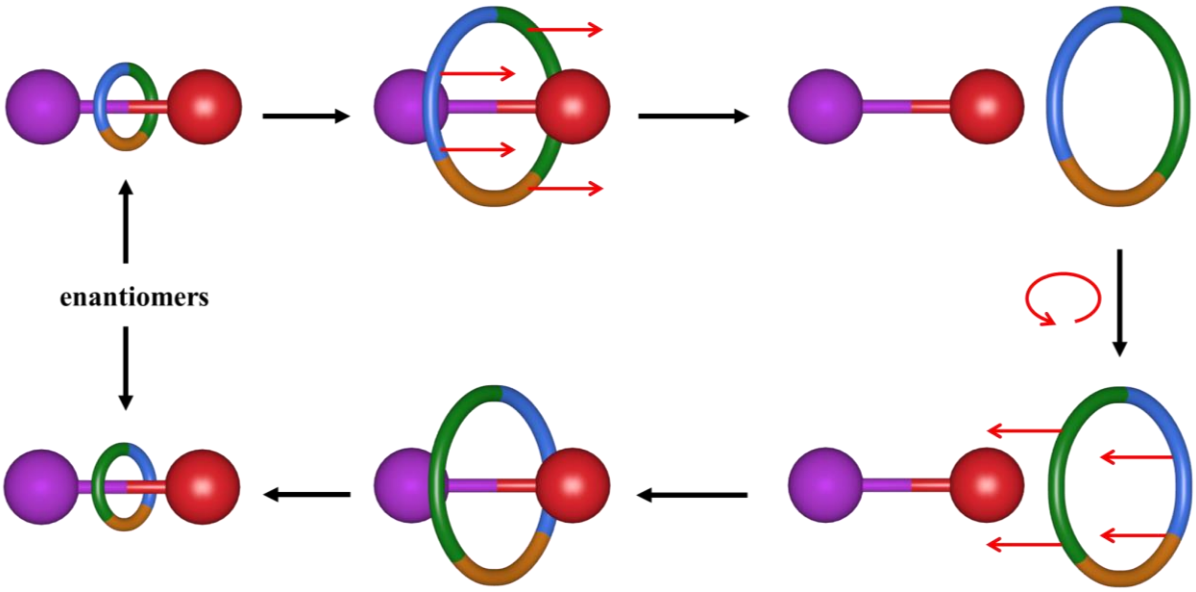

Figure 6.5 | Continuous deformation of the chiral rotaxane to yield the other enantiomer. If the ring is expanded, removed, flipped, replaced over the thread and then shrunk the opposite enantiomer can be obtained without the need to cleave any bonds.

These two advances paved the way toward the synthesis of the first topologically chiral molecule. In this work, which builds on the results outlined in Figure 6.4, Goldup and coworkers designed a linear molecule which has an azide moiety at one end and an alkyne with

a proximal covalent stereogenic unit in close proximity at the other end (Figure 6.6).[2] Coupling of these two molecules through an oriented macrocycle leads to the formation of two diastereomeric [2]catenanes, which are separable by regular chromatographic means. Subsequent cleavage of the covalent stereogenic unit produces a chiral species where all of the stereochemical information is topological in nature.

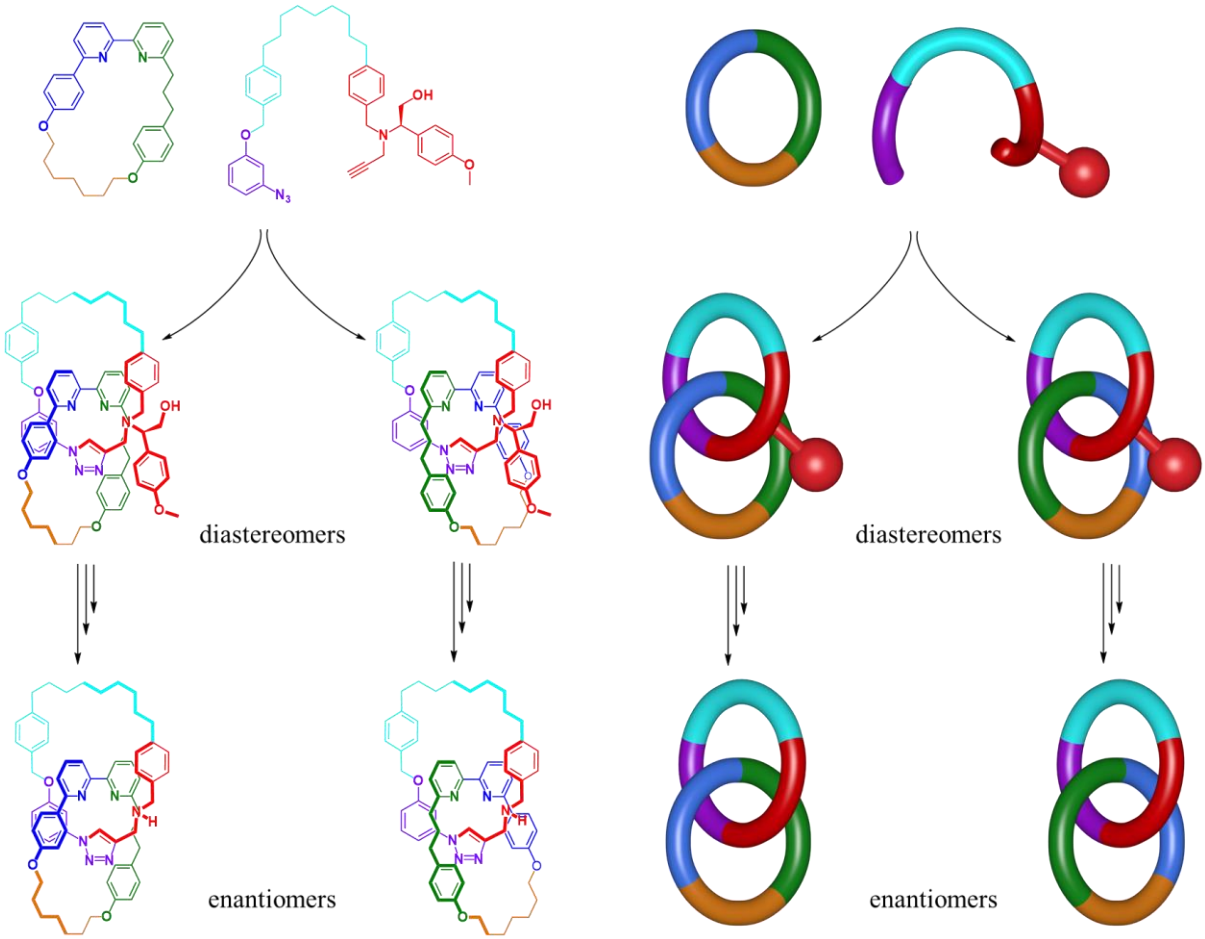

Figure 6.6 | Synthesis of a topologically chiral [2]catenane. Several synthetic steps are required to remove the chiral auxiliary group and are omitted here.[2]

It is not possible to rotate either of the two rings such that the [2]catenane perfectly mirrors its enantiomer. Unlike with the rotaxane, removal of the ring from the [2]catenane is no longer possible. In this system, the nature of the two rings is consequential in the expression of topological chirality. If one of the two macrocycles had a mirror axis, for instance, the resulting structures would not be chiral. This issue is cleverly circumvented in the present case through the design and use of an asymmetric 2,2'-bipyridine containing macrocycle.

6.3 Purely Topological Chirality Idea Outline

These works led us to question whether it would be possible to enantioselectively synthesise a molecular knot where the only stereochemical element is the knot itself. To achieve this, it was concluded that creating a knot which incorporates covalent stereogenic units into its structure would be a key first step.

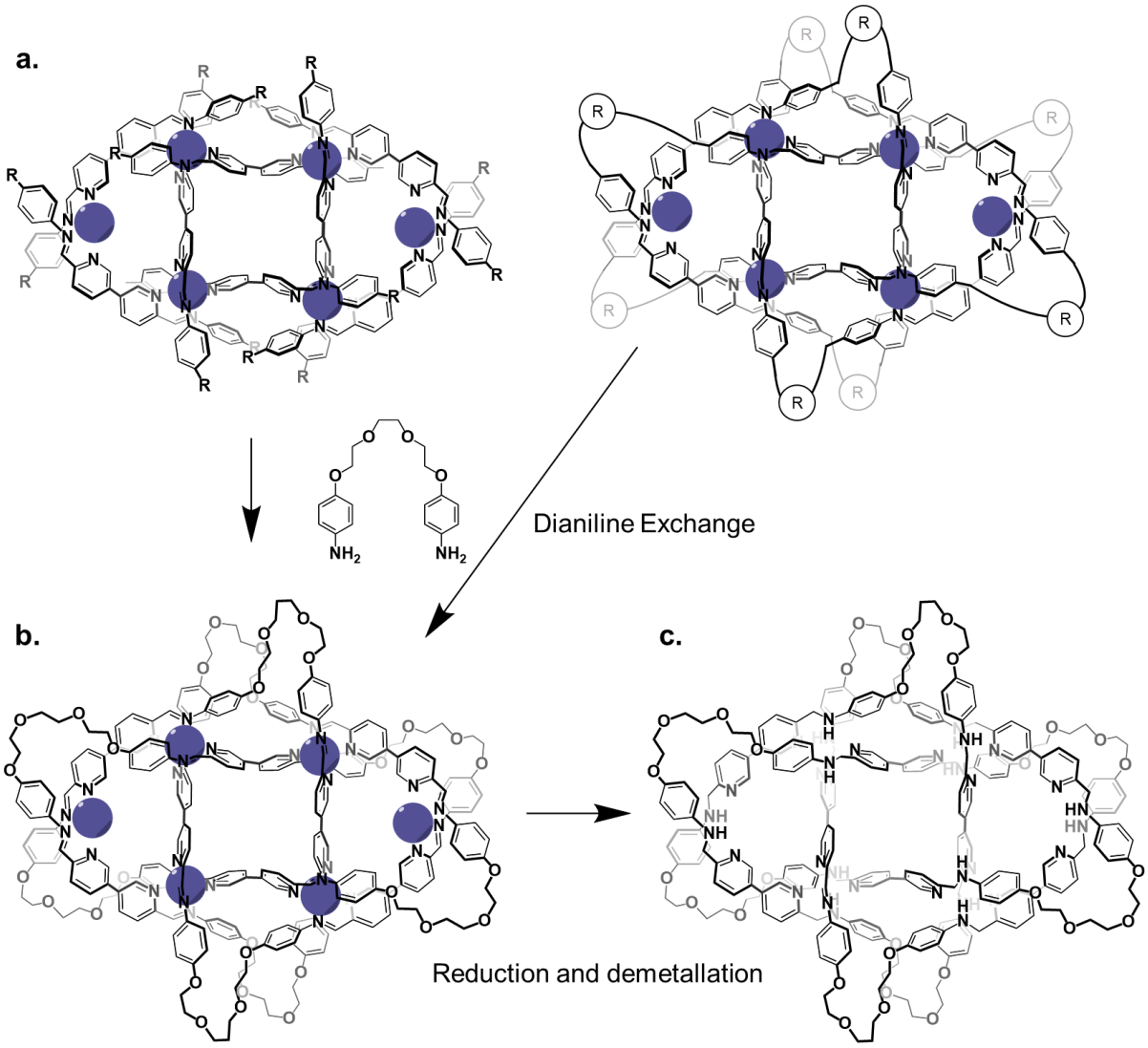

Figure 6.7 | a. Synthesis of either the parent extended circular helicate or the 8_{19} molecular knot with an enantiopure aniline containing subcomponent should lead to diastereoselectivity. R is a covalent stereogenic unit. **b.** Dianiline exchange with an achiral dianiline yields one enantiomer of **5.11** or **5.12**, depending on the metal salt used. **c.** Reduction and demetallation yields the inert, enantio-enriched 8_{19} molecular knot.

Inclusion of such units in a knot would mean two possible diastereomers could form and diastereoselectivity might be observed. The diastereomers come about when a given handedness of the aniline containing subcomponent pairs with one of either Δ or Λ metal centres in the assembly. These two species are chemically distinct and it is expected that one should be more stable than the other, leading to an uneven distribution of the two at equilibrium. Alternatively, a monoaniline which incorporates a covalent stereogenic unit could be used to diastereoselectively form an extended circular helicate, similar to **5.9**.

If such a diastereoselective synthesis could be achieved, the next step to achieving a purely topological form of chirality is the displacement of these chiral centres from the knot (or extended circular helicate) (Figure 6.7b). Importantly, this has to be accomplished without the destruction and racemisation of the central core of the knot. The core of the knot dictates the handedness of the organic knot. It was envisaged that cooperative effects in the binding of the ligands to the metal centres, and the number of covalent bonds which must be simultaneously cleaved to achieve racemisation would render the knot kinetically inert to racemisation for the reaction conditions used in the dianiline displacement step.

Subsequent reduction of the labile imine bonds to the corresponding secondary amine and demetallation of the knot would then yield the purely organic knot, which would be either enantiopure or enantio-enriched (Figure 6.7c). The key points which would determine the degree of enantio-enrichment are:

(i) How energetically favourable one diastereomer of the knot which incorporates the chiral aniline containing subcomponent is over the other.

(ii) How rapidly racemisation occurs under the conditions used in the aniline exchange step.

(iii) How reduction and demetallation affects the two different species which result from the aniline exchange step.

6.4 Attempted Diastereoselective Synthesis of Extended Circular Helicate

The first set of experiments carried out to achieve this goal of forming a topologically chiral molecular knot in an enantioselective manner involved the use of chiral monoanilines and amines. As described above, it was envisaged that assemblies incorporating enantiopure anilines would lead to the diastereoselective formation of the parent extended circular helicate (Figure 6.8).

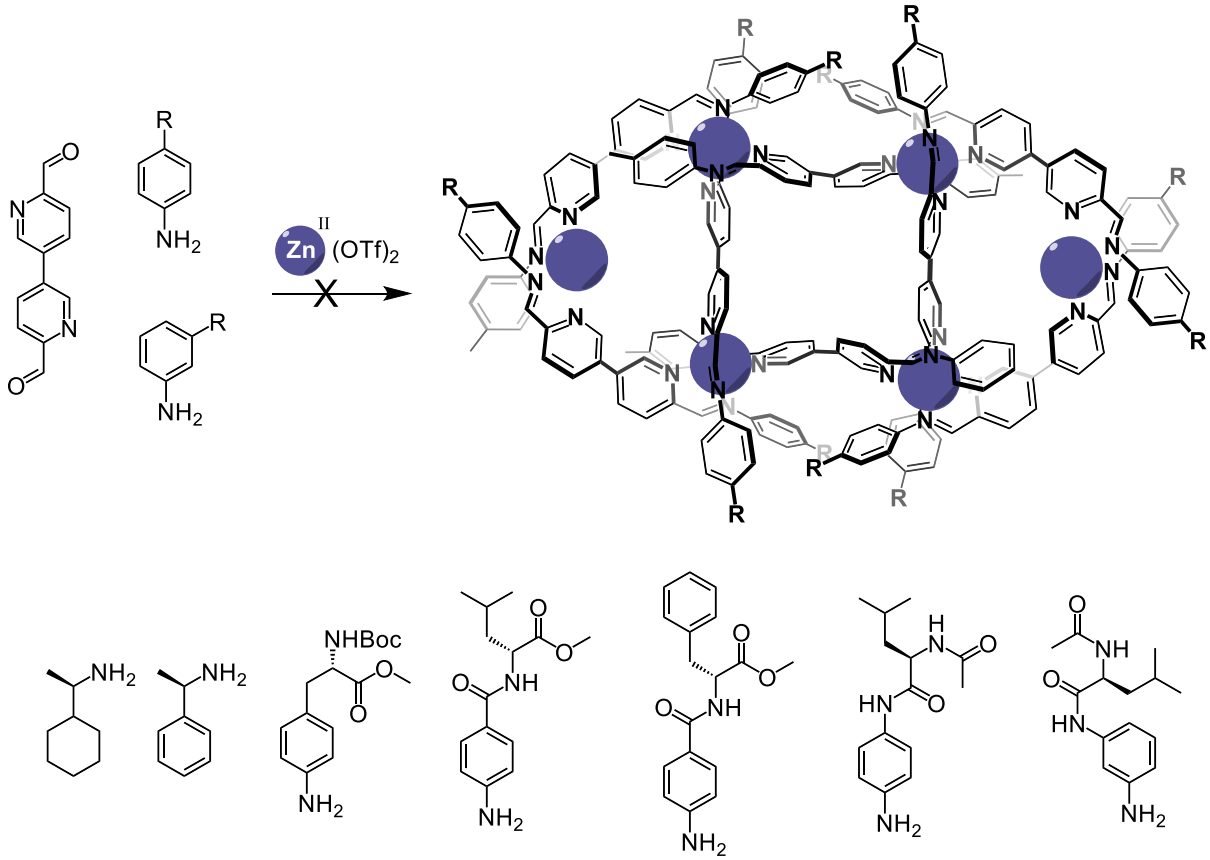

Figure 6.8 | Attempts to form extended circular helicates using chiral amines or monoanilines.

There is good precedence for this in previously reported work on the diastereoselective synthesis of metal-organic cages employing similar chemistry.[10] In this case, cooperativity and the chelate effect would also favour the displacement of the chiral monoaniline precursor with the achiral dianiline, a key step in the formation of the desired product.

Several different enantiopure amines and anilines were tested. However, in all cases the extended circular helicate was not observed to form. Many of the attempted assemblies resulted in insoluble precipitate. In others, small, ill-defined metal-organic structures were observed. The amine (as opposed to aniline) containing subcomponents yielded M_4L_6 tetrahedra. Most of the chiral anilines were substituted at the *para* position. Switching to a *meta* substitution pattern, due to concerns that steric clash may be an issue, did not lead to the extended circular helicate forming.

6.5 Diastereoselective Synthesis of a Zn^{II}-knot

The next strategy pursued to prepare a knot with enriched topological handedness was to employ dianiline subcomponents which have stereogenic units incorporated into them. To this end, enantiopure dianilines **6.1** and **6.2** were prepared from the corresponding trans-1,2-diaminocyclohexane.

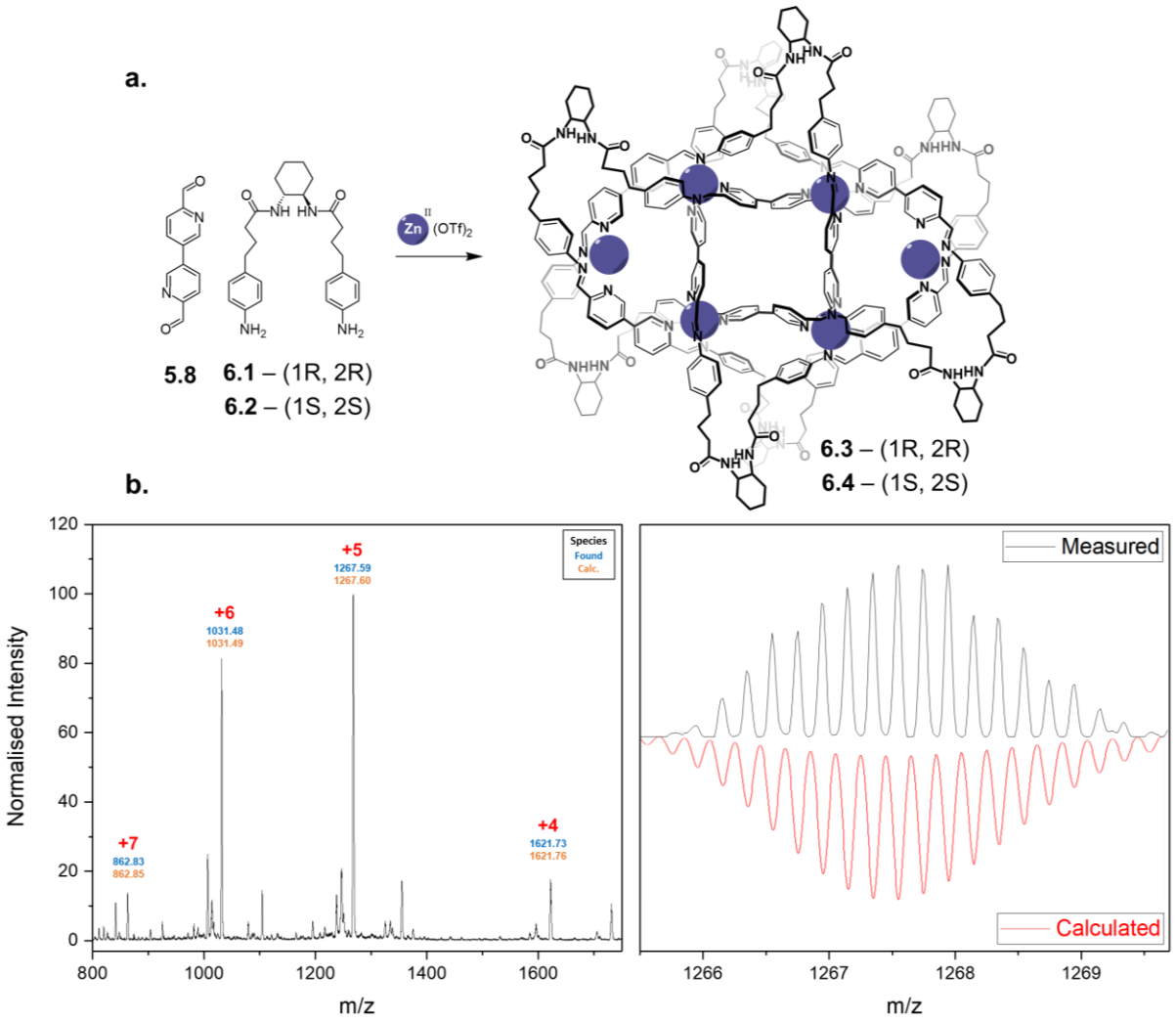

Figure 6.9 | a. Synthesis of Zn^{II} templated knot diastereomers **6.3** or **6.4** from their respective chiral subcomponent. **b.** Low resolution ESI- and HR-MS of **6.3**.

Treatment of subcomponent **5.8** (8 equiv.) with enantiopure dianiline **6.1** (8 equiv.) and $Zn(OTf)_2$ (6 equiv.) led to the formation of **6.3** in 73% isolated yield (Figure 6.9a). ESI- and

HR-MS were consistent with the formation of knot **6.3**, which has the same Zn_6L_1 structure as **5.12** (Figure 6.9b).

The d^{10} metal centres of **6.3**, again, consistent with results obtained for **5.12**, leads to the complex exhibiting diamagnetism. ^{1}H NMR spectroscopy revealed one major species in solution whose spectrum was consistent with the subcomponents adopting four distinct chemical environments, characteristic of this form of 8_{19} knot (Figure 6.10a).

Further splitting of the proton resonances, with one set of signals being significantly more intense than the other, was also observed. A magnified ^{1}H NMR spectrum of the aromatic region of **6.3** is available in the Experimental Section of this Chapter. The ratio of the major and minor peak was measured to be approximately 85:15 by deconvolution of the signals. Currently, it is uncertain as to whether these smaller peaks are the minor diastereomers or if they are a second unrelated structure. Both of these are probable solutions, given the propensity of **5.8** to form a broad range of supramolecular structures.[11,12]

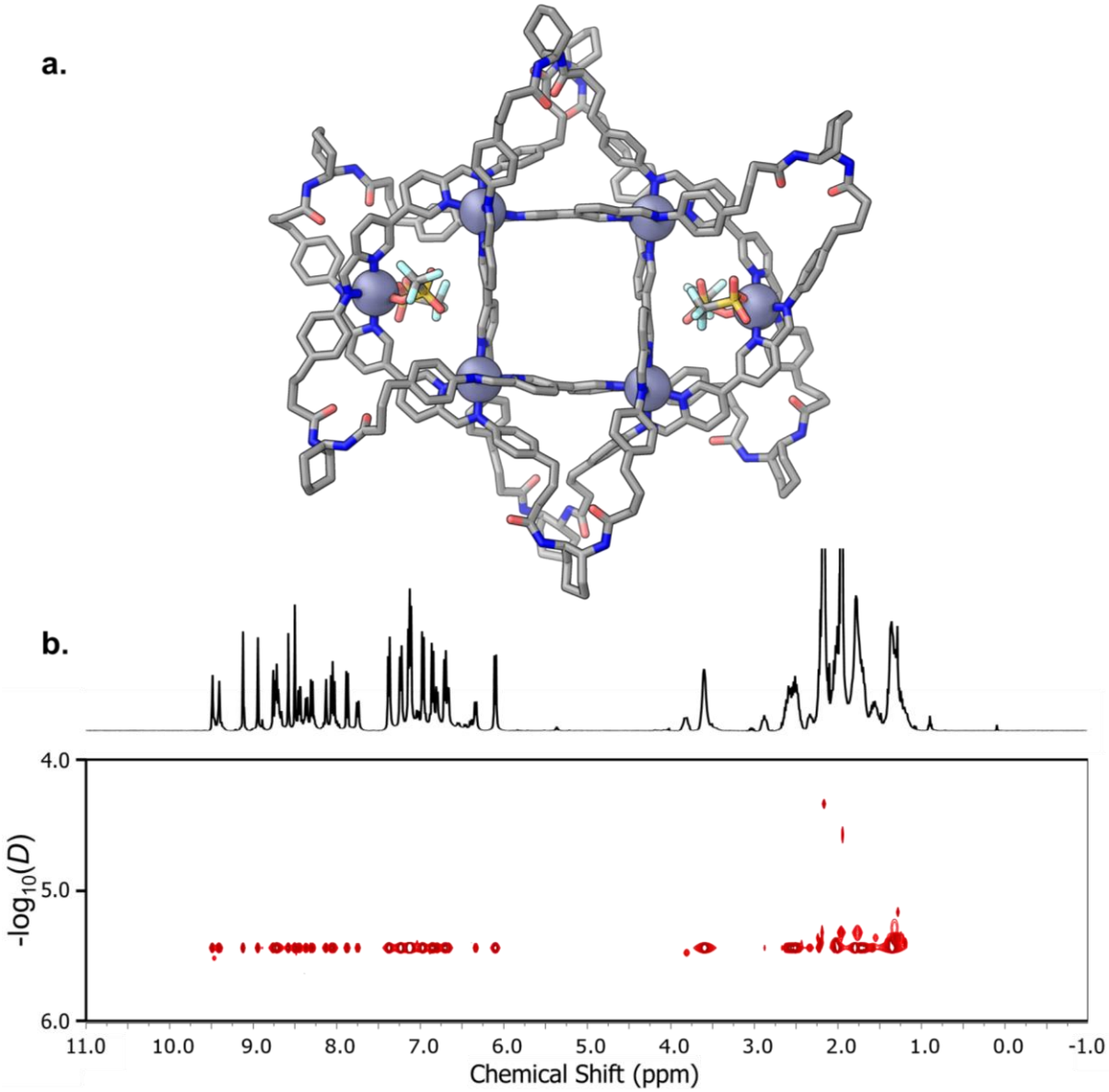

Figure 6.10 | a. Molecular model of **6.3** (MM3) based on the solid-state structure of **5.12**. ^{1}H NMR spectrum and diffusion ordered NMR spectrum of **6.3**, which exhibits four-fold desymmetrisation, as with **5.12**. The units of D are $cm^2\ s^{-1}$.

Attempts to purify the sample, to ascertain whether these small peaks were the result of impurities did not lead to any variation in the measured integral ratios, consistent with the minor species being the other diastereomer and not excess subcomponents or small organic oligomers. Both of the structures are observed to diffuse at a similar rate (Figure 6.10b). This result is further evidence that the two species may be the diastereomers of the knot. The fact

that one is significantly more abundant than the other suggests that one of the diastereomers is energetically favoured.

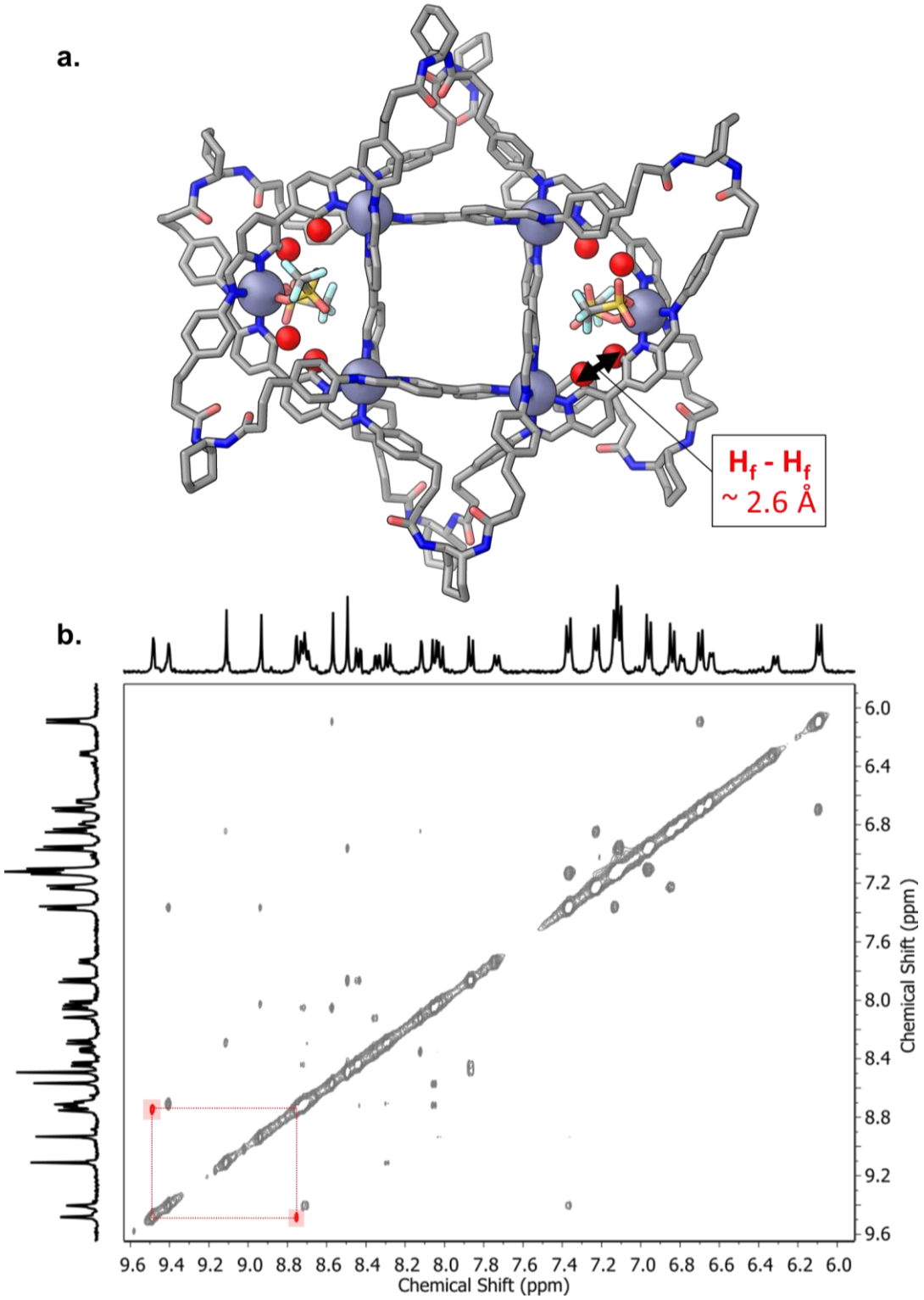

Figure 6.11 | a. Molecular model of **6.3** (MM3) with proximal H_f protons, which belong to a ligand in a *syn* configuration, highlighted as red spheres. **b.** ^1H – ^1H NOESY highlighting correlations between two H_f proton environments, consistent with the *syn* ligand conformation.

Complete assignment of the ^{1}H NMR spectrum was possible, using a ^{1}H–^{1}H COSY, ^{1}H–^{1}H NOESY and through comparison with the NMR data of **5.12**. Strong NOE correlations between two of the pyridyl protons (labelled H_f in the Experimental Section) provided the starting point for the full assignment of the aromatic region of the spectrum.

One noteworthy difference in the aromatic region of the ^{1}H NMR spectrum of **6.3** and **6.4** is the presence of four resonances between 6 and 8 ppm, which correspond to the NH amide protons of the chiral dianiline subcomponent. One of the resonances, located at 7.72 ppm is very down-field shifted relative to the other three (which are between 6.3 and 6.8 ppm). We hypothesise that this is a result of it being positioned in a very chemically distinct environment, such as in the vicinity of the peripheral Zn^{II} metal centres. It was not possible to establish from the NMR data which amide resonance corresponds to which aromatic ligand, as the aliphatic region couldn't be fully assigned due to the number of signals present, and their significant overlap.

Strong CD bands were observed between 250 nm and 450 nm, most likely corresponding to π–π^* ligand-based transitions. As is expected for a Zn^{II} complex, no MLCT band is observed. These intense bands mirror each other when the two enantiomers of the chiral dianilines, **6.1** and **6.2**, are used. This is consistent with the chiral dianilines having a strong effect on the overall knotted structure. However, by itself it is not conclusive evidence the handedness of the central helicate structure is affected.

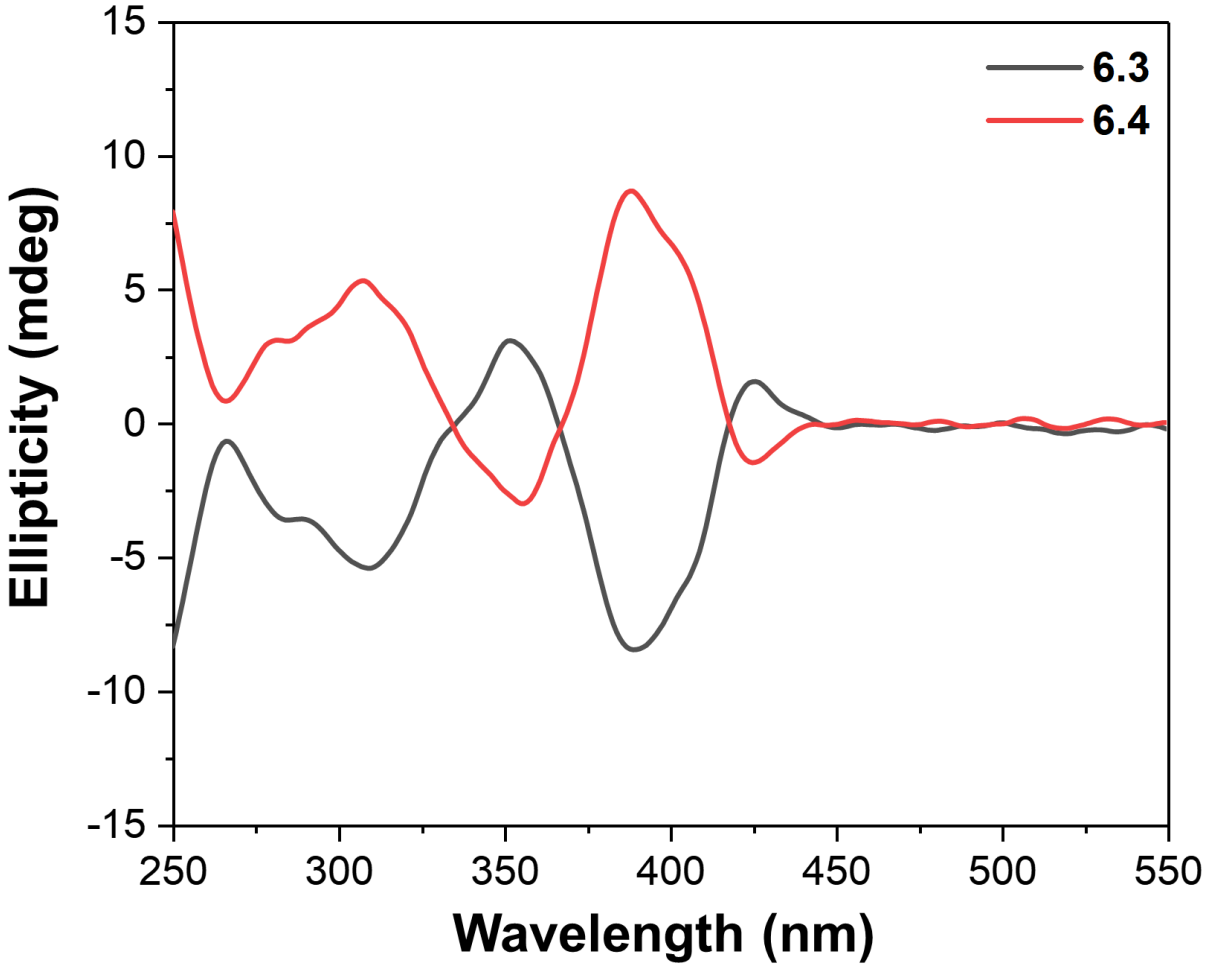

Figure 6.12 | Circular dichroism (CD) spectra of molecular knots **6.3** and **6.4**. A strong response is observed for the ligands of the knot. No MLCT band is observed as a consequence of Zn^{II} being d^{10}.

Given that Zn^{II} is d^{10} which prevents MLCT transitions from occurring, direct observation of the effect of the chiral dianiline on the metal centres absorption of light of different handedness is not possible. In the case of Fe^{II} this is not true. With this in mind, the Fe^{II} congeners of **6.3** and **6.4** were synthesised.

5.8 (8 equiv.) was treated with **6.1** (8 equiv.) with $Fe(OTf)_2$ (6 equiv.), which led to the formation of **6.5** in 61% isolated yield (Figure 6.13). ESI-MS was consistent with the formation of knot **6.5**, which has the same Fe_6L_1 structure as **5.11**.

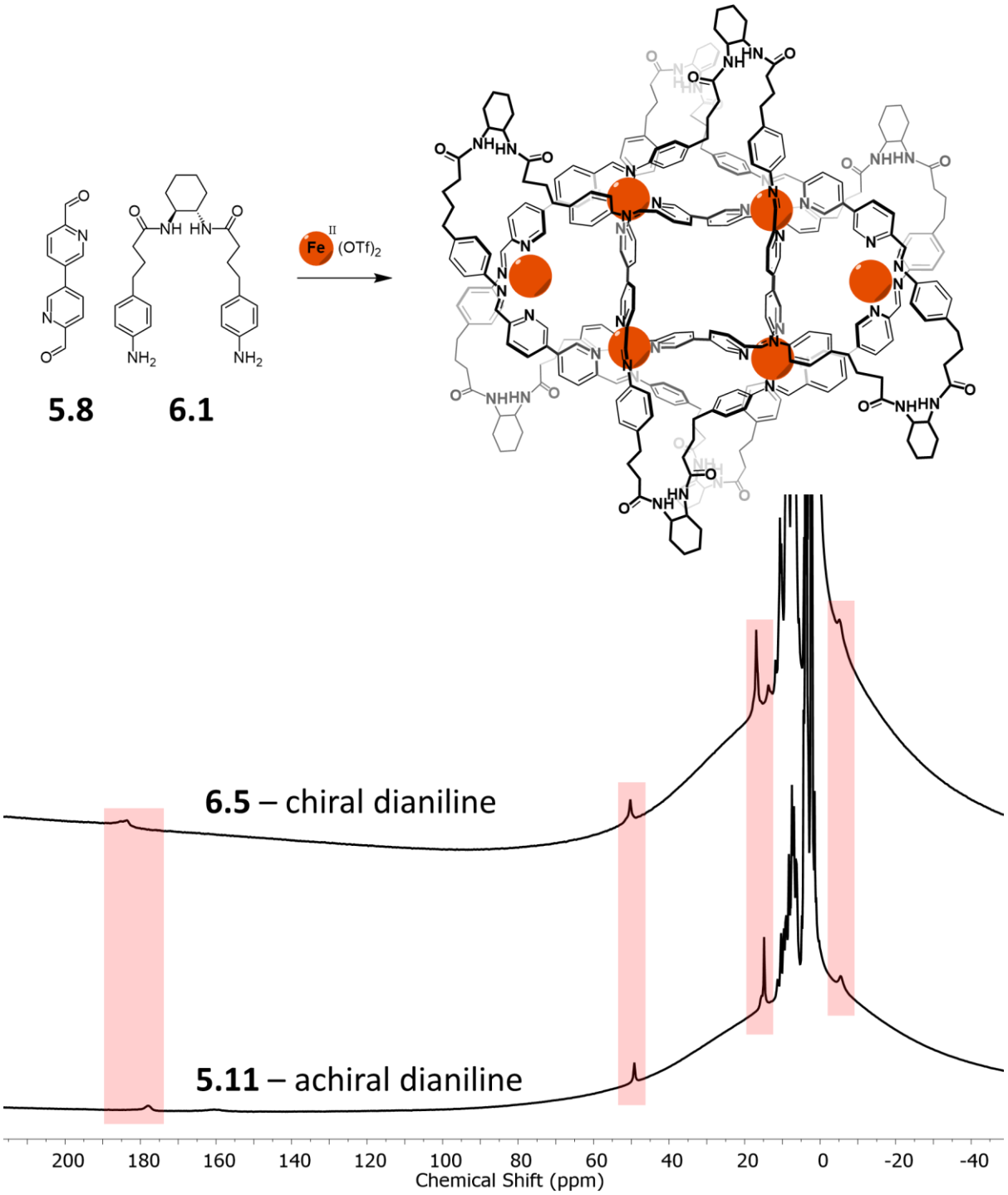

Figure 6.13 | a. Synthesis of Fe^{II} templated knot **6.5** from its subcomponents **5.8** and **6.1**. **b.** ^{1}H NMR spectra of **6.5** and **5.11**.

As with the original Fe^{II} knot **5.11**, synthesised with achiral dianiline **5.10**, the mixture of high-spin and low-spin metal centres leads to paramagnetic shifting and signal broadening in the NMR spectrum (Figure 6.13). While this makes interpretation of the data more challenging, a qualitative similarity between the spectrum for **6.5** and **5.11** was noted. The other

diastereomers, **6.6** was synthesised from **6.2** and produced MS and NMR data consistent with those of **6.5**.

As described above for the Zn^{II} templated structure, two diastereomers may form in this case with Fe^{II}. This means that two-fold splitting of the NMR signals is expected. Whilst the significant line broadening which results from the paramagnetic nature of the knot precludes any definitive conclusions, only one set of resonances was observed. This indicates one of two things; the formation of **6.5** and **6.6** is diastereroselective or splitting of the NMR signals is negligible for these species and just cannot be detected.

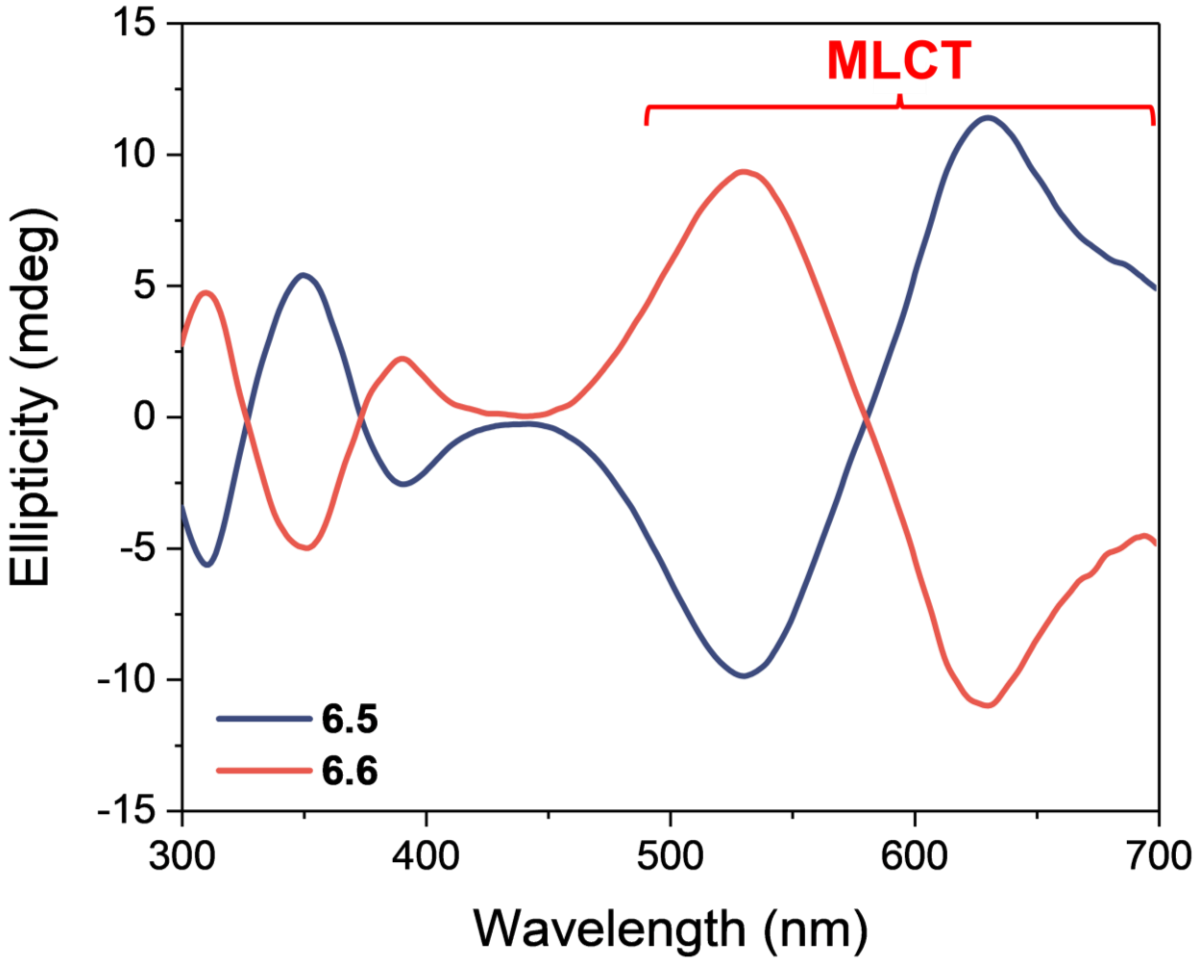

Figure 6.14 | Circular dichroism (CD) spectra of the two diastereomers of the Fe^{II} knot, **6.5** and **6.6**. A strong band is observed in the MLCT region, unlike with either the subcomponents or with the Zn^{II} based knots, **6.3** and **6.4**.

The metal centres are strongly absorbing, resulting from a strong MCLT band occurring from 450-700 nm. If the handedness of **6.5** and **6.6** is affected by the handedness of subcomponents

6.1 and **6.2**, a strong effect would be expected in this region. To probe this CD spectroscopy was used (Figure 6.14).

The most noticeable feature of the CD spectrum is the strong band observed in the MLCT region (450-700 nm). This contrasts to the CD spectra recorded for **6.3** and **6.4**, where no MLCT is observed (Figure 6.12). Further bands were noted from 300 nm to 420 nm, which correspond to π– π^* transitions on the ligands. These observations indicate one of two things about **6.5** and **6.6**. Either enantiopure **6.1** and **6.2** affects the distribution of Δ or Λ vertices within the knot, or this is an induced CD signal. The latter case seems improbable, given the strength of the bands, but cannot be precluded.

Given the strength of the CD signal and that it is consistent with the NMR results we concluded that such dianilines can significantly affect the distribution of Δ or Λ vertices in both **6.5** and **6.6**.

Efforts to obtain crystals of sufficient quality for analysis by X-ray diffraction have been unsuccessful thus far, in the case of both the Zn^{II} and Fe^{II} templated knots. Experimentally, this will the most instructive way to probe which of the two diastereomers is formed with a given enantiomer of the dianiline. Attempts to distinguish between the two possible structures using 1D and 2D NOESY experiments have not provided conclusive evidence either.

While this prevents us from concluding which handedness of knot results from a given enantiomer of the knot, we can conclude that the covalent chiral unit has a significant effect on the handedness of the overall knot. Given that the chiral centre is so remote from the metal centres which dictate the handedness of the knot and that **6.1** and **6.2** are relatively flexible, this result is somewhat surprising. We infer that even if individual energetic contributions of any single dianiline is quite small, the effect of having all eight of the anilines acting in concert with one another is greatly magnified, leading to a high diastereomeric excess.

In order to investigate whether this excess could be improved upon, a shorter, but chemically similar, chiral dianiline **6.7** was synthesised (Figure 6.15c). It was anticipated that if the covalent stereogenic units was brought closer to the metal centres, it would exert a greater influence on their handedness. However, this subcomponent was found to be incapable of assembling to given the corresponding 8_{19} knot.

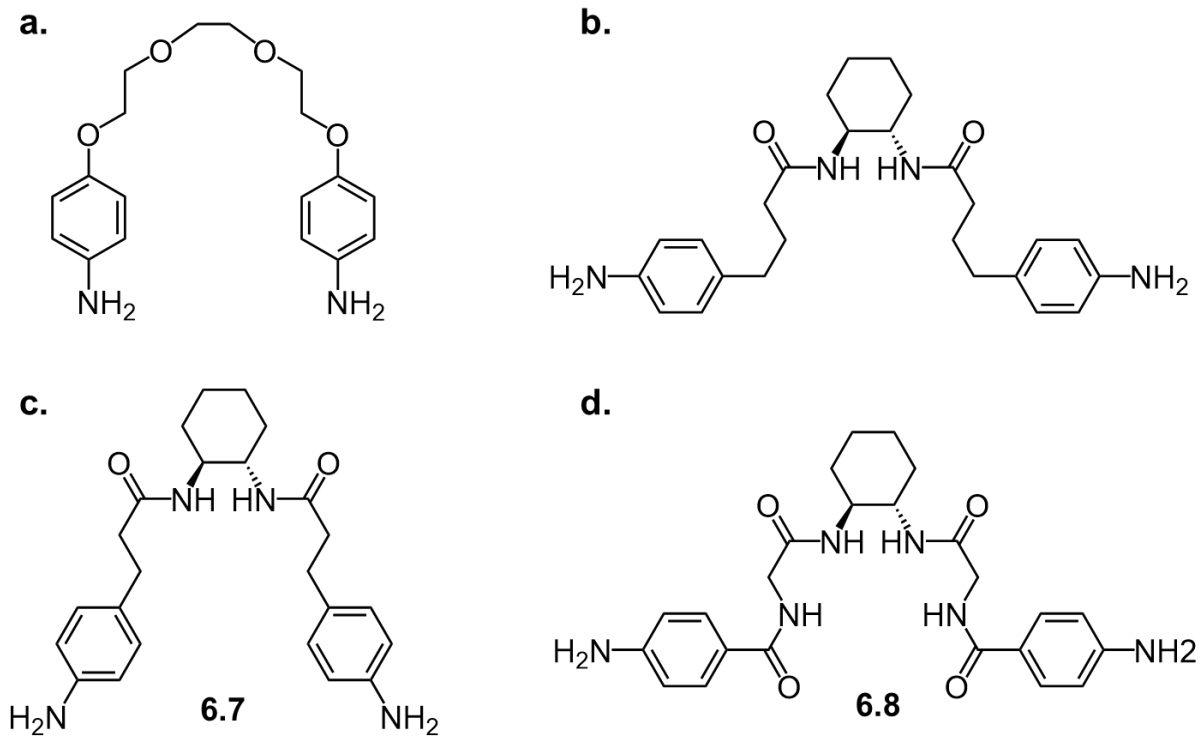

Figure 6.15 | a. Achiral dianiline **5.10** used in the synthesis of **5.11** and **5.12**. **b.** Chiral dianiline used in the synthesis of **6.3**, **6.4**, **6.5** and **6.6**. **c.** A shorter dianiline and **d.** an electron-poor dianiline did not assemble to give the expected 8_{19} molecular knot.

Furthermore, an electron-poor chiral dianiline **6.8** was synthesised, starting from glycine (Figure 6.15d). It was envisaged that the electron-withdrawing amide group *para* to the aniline would expedite the dianiline exchange step. Unfortunately this species was not observed to form, only the subcomponents were observed by ^{1}H NMR after several days at 70 °C. We infer that either the aniline is not sufficiently nucleophilic for the assembly to proceed, or the amide moiety introduces too much steric clash into the system to allow for the knot to assemble.

These two negative results, coupled with the observation that the M_6L_8 extended circular helicate couldn't form with a broad range of anilines indicates how challenging the synthesis of such molecular knots can be.

6.5 Knot Reduction

Recently published work in the Nitschke group by Dr. Roy Lavendomme, on a series of metal-organic imine-based macrocycles and cages, has shown that BH_3•THF in acetonitrile at room temperature gives a higher yield of the related secondary amine product from the imine than does $NaBH_4$, $LiAlH_4$, or NaH.[13]

Two key changes to the experimental protocol which increased the yield significantly were noted. First, the addition of BH_3•THF was performed stepwise (0.25 equiv./imine) every ten minutes. Second, the reduction was performed with methanol as a solvent (MeCN/MeOH, 5/1, v/v) to quench excess BH_3 after each addition, to avoid further deleterious reactions. These optimised conditions were found to significantly increased yields by minimising side reactions which produced undesired reduced products, such as the cleaved macrocycles. The reduced metal-organic assemblies were found to be difficult to characterise by NMR spectroscopy due to the presence of numerous diastereomers originating from the newly formed N stereocentres (bound to four different substituents: phenylene, CH_2, H and metal cation). Demetallation of the complexes by addition of ethylenediamine as a competing ligand afforded the reduced assemblies which were, in contrast, easily characterised by NMR spectroscopy.

A slightly adapted version of these optimised conditions were applied to **5.11** (Figure 6.16). All of the experiments described in this section were performed by Dr. Roy Lavendomme, with assistance from me. Further experimental detail is available in the Experimental Section of this Chapter. BH_3•THF (1 M, 3 equiv./imine) was added to a stirred acetonitrile/methanol (5/1, v/v) solution of **5.11** (one equiv.) at room temperature. The mixture was stirred for 10 minutes while the color of the solution changed from deep green to dark brown. Dichloromethane and ethylenediamine (4.5 equiv./Fe) were then added to demetallate the knot. The resulting mixture was then washed with water and extracted with dichloromethane. The combined organic layers were then passed through a pad of Celite and subsequently reduced to dryness, yielding **6.9** as a yellow-brown solid.

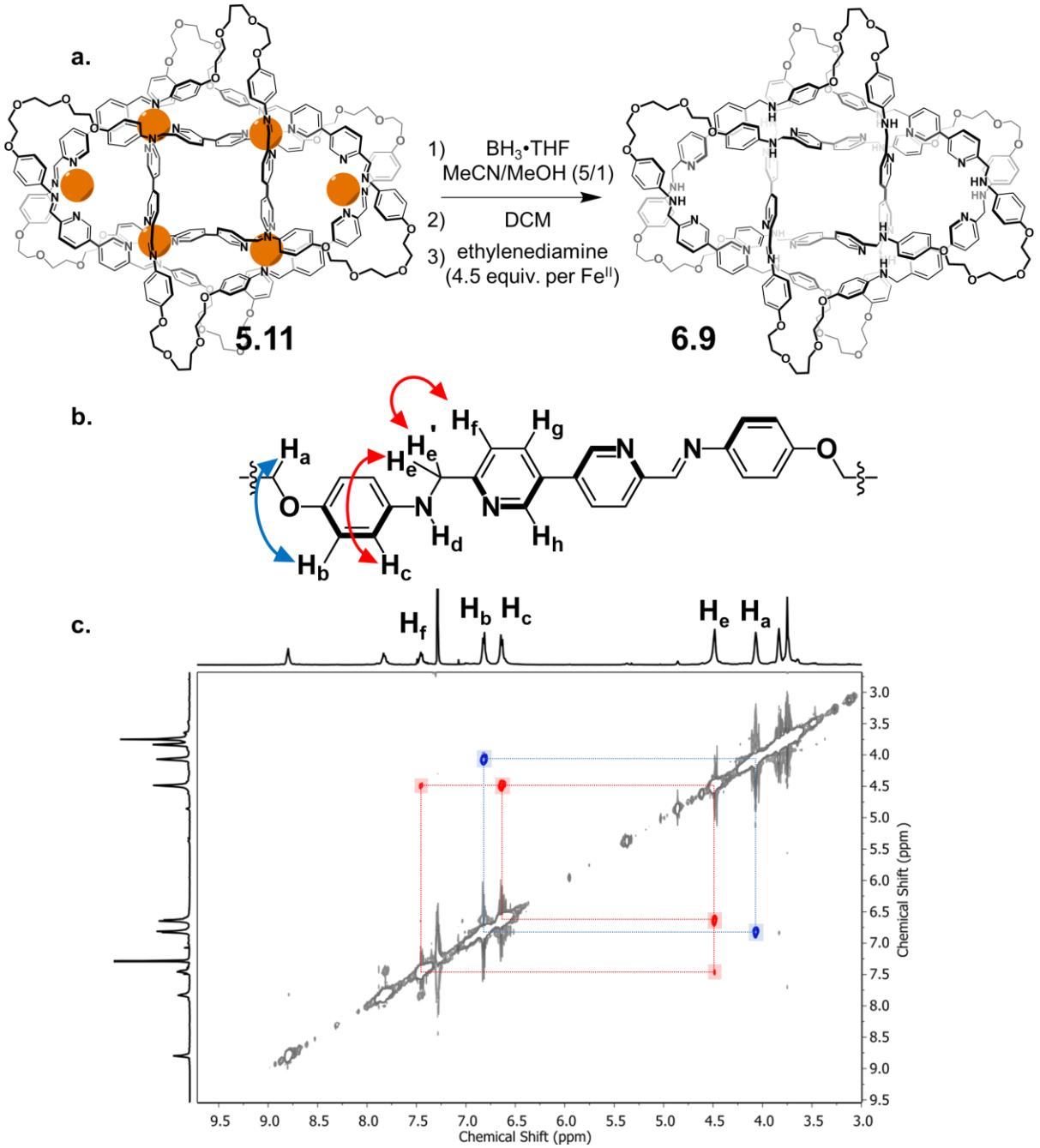

Figure 6.16 | **a**. Reduction of Fe^{II} templated knot **5.11** with BH_3•THF with subsequent demetallation yielding **6.9**. **b**. Tentatively assignment of the reduced, demetallated knot **6.9**. **c**. ^1H – ^1H NOESY of reduced knot, red correlations are observed between a CH_2 residue (H_e) and both a pyridyl proton (H_f) and an aniline proton (H_c). The other aniline proton resonance (H_b) correlates (shaded in blue) with a second CH_2 resonance (H_b) of the ethyl glycol chain.

Inspection of the ^{1}H NMR spectrum reveals nine resonances, consistent with the reduced and demetallated knot ligand adopting one chemical environment. Significant broadening of the spectrum is also noted. This could be consistent with reptation of the knot.[14,15]

Attempts to analyse this sample by mass spectrometry have been unsuccessful thus far, further optimisation of the conditions used is required. Preliminary studies of the resulting species indicate a series of promising NOE correlations, however. In particular, resonance which have been tentatively assigned to the pyridyl ring of the knot and the aniline residue can both be seen to be in close proximity with a CH_2 proton environment. We are currently assigning this to be the CH_2 which results from the reduction of the imine to a secondary amine.

6.6 Dianiline Substitution

In order to obtain a purely topologically chiral species, displacement of the covalent stereogenic units of **6.3** via aniline exchange was targeted. Achiral dianiline **5.10** (80 equiv.) was added to **6.3** (1 equiv.) in deuterated acetonitrile and the subsequent reaction, carried out at 60 °C, was monitored by ^{1}H NMR (Figure 6.17). ^{1}H NMR spectroscopy revealed the gradual release of the chiral dianiline subcomponent **6.1** over the course of 13 hours, with a corresponding amount of achiral **5.10** incorporated into the knot.

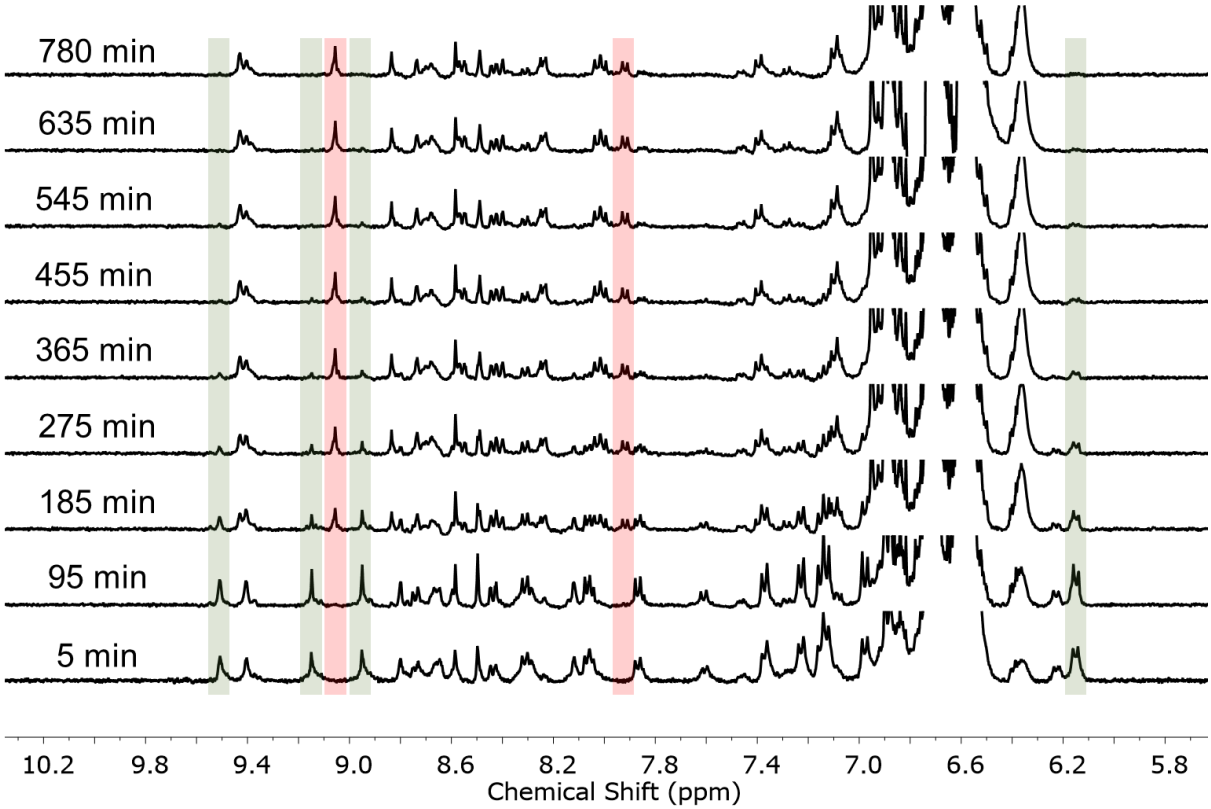

Figure 6.17 | Kinetic study of the displacement of **6.1** with **5.10**. The results in the transformation of **6.3** (highlighted in green) to **5.12** (shaded in red) over the course of 13 hours.

After complete consumption of **5.10** was observed, producing a ^{1}H NMR spectrum consistent with that of **5.12**, CD spectroscopic measurements were carried out on the sample, without any further purification. Disappointingly, the CD bands observed between 250 and 450 nm were found to completely disappear (Figure 6.18). This result indicates that the racemisation of the knot occurs as at approximately the same rate as the dianiline displacement process.

Noting that a CD trace should include a contribution from the now liberated chiral dianiline **6.1**, the CD spectrum of subcomponent **6.1** was measured and was found to have a very small response between 250 nm and 550 nm. This may be a result of the chromophores of **6.1** being spatially separate from the chiral centres and not feeling their effect as a result.

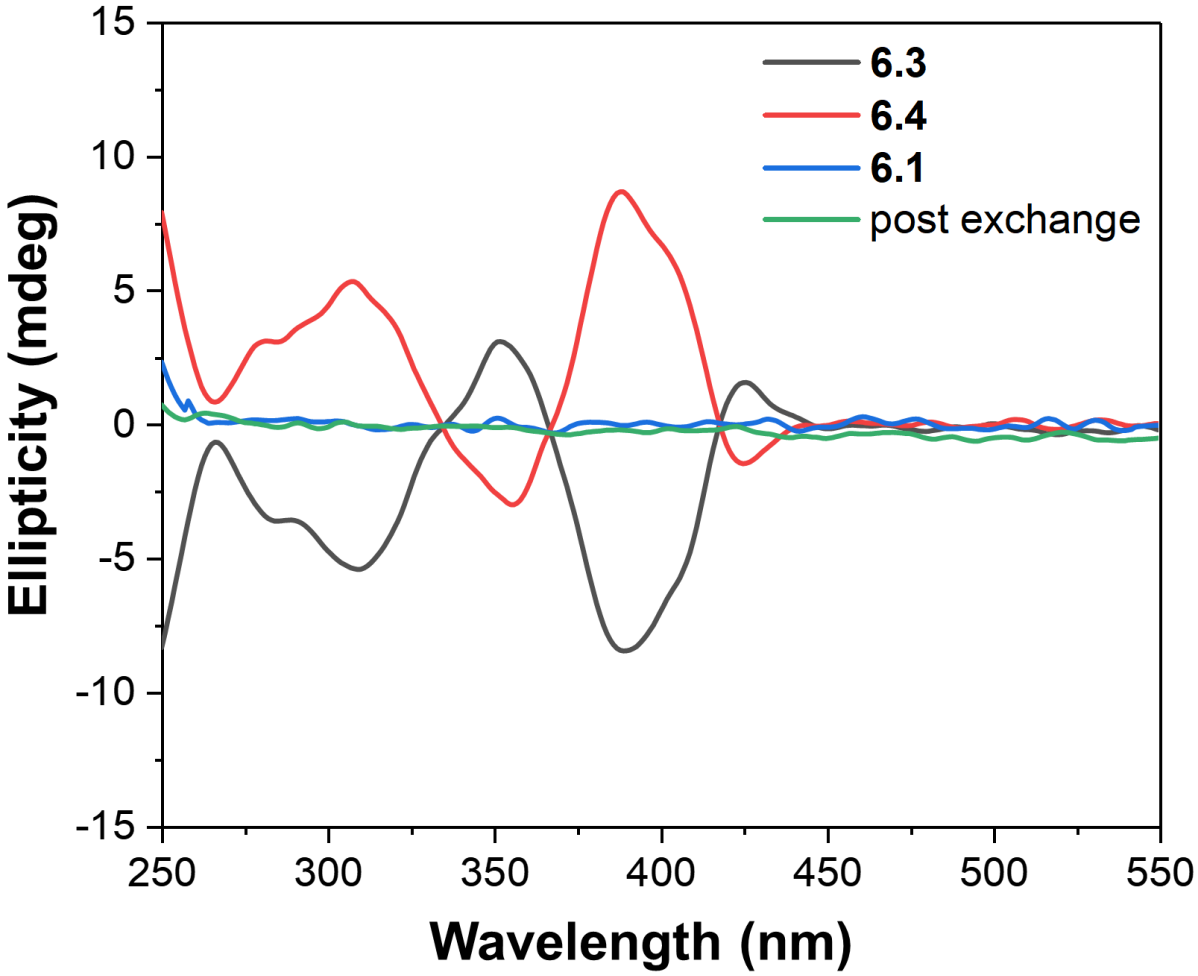

Figure 6.18 | Circular dichroism (CD) spectra of subcomponent **6.1**, Zn^{II} knots **6.3** and **6.4** and **6.3** following dianiline exchange.

These results were surprising to us. In order for racemisation to occur each of the metal centres has to convert from a Λ configuration to a Δ configuration, or vice versa for the other enantiomer of the knot. For this to occur, it was assumed that both deligation and imine hydrolysis (or transamination potentially) would have to occur. Therefore, it was reasoned that the rate of displacement of the chiral dianiline with the achiral dianiline should be faster than (and related to) the rate of racemisation.

However, given that the CD spectrum was recorded immediately after the dianiline displacement had gone to completion, this doesn't seem to be the case. We speculate that this may be a consequence of the slow rate of the dianiline displacement and the elevated temperatures at which the reaction was carried out at. These conditions were arrived at as lower equivalents of dianiline and lower temperatures were found to proceed far too slowly to be practical (reaction half-life of six or more days at room temperature for the same number of equivalents of **5.10**).

Further to this, the reaction almost certainly proceeds via a series of intermediates in which one or more of the chiral dianilines have been replaced with an achiral unit. As each chiral unit is removed its contribution to the energetic difference between the two diastereomers of the knot is also removed. This could mean that the knots which are partially substituted, not just the completely substituted ones, may begin to racemise. Further investigation of this process would be required before any firm conclusions could be drawn, however.

6.7 Future Work

There seems to be a relatively limited range of subcomponents that are capable of forming either the 8_{19} knot or M_6L_8 extended circular helicate, when using dianilines and monoanilines, respectively. This is evidenced in the inability of the extended circular helicate to form with monoanilines with chiral auxiliaries and in the attempted synthesis of the knot with shortened chiral dianiline **6.7**. Given this fact, any changes to the system will require careful consideration if the three following goals are to be meet:

(i) Actually forming the knot

(ii) Rapid displacement of the chiral dianiline with an achiral one

(iii) Maintenance of the handedness of the knot

One route which we are currently working toward is the inclusion of electron-withdrawing groups into the aniline residues of the chiral dianiline (Figure 6.19). **5.10** is relatively electron-rich with a Hammett parameter of approximately -0.25, which is very similar to that of achiral **6.1** and **6.2**, with Hammett parameters of approximately -0.170. A consequence of this is that the displacement is slowed down significantly as there is no large thermodynamic driving force for the displacement. Various other experiments were carried out in our attempts to displace the chiral dianiline with lower temperatures and equivalents of the achiral dianiline, none of which went to completion.

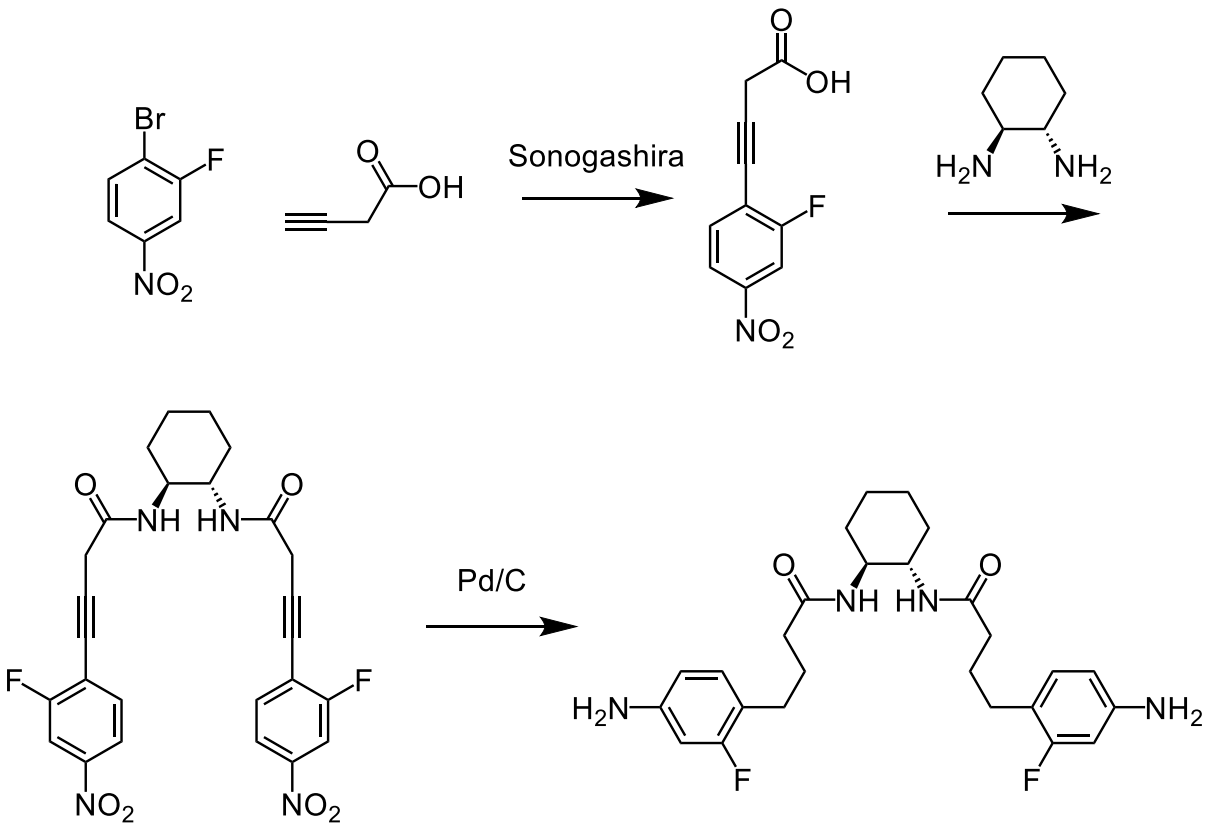

Figure 6.19 | Proposed synthetic route toward a more electron-deficient chiral dianiline.

It was anticipated that incorporation of compact, electron-withdrawing moieties into the chiral dianiline subcomponent will expedite the displacement process, while not interfering in the assembly process. Assuming that we are able to achieve these goals, reduction and demetallation of the knot to give the purely organic knot will be carried out, using the protocols outlined in Section 6.5. CD spectroscopy and chiral-stationary phase HPLC will then we carried out to investigate and quantify the enantiomeric excess of the topologically chiral knot.

6.8 Conclusions

This Chapter has described the formation of a new molecular 8_{19} knot which incorporates covalent stereogenic units into its structure. **5.11** and **5.12**, the 8_{19} molecular knots described in Chapter 5 and formed from achiral dianilines, both exist as a pair of racemic enantiomers where the chirality is encoded in the handedness of the metal vertices of the complex, and therefore in the handedness of the organic knot. In contrast, the inclusion of covalent stereogenic units into dianilines **6.1** and **6.2** appears to lead to the formation of two diastereomers, with one being energetically favoured over the other.

Four distinct knots were synthesised. Two of these are templated by Zn^{II}, namely **6.3** and **6.4**, which are enantiomers of each other. They are diamagnetic and produce NMR data similar to those of **5.12**, formed with an achiral ethylene glycol based dianiline. **6.5** and **6.6** were templated by Fe^{II} and, like **5.11**, exhibit paramagnetism. The effect of the handedness of the dianiline subcomponents on these structures was investigated by NMR and CD spectroscopy, with the results indicating the covalent stererogenic units have a significant effect on the handedness of the knot.

Efforts towards the reduction of these knots to yield purely organic species has also been described. Finally, ongoing work on the displacement of the chiral dianiline subcomponents from **6.3** and **6.4** with achiral dianilines has been detailed. While displacement of one subcomponent for the other has been achieved, it has resulted in the racemisation of the knot under all reaction conditions tried so far.

Future work will focus on finding the appropriate combination of dianiline building blocks and reaction conditions which will allow for both rapid dianiline displacement and the maintenance of the complex's structure and, consequently, the topological chirality of the knot.

6.9 Experimental Section

Synthesis of **6.1**, **6.2**, **6.7**, and **6.8** was carried out by Dr. Charlie McTernan of the University of Cambridge.

*Synthesis of **6.3** and **6.4***

As with **5.11**, assembly of **6.3** and **6.4** was highly sensitive to the stoichiometry of the subcomponents. The synthesis of **6.3** is described here, **6.4** was synthesised in an identical manner with the opposite enantiomer of dianiline.

6,6´-diformyl-3,3´-bipyridine $\mathbf{L^1}$ (14.2 mg, 67 mmol, 8 equiv.), **6.1** (1R, 2R) (29.5 mg, 66 mmol, 8 equiv.) and $Zn(OTf)_2$ (18.4 mg, 49 mmol, 6 equiv.) were added to a small Schlenk flask (total volume 25 mL). CH_3CN (8 mL) was added along with a Teflon-coated magnetic stir-bar. The sealed Schlenk flask was sonicated for 10 minutes at 70 °C and left to stir at 90 °C for 18 hours. The light yellow reaction mixture was allowed to cool to room temperature and was then filtered through a glass fibre filter (0. 7 μm pore size). The acetonitrile solution was concentrated under a stream of N_2 to a volume of 2 mL. Addition of diisopropyl ether (6 mL) resulted in the precipitation of a yellow solid. The suspension was then centrifuged (10 min, 3000 RPM), the eluent decanted. Further diisopropyl ether (2 mL) was added, the powder was resuspended by sonication and then centrifuged. Again, the eluent was decanted. The residue was then dried *in vacuo* to afford the solid product as a fine light yellow powder (44 mg, 73%).

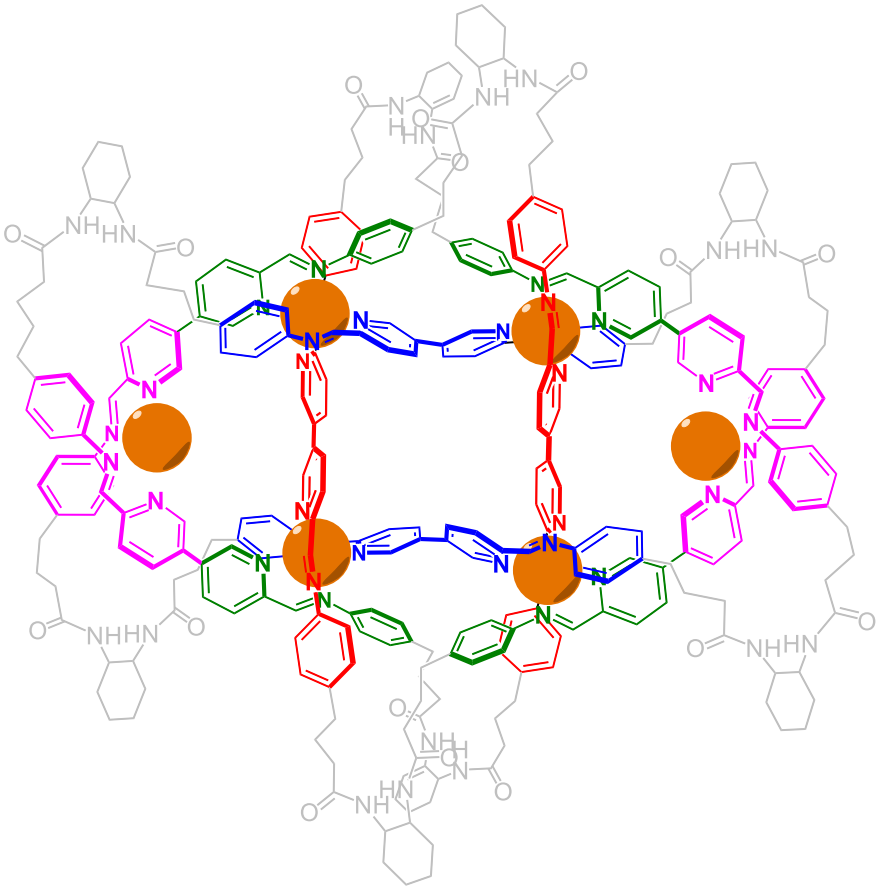

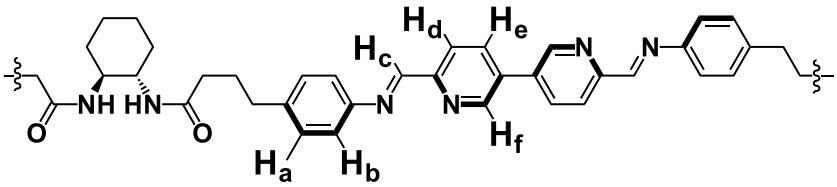

^{1}H NMR (500 MHz, 298 K, CD_3CN) δ: 9.48 (H_f, d, J = 2.1 Hz, 4H), 9.40 (H_f, d, J = 2.1 Hz, 4H), 9.11 (H_c, s, 4H), 8.93 (H_c, s, 4H), 8.75 (H_f, s, 4H), 8.72 (H_e, dd, J = 7.9, 2.1 Hz, 4H), 8.70 (H_e, dd, J = 7.9, 2.1 Hz, 4H), 8.57 (H_c, s, 4H), 8.49 (H_c, s, 4H), 8.44 (H_e, dd, J = 8.0, 2.1 Hz, 4H), 8.33 (H_e, dd, J = 8.3, 2.2 Hz, 4H), 8.28 (H_d, d, J = 8.3 Hz, 4H), 8.11 (H_f, d, J = 2.2 Hz, 4H),8.05 (H_d, d, J = 2.2 Hz, 4H), 8.02 (H_d, d, J = 2.2 Hz, 4H), 7.86 (H_d, d, J = 8.0 Hz, 4H), 7.76 (H, d, J = 8.6 Hz, 4H, amide NH), 7.36 (H_b, d, J = 8.3 Hz, 8H), 7.22 (H_a, d, J = 8.2 Hz, 8H), 7.12 (H_a, d, J = 8.2 Hz, 8H), 7.10 (H_a, d, J = 8.4 Hz, 8H), 6.96 (H_b, d, J = 8.5 Hz, 8H), 6.84 (H_b, d, J = 8.0 Hz, 8H), 6.79 (H_g, d, J = 6.5 Hz, 4H, amide NH), 6.69 (H_a, d, J = 8.7 Hz, 8H), 6.64 (H_g, d, J = 6.7 Hz, 4H, amide NH), 6.37 (H_g, d, J = 8.1 Hz, 8H, amide NH),6.09 (H_b, d, J = 8.3 Hz, 8H), 3.81 (H_h, m, 4H, cyclohexane), 3.59 (H_h, m, 12H, overlapped, cyclohexane)

^{13}C NMR (125 MHz, 298 K, CD_3CN) δ: 174.0 (carbonyl), 173.8 excess dianiline subcomponent), 173.45 (carbonyl), 173.21 (carbonyl), 172.84 (carbonyl), 165.45 (imine), 163.19 (imine), 161.82 (imine), 158.33 (imine), 150.23 (pyridine), 149.90 (pyridine), 148.87 (pyridine), 147.63 (pyridine), 147.47 (pyridine), 147.13 (pyridine), 147.00 (pyridine), 146.68 (pyridine), 146.04 (pyridine), 145.48 (pyridine), 144.76 (pyridine), 144.45 (pyridine), 144.12 (pyridine), 143.94 (pyridine), 143.88 (pyridine), 143.72 (pyridine), 142.87 (pyridine), 142.66 (pyridine), 142.45 (pyridine), 142.02 (pyridine), 140.72 (pyridine), 138.88 (pyridine), 137.49 (pyridine), 136.83 (pyridine), 136.07 (pyridine), 131.68 (aniline), 131.63 (aniline), 131.32 (aniline), 131.19 (aniline), 130.74 (aniline), 130.35 (aniline), 130.09 (aniline), 129.97 (excess dianiline subcomponent), 129.88 (aniline), 128.94 (aniline), 123.91 (aniline), 122.47 (aniline), 122.33 (aniline), 122.24 (aniline), 115.57 (excess dianiline subcomponent), 55.42 (cyclohexane), 54.26 (excess dianiline subcomponent), 54.15 (cyclohexane), 53.73 (cyclohexane), 52.12 (cyclohexane), 37.55 (aliphatic), 36.78 (aliphatic), 36.50 (aliphatic), 36.30 (aliphatic), 36.23 (aliphatic), 35.67 (aliphatic), 35.54 (aliphatic), 34.97 (aliphatic), 34.36 (aliphatic), 34.12 (aliphatic), 33.73 (aliphatic), 33.42 (aliphatic), 33.12 (aliphatic), 32.91 (aliphatic), 32.65 (aliphatic), 28.75 (aliphatic), 28.70 (aliphatic), 28.54 (aliphatic), 26.61 (aliphatic), 26.00, (aliphatic) 25.66 (aliphatic), 25.55 (aliphatic), 25.48 (aliphatic)

Accurate counting of peaks in the aliphatic region of the ^{13}C NMR spectrum was not possible due to overlapping signals.

HRMS (ESI-LTQ Orbitrap XL, CH_3CN) m/z found 1267.5611, calculated for 1267.5612 for the +5 charged species.

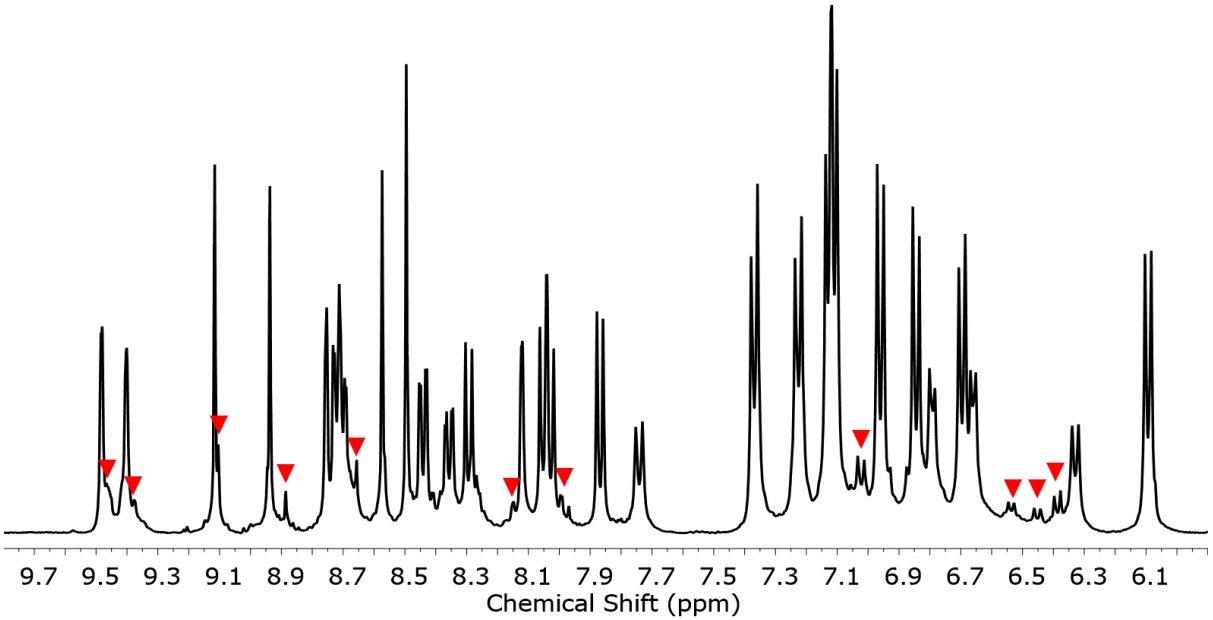

Figure 6.20 | Aromatic region of the ^{1}H NMR spectrum of **6.3**. Peaks of a second species which is observed to diffuse alongside the major species are highlighted with red triangles. These peaks are proposed to be those of the minor diastereomers but may be those of an unrelated structure.

*Synthesis of **6.5** and **6.6***

The synthesis of **6.5** is described here, **6.6** is synthesised in an identical manner using opposite handedness of the chiral dinaniline. 6,6´-diformyl-3,3´-bipyridine **L**[1] (14.2 mg, 67 mmol, 8 equiv.), **6.1** (1R, 2R) (29.5 mg, 66 mmol, 8 equiv.) and $Fe(OTf)_2$ (17.9 mg, 50 mmol, 6 equiv.) were added to a Schlenk flask in a glovebox. Degassed and dried CH_3CN (8 mL) was added along with a Teflon-coated magnetic stir-bar. The sealed Schlenk flask was removed from the glovebox and left to stir at 80 °C for 54 hours. The dark blue reaction mixture was allowed to cool to room temperature and was then filtered through a glass fibre filter (0. 7 µm pore size). The acetonitrile was concentrated under a stream of N_2 to a volume of 2 mL. Addition of diisopropyl ether (6 mL) resulted in the precipitation of a dark blue solid. The suspension was then centrifuged (10 min, 3000 RPM), the eluent decanted. Further diisopropyl ether (6 mL) was added, the powder was resuspended by sonication and then centrifuged. Again, the eluent was decanted. The residue was then dried *in vacuo* to afford the solid product as a fine dark blue powder (37 mg, 61%).

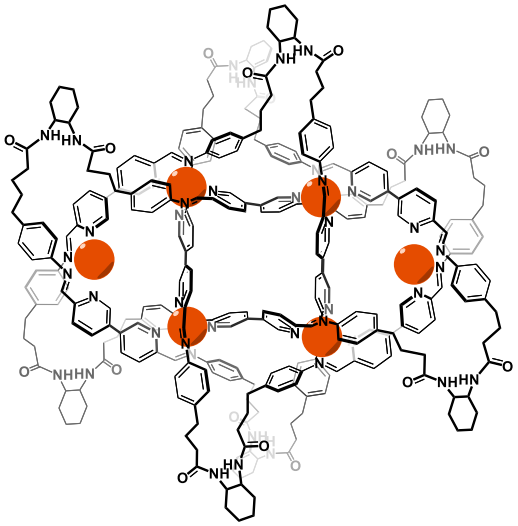

^{1}H NMR (500 MHz, 298 K, CD_3CN) δ: 177.5, 159.8, 49.0, 15.4, 14.7, 14.5, 11.1, 10.3, 9.6, 9.4, 9.1, 8.8, 8.7, 8.2, 7.7, 7.5, 7.3, 7.0, 6.8, 6.8, 6.3, 6.0, 5.8, 4.7, 4.3, 4.1, 4.0, 3.7, 3.6, 3.4, 2.9, 2.5, 1.3, -5.5.

Accurate counting of peaks ws not possible do to significant signal broadening and overlap.

HRMS (ESI-LTQ Orbitrap XL, CH_3CN) m/z found 1256.1710, calculated for 1256.1707 for the +5 charged species.

*Synthesis of **6.9***

To a stirred solution of **5.11** (62 mg, 10 µmol, 1 equiv.) in MeCN/MeOH (5/1, v/v, 12 mL total volume) at room temperature was added BH_3•THF (1 M, 480 µL, 480 µmol, 3 equiv./imine). The mixture was stirred for 10 minutes while the color of the solution changed from deep green to dark brown. CH_2Cl_2 (10 mL) and ethylenediamine (18 µL, 0.27 mmol, 4.5 equiv./Fe) were then added and the mixture was stirred for 10 minutes. The resulting suspension was poured in 30 mL H_2O and the mixture was extracted with 10 × 5 mL CH_2Cl_2 (note: the emulsions were broken mechanically). The combined organic layers were filtered on cotton covered with sand then solvents were removed under vacuum. The residue was dissolved in CH_2Cl_2, filtered on Celite® and dried under vacuum affording the reduced and demetallated knot **6.9** (25.4 mg, 6.19 µmol assuming pure sample). Yield: 62%.

6.10 References

(1) Bordoli, R. J.; Goldup, S. M. An Efficient Approach to Mechanically Planar Chiral Rotaxanes. *J. Am. Chem. Soc*. **2014**, *136*, 4817–4820.

(2) Denis, M.; Lewis, J. E. M.; Modicom, F.; Goldup, S. M. An Auxiliary Approach for the Stereoselective Synthesis of Topologically Chiral Catenanes. *Chem* **2019**, *5*, 1512–1520.

(3) Dietrich-Buchecker, C. O.; Sauvage, J. -P. A Synthetic Molecular Trefoil Knot. *Angew. Chem. Int. Ed. English* **1989**, 28, 189–192.

(4) Chambron, J.-C.; Dietrich-Buchecker, C.; Nae¨lnae¨, G.; Rapenne, N.; Sauvage, J.-P. Resolution of Topologically Chiral Molecular Objects. *Chirality* **1998**, *10*, 125-133.

(5) Danon, J. J.; Krüger, A.; Leigh, D. A.; Lemonnier, J.-F.; Stephens, A. J.; Vitorica-Yrezabal, I. J.; Woltering, S. L. Braiding a Molecular Knot with Eight Crossings. *Science* **2017**, *355*, 159–162.

(6) Ponnuswamy, N.; Cougnon, F. B. L.; Clough, J. M.; Pantoş, G. D.; Sanders, J. K. M. Discovery of an Organic Trefoil Knot. *Science* **2012**, *338*, 783–785.

(7) Gil-Ramírez, G.; Hoekman, S.; Kitching, M. O.; Leigh, D. A.; Vitorica-Yrezabal, I. J.; Zhang, G. Tying a Molecular Overhand Knot of Single Handedness and Asymmetric Catalysis with the Corresponding Pseudo-D_3-Symmetric Trefoil Knot. *J. Am. Chem. Soc*. **2016**, *138*, 13159–13162.

(8) Feigel, M.; Ladberg, R.; Engels, S.; Herbst-Irmer, R.; Fröhlich, R. A Trefoil Knot Made of Amino Acids and Steroids. *Angew. Chem. Int. Ed*. **2006**, *45*, 5698–5702.

(9) Jinks, M. A.; de Juan, A.; Denis, M.; Fletcher, C. J.; Galli, M.; Jamieson, E. M. G.; Modicom, F.; Zhang, Z.; Goldup, S. M. Stereoselective Synthesis of Mechanically Planar Chiral Rotaxanes. *Angew. Chem. Int. Ed*. **2018**, *57*, 14806–14810.

(10) Castilla, A. M.; Miller, M. A.; Nitschke, J. R.; Smulders, M. M. J. Quantification of Stereochemical Communication in Metal-Organic Assemblies. *Angew. Chem. Int. Ed*. **2016**, *55*, 10616–10620.

(11) Riddell, I. A.; Smulders, M. M. J.; Clegg, J. K.; Hristova, Y. R.; Breiner, B.; Thoburn, J. D.; Nitschke, J. R. Anion-Induced Reconstitution of a Self-Assembling System to Express a Chloride-Binding $Co_{10}L_{15}$ Pentagonal Prism. *Nat. Chem*. **2012**, *4*, 751–756.

(12) Riddell, I. A.; Hristova, Y. R.; Clegg, J. K.; Wood, C. S.; Breiner, B.; Nitschke, J. R. Five Discrete Multinuclear Metal-Organic Assemblies from One Ligand: Deciphering the Effects of Different Templates. *J. Am. Chem. Soc*. **2013**, *135*, 2723–2733.

(13) Lavendomme, R.; Ronson, T. K.; Nitschke, J. R. Metal and Organic Templates Together Control the Size of Covalent Macrocycles and Cages. *J. Am. Chem. Soc*. **2019**, accepted

(14) Danon, J. J.; Krüger, A.; Leigh, D. A.; Lemonnier, J. F.; Stephens, A. J.; Vitorica-Yrezabal, I. J.; Woltering, S. L. Braiding a Molecular Knot with Eight Crossings. *Science* **2017**, 355, 159-162.

(15) Zhang, L.; Stephens, A. J.; Nussbaumer, A. L.; Lemonnier, J.-F.; Jurček, P.; Vitorica-Yrezabal, I. J.; Leigh, D. A. Stereoselective Synthesis of a Composite Knot with Nine Crossings. *Nat. Chem*. **2018**, *10*, 1083–1088.

7

Future Work and Conclusions

This Chapter will discuss possible avenues toward new, topologically complex synthetic molecules. In particular, it will outline how three-dimensional metal-organic architectures could act as the framework around which the organic knot or catenane is woven. This is an extension of the two-dimensional circular helicate strategy, first introduced by Leigh,[1–3] which was itself an extension of the one-dimensional strategy developed by Sauvage.[4]

The chemistry outlined in the Chapter follows on from the work outlined in Chapters 5 and 6 of this thesis. It is envisaged that this work could lead to the synthesis of the most topologically complex knotted and interlocked molecules described. To date, the highest crossing number reported in any knotted molecule is nine.[5] The two knotted structures described here would have crossing numbers of fifteen and twenty-four. A design strategy for several multiply-interlocked [2] and [3]catenanes is also outlined.

7.1 Background

As described in Chapter 5, there are several ways to synthesise topologically complex molecules. Previous reports have utilised π–π stacking,[6] hydrogen bonding[7,8] and the hydrophobic effect[9] to form such species. Perhaps the most extensively employed strategy has been the use of coordination-driven self-assembly.

Beginning with Sauvage's work in the later 1980s, this approach has relied on the organisation of a set of coordinating organic molecules around the cationic metal centres. This process is then followed by a chemical transformation whereby pairs of proximal termini are coupled together, leading to a single organic molecule which traces a continuous path around the metal centres.

In its first iteration linear helicates were employed. This strategy made possible the synthesis of [2]catenanes,[10] a trefoil knot[4] and a Solomon link.[11] Increasing the number of turns in the helicate, and therefore its length, could in principle lead to more topologically complex species. In practice, this proved unsuccessful. The next in the series of molecules targeted by Sauvage was the pentafoil knot. However, it was found that as the length of the linear helicate was increased beyond this point, the probably of the desired connections forming, and therefore the yield of the knot, becomes negligible.

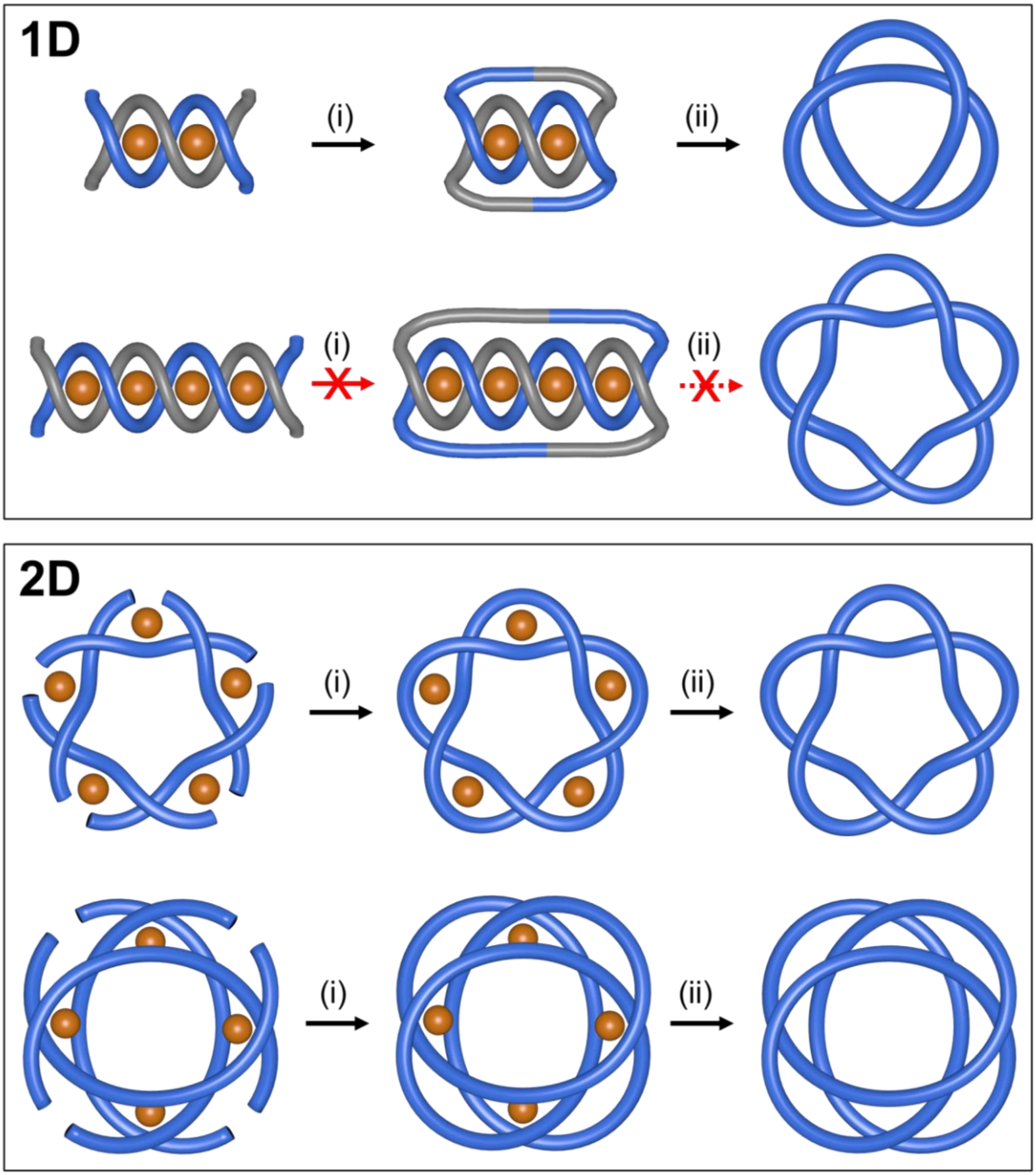

Figure 7.1 | Progress in the synthesis of molecular knots, starting with the trefoil knot formed from a one-dimensional linear double helicate. Extending the helicate to form a pentafoil knot failed, as the termini were too far apart. Two-dimensional circular helicates offer an alternative strategy and have enabled the synthesis of highly interwoven knots and catenanes, such as the pentafoil and 8_{19} knots. (i) represents a terminus-to-terminus coupling reaction while (ii) denotes demetallation to yield the purely organic knotted molecule.

In order to circumvent this problem, Leigh recognised that circular helicates could offer an alternative pathway to forming knots and catenanes. This approach essentially provides an extra dimension in which to organise the coordinating organic molecules around the metal centres, from one dimension up to two dimensions. This alters the ways in which ligand termini can be held together and, perhaps more importantly, how they can be held away from others, preventing undesired competing connections. This work led to the first syntheses of a pentafoil knot[1] and a Star of David Catenane,[2] as well as a new high-yielding synthesis of a Solomon link.[12] Varying the direction at which the functionalities at the termini of the ligands project from the two-dimensional grids has also allowed for the synthesis of a variety of other species such an 8_{19} knot[3] and a composite knot with a crossing number of nine,[5] the highest reported thus far.

This approach to knot and catenane synthesis is far from exhausted. There is a vast array of metal-organic molecular grids and circular helicates to select from, and the intelligent design of new connection patterns between ligand termini leaves open the possibility of designing a broad range of topologically complex molecules. With that said, working with two-dimensional motifs does necessarily place certain restrictions on what is achievable. For instance, the number of strands one can weave around the metal centres is fundamentally limited by the preferred coordination mode of the metal centre and the denticity of the ligand's coordinating motifs.

Three-dimensional architectures, of which there are many reported examples, could offer new opportunities. Here I will outline a set of structures and connection patterns which appear to be particularly promising.

7.2 Metal-Organic Polyhedra

The M_6L_8 extended circular helicate **5.9** is geometrically interesting for a number of reasons in its own right, as has been described in Chapter 5. It is also a rather anomalous result in a family of closely related molecules.

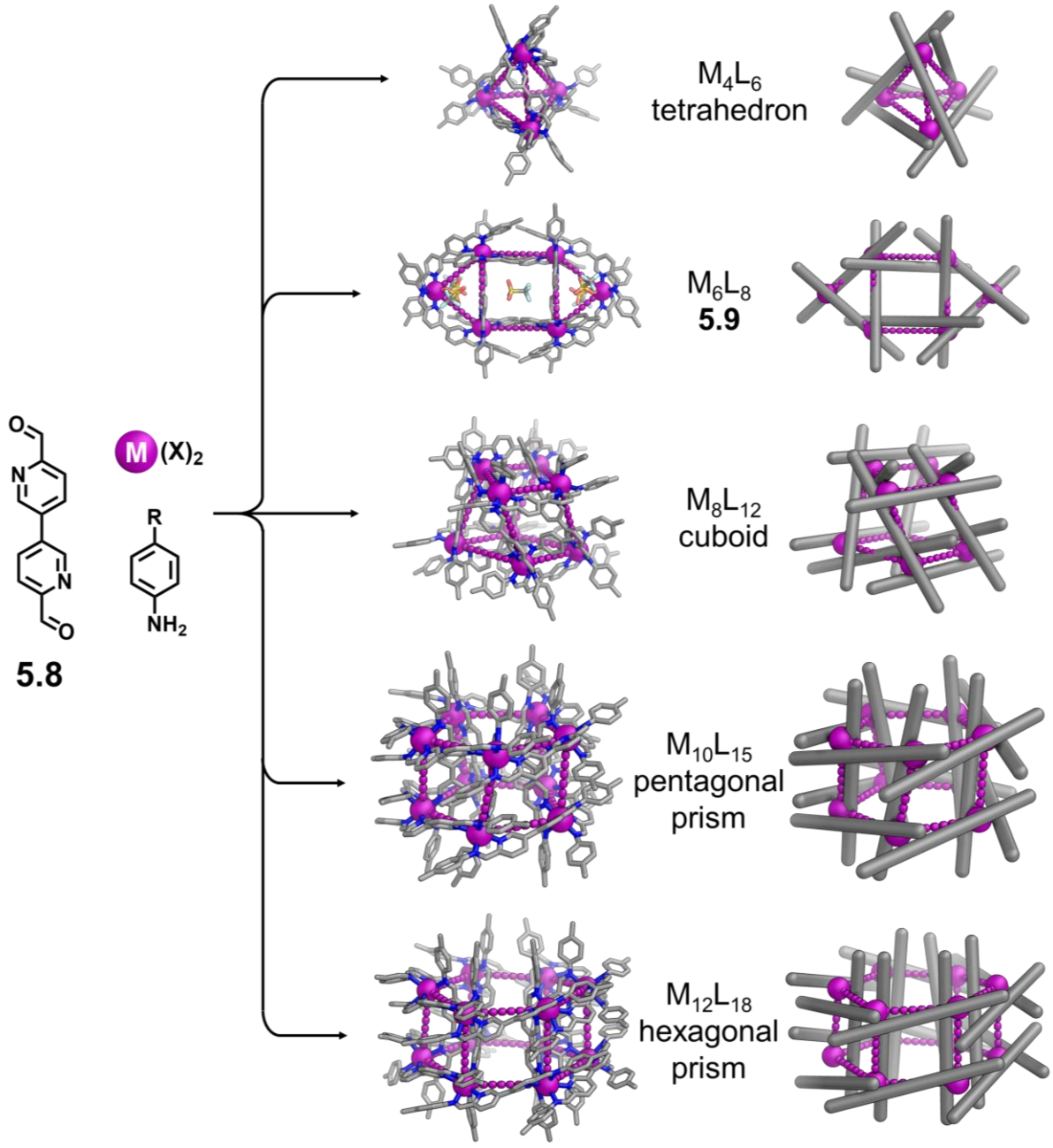

Figure 7.2 | Crystal structures and schematic presentations of each of the reported metal-organic structures formed using subcomponent **5.8**. The assembly obtained depends on the templating anion used, as well as the cation in certain cases. From the top; M_4L_6 tetrahedron, M_6L_8 grid, M_8L_{12} cuboid, $M_{10}L_{15}$ pentagonal prism and $M_{12}L_{18}$ hexagonal prism.

Extended circular helicate **5.9** is the only *quasi*-planar metal-organic structure formed with dialdehyde subcomponent **5.8**. Each of the other structures formed are three-dimensional polyhedra, ranging in size from a M_4L_6 tetrahedron up to a $M_{12}L_{18}$.[13,14] These structures have been characterised in solution, as well as in the solid state. It is reasonable to assume that this set of subcomponents may be capable of producing other interesting assemblies.

There are a number of reasons for this structural diversity. Metal-organic structures built around octahedral coordination complexes can have two types of vertices, *mer* and *fac*. Depending on which of these two stereochemical states the vertices adopt, different supramolecular structures will result. The M_4L_6 tetrahedron is based on four *fac* vertices, the M_6L_8 grid (used in Chapters 5 and 6 of this thesis) and the M_8L_{12} cuboid are based on a mixture of *mer* and *fac* vertices, while the $M_{10}L_{12}$ and $M_{12}L_{18}$ barrels are based entirely on *mer* vertices.

Several reasons for a preference for a *mer* or *fac* configuration have been postulated, and characteristic features of the two states have been noted.[15] *Mer* vertices typically lead to electron-rich (aniline) and electron-poor (pyridyl) aromatic rings being organised in stacked arrangements, separated by distances of 3–5 Å, unlike in *fac* based structures. This suggests that π–π stacking plays an important role in stabilising the larger structures based on *mer* vertices. A second important feature is that *fac* vertices lead to smaller assemblies. Therefore, they are typically entropically favoured.

Anion templation is also observed to play a crucial role. In each crystal structures obtained thus far, anions have been found to interact with pockets inside and around the assemblies. In solution this can be used to template certain assemblies which would otherwise exist as a mixture of products. Several other factors such as temperature, concentration and solvent composition have been found to play a role in the assembly of this system of subcomponents.[13,16]

7.3 Connection Patterns

Owing to the number of ligand termini in each of these structures (twelve in the case of the M_4L_6 tetrahedron and thirty-six for the $M_{12}L_{18}$ hexagonal prism) and the way in which they project out from the architectures into space, it is quite difficult to visualise what structure may result from a given pattern of connections.

It is instructive to consider one particular example and, using the methods developed in that case, to shed light on what may happen for the other structures. The example chosen was the $M_{10}L_{15}$ pentagonal prism. This structure is one of the best studied in the family of polyhedra described above.

The prism is built around a series of ten *mer* vertices, which organise the fifteen ligands in a pentagonal prismatic arrangement. Five of the ligands can be described as axial, running from the top to the bottom of the prism, while the remaining ten form two identical circular helicates which run around the top and bottom of the prism. In Figure 7.3 the axial ligands have been shaded in white, while the top and bottom circular helicates have been shaded in orange and blue, respectively.

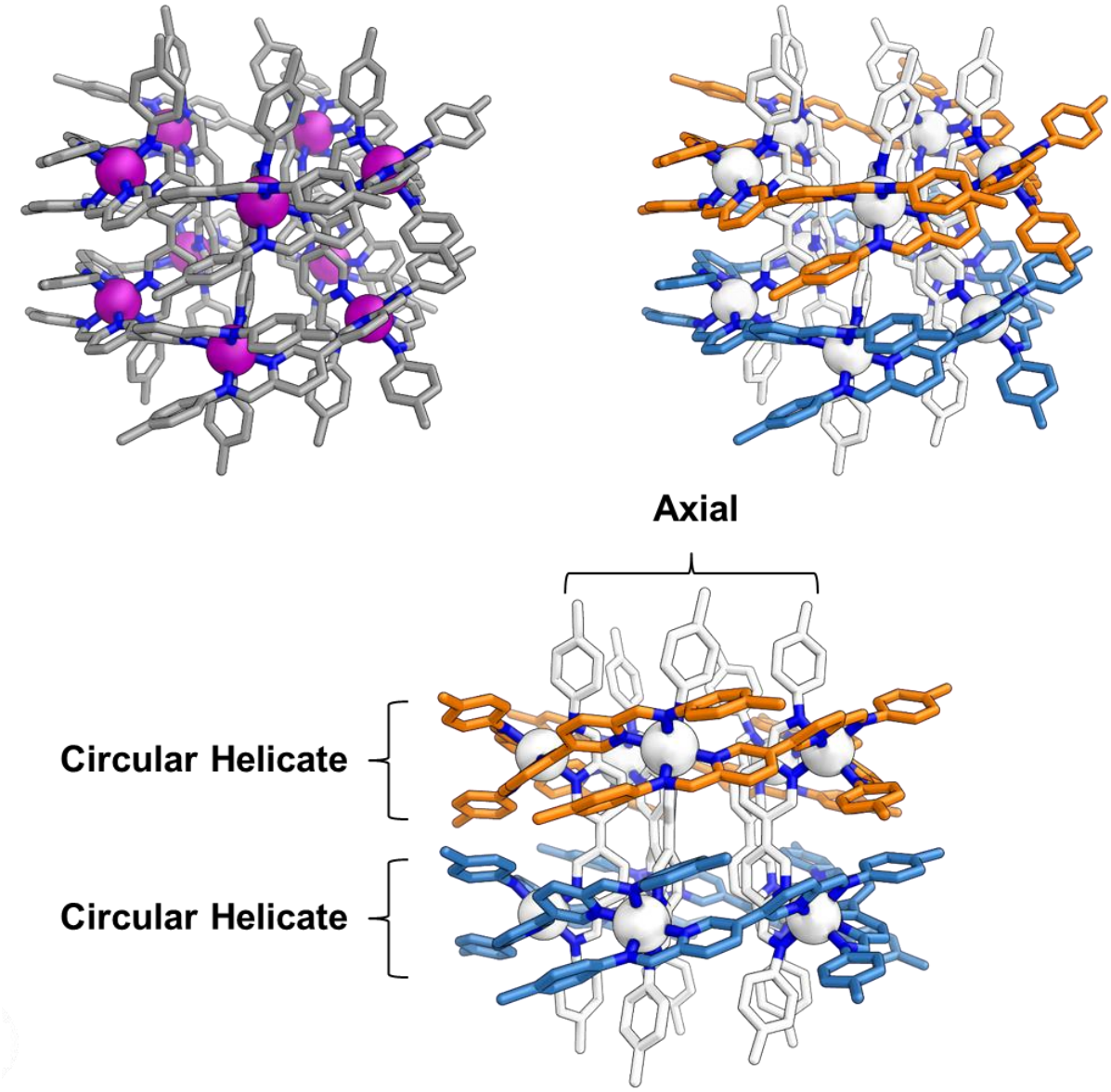

Figure 7.3 | Regions of the pentagonal prism. The axial ligands have been shaded in white, while the two helicates are coloured in orange and blue. The structure is homochiral.

Recognising these distinct regions in the prism make it possible to start considering which types of connections between the different termini are feasible. Just as the ligands can be separated into different groups within the prism, the types of connections can be broken up into two different categories. These have been labelled helicate-to-axial and helicate-to-helicate (Figure 7.4).

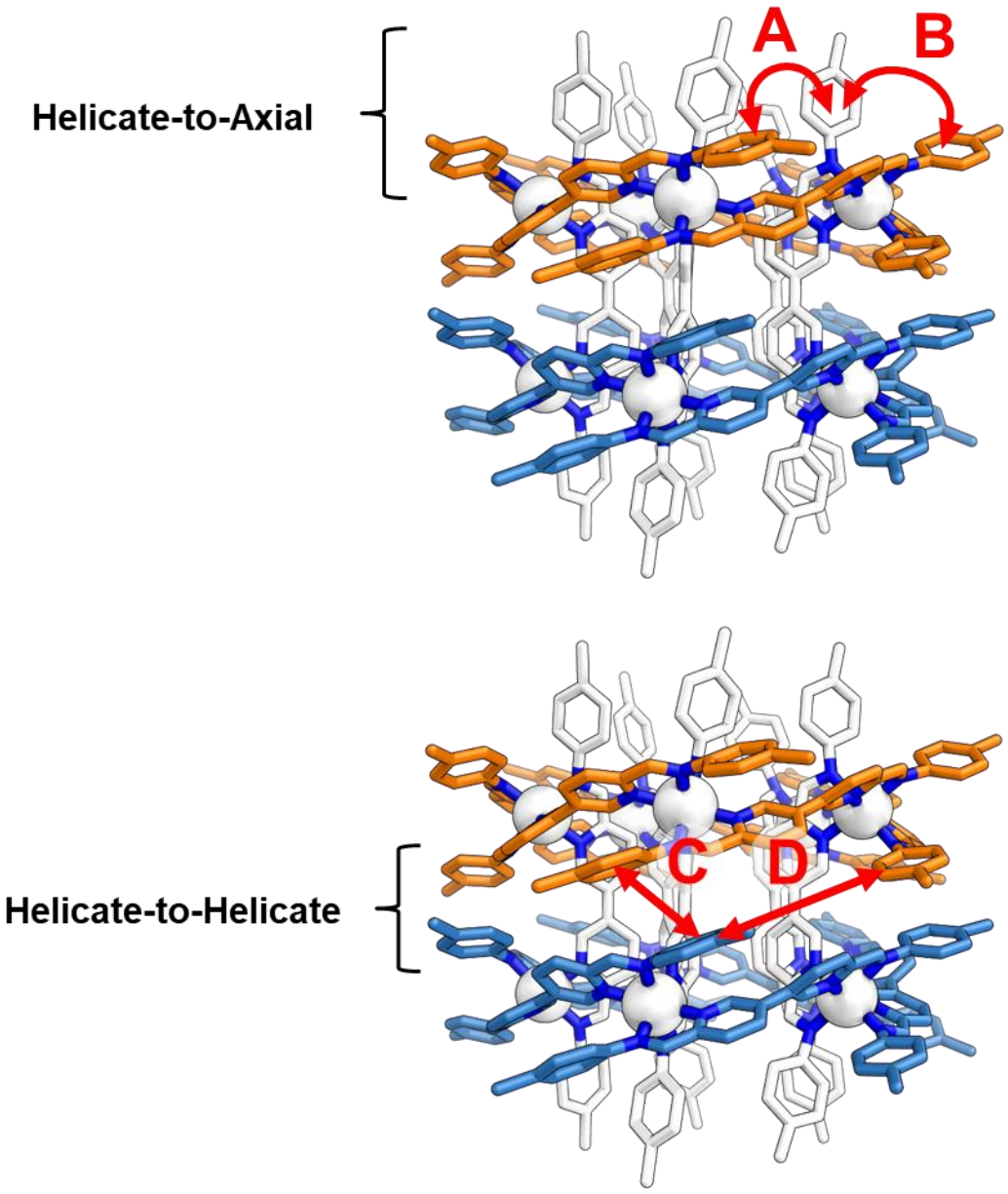

Figure 7.4 | The types of connections can be divided up into two categories, helicate-to-axial and helicate-to-helicate. In each of these two categories there are two connection types. For helicate-to-axial these are **A** and **B**, for helicate-to-helicate they are **C** and **D**. Each connection type is distinct and could be targeted with the judicious selection of an appropriate linker. Only one of **A** or **B** can occur in a given structure, similarly for **C** and **D**.

The next task is to consider which aniline residues are held in close proximity to one another in each connection region. These proximal aniline residues will act as the points at which the ligands can be connected. For simplicity's sake, only the distance between the phenyl ring

centroids were considered at this stage. Chemical detail such as the substitution pattern of the ring, steric clash and torsion angles, all of which are fundamentally important, are neglected for now, but revisited at a later stage for all interesting candidates identified.

This analysis revealed two possible connection types in each of the two connection regions; **A** and **B** for the helicate-to-axial region, **C** and **D** for the helicate-to-helicate region. The phenyl centroid to phenyl centroid distances in each case were measured to be 10.5 ± 0.4 Å (**A**), 5.4 ± 0.2 Å (**B**), 4.4 ± 0.1 Å (**C**) and 10.2 ± 0.2 Å (**D**). These distances are similar to those spanned in previously reported catenanes and knots.[3,17]

These connections are organised in pairs, and so it follows that there are four possible knotting patterns. These are **AC**, **AD**, **BC** and **BD**. Note that it is not possible to have **CD**, for example, as this would require the use of certain aniline residues twice and therefore isn't feasible. At this stage it is possible to consider the connecting of the ligand termini in these different patterns. Although difficult to demonstrate clearly, this analysis produced a number of interesting results.

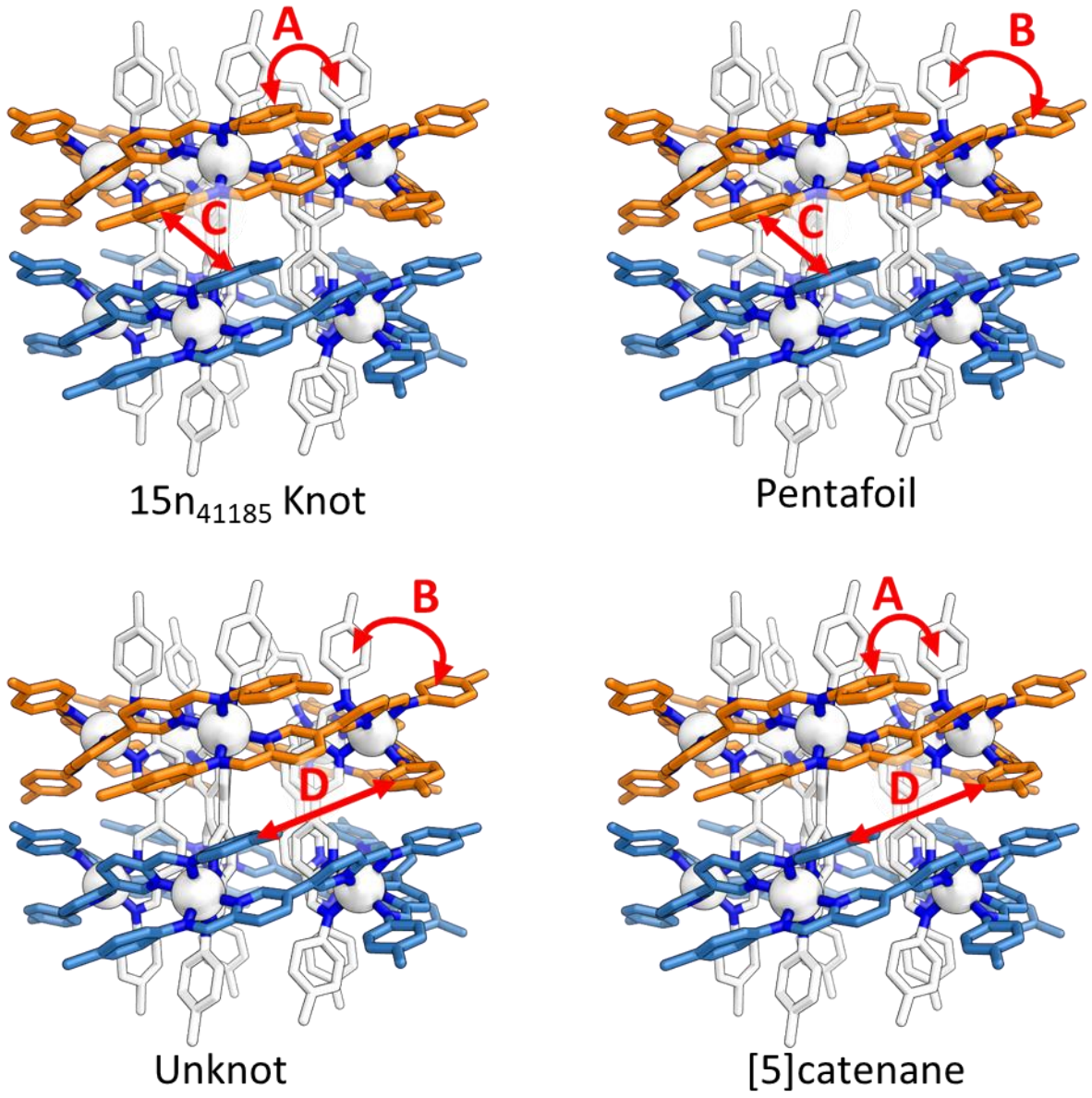

Figure 7.5 | The four possible connection permutations for the pentagonal prism. In each case only one connection of each type is shown for clarity.

In short, four topologically interesting structures were found. An **AC** connection pattern leads to a $15n_{41185}$ knot, which is a torus knot.[18] **AB** leads to a 5_1 or pentafoil knot. **BD** leads to an unknot or macrocycle which incorporates all of the subcomponents. And finally, **AD** leads to a [5]catenane, where each of the five macrocycles includes three equivalents of both **5.8** and the flexibly linked dianiline subcomponent.

The $15n_{41185}$ knot and [5]catenane stand out as two particularly interesting targets. In the latter case, each macrocycle is independently tied to the other four macrocycles. The removal of one

of the macrocycles from the system would yield the [4]catenane, removing two gives the [3]catenane, and so forth. The $15n_{41185}$ knot would have the highest number of crossing points of any molecular knot by some margin.

In order to more clearly understand how one of these target molecules might be targeted, particular attention was paid to the **AC** connection pattern which gives the 15 crossing knot. The details of this analysis are outlined below.

7.4 15 Crossing Knot

In the previous section of this chapter the centroid to centroid distances of the aniline residues were found to be 10.5 ± 0.4 Å for **A** and 4.4 ± 0.1 Å for **C**. These two measurements give a very rough estimate of the feasibilities of the connections. A closer investigation of the connections is required to ascertain their feasibility and to devise a strategy for favouring one over the other competing connections. For example, any linker designed to make connection type **A** could lead to connection type **B** if the linker isn't carefully selected. This would lead to a pentafoil knot forming, which is comparatively less interesting.

If a strategy like that described in Chapters 5 and 6 is used, where the dialdehyde subcomponent and a single type of flexible dianiline are combined, the linker must also be capable of forming the two types of connections required (helicate-to-helicate and helicate-to-axial, Figure 7.4). The 8_{19} knot described earlier in this thesis attests to the feasibility of this approach.

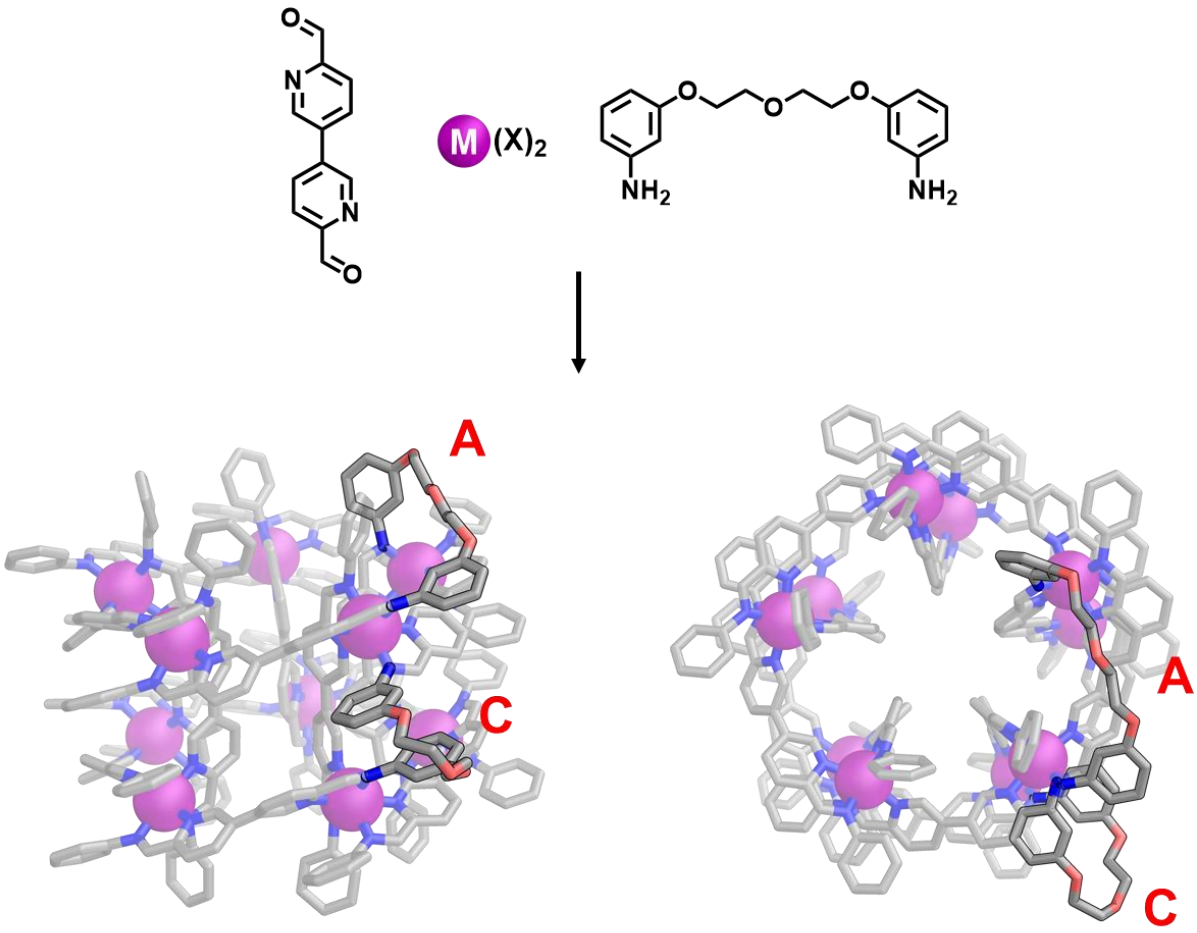

Figure 7.6 | One of each of the connection types **A** and **C**. The thirteen other connections have been omitted for clarity, but are symmetry equivalent to those shown here. In total there are ten **A** and five **C** connections.

In Figure 7.6, two of the connections (type **A** and **C**) are modelled with a small ethyl glycol based dianiline, similar to **5.10** used in Chapter 5. The model is based on a crystal structure obtained for the Ni^{II} pentagonal prism. Inspection of this structure shows that *meta*-substitution of the aniline residue may favour both connection **A** and **C**. In contrast, *para*-substitution would favour connection types **B** and **D**. The resulting configurations of the ethyl glycol fragment were compared to several hundred examples available in the CCDC and appear to be viable.

In effect, **A** and **B** are the competing connections for a *meta*-substituted flexible dianiline. It is important to note that there is significant variation in the position of ligands in the structure which are seen to be chemically equivalent in solution. This is most likely due to crystal packing effects. Given this, and the level of calculation used to model these molecules, trying

to infer too much about which linker will favour **A** or **B** is quite meaningless. In reality, it would be more productive to try a (relatively small) range of dianilines and to experimentally verify the nature of the connection. As each of the possible outcomes are interesting in their own right, the risk of such an approach seems acceptable.

7.5 Scope of the Approach

The previous two sections have outlined how this new approach to the synthesis of molecular knots might apply to the $M_{10}L_{15}$ pentagonal prism. The principle applies in the same way to the M_8L_{12} cuboid and the $M_{12}L_{18}$ hexagonal prism described earlier (Figure 7.2). In each case, there are at least four feasible connection patterns, as with the pentagonal prism. All of these appear to yield complex catenanes or knots.

One of the connection patterns, **AD**, in the $M_{12}L_{18}$ hexagonal prism has been tentatively assigned as a 24 crossing knot. This example is almost certainly a torus knot, however finding an appropriate Alexander-Briggs notation for it has proven challenging. This is presumably because as the number of crossing points increases, the number of possible knots grows exponentially. For perspective, there are over 1.7 million knots with sixteen or fewer crossings.[19] The most extensive tabulation of knots seems to only extend to knots with 22 or fewer crossings.[20]

The three other connection patterns, **AC**, **BC** and **BD**, applied to the hexagonal prism, lead to three distinct catenated species. **AC** and **BC** are [2]catenanes while **BD** is a [3]catenane. It appears that the [2]catenanes, resulting from **AC** and **BC** connections, are at least triply interlocked. In the [3]catenane, each of the macrocycles are independently interlocked. That is to say, it is not a Borromean link. If one link is removed, the two others remain interlocked. In fact, the removal of one macrocycle generates another topologically interesting molecule, a Solomon link, where the [2]catenane is doubly interlocked. What this says about the nature of the interlocking in the parent [3]catenane is still unclear, but it is certainly a very intricate braiding pattern, whatever it turns out to be.

7.6 Conclusion

In conclusion, this idea of using three-dimensional supports to organise ligands in space to enable complex weaving is nothing more than an extension of the fantastic work of Sauvage, Leigh, Stoddart, Nitschke and many others. It proposes that working with an extra dimension could give access to a new family of exceptionally complex interlocked molecules and therefore warrants further investigation. I will be undertaking these investigations in the Leigh group, in collaboration with the Nitschke group.

This idea builds directly on the work described in Chapters 5 and 6 of this thesis on the synthesis of a new form of 8_{19} knot. This new form exhibits D_2 symmetry, unlike the only other reported 8_{19} knot which has D_4 point symmetry.[21] The ability to form desymmetrised knots may one day enable the regioselective functionalisation of these topologically interesting species.

We have taken significant steps toward the first enantioselective synthesis of a molecule whose stereogenic unit is completely unconditional and topological in nature. There are still numerous challenges left to overcome if this goal is to be realised. If the aniline exchange strategy we are aiming to develop is to work, a route which involves rapid aniline exchange while maintaining the integrity and topological chirality of the knot must be devised.

This thesis has also described the formation of a series of geometrically complex polyhedra, all constructed around bimetallic vertices. Three new structures types were identified; homo-bimetallic octahedra **3.9** and **3.10**, hetero-bimetallic tetrahedra **3.11** and **3.12** and trigonal prism **4.2**. Perhaps more importantly though, this work has shown that bimetallic vertices can be treated as structurally and coordinatively flexible building blocks in the construction of metal-organic polyhedra. This is in much the same way that flexible organic components have been used to construct amazingly complex architectures.[22,23]

Finding such components and strategies which allow for serendipitous results to spring forth has been, and will continue to be, an integral part of the field of supramolecular self-assembly. Of course, complete reliance on such an approach to generate results and data which can drive our understanding of the processes guiding the assembly of molecules will not be sufficient. Chapters 5, 6 and 7 of this thesis are an example of how considered tailoring of molecules can lead to interesting species.

Extended circular helicate **5.9** came about as a result of serendipity, as did nearly all of the other polyhedra described in Figure 7.2. Importantly though, each serendipitous result informed the design of the following experiment, which enable the synthesis of such a complex set of polyhedral architectures. The design of the 8_{19} molecular knots described in this thesis then built on this. This interplay of serendipity and hypothesis-driven inquiry is key to the design of interesting, surprising and impressive molecules and molecular systems.

7.6 References

(1) Ayme, J.-F.; Beves, J. E.; Leigh, D. A.; McBurney, R. T.; Rissanen, K.; Schultz, D. A Synthetic Molecular Pentafoil Knot. *Nat. Chem*. **2012**, *4*, 15–20.

(2) Leigh, D. A.; Pritchard, R. G.; Stephens, A. J. A Star of David Catenane. *Nat. Chem*. **2014**, *6*, 978–982.

(3) Danon, J. J.; Krüger, A.; Leigh, D. A.; Lemonnier, J.-F.; Stephens, A. J.; Vitorica-Yrezabal, I. J.; Woltering, S. L. Braiding a Molecular Knot with Eight Crossings. *Science* **2017**, *355*, 159–162.

(4) Dietrich-Buchecker, C. O.; Sauvage, J. -P. A Synthetic Molecular Trefoil Knot. *Angew. Chem. Int. Ed. English* **1989**, *28*, 189–192.

(5) Zhang, L.; Stephens, A. J.; Nussbaumer, A. L.; Lemonnier, J.-F.; Jurček, P.; Vitorica-Yrezabal, I. J.; Leigh, D. A. Stereoselective Synthesis of a Composite Knot with Nine Crossings. *Nat. Chem*. **2018**, 10, 1083–1088.

(6) Ashton, P. R.; Matthews, O. A.; Menzer, S.; Raymo, F. M.; Spencer, N.; Stoddart, J. F.; Williams, D. J. Molecular Meccano, 27. A Template-Directed Synthesis of a Molecular Trefoil Knot. *Liebigs Ann*. **1997**, *12*, 2485–2494.

(7) Carver, F. J.; Hunter, C. A.; Shannon, R. J. Directed Macrocyclisation Reactions. *J. Chem. Soc. Chem.* Commun. **1994**, *10*, 1277.

(8) Safarowsky, O.; Nieger, M.; Fröhlich, R.; Vögtle, F. A Molecular Knot with Twelve Amide Groups—One-Step Synthesis, Crystal Structure, Chirality. *Angew. Chem. Int. Ed*. **2000**, *39*, 1616–1618.

(9) Ponnuswamy, N.; Cougnon, F. B. L.; Clough, J. M.; Pantoş, G. D.; Sanders, J. K. M. Discovery of an Organic Trefoil Knot. *Science* **2012**, *338*, 783–785.

(10) Cesario, M.; Dietrich-Buchecker, C. O.; Guilhem, J.; Pascard, C.; Sauvage, J. P. Molecular Structure of a Catenand and Its Copper(I) Catenate: Complete Rearrangement of the Interlocked Macrocyclic Ligands by Complexation. *J. Chem. Soc. Chem. Commun*. **1985**, *5*, 244.

(11) Nierengarten, J. F.; Dietrich-Buchecker, C. O.; Sauvage, J. P. Synthesis of a Doubly Interlocked [2]-Catenane. *J. Am. Chem. Soc*. **1994**, *116*, 375–376.

(12) Beves, J. E.; Campbell, C. J.; Leigh, D. A.; Pritchard, R. G. Tetrameric Cyclic Double Helicates as a Scaffold for a Molecular Solomon Link. *Angew. Chem. Int. Ed*. **2013**, *52*, 6464–6467.

(13) Riddell, I. A.; Hristova, Y. R.; Clegg, J. K.; Wood, C. S.; Breiner, B.; Nitschke, J. R. Five Discrete Multinuclear Metal-Organic Assemblies from One Ligand: Deciphering the Effects of Different Templates. *J. Am. Chem. Soc*. **2013**, *135*, 2723–2733.

(14) Riddell, I. A.; Ronson, T. K.; Clegg, J. K.; Wood, C. S.; Bilbeisi, R. A.; Nitschke, J. R. Cation- and Anion-Exchanges Induce Multiple Distinct Rearrangements within Metallosupramolecular Architectures. *J. Am. Chem. Soc*. **2014**, *136*, 9491–9498.

(15) Kieffer, M.; Pilgrim, B. S.; Ronson, T. K.; Roberts, D. A.; Aleksanyan, M.; Nitschke, J. R. Perfluorinated Ligands Induce Meridional Metal Stereochemistry to Generate M_8L_{12} , $M_{10}L_{15}$, and $M_{12}L_{18}$ Prisms. *J. Am. Chem. Soc*. **2016**, *138*, 6813–6821.

(16) Riddell, I. A.; Smulders, M. M. J.; Clegg, J. K.; Hristova, Y. R.; Breiner, B.; Thoburn, J. D.; Nitschke, J. R. Anion-Induced Reconstitution of a Self-Assembling System to Express a Chloride-Binding $Co_{10}L_{15}$ Pentagonal Prism. *Nat. Chem*. **2012**, *4*, 751–756.

(17) Wood, C. S.; Ronson, T. K.; Belenguer, A. M.; Holstein, J. J.; Nitschke, J. R. Two-Stage Directed Self-Assembly of a Cyclic [3]Catenane. *Nat. Chem*. **2015**, *7*, 354–358.

(18) Marenda, M.; Orlandini, E.; Micheletti, C. Discovering Privileged Topologies of Molecular Knots with Self-Assembling Models. *Nat. Commun*. **2018**, *9*, 3051.

(19) Horner, K. E.; Miller, M. A.; Steed, J. W.; Sutcliffe, P. M. Knot Theory in Modern Chemistry. *Chem. Soc. Rev*. **2016**, *45*, 6432–6448.

(20) Hoste, J. The Enumeration and Classification of Knots and Links. *Handb. Knot Theory* **2005**, 209–232.

(21) Danon, J. J.; Krüger, A.; Leigh, D. A.; Lemonnier, J. F.; Stephens, A. J.; Vitorica-Yrezabal, I. J.; Woltering, S. L. Braiding a Molecular Knot with Eight Crossings. *Science* **2017**, *355*, 159-162.

(22) Al-Rasbi, N. K.; Tidmarsh, I. S.; Argent, S. P.; Adams, H.; Harding, L. P.; Ward, M. D. Mixed-Ligand Molecular Paneling: Dodecanuclear Cuboctahedral Coordination Cages Based on a Combination of Edge-Bridging and Face-Capping Ligands. *J. Am. Chem. Soc.* **2008**, *130*, 11641–11649.

(23) Hasenknopf, B.; Lehn, J.-M.; Boumediene, N.; Dupont-Gervais, A.; Van Dorsselaer, A.; Kneisel, B.; Fenske. D. Self-Assembly of Tetra- and Hexanuclear Circular Helicates. *J. Am. Chem. Soc*. **1997**, *119*, 10956-10962.